UC Berkeley
UC Berkeley Electronic Theses and Dissertations

Title

Fluorescence Lifetime Imaging with Voltage Sensitive Fluorophores to Interrogate Membrane Potential in Cellular Physiology

Permalink

https://escholarship.org/uc/item/77q3m5gn

Author

Yaeger-Weiss, Susanna

Publication Date

2024

Peer reviewed|Thesis/dissertation

eScholarship.org Powered by the California Digital Library
University of California

Fluorescence Lifetime Imaging with Voltage Sensitive Fluorophores to Interrogate Membrane Potential in Cellular Physiology

By

Susanna Katherine Yaeger-Weiss

A dissertation submitted in partial satisfaction of the

requirements for the degree of

Doctor of Philosophy

in

Chemistry

in the

Graduate Division

of the

University of California, Berkeley

Committee in Charge:

Professor Evan W. Miller, Chair
Professor Matthew Francis
Professor Markita Landry

Summer 2024

Fluorescence Lifetime Imaging with Voltage Sensitive Fluorophores to Interrogate Membrane Potential in Cellular Physiology

© 2024

By Susanna Katherine Yaeger-Weiss

Abstract

Fluorescence Lifetime Imaging with Voltage Sensitive Fluorophores to Interrogate Membrane Potential in Cellular Physiology

by

Susanna Katherine Yaeger-Weiss

Doctor of Philosophy in Chemistry

University of California, Berkeley

Professor Evan W. Miller, Chair

Membrane potential (V_m) is a critical biophysical property in electrically excitable and non-electrically excitable cells. Established methods for measuring V_m successfully report the large, rapid changes that trigger key signaling pathways in electrically excitable cells but lack the capabilities to record over extended time periods or reliably quantify smaller changes in V_m. Emerging evidence suggests that smaller fluctuations in membrane potential occurring over seconds to hours may have a regulatory role in fundamental physiological processes in non-electrically excitable cells, such as cell cycle progression. However, robust characterization of membrane potential dynamics and possible mechanisms of bioelectric control has been limited by insufficient techniques for quantifying V_m over these physiologically relevant timescales. Fluorescence lifetime imaging with VoltageFluor dyes (VF-FLIM) provides a new approach for making minimally invasive and high-throughput measurements of absolute membrane potential over extended timescales.

This dissertation demonstrates the application of VF-FLIM to quantify membrane potential and track changes in non-electrically excitable cells. Chapter 1 introduces techniques for measuring membrane potential and summarizes evidence for membrane potential dynamics and bioelectric signaling during cell cycle progression. Chapter 2 presents initial work using VF-FLIM to identify differences in membrane potential across cell cycle phases, revealing a ~10 mV depolarization in G_2/M phase cells compared to cells in G_1 and S phase. Chapter 3 expands on this work and describes efforts towards monitoring real-time changes in V_m in live cells with development of a stable cell line expressing the sensor DHB-mVenus to track cell cycle progression, combined with a red-shifted VoltageFluor. Chapter 4 explores characterization of membrane potential dynamics induced by epidermal growth factor receptor signaling (EGFR), spanning four different EGFR ligands across two cell lines showing disparate responses to EGFR stimulation. A general protocol for VF-FLIM experiments in provided in Chapter 5, and Chapter 6 details essential considerations for data acquisition and analysis. Together, this work highlights the utility of VF-FLIM as an approach for optically recording V_m over extended time scales and offers new insights into membrane potential dynamics during cell cycle progression and epidermal growth factor receptor signaling in non-electrically excitable cells.

Table of Contents

Acknowledgements……..…...**ii**

Chapter 1: Bioelectrical Signaling During the Cell Cycle……...**1**

Chapter 2: Optical Estimation of Membrane Potential Throughout the Cell Cycle……..….**16**

Chapter 3: Tracking Changes in Membrane Potential Throughout the Cell Cycle……**35**

Chapter 4: EGFR-Induced Changes in Membrane Potential Across Cell Lines……**71**

Chapter 5: VoltageFluor Dyes and Fluorescence Lifetime Imaging for Optical Measurement of Membrane Potential…….**118**

Chapter 6: Optimizing Fluorescence Lifetime Acquisition and Fit Parameters for a New Microscope Setup…….**142**

Acknowledgements

I would like to thank all of my friends, family, and mentors who have helped guide me in this journey through graduate school. It's been a long road full of ups and downs, and I'm so appreciative of everyone who supported me.

To my mom, thank you for always believing in me. I couldn't have done this without your unwavering love, support, and encouragement throughout my entire life. Thank you for celebrating all of my successes, big and small, and encouraging me to push through the difficult times with grit, determination, and a good sense of humor. Grandma, I miss you every day. Thank you for always reminding me to keep my chin up and believe in myself. Aunt Sara, thank you for introducing me to the fun sides of science and math from a young age. And thanks for always helping me with my math homework – I quite literally might not have made it here without your help learning algebra and geometry.

To my brother, Ben, and sister-in-law, Jess, I'm so glad you moved out to California the same summer I did – it made moving across the country a lot less scary. Thank you for all of your support, from sending daily cat pictures and funny TikToks to being my second home in California, then Arizona, and now Minnesota. To Dad, Margaret, and the rest of my family in Minnesota, I'm so appreciative of all your love and support from afar.

To Evan, my PhD advisor, thank you for your mentorship and guidance over the last six years. Thank you for supporting me through the many hurdles I encountered, from the expected (qualifying exam and thesis writing) to the unexpected (a global pandemic) to the utterly absurd (finding out that two lasers were switched for years). I appreciated all of your guidance, from designing experiments to particularly tricky troubleshooting. I left every meeting feeling a little bit more confident in myself, and you helped me grow so much as a scientist and mentor during graduate school. Thank you for fostering a collaborative and welcoming community in lab. I couldn't imagine completing my PhD anywhere else.

To all the members of the Miller Lab, past and present, it's been a joy to work with all of you. Thank you for consistently making work fun, even when experiments went wrong or our lab was covered in construction materials or it was 90°F inside Hildebrand. Marisol and Kayli, I couldn't have asked for a better cohort, and our friendship in lab and outside of it was such a gift. Josh, Brittany, Ben (and Katie), Marisol, Kayli, Pavel, Anneliese, Jack, Julia, Kayla – our pandemic lawn hangs were a godsend. I'll miss Friday lunches, crossword puzzles, and karaoke nights with all of you. To Julia Lazzari-Dean and Anneliese Gest, thank you for being the best FLIM mentors. Julia, thanks for introducing me to FLIM and taking the time to answer all of my questions (and as a rotation student without any microcopy experience, I had a lot). Anneliese, it was a pleasure to learn from you and alongside you. I'm so glad we worked together, and I appreciated always being able to go to you for advice (and cat pics), even after you graduated.

Marisol, Kayli, Kerry, Nicole, Michelle, and Jamie – thank you for many much-needed girls' nights featuring lots of laughter, occasionally juicy gossip, and plenty of wine.

To Michael Daugherty, thank you for always encouraging me and cheering me on, from summer softball games to the final push of thesis writing. I love you so much, and I can't wait to celebrate and enjoy life outside grad school with you.

To Emily, Sami, and Emma, my first friends. From making up elaborate games during elementary school recess, to endless marathons of Buffy the Vampire Slayer at sleepovers, to celebrating Sami's wedding this summer, I'm so thankful for your lasting friendship.

Natalie and Maria – I'm endlessly grateful to both of you for keeping me grounded to life outside of grad school. Thank you for all of the encouraging phone calls and texts, beautiful pictures of nature, and extensive conversations about Taylor Swift.

To the members of the Snapchat group "cat snaps only" (Kyra, Emma, Liz, Kody, and Lisa), sharing pictures of our cats living their best lives truly brightens my day, and I'm glad it's been an easy way for all of us to stay in touch.

To my cat, Luna, thank you for keeping me company during many late nights of data analysis and writing. Yes, you can have an extra treat to celebrate when I'm done.

Thanks to the many other people who have supported my academic journey over the years. To Holly Aaron and Feather Ives, thank you for everything you do to keep to the Molecular Imaging Center running and for the opportunity to speak at AIM. To Silvia Cavagnero, my undergrad PI at UW Madison, thank you for giving me the opportunity to start research after my freshman year and guiding me all the way through to grad school. To my high school Academic Decathlon coaches, Flotty and Grivy – although most of the random knowledge I acquired during 3 years of Acadec hasn't exactly been relevant to my daily life (apart from doing crossword puzzles), the love of research you encouraged and public speaking skills you helped me develop have been essential.

Lastly, to the reader, thank you for taking the time to learn about my work over the past six years. Please don't tell me if you find any typos.

Chapter 1
Bioelectrical Signaling During the Cell Cycle

Abstract

All cells maintain an ionic gradient across the plasma membrane, producing a transmembrane potential (V_m). Changes in V_m ranging from tens of millivolts to nearly 100 millivolts occur over milliseconds to hours and serve as a critical bioelectric signal in many cellular processes. However, many existing tools for recording changes in membrane potential are optimized for quantifying large, rapid changes and are unsuitable for measuring smaller fluctuations over longer timescales associated with physiological processes like cell cycle progression. Recent advances in optical approaches, such as the use of fluorescence lifetime imaging, provide new opportunities for quantifying V_m over extended timescales. This introductory chapter presents an overview of techniques for recording changes in membrane potential and summarizes emerging evidence for the role of membrane potential dynamics in cell cycle progression.

Measuring Membrane Potential

Membrane potential (V_m) is an essential biophysical property for all cells. V_m arises from the ionic gradient across the selectively-permeable plasma membrane and is maintained by numerous selectively-permeable ion channels and ATP-utilizing pumps. In mammalian cells, V_m is primarily governed by the difference in extracellular and intracellular concentrations of K^+ ions and their movement through potassium leak channels, producing a negative resting potential.[1] Other ions including Na^+, Cl^-, and Ca^{2+} also contribute to the electrochemical gradient, with an estimated 10-50% of a cell's energy budget directed towards maintaining resting potential through the ATP-driven Na^+/K^+ pump.[2]

Rapid changes in V_m serve as an important bioelectric signal in electrically excitable cells like neurons and cardiomyocytes. Within milliseconds or seconds, action potentials of nearly 100 mV changes in V_m trigger neurotransmitter release in neurons[3] and contraction in cardiomyocytes.[4] In non-electrically excitable cells, smaller fluctuations in V_m occurring over seconds to hours have been linked to differentiation, migration, volume control, cell division, and cell cycle progression.[5–9] Established methods for measuring V_m are optimized for reporting the large, rapid changes associated with action potentials but lack the capabilities to record over extended time periods or reliably quantify smaller changes in V_m, thus motivating the need for new tools to measure V_m dynamics over longer time scales and further elucidate its role in these fundamental biophysical processes.

Electrode-based techniques like patch-clamp electrophysiology are the gold standard for measuring membrane potential in cells.[10–12] In whole-cell patch-clamp electrophysiology, the plasma membrane is ruptured with a micropipette to bring a recording electrode into direct contact with the cytosol. V_m is determined from the difference between the cytosolic electrode and a reference electrode in the extracellular bath solution. Whole-cell patch-clamp enables direct measurements of V_m with high temporal resolution and sub-mV precision. However, rupture of the plasma membrane is highly invasive and disrupts the physiological processes of interest. Patch-clamp recordings are also intractable to maintain over longer time scales. Furthermore, the technique is low throughput, requiring several minutes to obtain a whole-cell recording of a single cell. Spatial resolution is also limited since the electrode only probes the cell at a single point, which may or may not be representative of the potential throughout the entire membrane.

Optical approaches utilizing voltage-sensitive fluorophores facilitate analysis of many cells at once with high spatial resolution, providing a high throughput and minimally invasive alternative for visualizing fluctuations in membrane potential. These small-molecule or protein-based sensors are designed such that fluorescence intensity is modulated by changes in V_m.[13–17]However, fluorescence intensity can also be affected by dye loading, illumination intensity, photobleaching, and cellular morphology, making it difficult to directly correlate fluorescence intensity to voltage through electrophysiological calibration. Single color intensity-based optical methods can reliably report relative changes in membrane potential but are limited in their ability to quantify absolute millivolt values of V_m.

Ratio-based voltage sensors employ a two color approach to combat variations in dye loading and cell morphology. By measuring relative changes in intensity across two fluorescence channels, the known stoichiometric ratio between the two signals can be used to correct for artifacts in fluorescence intensity. Ratio-based V_m probes most commonly rely on Förster resonance energy transfer (FRET) or electrochromism to report changes in membrane potential. FRET-based V_m sensors display voltage-dependent energy transfer between a donor and an acceptor fluorophore and offer a higher signal-to-noise compared to single color techniques. However, FRET ratios can be highly variable between cells and across days. Genetically encoded FRET probes exhibit differences in photobleaching and protein maturation, while small-molecule FRET-oxonol sensors show variations in loading between cells.[15,18–20] Electrochromic ratio-based probes display changes in excitation or emission spectra of a single fluorophore in response to membrane potential and have excellent spatiotemporal resolution but limited sensitivity.[21–25] Furthermore, individual cells show varying relationships between voltage and the electrochromic ratio and attempts to translate ratio-based eletrophysiological calibrations between cells have been unsuccessful. Overall, the variability associated with FRET-based and electrochromic ratio-based sensors makes it challenging to reliably calibrate the ratiometric signal to voltage.

Fluorescence lifetime (τ_{fl}) measures the amount of time a population of fluorophores remain in its excited state and is an alternative readout to fluorescence intensity. Fluorescence lifetime is an intrinsic property and depends only on the rates of radiative and nonradiative decay pathways from the excited state, making it largely independent of extrinsic properties. Although lifetime can be sensitive to temperature and ionic strength, it is unaffected by the variables that complicate intensity-based calibrations like dye concentration, illumination intensity, photobleaching, and cellular morphology.[26,27] Fluorescence lifetime imaging (FLIM) has been successfully used to make high-throughput and minimally invasive recordings of numerous biophysical parameters including direct quantification of intracellular Ca^{2+} concentration[28,29] and intracellular pH[30,31] through lifetime calibrations. Although FLIM requires acquisition times on the order of seconds and thus has lower temporal resolution compared to electrophysiological or other optical methods, this is not a significant limitation for visualizing slower V_m dynamics over the longer time scales associated with cellular processes. Recently, novel approaches combining FLIM with wide-field fluorescence microscopes, rather than the point-scanning confocal systems typically used for FLIM, have also enabled faster acquisition times and visualization of millisecond action potentials.[32,33] However, efforts towards developing a lifetime-voltage calibration with genetically encoded voltage indicators (GEVIs) have been hindered by limited sensitivity and complex relationships between lifetime and voltage.[34–36] Conversely, small-molecule fluorescent voltage indicators offer a promising path towards quantification of absolute V_m with FLIM.

VoltageFluors (VFs) are small-molecule organic dyes that report changes in membrane potential through a photoinduced electron transfer (PeT) based mechanism. VF dyes consist of a fluorescent dye head connected to an electron-rich, lipophilic molecular wire that promotes localization to the plasma membrane (**Figure 1.1a**). Fluorescence of the dye head is quenched via PeT from the electron donor moiety, and the rate of PeT quenching is modulated by the transmembrane potential. At hyperpolarized potentials, PeT is accelerated by the transmembrane electric field and quickly quenches the fluorophore, resulting in dimmer fluorescence intensity. Upon depolarization, the shift in the electric field diminishes the rate of PeT quenching, thereby brightening fluorescence intensity (**Figure 1.1b**). Fluorescence lifetime is also modulated by the rate of PeT, as it is one of the nonradiative decay pathways out of the excited state. Fast rates of PeT under hyperpolarizing conditions shorten the fluorescence lifetime, while depolarization attenuates PeT quenching and lengthens the lifetime. VF dyes also offer fast response kinetics, high sensitivity, and low toxicity.

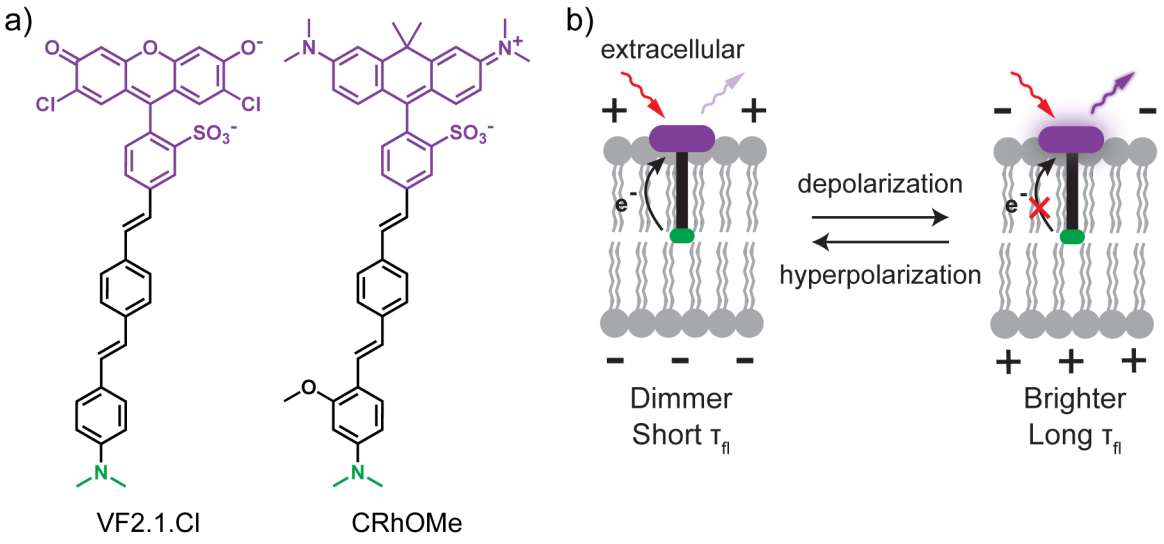


Figure 1.1 Scaffold and mechanism of VoltageFluor dyes.
a) Two classic VoltageFluor (VF) dyes are fluorescein-based VF2.1.Cl[37] and carborhodamine-based CRhOMe.[38] VFs consist of a fluorescent dye head (purple) connected to a molecular wire (black) and electron donor (green). **b)** VFs respond to changes in membrane potential through a photoinduced electron transfer (PeT) mechanism. At rest or hyperpolarized potentials, a high rate of PeT quickly quenches the fluorescent dye head, indicated by dim intensity and short lifetime. Upon depolarization, the rate of PeT decreases and fluorescence intensity increases, while the lifetime lengthens.

Fluorescence lifetime imaging with VF dyes (VF-FLIM) has been recently established as a new optical method to quantify absolute membrane with single cell resolution. Like other optical approaches, VF-FLIM is high throughput, minimally invasive, and offers good spatiotemporal resolution. The lifetime of VF dyes changes linearly in response to membrane potential, and since lifetime is largely independent of external variables, this facilitates development of a direct calibration between lifetime and voltage. The use of whole-cell patch-clamp electrophysiology as a standard yields a linear lifetime-voltage calibration that is generalizable for a particular cell type and VF dye. Once this relationship has been determined, lifetime measurements made on additional cells can be converted to voltage without recalibration. VF-FLIM reports V_m from single measurements with 10 to 23 mV accuracy, depending on the cell line, and tracks changes in membrane potential with 5 mV accuracy across all cell lines evaluated. This technique was

developed with the fluorescein-based probe VF2.1.Cl but has been successfully extended to the red-shifted, rhodamine-based probe CRhOMe with comparable voltage resolution. VF-FLIM offers a new method for quantitatively recording membrane potential over long timescale physiological processes like cell cycle progression.

Membrane Potential and Cell Cycle Progression

Regulation of the cell cycle has been extensively studied due to its essential biological role. Cell cycle progression is predominantly controlled by cyclin-dependent kinases (CDKs) which are activated by cyclin protein subunits.[39,40] Upon cyclin binding, CDKs adopt their active conformation and can phosphorylate key substrates to drive cell cycle progression. Cyclin expression and activity of CDK/cyclin pairs are varied throughout the cell cycle to ensure proper movement through the phases. The transitions from G_1 to S phase and G_2 to M phase are highly regulated cell cycle checkpoints.[41,42] If damaged or incompletely replicated DNA is detected, cyclin-dependent kinase inhibitor proteins (CKIs) can inhibit CDK activity to prevent progression until necessary repair pathways can be executed.

Emerging evidence illustrates cell cycle-dependent fluctuations in membrane potential, arising from variations in ion channel expression or activity throughout the cell cycle (**Figure 1.2**). These modulations broadly correspond to critical regulatory junctures like the G_1/S and G_2/M transitions, thus suggesting a possible role for membrane potential in cell cycle progression. However, possible mechanisms of bioelectric control through membrane potential dynamics have not been elucidated.[5,43,44]

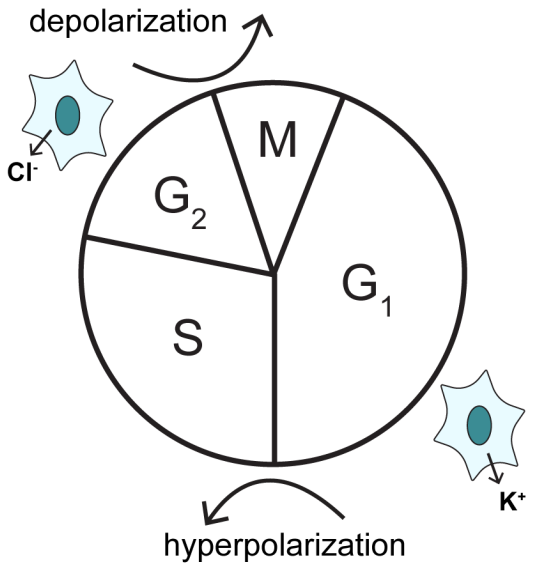


Figure 1.2. Cell cycle-dependent changes in ion flux and resting membrane potential.
This schematic summarizes various studies illustrating fluctuations in ion gradients and membrane potential throughout the cell cycle. The G_1/S transition is linked to membrane hyperpolarization, preceded by increased K^+ efflux from activation of ATP-sensitive, voltage-gated, and Ca^{2+}-activated potassium channels. Chloride ion channels are activated during G_2 and increase Cl^- efflux.

Studies across various cell types suggest that hyperpolarization is required for cells to transition from G_1 to S phase. Electrophysiological V_m measurements of MCF-7 breast cancer cells and V79 Chinese hamster lung cells across cell cycle phases reveal hyperpolarized potentials among cells in S phase relative to cells in other phases.[45,46] Furthermore, depolarization of the membrane inhibits progression to S phase in these cell types[45–47] as well as in lymphocytes, astrocytes, Schwann cells, and mouse neuroblastoma cells. MCF-7, V79, and mouse neuroblastoma cells continue to exhibit relatively hyperpolarized potentials throughout S phase. At the G_2/M transition, V79 and mouse neuroblastoma cells show depolarized potentials.

Numerous studies have also revealed varying levels of ion channel expression or activity throughout the cell cycle, particularly among potassium channels. The G_1/S transition is characterized by increased activity of ATP-sensitive,[47,48] voltage-gated,[49,50] and Ca^{2+}-activated[51,52] potassium channels generally corresponding to a hyperpolarizing efflux of K^+ which seems to be required for cell cycle progression.[53,54] Inhibition of these potassium channels arrests cells in G_1, further suggesting a necessary role for K^+ currents in cell cycle progression.[54–57] In rat oligodendrocyte precursors, blockade of voltage-gated potassium channels is specifically linked to accumulation of two CKIs, p27 and p21, which inhibit cell cycle progression through G_1.[56]

Several chloride ion channels display increased expression and high activity near the G_2/M transition, resulting in chloride efflux and depolarization.[58–60] The NCC27 intracellular chloride ion channel is exclusively expressed on the plasma membrane during G_2 and M, and inhibition of this channel arrests cells in G_2/M. [59,61] Expression of the inwardly rectifying ClC-2 ion channel is highest during M phase and rapidly decreases after cells divide.[60] Chloride efflux is also correlated with cell volume control, particularly as cells prepare for division in M phase.[62,63]

Increasing evidence also supports a correlation between V_m and proliferative activity across somatic cells. Quiescent, non-dividing cells tend to exhibit hyperpolarized membrane potentials, whereas more depolarized cells generally have high proliferative and mitotic activity.[64,65] Cancerous cells in particular are depolarized relative to non-cancerous cells and display abnormally high proliferation, motivating further examination of cell cycle progression and dysregulation in relation to cancer.[8,66,67]

Studies across various types of cancerous cells have revealed aberrant changes in expression levels and activity of potassium, sodium, chloride, and calcium ion channels.[68–72] Several calcium-activated[51,73–76] and voltage-gated[77–80] K^+ channels show increased expression or high activity in cancer cells, and inhibition of these channels has been shown to arrest cells and decrease proliferation. The inwardly rectifying human ether-a-go-go-related gene (hERG) K^+ channels are particularly upregulated in many types of cancerous cells, and their inhibition results in reduced proliferation and triggers apoptosis.[81–84]

While intracellular K^+ concentrations are similar in cancerous and non-cancerous cells, cancerous cells exhibit increase intracellular Na^+ which may be a key determinant of the depolarized potentials.[85–87] Enhanced expression of voltage-gated Na^+ channels is also observed across cancers. Although inhibition of their activity has not been observed to reduce proliferation, they are correlated with metastatic capacity.[70,71] These ion channels are significantly upregulated in

strongly metastatic breast cancer and prostate cancer cells compared to weakly metastatic cell lines of the same type of cancer.[88–90]

Voltage-gated chloride channels are also highly expressed in several types of cancer, and increased chloride efflux may contribute to depolarized membrane potentials.[66] Particularly high expression levels have been noted in gliomas, where inhibition of the CLC-3 chloride channel decreases proliferation.[91,92]

Numerous cancer cell lines also exhibit upregulation and overexpression of voltage-gated calcium channels, many of which can be inhibited to reduce cell proliferation.[66] Further evidence suggests that ion channel complexes between voltage-gated Ca^{2+} channels and calcium-activated K^+ channels contribute to proliferation, migration, and metastasis in cancerous cells.[93]

Inhibition of relevant ion channels offers a potential path for new cancer therapeutics, while ion channel expression levels can function as a biomarkers for tumor detection or prognosis.[66,94–96] Ion channels present substantial opportunities for advances in biomedicine, necessitating further characterization of how resting membrane potential may be involved in cell cycle regulation or dysregulation across normal and cancerous cells.

Mechanisms by which changes in membrane potential may be transduced to regulate proliferation are not fully understood, although increasing evidence highlights calcium signaling as a likely pathway.[43,44,69,97] Intracellular calcium signaling occurs throughout the cell cycle and is necessary for G_1 progression and transition into S phase.[98–100] Membrane hyperpolarization increasing the electrochemical gradient for calcium may lead to Ca^{2+} influx, as required for G_1/S progression, while in turn activating calcium-dependent potassium ion channels and creating a positive feedback loop for sustained signaling.[43,54,67,101] Sodium influx is also necessary for uptake of metabolic substrates and progression through G_1, and hyperpolarization would similarly increase its electrochemical gradient and stimulate Na^+ influx.[43,102,103] Other possible mechanisms for membrane potential signal transduction include proteins that undergo voltage-induced conformational changes to activate integrin-linked cascades, voltage-sensitive phosphatases, and influx of mitogens such as serotonin through voltage-dependent membrane transporters.[43,44]

Conclusion

Increasing evidence suggests that fluctuations in membrane potential, arising from variations in ion channel expression or activity, contribute to regulation and dysregulation of cell proliferation in normal and cancerous cells. This relationship offers significant opportunities for novel therapeutics and advances in biomedicine, however, possible mechanisms of bioelectric control through membrane potential are still unclear. Improved methods for quantifying membrane potential over extended time scales, such as VF-FLIM, offer new modalities for investigating links between bioelectric signals and physiological processes like proliferation and cell cycle progression.

This dissertation describes the application of VF-FLIM to quantify membrane potential values and monitor changes in non-electrically excitable cells. Chapter 2 details initial efforts towards identifying differences in membrane potential across cell cycle phases. Chapter 3 expands on this

work to track changes in V_m over time in live cells. Chapter 4 focuses on characterization of membrane potential dynamics in response to epidermal growth factor receptor signaling. Chapters 5 and 6 provide a general protocol for VF-FLIM experiments and key considerations for data acquisition and analysis.

References

(1) Alberts, B.; Johnson, A.; Lewis, J.; Raff, M.; Roberts, K.; Walter, P. Ion Channels and the Electrical Properties of Membranes. In *Molecular Biology of the Cell. 4th edition*; Garland Science, 2002.

(2) Rolfe, D. F.; Brown, G. C. Cellular Energy Utilization and Molecular Origin of Standard Metabolic Rate in Mammals. *Physiol. Rev.* **1997**, *77* (3), 731–758. https://doi.org/10.1152/physrev.1997.77.3.731.

(3) Bean, B. P. The Action Potential in Mammalian Central Neurons. *Nat. Rev. Neurosci.* **2007**, *8* (6), 451–465. https://doi.org/10.1038/nrn2148.

(4) Nattel, S.; Carlsson, L. Innovative Approaches to Anti-Arrhythmic Drug Therapy. *Nat. Rev. Drug Discov.* **2006**, *5* (12), 1034–1049. https://doi.org/10.1038/nrd2112.

(5) Abdul Kadir, L.; Stacey, M.; Barrett-Jolley, R. Emerging Roles of the Membrane Potential: Action Beyond the Action Potential. *Front. Physiol.* **2018**, *9*. https://doi.org/10.3389/fphys.2018.01661.

(6) Tsuchiya, W.; Okada, Y. Membrane Potential Changes Associated with Differentiation of Enterocytes in the Rat Intestinal Villi in Culture. *Dev. Biol.* **1982**, *94* (2), 284–290. https://doi.org/10.1016/0012-1606(82)90348-7.

(7) Cone, C. D.; Cone, C. M. Induction of Mitosis in Mature Neurons in Central Nervous System by Sustained Depolarization. *Science* **1976**, *192* (4235), 155–158. https://doi.org/10.1126/science.56781.

(8) Huang, X.; Jan, L. Y. Targeting Potassium Channels in Cancer. *J. Cell Biol.* **2014**, *206* (2), 151–162. https://doi.org/10.1083/jcb.201404136.

(9) Chen, L.; Becker, T. M.; Koch, U.; Stauber, T. The LRRC8/VRAC Anion Channel Facilitates Myogenic Differentiation of Murine Myoblasts by Promoting Membrane Hyperpolarization. *J. Biol. Chem.* **2019**, *294* (39), 14279–14288. https://doi.org/10.1074/jbc.RA119.008840.

(10) Lazzari-Dean, J. R.; Gest, A. M. M.; Miller, E. W. Measuring Absolute Membrane Potential Across Space and Time. *Annu. Rev. Biophys.* **2021**, *50*, 447–468. https://doi.org/10.1146/annurev-biophys-062920-063555.

(11) Armstrong, C. M.; Gilly, W. F. [5] Access Resistance and Space Clamp Problems Associated with Whole-Cell Patch Clamping. In *Methods in Enzymology*; Ion Channels; Academic Press, 1992; Vol. 207, pp 100–122. https://doi.org/10.1016/0076-6879(92)07007-B.

(12) Peterka, D. S.; Takahashi, H.; Yuste, R. Imaging Voltage in Neurons. *Neuron* **2011**, *69* (1), 9–21. https://doi.org/10.1016/j.neuron.2010.12.010.

(13) Liu, P.; Miller, E. W. Electrophysiology, Unplugged: Imaging Membrane Potential with Fluorescent Indicators. *Acc. Chem. Res.* **2020**, *53* (1), 11–19. https://doi.org/10.1021/acs.accounts.9b00514.

(14) Kulkarni, R. U.; Miller, E. W. Voltage Imaging: Pitfalls and Potential. *Biochemistry* **2017**, *56* (39), 5171–5177. https://doi.org/10.1021/acs.biochem.7b00490.

(15) Adams, D. S.; Levin, M. General Principles for Measuring Resting Membrane Potential and Ion Concentration Using Fluorescent Bioelectricity Reporters. *Cold Spring Harb. Protoc.* **2012**, *2012* (4), pdb.top067710. https://doi.org/10.1101/pdb.top067710.
(16) Xu, Y.; Zou, P.; Cohen, A. E. Voltage Imaging with Genetically Encoded Indicators. *Curr. Opin. Chem. Biol.* **2017**, *39*, 1–10. https://doi.org/10.1016/j.cbpa.2017.04.005.
(17) Yang, H. H.; St-Pierre, F. Genetically Encoded Voltage Indicators: Opportunities and Challenges. *J. Neurosci.* **2016**, *36* (39), 9977–9989. https://doi.org/10.1523/JNEUROSCI.1095-16.2016.
(18) González, J. E.; Tsien, R. Y. Improved Indicators of Cell Membrane Potential That Use Fluorescence Resonance Energy Transfer. *Chem. Biol.* **1997**, *4* (4), 269–277. https://doi.org/10.1016/s1074-5521(97)90070-3.
(19) Briggman, K. L.; Kristan, W. B.; González, J. E.; Kleinfeld, D.; Tsien, R. Y. Monitoring Integrated Activity of Individual Neurons Using FRET-Based Voltage-Sensitive Dyes. In *Membrane Potential Imaging in the Nervous System: Methods and Applications*; Canepari, M., Zecevic, D., Eds.; Springer: New York, NY, 2011; pp 61–70. https://doi.org/10.1007/978-1-4419-6558-5_6.
(20) Zou, P.; Zhao, Y.; Douglass, A. D.; Hochbaum, D. R.; Brinks, D.; Werley, C. A.; Harrison, D. J.; Campbell, R. E.; Cohen, A. E. Bright and Fast Multicoloured Voltage Reporters via Electrochromic FRET. *Nat. Commun.* **2014**, *5* (1), 4625. https://doi.org/10.1038/ncomms5625.
(21) Loew, L. M.; Scully, S.; Simpson, L.; Waggoner, A. S. Evidence for a Charge-Shift Electrochromic Mechanism in a Probe of Membrane Potential. *Nature* **1979**, *281* (5731), 497–499. https://doi.org/10.1038/281497a0.
(22) Montana, V.; Farkas, D. L.; Loew, L. M. Dual-Wavelength Ratiometric Fluorescence Measurements of Membrane Potential. *Biochemistry* **1989**, *28* (11), 4536–4539. https://doi.org/10.1021/bi00437a003.
(23) Zhang, J.; Davidson, R. M.; Wei, M.; Loew, L. M. Membrane Electric Properties by Combined Patch Clamp and Fluorescence Ratio Imaging in Single Neurons. *Biophys. J.* **1998**, *74* (1), 48–53. https://doi.org/10.1016/S0006-3495(98)77765-3.
(24) Bullen, A.; Saggau, P. High-Speed, Random-Access Fluorescence Microscopy: II. Fast Quantitative Measurements With Voltage-Sensitive Dyes. *Biophys. J.* **1999**, *76* (4), 2272–2287. https://doi.org/10.1016/S0006-3495(99)77383-2.
(25) Fromherz, P.; Hübener, G.; Kuhn, B.; Hinner, M. J. ANNINE-6plus, a Voltage-Sensitive Dye with Good Solubility, Strong Membrane Binding and High Sensitivity. *Eur. Biophys. J.* **2008**, *37* (4), 509–514. https://doi.org/10.1007/s00249-007-0210-y.
(26) Yellen, G.; Mongeon, R. Quantitative Two-Photon Imaging of Fluorescent Biosensors. *Curr. Opin. Chem. Biol.* **2015**, *27*, 24–30. https://doi.org/10.1016/j.cbpa.2015.05.024.
(27) Berezin, M. Y.; Achilefu, S. Fluorescence Lifetime Measurements and Biological Imaging. *Chem. Rev.* **2010**, *110* (5), 2641–2684. https://doi.org/10.1021/cr900343z.
(28) van der Linden, F. H.; Mahlandt, E. K.; Arts, J. J. G.; Beumer, J.; Puschhof, J.; de Man, S. M. A.; Chertkova, A. O.; Ponsioen, B.; Clevers, H.; van Buul, J. D.; Postma, M.; Gadella, T. W. J.; Goedhart, J. A Turquoise Fluorescence Lifetime-Based Biosensor for Quantitative Imaging of Intracellular Calcium. *Nat. Commun.* **2021**, *12* (1), 7159. https://doi.org/10.1038/s41467-021-27249-w.

(29) Zheng, K.; Jensen, T. P.; Rusakov, D. A. Monitoring Intracellular Nanomolar Calcium Using Fluorescence Lifetime Imaging. *Nat. Protoc.* **2018**, *13* (3), 581–597. https://doi.org/10.1038/nprot.2017.154.
(30) Lin, H.-J.; Herman, P.; Lakowicz, J. R. Fluorescence Lifetime-Resolved pH Imaging of Living Cells. *Cytom. Part J. Int. Soc. Anal. Cytol.* **2003**, *52* (2), 77–89. https://doi.org/10.1002/cyto.a.10028.
(31) Rennick, J. J.; Nowell, C. J.; Pouton, C. W.; Johnston, A. P. R. Resolving Subcellular pH with a Quantitative Fluorescent Lifetime Biosensor. *Nat. Commun.* **2022**, *13* (1), 6023. https://doi.org/10.1038/s41467-022-33348-z.
(32) Bowman, A. J.; Huang, C.; Schnitzer, M. J.; Kasevich, M. A. Wide-Field Fluorescence Lifetime Imaging of Neuron Spiking and Sub-Threshold Activity in Vivo. *Science* **2023**, *380* (6651), 1270–1275. https://doi.org/10.1126/science.adf9725.
(33) Zickus, V.; Wu, M.-L.; Morimoto, K.; Kapitany, V.; Fatima, A.; Turpin, A.; Insall, R.; Whitelaw, J.; Machesky, L.; Bruschini, C.; Faccio, D.; Charbon, E. Fluorescence Lifetime Imaging with a Megapixel SPAD Camera and Neural Network Lifetime Estimation. *Sci. Rep.* **2020**, *10* (1), 20986. https://doi.org/10.1038/s41598-020-77737-0.
(34) Dumas, D.; Stoltz, J.-F. New Tool to Monitor Membrane Potential by FRET Voltage Sensitive Dye (FRET-VSD) Using Spectral and Fluorescence Lifetime Imaging Microscopy (FLIM). Interest in Cell Engineering. *Clin. Hemorheol. Microcirc.* **2005**, *33* (3), 293–302.
(35) Brinks, D.; Klein, A. J.; Cohen, A. E. Two-Photon Lifetime Imaging of Voltage Indicating Proteins as a Probe of Absolute Membrane Voltage. *Biophys. J.* **2015**, *109* (5), 914–921. https://doi.org/10.1016/j.bpj.2015.07.038.
(36) Hou, J. H.; Venkatachalam, V.; Cohen, A. E. Temporal Dynamics of Microbial Rhodopsin Fluorescence Reports Absolute Membrane Voltage. *Biophys. J.* **2014**, *106* (3), 639–648. https://doi.org/10.1016/j.bpj.2013.11.4493.
(37) Miller, E. W.; Lin, J. Y.; Frady, E. P.; Steinbach, P. A.; Kristan, W. B.; Tsien, R. Y. Optically Monitoring Voltage in Neurons by Photo-Induced Electron Transfer through Molecular Wires. *Proc. Natl. Acad. Sci.* **2012**, *109* (6), 2114–2119. https://doi.org/10.1073/pnas.1120694109.
(38) Gest, A. M. M.; Lazzari-Dean, J. R.; Ortiz, G.; Yaeger-Weiss, S. K.; Boggess, S. C.; Miller, E. W. A Red-Emitting Carborhodamine for Monitoring and Measuring Membrane Potential. *Proc. Natl. Acad. Sci.* **2024**, *121* (14), e2315264121. https://doi.org/10.1073/pnas.2315264121.
(39) Lim, S.; Kaldis, P. Cdks, Cyclins and CKIs: Roles beyond Cell Cycle Regulation. *Development* **2013**, *140* (15), 3079–3093. https://doi.org/10.1242/dev.091744.
(40) Vermeulen, K.; Van Bockstaele, D. R.; Berneman, Z. N. The Cell Cycle: A Review of Regulation, Deregulation and Therapeutic Targets in Cancer. *Cell Prolif.* **2003**, *36* (3), 131–149. https://doi.org/10.1046/j.1365-2184.2003.00266.x.
(41) Barnum, K. J.; O'Connell, M. J. Cell Cycle Regulation by Checkpoints. In *Cell Cycle Control: Mechanisms and Protocols*; Noguchi, E., Gadaleta, M. C., Eds.; Springer: New York, NY, 2014; pp 29–40. https://doi.org/10.1007/978-1-4939-0888-2_2.
(42) Johnson, D. G.; Walker, C. L. CYCLINS AND CELL CYCLE CHECKPOINTS. *Annu. Rev. Pharmacol. Toxicol.* **1999**, *39* (Volume 39, 1999), 295–312. https://doi.org/10.1146/annurev.pharmtox.39.1.295.

(43) Blackiston, D. J.; McLaughlin, K. A.; Levin, M. Bioelectric Controls of Cell Proliferation: Ion Channels, Membrane Voltage and the Cell Cycle. *Cell Cycle* **2009**, *8* (21), 3527–3536. https://doi.org/10.4161/cc.8.21.9888.
(44) Sundelacruz, S.; Levin, M.; Kaplan, D. L. Role of Membrane Potential in the Regulation of Cell Proliferation and Differentiation. *Stem Cell Rev. Rep.* **2009**, *5* (3), 231–246. https://doi.org/10.1007/s12015-009-9080-2.
(45) Wonderlin, W. F.; Woodfork, K. A.; Strobl, J. S. Changes in membrane potential during the progression of MCF-7 human mammary tumor cells through the cell cycle. *J. Cell. Physiol.* **1995**, *165* (1), 177–185. https://doi.org/10.1002/jcp.1041650121.
(46) Sachs, H. G.; Stambrook, P. J.; Ebert, J. D. Changes in Membrane Potential during the Cell Cycle. *Exp. Cell Res.* **1974**, *83* (2), 362–366. https://doi.org/10.1016/0014-4827(74)90350-4.
(47) Klimatcheva, E.; Wonderlin, W. F. An ATP-Sensitive K+ Current That Regulates Progression Through Early G1 Phase of the Cell Cycle in MCF-7 Human Breast Cancer Cells. *J. Membr. Biol.* **1999**, *171* (1), 35–46. https://doi.org/10.1007/s002329900556.
(48) Woodfork, K. A.; Wonderlin, W. F.; Peterson, V. A.; Strobl, J. S. Inhibition of ATP-Sensitive Potassium Channels Causes Reversible Cell-Cycle Arrest of Human Breast Cancer Cells in Tissue Culture. *J. Cell. Physiol.* **1995**, *162* (2), 163–171. https://doi.org/10.1002/jcp.1041620202.
(49) Wang, W.; Fan, Y.; Wang, S.; Wang, L.; He, W.; Zhang, Q.; Li, X. Effects of Voltage-Gated K+ Channel on Cell Proliferation in Multiple Myeloma. *Sci. World J.* **2014**, *2014* (1), 785140. https://doi.org/10.1155/2014/785140.
(50) Ouadid-Ahidouch, H.; Le Bourhis, X.; Roudbaraki, M.; Toillon, R. A.; Delcourt, P.; Prevarskaya, N. Changes in the K+ Current-Density of MCF-7 Cells during Progression through the Cell Cycle: Possible Involvement of a h-Ether.a-Gogo K+ Channel. *Receptors Channels* **2001**, *7* (5), 345–356.
(51) Ouadid-Ahidouch, H.; Roudbaraki, M.; Delcourt, P.; Ahidouch, A.; Joury, N.; Prevarskaya, N. Functional and Molecular Identification of Intermediate-Conductance Ca(2+)-Activated K(+) Channels in Breast Cancer Cells: Association with Cell Cycle Progression. *Am. J. Physiol. Cell Physiol.* **2004**, *287* (1), C125-134. https://doi.org/10.1152/ajpcell.00488.2003.
(52) Lepple-Wienhues, A.; Berweck, S.; Böhmig, M.; Leo, C. P.; Meyling, B.; Garbe, C.; Wiederholt, M. K+ Channels and the Intracellular Calcium Signal in Human Melanoma Cell Proliferation. *J. Membr. Biol.* **1996**, *151* (2), 149–157. https://doi.org/10.1007/s002329900066.
(53) Wonderlin, W. F.; Strobl, J. S. Potassium Channels, Proliferation and G1 Progression. *J. Membr. Biol.* **1996**, *154* (2), 91–107. https://doi.org/10.1007/s002329900135.
(54) Ouadid-Ahidouch, H.; Ahidouch, A. K+ Channel Expression in Human Breast Cancer Cells: Involvement in Cell Cycle Regulation and Carcinogenesis. *J. Membr. Biol.* **2008**, *221* (1), 1–6. https://doi.org/10.1007/s00232-007-9080-6.
(55) Amigorena, S.; Choquet, D.; Teillaud, J. L.; Korn, H.; Fridman, W. H. Ion Channel Blockers Inhibit B Cell Activation at a Precise Stage of the G1 Phase of the Cell Cycle. Possible Involvement of K+ Channels. *J. Immunol.* **1990**, *144* (6), 2038–2045. https://doi.org/10.4049/jimmunol.144.6.2038.
(56) Ghiani, C. A.; Yuan, X.; Eisen, A. M.; Knutson, P. L.; DePinho, R. A.; McBain, C. J.; Gallo, V. Voltage-Activated K+ Channels and Membrane Depolarization Regulate Accumulation of the Cyclin-Dependent Kinase Inhibitors P27(Kip1) and P21(CIP1) in

Glial Progenitor Cells. *J. Neurosci. Off. J. Soc. Neurosci.* **1999**, *19* (13), 5380–5392. https://doi.org/10.1523/JNEUROSCI.19-13-05380.1999.
(57) Chittajallu, R.; Chen, Y.; Wang, H.; Yuan, X.; Ghiani, C. A.; Heckman, T.; McBain, C. J.; Gallo, V. Regulation of Kv1 Subunit Expression in Oligodendrocyte Progenitor Cells and Their Role in G1/S Phase Progression of the Cell Cycle. *Proc. Natl. Acad. Sci. U. S. A.* **2002**, *99* (4), 2350–2355. https://doi.org/10.1073/pnas.042698399.
(58) Chen, L.; Wang, L.; Zhu, L.; Nie, S.; Zhang, J.; Zhong, P.; Cai, B.; Luo, H.; Jacob, T. J. C. Cell Cycle-Dependent Expression of Volume-Activated Chloride Currents in Nasopharyngeal Carcinoma Cells. *Am. J. Physiol.-Cell Physiol.* **2002**, *283* (4), C1313–C1323. https://doi.org/10.1152/ajpcell.00182.2002.
(59) Valenzuela, S. M.; Mazzanti, M.; Tonini, R.; Qiu, M. R.; Warton, K.; Musgrove, E. A.; Campbell, T. J.; Breit, S. N. The Nuclear Chloride Ion Channel NCC27 Is Involved in Regulation of the Cell Cycle. *J. Physiol.* **2000**, *529* (Pt 3), 541–552. https://doi.org/10.1111/j.1469-7793.2000.00541.x.
(60) Zheng, Y.-J.; Furukawa, T.; Ogura, T.; Tajimi, K.; Inagaki, N. M Phase-Specific Expression and Phosphorylation-Dependent Ubiquitination of the ClC-2 Channel*. *J. Biol. Chem.* **2002**, *277* (35), 32268–32273. https://doi.org/10.1074/jbc.M202105200.
(61) Rao, S. G.; Ponnalagu, D.; Patel, N. J.; Singh, H. Three Decades of Chloride Intracellular Channel Proteins: From Organelle to Organ Physiology. *Curr. Protoc. Pharmacol.* **2018**, *80* (1), 11.21.1-11.21.17. https://doi.org/10.1002/cpph.36.
(62) Habela, C. W.; Sontheimer, H. Cytoplasmic Volume Condensation Is an Integral Part of Mitosis. *Cell Cycle Georget. Tex* **2007**, *6* (13), 1613–1620.
(63) Habela, C. W.; Ernest, N. J.; Swindall, A. F.; Sontheimer, H. Chloride Accumulation Drives Volume Dynamics Underlying Cell Proliferation and Migration. *J. Neurophysiol.* **2009**, *101* (2), 750–757. https://doi.org/10.1152/jn.90840.2008.
(64) Cone, C. D. Unified Theory on the Basic Mechanism of Normal Mitotic Control and Oncogenesis. *J. Theor. Biol.* **1971**, *30* (1), 151–181. https://doi.org/10.1016/0022-5193(71)90042-7.
(65) Cone, Jr., Clarence D. Variation of the Transmembrane Potential Level as a Basic Mechanism of Mitosis Control. *Oncology* **1970**, *24* (6), 438–470. https://doi.org/10.1159/000224545.
(66) Rao, V. R.; Perez-Neut, M.; Kaja, S.; Gentile, S. Voltage-Gated Ion Channels in Cancer Cell Proliferation. *Cancers* **2015**, *7* (2), 849–875. https://doi.org/10.3390/cancers7020813.
(67) Yang, M.; Brackenbury, W. J. Membrane Potential and Cancer Progression. *Front. Physiol.* **2013**, *4*. https://doi.org/10.3389/fphys.2013.00185.
(68) Kunzelmann, K. Ion Channels and Cancer. *J. Membr. Biol.* **2005**, *205* (3), 159–173. https://doi.org/10.1007/s00232-005-0781-4.
(69) Becchetti, A. Ion Channels and Transporters in Cancer. 1. Ion Channels and Cell Proliferation in Cancer. *Am. J. Physiol. Cell Physiol.* **2011**, *301* (2), C255-265. https://doi.org/10.1152/ajpcell.00047.2011.
(70) Fiske, J. L.; Fomin, V. P.; Brown, M. L.; Duncan, R. L.; Sikes, R. A. Voltage-Sensitive Ion Channels and Cancer. *Cancer Metastasis Rev.* **2006**, *25* (3), 493–500. https://doi.org/10.1007/s10555-006-9017-z.
(71) Brackenbury, W. J. Voltage-Gated Sodium Channels and Metastatic Disease. *Channels* **2012**, *6* (5), 352–361. https://doi.org/10.4161/chan.21910.

(72) Peretti, M.; Angelini, M.; Savalli, N.; Florio, T.; Yuspa, S. H.; Mazzanti, M. Chloride Channels in Cancer: Focus on Chloride Intracellular Channel 1 and 4 (CLIC1 AND CLIC4) Proteins in Tumor Development and as Novel Therapeutic Targets. *Biochim. Biophys. Acta* **2015**, *1848* (10 Pt B), 2523–2531. https://doi.org/10.1016/j.bbamem.2014.12.012.
(73) Ouadid-Ahidouch, H.; Roudbaraki, M.; Ahidouch, A.; Delcourt, P.; Prevarskaya, N. Cell-Cycle-Dependent Expression of the Large Ca2+-Activated K+ Channels in Breast Cancer Cells. *Biochem. Biophys. Res. Commun.* **2004**, *316* (1), 244–251. https://doi.org/10.1016/j.bbrc.2004.02.041.
(74) Weaver, A. K.; Bomben, V. C.; Sontheimer, H. Expression and Function of Calcium-Activated Potassium Channels in Human Glioma Cells. *Glia* **2006**, *54* (3), 223–233. https://doi.org/10.1002/glia.20364.
(75) Parihar, A. S.; Coghlan, M. J.; Gopalakrishnan, M.; Shieh, C.-C. Effects of Intermediate-Conductance Ca2+-Activated K+ Channel Modulators on Human Prostate Cancer Cell Proliferation. *Eur. J. Pharmacol.* **2003**, *471* (3), 157–164. https://doi.org/10.1016/s0014-2999(03)01825-9.
(76) Jäger, H.; Dreker, T.; Buck, A.; Giehl, K.; Gress, T.; Grissmer, S. Blockage of Intermediate-Conductance Ca2+-Activated K+ Channels Inhibit Human Pancreatic Cancer Cell Growth in Vitro. *Mol. Pharmacol.* **2004**, *65* (3), 630–638. https://doi.org/10.1124/mol.65.3.630.
(77) Huang, X.; Dubuc, A. M.; Hashizume, R.; Berg, J.; He, Y.; Wang, J.; Chiang, C.; Cooper, M. K.; Northcott, P. A.; Taylor, M. D.; Barnes, M. J.; Tihan, T.; Chen, J.; Hackett, C. S.; Weiss, W. A.; James, C. D.; Rowitch, D. H.; Shuman, M. A.; Jan, Y. N.; Jan, L. Y. Voltage-Gated Potassium Channel EAG2 Controls Mitotic Entry and Tumor Growth in Medulloblastoma via Regulating Cell Volume Dynamics. *Genes Dev.* **2012**, *26* (16), 1780–1796. https://doi.org/10.1101/gad.193789.112.
(78) Arcangeli, A. Expression and Role of hERG Channels in Cancer Cells. *Novartis Found. Symp.* **2005**, *266*, 225–232; discussion 232-234.
(79) Arcangeli, A.; Bianchi, L.; Becchetti, A.; Faravelli, L.; Coronnello, M.; Mini, E.; Olivotto, M.; Wanke, E. A Novel Inward-Rectifying K+ Current with a Cell-Cycle Dependence Governs the Resting Potential of Mammalian Neuroblastoma Cells. *J. Physiol.* **1995**, *489* (2), 455–471. https://doi.org/10.1113/jphysiol.1995.sp021065.
(80) Babcock, J. J.; Li, M. hERG Channel Function: Beyond Long QT. *Acta Pharmacol. Sin.* **2013**, *34* (3), 329–335. https://doi.org/10.1038/aps.2013.6.
(81) He, S.; Moutaoufik, M. T.; Islam, S.; Persad, A.; Wu, A.; Aly, K. A.; Fonge, H.; Babu, M.; Cayabyab, F. S. HERG Channel and Cancer: A Mechanistic Review of Carcinogenic Processes and Therapeutic Potential. *Biochim. Biophys. Acta BBA - Rev. Cancer* **2020**, *1873* (2), 188355. https://doi.org/10.1016/j.bbcan.2020.188355.
(82) Glassmeier, G.; Hempel, K.; Wulfsen, I.; Bauer, C. K.; Schumacher, U.; Schwarz, J. R. Inhibition of HERG1 K+ Channel Protein Expression Decreases Cell Proliferation of Human Small Cell Lung Cancer Cells. *Pflugers Arch.* **2012**, *463* (2), 365–376. https://doi.org/10.1007/s00424-011-1045-z.
(83) Jehle, J.; Schweizer, P. A.; Katus, H. A.; Thomas, D. Novel Roles for hERG K(+) Channels in Cell Proliferation and Apoptosis. *Cell Death Dis.* **2011**, *2* (8), e193. https://doi.org/10.1038/cddis.2011.77.
(84) Wang, H.; Zhang, Y.; Cao, L.; Han, H.; Wang, J.; Yang, B.; Nattel, S.; Wang, Z. HERG K+ Channel, a Regulator of Tumor Cell Apoptosis and Proliferation. *Cancer Res.* **2002**, *62* (17), 4843–4848.

(85) Cameron, I. L.; Smith, N. K.; Pool, T. B.; Sparks, R. L. Intracellular Concentration of Sodium and Other Elements as Related to Mitogenesis and Oncogenesis in Vivo. *Cancer Res.* **1980**, *40* (5), 1493–1500.
(86) Sparks, R. L.; Pool, T. B.; Smith, N. K.; Cameron, I. L. Effects of Amiloride on Tumor Growth and Intracellular Element Content of Tumor Cells in Vivo. *Cancer Res.* **1983**, *43* (1), 73–77.
(87) Smith, N. R.; Sparks, R. L.; Pool, T. B.; Cameron, I. L. Differences in the Intracellular Concentration of Elements in Normal and Cancerous Liver Cells as Determined by X-Ray Microanalysis. *Cancer Res.* **1978**, *38* (7), 1952–1959.
(88) Roger, S.; Besson, P.; Le Guennec, J.-Y. Involvement of a Novel Fast Inward Sodium Current in the Invasion Capacity of a Breast Cancer Cell Line. *Biochim. Biophys. Acta* **2003**, *1616* (2), 107–111. https://doi.org/10.1016/j.bbamem.2003.07.001.
(89) Bennett, E. S.; Smith, B. A.; Harper, J. M. Voltage-Gated Na+ Channels Confer Invasive Properties on Human Prostate Cancer Cells. *Pflugers Arch.* **2004**, *447* (6), 908–914. https://doi.org/10.1007/s00424-003-1205-x.
(90) Diss, J. K.; Archer, S. N.; Hirano, J.; Fraser, S. P.; Djamgoz, M. B. Expression Profiles of Voltage-Gated Na(+) Channel Alpha-Subunit Genes in Rat and Human Prostate Cancer Cell Lines. *The Prostate* **2001**, *48* (3), 165–178. https://doi.org/10.1002/pros.1095.
(91) Olsen, M. L.; Schade, S.; Lyons, S. A.; Amaral, M. D.; Sontheimer, H. Expression of Voltage-Gated Chloride Channels in Human Glioma Cells. *J. Neurosci. Off. J. Soc. Neurosci.* **2003**, *23* (13), 5572–5582. https://doi.org/10.1523/JNEUROSCI.23-13-05572.2003.
(92) Hong, S.; Bi, M.; Wang, L.; Kang, Z.; Ling, L.; Zhao, C. CLC-3 Channels in Cancer (Review). *Oncol. Rep.* **2015**, *33* (2), 507–514. https://doi.org/10.3892/or.2014.3615.
(93) Guéguinou, M.; Chantôme, A.; Fromont, G.; Bougnoux, P.; Vandier, C.; Potier-Cartereau, M. KCa and Ca(2+) Channels: The Complex Thought. *Biochim. Biophys. Acta* **2014**, *1843* (10), 2322–2333. https://doi.org/10.1016/j.bbamcr.2014.02.019.
(94) Wulff, H.; Castle, N. A.; Pardo, L. A. Voltage-Gated Potassium Channels as Therapeutic Targets. *Nat. Rev. Drug Discov.* **2009**, *8* (12), 982–1001. https://doi.org/10.1038/nrd2983.
(95) Prevarskaya, N.; Skryma, R.; Shuba, Y. Ion Channels in Cancer: Are Cancer Hallmarks Oncochannelopathies? *Physiol. Rev.* **2018**, *98* (2), 559–621. https://doi.org/10.1152/physrev.00044.2016.
(96) D'Amico, M.; Gasparoli, L.; Arcangeli, A. Potassium Channels: Novel Emerging Biomarkers and Targets for Therapy in Cancer. *Recent Patents Anticancer Drug Discov.* **2013**, *8* (1), 53–65. https://doi.org/10.2174/15748928130106.
(97) Urrego, D.; Tomczak, A. P.; Zahed, F.; Stühmer, W.; Pardo, L. A. Potassium Channels in Cell Cycle and Cell Proliferation. *Philos. Trans. R. Soc. B Biol. Sci.* **2014**, *369* (1638), 20130094. https://doi.org/10.1098/rstb.2013.0094.
(98) Santella, L.; Ercolano, E.; Nusco, G. A. The Cell Cycle: A New Entry in the Field of Ca2+ Signaling. *Cell. Mol. Life Sci. CMLS* **2005**, *62* (21), 2405–2413. https://doi.org/10.1007/s00018-005-5083-6.
(99) Hazelton, B.; Mitchell, B.; Tupper, J. Calcium, Magnesium, and Growth Control in the WI-38 Human Fibroblast Cell. *J. Cell Biol.* **1979**, *83* (2 Pt 1), 487–498. https://doi.org/10.1083/jcb.83.2.487.
(100) Choi, J.; Chiang, A.; Taulier, N.; Gros, R.; Pirani, A.; Husain, M. A Calmodulin-Binding Site on Cyclin E Mediates Ca2+-Sensitive G1/S Transitions in Vascular Smooth Muscle

Cells. *Circ. Res.* **2006**, *98* (10), 1273–1281. https://doi.org/10.1161/01.RES.0000223059.19250.91.
(101) Ziechner, U.; Schönherr, R.; Born, A.-K.; Gavrilova-Ruch, O.; Glaser, R. W.; Malesevic, M.; Küllertz, G.; Heinemann, S. H. Inhibition of Human Ether à Go-Go Potassium Channels by Ca2+/Calmodulin Binding to the Cytosolic N- and C-Termini. *FEBS J.* **2006**, *273* (5), 1074–1086. https://doi.org/10.1111/j.1742-4658.2006.05134.x.
(102) Mummery, C. L.; Boonstra, J.; van der Saag, P. T.; de Laat, S. W. Modulations of Na+ Transport during the Cell Cycle of Neuroblastoma Cells. *J. Cell. Physiol.* **1982**, *112* (1), 27–34. https://doi.org/10.1002/jcp.1041120106.
(103) Koch, K. S.; Leffert, H. L. Increased Sodium Ion Influx Is Necessary to Initiate Rat Hepatocyte Proliferation. *Cell* **1979**, *18* (1), 153–163. https://doi.org/10.1016/0092-8674(79)90364-7.

Chapter 2

Optical Estimation of Membrane Potential Throughout the Cell Cycle

Abstract

Membrane potential (V_m) is fundamental for biophysical processes in electrically excitable and non-electrically excitable cells. Changes in membrane potential have been well-studied for electrically excitable cells, where large, rapid changes in V_m trigger key signaling pathways like neurotransmitter release. Increasing evidence suggests that smaller changes in membrane potential may have a regulatory role in slower physiological processes in non-electrically excitable cells, such as cell cycle progression. However, characterization of these dynamics has been limited by insufficient techniques for non-invasively measuring membrane potential over seconds to hours. Fluorescence lifetime imaging with VoltageFluor dyes (VF-FLIM) enables minimally invasive, high-throughput measurements of absolute membrane potential over these physiologically relevant timescales. This work describes initial efforts towards characterizing resting V_m throughout cell cycle phases.

Introduction

All cells have a resting membrane potential (V_m) that arises from maintenance of ionic gradients across a selectively permeable plasma membrane. Electrically excitable cells like neurons and cardiomyocytes experience changes in V_m that drive downstream signaling like neurotransmitter release or muscle contraction, respectively. These large, nearly 100 mV changes in V_m occur rapidly over milliseconds to seconds. In non-electrically excitable cells, smaller changes in V_m around tens of millivolts that happen over seconds to hours have also been linked to fundamental cellular processes including differentiation, migration, volume control, cell division, and cell cycle progression.[1–5]

Cell cycle regulation has been extensively studied due to its fundamental role in biology, however, possible mechanisms of bioelectric control through membrane potential have not been elucidated. Cyclin-dependent kinases (CDKs) are key regulators of the cell cycle.[6,7] CDKs bind to their cyclin subunits, upon which CDKs adopt their active conformation and can phosphorylate essential substrates to drive DNA synthesis and mitotic progression. CDK/cyclin pairs are sequentially activated throughout the cell cycle to ensure proper movement through the phases. The transitions from G_1 to S phase and G_2 to M phase are highly regulated cell cycle checkpoints.[8,9] If cells detect damaged or incompletely replicated DNA, CDK activity can be inhibited by binding of cyclin-dependent kinase inhibitor proteins (CKIs), leading to cell cycle arrest until repair pathways can be executed.

Emerging evidence suggests membrane potential may be modulated throughout the cell cycle in some types of cells, particularly at key regulatory points like the G_1/S and G_2/M transitions.[10–13] Early measurements of V_m in sarcoma cells illustrated a relationship between V_m and cell cycle progression, with the cells transiently hyperpolarizing before entering M phase and depolarizing as they transition through mitosis.[14,15] Additional studies in CHO cells demonstrated that hyperpolarization to potentials around -70 mV inhibited mitotic activity, but return to their normal resting potential of -10 mV reversed the cell cycle arrest.[16,17] In mature neurons, sustained depolarization induced DNA synthesis and led to mitosis.[14,18,19]

Further experiments indicated a general correlation between V_m and proliferative activity across somatic cells.[20–22] Cells with a highly hyperpolarized V_m are generally quiescent and do not undergo mitosis, while more depolarized cells tend to have high proliferative and mitotic activity. Cancerous cells in particular are generally depolarized, and studies of malignant transformation of normal cells showed corresponding depolarizing of V_m.[4,10,12] Membrane potential measurements of MCF-7 breast cancer cells are also suggestive of hyperpolarization as cells progress from G_1 to S phase and depolarization at the transition from G_2 to M phase.[23–27] In various cell types including lymphocytes, Schwann cells, astrocytes, oligodendrocytes, and various cancer cells, inhibition of K^+ channels hinders proliferation.[24,28,29] Across most cell types evaluated, K^+ flux changes resulting in depolarization leads to proliferation, although there are instances in which depolarization inhibits proliferation.[13] However, efforts towards robustly characterizing V_m across cell types and over the longer timescales of cell cycle progression have been limited by insufficient techniques.

Patch-clamp electrophysiology has historically been considered the gold standard of measuring membrane potential because it allows for quantitative measurements of V_m. However, it is inherently invasive and low throughput, as well as impractical for recording voltage over longer timescales from seconds to hours. Optical methods like intensity-based voltage imaging allow for less invasive and high throughput visualization of changes in V_m, but quantification of absolute V_m is difficult. Fluorescence intensity can be highly variable depending on dye loading, cell morphology, photobleaching, and illumination intensity. These additional variables make it challenging to directly correlate fluorescence intensity with voltage.[30] However, fluorescence lifetime is an intrinsic property of the dye and is independent of the factors that affect confound intensity-based measurements.[31]

VoltageFluors (VFs) are voltage-sensitive small molecule dyes that localize to the plasma membrane and respond to changes in V_m through a photoinduced electron transfer (PeT) mechanism, resulting in modulation of fluorescence intensity and lifetime and allowing for quantification of membrane potential through fluorescence lifetime imaging (FLIM).[32,33] In cells at rest, the membrane potential is relatively hyperpolarized and PeT occurs quickly, resulting in dimmer fluorescence intensity and shorter fluorescence lifetime. Upon depolarization, the rate of PeT is diminished, and fluorescence intensity becomes brighter, while the fluorescence lifetime increases. The relationship between lifetime and voltage is linear and has been characterized through simultaneous FLIM and patch-clamp electrophysiology to produce cell-type type specific calibrations between membrane potential and fluorescence lifetime.[30,32] After developing a calibration, lifetime data can be easily converted to voltage without the need for further electrophysiology. VF-FLIM was developed using the green VoltageFluor VF2.1.Cl and calibrated across several cell types, establishing it as a non-invasive and high throughput technique for optical determination of absolute membrane potential.

Although preliminary evidence suggests that changes in membrane potential occur during the cell cycle, the possible role of V_m in cell cycle regulation is still unknown. Characterization of membrane potential throughout the cell cycle has been limited by insufficient voltage imaging methods. VF-FLIM offers a new method for making high-throughput, quantitative measurements of V_m. This chapter describes preliminary work towards identifying differences in V_m associated with cell cycle phases.

Results and Discussion

Initial experiments focused on the possible hyperpolarization at the G_1/S checkpoint. Treatment with thymidine has been shown to effectively synchronize cells at the G_1/S boundary.[34–36] We validated the cell cycle arrest through incubation with EdU (5-ethynyl-2'-deoxyuridine), a nucleoside analog that is incorporated into cells during DNA synthesis in S phase. EdU can be detected through a copper (I) catalyzed click reaction with an AlexaFluo647 azide.[37,38] HEK293T cells were treated with 2mM thymidine for 16-18 hours or left unsynchronized. After thymidine treatment, all cells were incubated with EdU for 15 minutes to allow for cells in S phase to incorporate the EdU during DNA synthesis. Cells were subsequently fixed, permeabilized, and reacted with the Alexa Fluor 647 azide for EdU detection. Epifluorescence images showed EdU labeling in unsynchronized cells, but no EdU was detected in the thymidine treated cells, indicating that the cells were synchronized (**Figure 2.1a**). Flow cytometry experiments confirmed the synchronization, with around 24% of the unsynchronized cells labeled with EdU, compared to under 1% of the thymidine treated cells (**Figure 2.1b**).

We then acquired fluorescence lifetime images of unsynchronized and thymidine treated HEK293T cells loaded with VF2.1.Cl and used the previously established calibration[32] to convert from lifetime to voltage (**Figure 2.1c,d**). Unsynchronized cells had a resting membrane potential of -55 ± 5 mV (mean ± SEM, including propagated error from lifetime-voltage calibration), consistent with previous measurements of VF2.1.Cl in HEK293T cells. Thymidine treated HEK293T cells exhibited a similar V_m at -57 ± 5 mV. There was not a significant difference in resting lifetime between the two conditions (n.s. $p > 0.05$, two-sided, unpaired, unequal variances t-test). The distributions of measured membrane potential values showed substantial overlap between the two conditions (**Figure 2.1e**).

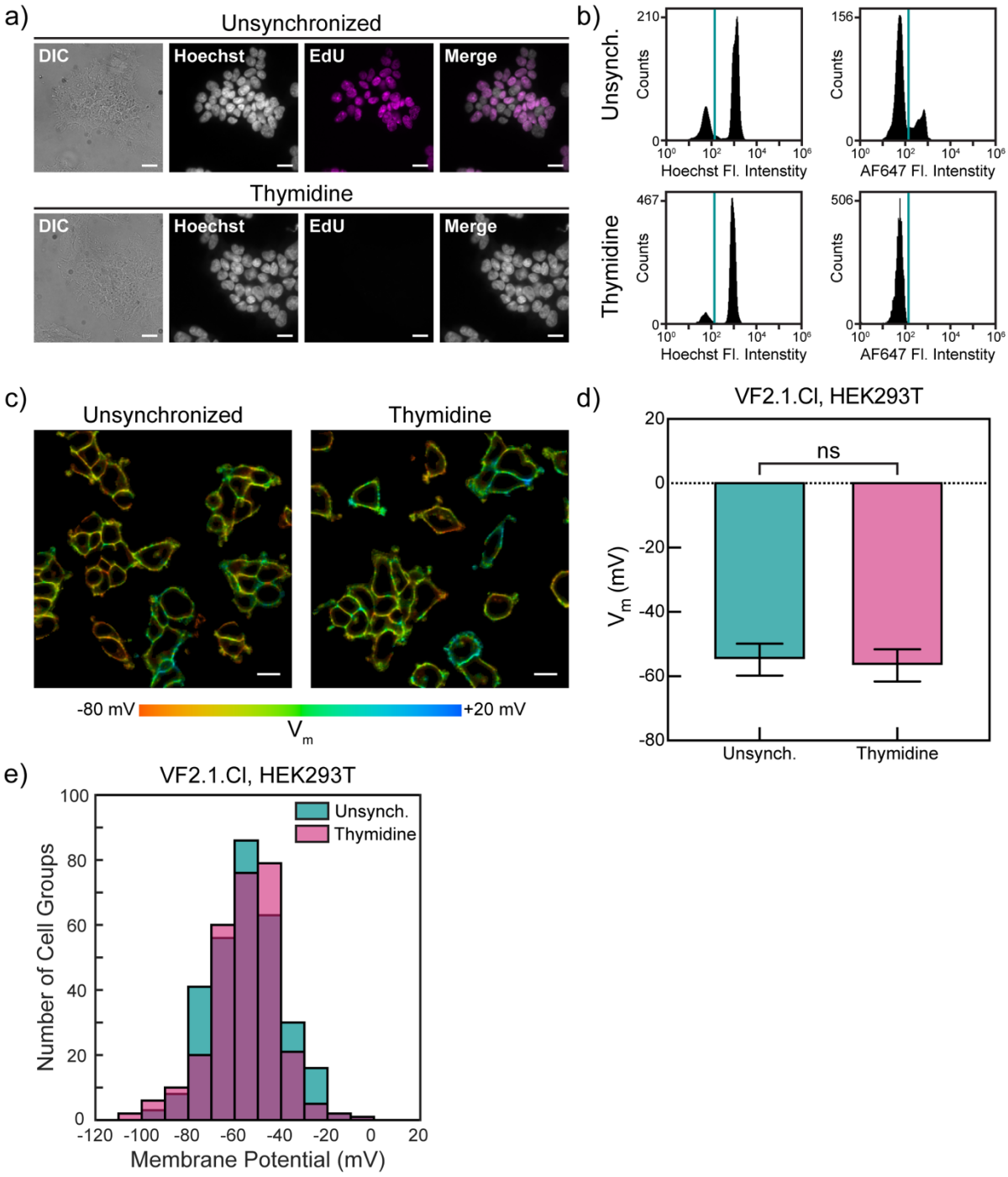


Figure 2.1. Unsynchronized and thymidine-treated HEK293T cells.
a) Unsynchronized or thymidine-treated HEK293T cells incubated with EdU detected by AlexaFluor647. Cells were also stained with Hoechst 33342. **b)** Representative flow cytometry histograms of number of cells vs fluorescence intensity of Hoechst 33342 or EdU-AlexaFluor647 in HEK293T cells, either unsynchronized (top) or treated with thymidine (bottom). Teal vertical lines indicate gates between cells identified as negative (left) or positive (right) for Hoechst 33342 or EdU-AlexaFluor647 fluorescence. **c)** Representative lifetime-intensity overlay images of unsynchronized or thymidine-treated HEK293T cells loaded to 100 nM VF2.1.Cl. Scale bar is 20 µm. **d)** Average membrane potential measured in unsynchronized (-55 ± 5 mV) or thymidine-treated (-57 ± 5 mV) HEK293T cells loaded with 100 nM VF2.1.Cl. Data are mean ± SEM (including propagated error from

the lifetime-voltage calibration). Sample sizes (number of ROIs): unsynchronized 306, thymidine 282. There is not a significant difference in V_m between the two conditions (n.s. $p > 0.05$, two-sided, unpaired, unequal variances t-test). **e)** Histograms of V_m values observed in unsynchronized (n = 306) or thymidine-treated (n = 282) HEK293T cells.

We also completed similar experiments with unsynchronized and thymidine treated MCF-7 cells, which have been shown to hyperpolarize at the G_1/S transition and depolarize at the G2/M transition.[23–27] After treatment with 2 mM thymidine, flow cytometry experiments confirmed the synchronization in MCF-7 cells. Approximately 28% of the unsynchronized cells showed EdU labeling, while fewer than 1% of the thymidine treated cells were labeled (**Figure 2.2a**).

FLIM experiments with VF2.1.Cl revealed a slightly larger difference in V_m between unsynchronized and thymidine treated MCF-7 cells compared to HEK293T cells (**Figure 2.2b,c**). Unsynchronized cells had a resting potential of -36 ± 5 mV, while thymidine treated cells were slightly hyperpolarized at -43 ± 5 mV (mean ± SEM, including propagated error from lifetime-voltage calibration). However, this difference in V_m was still not statistically significant (n.s. $p > 0.05$, two-sided, unpaired, unequal variances t-test). As in HEK293T cells, distributions of the measured V_m values were similar (**Figure 2.2d**).

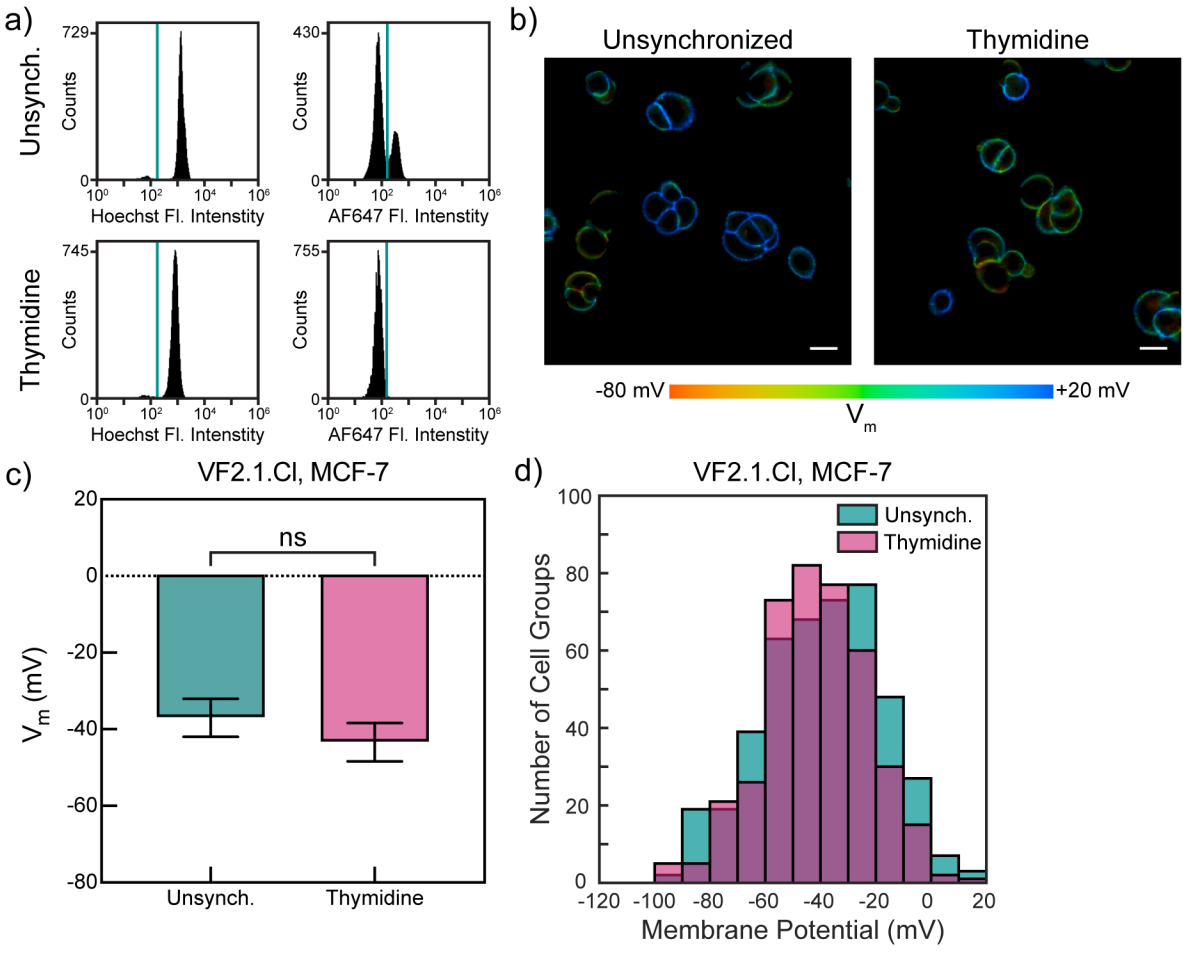


Figure 2.2. Unsynchronized and thymidine-treated MCF-7 cells.

a) Representative flow cytometry histograms of number of cells vs fluorescence intensity of Hoechst 33342 or EdU-AlexaFluor647 in MCf-7 cells, either unsynchronized (top) or treated with thymidine (bottom). Teal vertical lines indicate gates between cells identified as negative (left) or positive (right) for Hoechst 33342 or EdU-AlexaFluor647 fluorescence. **b)** Representative lifetime-intensity overlay images of unsynchronized or thymidine-treated MCF-7 cells loaded to 150 nM VF2.1.Cl. Scale bar is 20 μm. **d)** Average membrane potential measured in unsynchronized (-36 ± 5 mV) or thymidine-treated (-43 ± 5 mV) MCF-7 cells loaded with 150 nM VF2.1.Cl. Data are mean ± SEM (including propagated error from the lifetime-voltage calibration). Sample sizes (number of ROIs): unsynchronized 445, thymidine 397. There is not a significant difference in V_m between the two conditions (n.s. $p > 0.05$, two-sided, unpaired, unequal variances t-test). **d)** Histograms of V_m values observed in unsynchronized (n = 445) or thymidine-treated (n = 397) MCF-7 cells.

Although we did not observe a difference in V_m between unsynchronized and thymidine treated HEK293T or MCF-7 cells, we wanted to measure V_m at other points in the cell cycle, as well as develop a method to identify cell cycle phase, to better characterize the relationship between V_m and cell cycle phase.

Tracking expression of the proteins Cdt1 and geminin has been established as a reliable method to differentiate cells in G_1 from cells in S, G_2, or M.[39] Cdt1 is expressed throughout G_1 but degraded as cells transition into S phase. Geminin expression begins at the start of S phase and continues throughout G_2 and M before being degraded during cell division.[40] By combining EdU labeling with detection of Cdt1 and geminin, we successfully distinguished between cells in G_1, S, and G_2/M (**Figure 2.3a**).

MCF-7 cells were plated in gridded dishes and allowed to grow unsynchronized or treated with thymidine, tamoxifen, or 17β-estradiol to increase the proportion of cells at various points in the cell cycle. Some cells were treated with 2 mM thymidine for 24 hours for synchronization at the G_1/S boundary. Other cells were treated with a combination of tamoxifen and 17β-estradiol. Treatment with tamoxifen synchronizes MCF-7 cells in G_1, and subsequent treatment with 17β-estradiol stimulates progression after approximately 6-8 hours, enriching the fractions of cells in S, G_2, and M.[41] For our experiments, MCF-7 cells were treated with μM tamoxifen for 72 hours, and a subset of these cells were then treated with 1 nM 17β-estradiol for 18 hours.

On the day of FLIM imaging, cells were incubated with 10 μM EdU for 15 minutes to identify the cells in S phase. Following the EdU incubation, cells were loaded with 150 VF2.1.Cl for 25 minutes and FLIM images were acquired, along with the corresponding locations of each imaged field of view on the gridded dish. Immediately following FLIM acquisition for each dish, cells were fixed and later permeabilized for EdU detection and immunostaining. EdU was detected with Alexa Fluor 647 as previously described. Cells were also incubated with primary antibodies against Cdt1 and geminin and the appropriate secondary antibodies conjugated to Alexa Fluor 488 or Alexa Fluor 546, respectively. Epifluorescence imaging was then performed to visualize the Cdt1, geminin, and EdU content of each cell previously analyzed through FLIM. We returned to each FLIM field of view on the gridded dishes and acquired the corresponding epifluorescence images (**Figure 2.3b**).

We then analyzed the resulting FLIM and epifluorescence images to determine V_m and cell cycle phase (**Figure 2.3c**). After spatial binning of FLIM images, the lifetime decay at each binned pixel was fit to a two-component exponential decay to calculate the resting lifetime, reported as the amplitude-weighted mean of the two exponential components. The cell membranes of individual cells were identified through hand-drawn regions of interest (ROIs) and the lifetime at each included pixel was

averaged to yield the mean lifetime of each cell. This lifetime was then converted to voltage through the previously established lifetime-voltage calibration[32] for VF2.1.Cl in MCF-7 cells.

Epifluorescence images were analyzed through manual tracing of whole-cell ROIs. Identification of cellular ROIs was aided by comparison with the corresponding FLIM images. The fluorescence intensity of each fluorophore was measured across the cellular ROIs and thresholded to classify cells as positive or negative for Cdt1, EdU, or geminin. Cells positive for Cdt1 were assigned to G_1 phase, cells positive for EdU and geminin were classified as S phase, and cells positive for geminin were categorized as G_2/M phase. Cell cycle phase and V_m were then correlated across each field of view (**Figure 2.3d**).

This analysis was completed for 393 cells total and quantified V_m across cells in G_1, S, and G_2/M (**Figure 2.3e**). Cells in G_1 and S phase exhibited similar resting membrane potentials at -55 ± 5 mV and -58 ± 5 mv (mean ± SEM, including propagated error from lifetime-voltage calibration). Comparatively, cells in G_2/M were depolarized by approximately 10 mV at -46 ± 5 mV. Resting V_m was not significantly different between cells in G_1 and S phase, but there was a statistical difference between each of these populations compared to the cells in G_2/M (Brown-Forsythe and Welch one-way ANOVA, Dunnett post hoc testing). The relative depolarization of G_2/M phase cells is consistent with reports in the literature of depolarization at the G_2/M transition in MCF-7 cells.

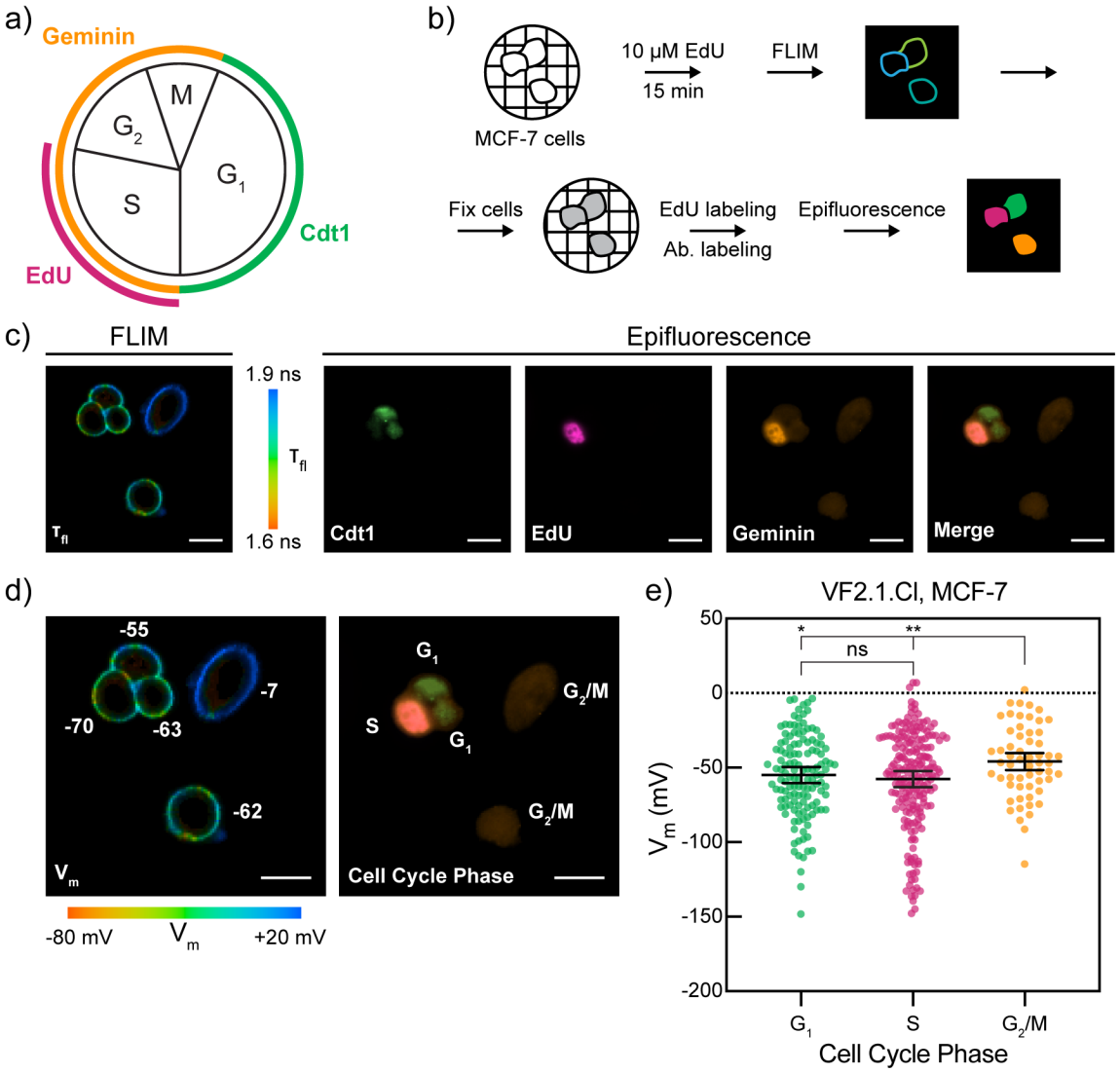


Figure 2.3. Correlation of V_m and cell cycle phase in MCF-7 cells.
a) Identification of cell cycle phases with Cdt1, EdU, and geminin. Cdt1 is expressed during G_1, while geminin is expressed during S, G_2, and M phases. EdU is incorporated into cells during DNA synthesis in S phase. **b)** Schematic of experiments to correlate V_m with cell cycle phase. MCF-7 cells plated on gridded dishes were incubated with 10 μM EdU for 15 minutes to enable identification of cells in S phase. Following fluorescence lifetime imaging, cells were fixed and prepared for cell cycle phase analysis. EdU was detected via a click reaction with AlexaFluor 647. Cells were also incubated with appropriate secondary antibodies for Cdt1 and geminin. Cells were subsequently visualized via epifluorescence. **c)** Representative lifetime-intensity overlay and epifluorescence images of MCF-7 cells loaded with 150 nM VF2.1.Cl and analyzed for cell cycle phase. **d)** Representative lifetime-intensity and merged epifluorescence images of MCF-7 cells showing the membrane potential (mV) and corresponding cell cycle phase. V_m values for individual cell ROIs were calculated from the lifetime-voltage calibration for VF2.1.Cl in HEK293T cells. **e)** Average lifetimes observed in MCF-7 cells loaded with 150 nM VF2.1.Cl and analyzed for cell cycle phase (G_1 -55 ± 5 mV, S -58 ± 5 mV, G_2/M 46 ± 6 mV. Data are mean ± SEM (including propagated error from the lifetime-voltage calibration). Sample sizes (number of cells): G_1 133, S 202, G_2/M 58. Asterisks indicate significant differences between the cell cycle phases (n.s. $p > 0.05$, * $p < 0.05$, ** $p < 0.01$, *** $p < 0.001$, **** $p < 0.0001$, Brown-Forsythe and Welch one-way ANOVA, Dunnett post hoc testing). All scale bars are 20 μm.

The observed difference in V_m between G_1/S phase and G_2/M phase served as a promising start towards characterizing membrane potential throughout the cell cycle. However, these measurements were limited by fixation to determine cell cycle phase, which prevented us from making multiple measurements of a single cell. The intra-cell RMSD (3.4 mV) of the lifetime-calibration is about seven-fold larger than the inter-cell RMSD (23 mV), so VF-FLIM is most accurate when recording changes in V_m within an individual cell. In future work, we sought to work with unsynchronized live cells and track fluctuations in V_m in single cells over time.

Conclusion

This chapter presents preliminary work identifying differences in resting membrane potential in fixed and synchronized cells in different phases on the cell cycle. HEK293T and MCF-7 cells synchronized around the G_1/S border with thymidine did not differ in V_m compared to unsynchronized cells. However, further experiments employing Cdt1, EdU, and geminin to determine the phase of analyzed MCF-7 cells were more revealing. MCF-7 cells in G_2/M phase were depolarized by approximately 10 mV relative to cells in G_1 and S phase, motivating further investigation of this difference. The following chapter highlights subsequent studies of membrane potential in live cells as they progress through the cell cycle.

Methods

Cell Culture

HEK293T and MCF-7 cells were obtained from the UC Berkeley Cell Culture Facility. Both cell lines were verified by STR profiling (short tandem repeat) and were tested routinely for mycoplasma. Cell lines were discarded after 25 passages. Cells were maintained and plated in Dulbecco's Modified Eagle Medium (DMEM; Gibco) supplemented with 4.5 g/L glucose, 2 mM GlutaMAX (Gibco), and 10% seradigm fetal bovine serum (FBS; Gibco) in a 37°C humidified incubator at 5% CO_2. Media for MCF-7 cells was supplemented with 1 mM sodium pyruvate (Gibco) and 1x non-essential amino acids (Gibco). Cells were passaged into fresh complete media every few days following dissociation with trypsin-EDTA (Gibco, 0.05% for HEK293T, 0.25% for MCF-7). Residual trypsin was removed from MCF-7 cells by centrifugation for 5 minutes at 300xg before resuspension in fresh complete medium.

For flow cytometry experiments, HEK293T or MCF-7 cells were plated in 6-well tissue culture plates at a density of 42,000 cells/cm^2 (HEK293T) or 31,000 cells/cm^2 (MCF-7).

For imaging experiments, 12 mm or 25 mm #1.5 glass coverslips were pre-coated with poly-D-lysine (PDL) prior to plating cells. Coverslips were incubated in PDL (0.1 mg/mL in PBS; Sigma-Aldrich) for at least 1 hour in a 37°C humidified incubator and then washed twice with sterile water and twice with 1x Dulbecco's Phosphate Buffered Saline (dPBS; Gibco). For epifluorescence imaging of EdU labeling, HEK293T cells were plated onto 12 mm coverslips in 24-well tissue culture plates at a density of 53,000 cells/cm^2. For FLIM experiments, HEK293T or MCF-7 cells were plated on 25 mm coverslips in 6-well tissue culture plates at a density of 42,000 cells/cm^2 (HEK293T) or 31,000 cells/cm^2 (MCF-7).

For FLIM experiments to correlate V_m and cell cycle phase, MCF-7 cells were plated in 35 mm #1.5 glass bottom imaging dishes with a 500 μm grid (Ibidi, cat. No 81168). Dishes were pre-coated with PDL prior to plating as described above. Plating density varied depending on the treatment conditions: no synchronization 31,000 cells/cm^2; thymidine treatment 16,000 cells/cm^2; tamoxifen and 17β-estradiol treatment 10,000 cells/cm^2.

Thymidine Treatment

Thymidine (Sigma-Aldrich) was made up as a 100 mM stock in dPBS and stored at 4°C. For HEK293T cells used in flow cytometry and epifluorescence experiments, cells were rinsed once with dPBS and changed to fresh complete medium containing 2 mM thymidine or vehicle 24 hours after plating. HEK293T cells were prepared for flow cytometry or imaged after 16 to 18 hours of treatment. For FLIM experiments, thymidine/vehicle treatment was either started immediately after plating or 24 hours later, and HEK293T cells were imaged after 16 to 18 hours.

For MCF-7 cells used in flow cytometry and FLIM experiments, cells were rinsed once with dPBS and changed to fresh complete medium containing 2 mM thymidine or vehicle 16 hours after plating. MCF-7 were treated for 24 hours before flow cytometry sample preparation or FLIM.

Tamoxifen and 17β-Estradiol Treatment
Tamoxifen citrate (Sigma-Aldrich) was made up as a 1 mM stock in 95% ethanol and stored at -20°C. 17β-estradiol (Sigma-Aldrich) was made up as a 1 μM stock in 95% ethanol and stored at -20°C. Immediately after MCF-7 cells were plated, tamoxifen (final concentration 2 μM) or vehicle was added. After 72 hours, half of the tamoxifen-treated cells were rinsed once with dPBS and changed to fresh complete medium containing 17β-estradiol (final concentration 1 nM) or vehicle. Cells were imaged after 18 hours of 17β-estradiol treatment, or continued tamoxifen treatment.

EdU Labeling and Detection
EdU labeling and detection was performed using the Click-iT EdU Alexa Fluor 647 Cell Proliferation Kit (Invitrogen). The Click-iT reaction mixture, including the Alexa Fluor 647 azide, was prepared according to the manufacturer's instructions.

For EdU labeling of HEK293T cells for epifluorescence, cells were incubated with 10 μM EdU in complete medium for 15 minutes at 37°C in a humidified incubator. Cells were subsequently fixed with 4% paraformaldehyde in dPBS for 15 minutes at room temperature (RT) in a chemical fume hood. After two washes with 3% w/v bovine serum albumin (BSA; Sigma Aldrich) in dPBS, cells were permeabilized with 0.3% v/v Triton-X (Sigma-Aldrich) in dPBS for 20 minutes at RT. Cells were washed twice more with 3% BSA before adding the Click-iT reaction mixture. Cells were incubated with the reaction mixture for 30 minutes at RT. After two washes with 3% BSA and one wash with dPBS, cells were incubated with 10 μM Hoechst 33342 in dPBS for 30 minutes at RT. Cells were washed twice more with dPBS, then stored in dPBS at 4°C until imaging experiments were performed.

For EdU labeling of HEK293T and MCF-7 cells for flow cytometry, cells were incubated with 10 μM EdU in complete medium for 15 minutes at 37°C in a humidified incubator. Cells were then dissociated with trypsin-EDTA (0.05% for HEK293T, 0.25% for MCF-7), quenched with complete medium, and centrifuged for 5 minutes at 200xg before resuspension in dPBS. Cells were centrifuged at 200xg for 5 minutes, resuspended in 1% w/v BSA, and centrifuged again. Cells were resuspended in 4% paraformaldehyde and incubated for 15 minutes at RT to fix the cells. Cells were pelleted via centrifugation, resuspended in 1% BSA, and pelleted again before resuspension in 0.3% TritonX-100 for 10 minutes at RT. After permeabilization, cells were pelleted, resuspended in 1% BSA, then pelleted again. Cells were resuspended in the Click-iT reaction mixture and incubated for 30 minutes at RT, then centrifuged and resuspended in 1% BSA. For Hoechst 33342 staining, cells were pelleted then resuspended in 10 μM Hoechst in dPBS and incubated for 15 minutes at RT. Cells were pelleted and resuspended in dPBS. Samples were kept on ice until analysis.

For EdU labeling combined with immunohistochemistry for cell cycle analysis, MCF-7 cells were incubated with 10 μM EdU in complete medium for 15 minutes at 37°C in a humidified incubator. Cells were then incubated with 150 nM VF2.1.Cl in imaging buffer (*VoltageFluor Loading*) and FLIM images were acquired (*Fluorescence Lifetime Data Acquisition*). Immediately after each gridded dish was imaged, cells were fixed with 4% paraformaldehyde for 20 minutes at RT, rinsed three times with dPBS, and stored on ice in dPBS while the remaining gridded dishes were imaged. Following imaging of all dishes, cells were permeabilized with 0.3% TritonX-100 for 10 minutes at RT, then rinsed three times with dPBS. Blocking for immunostaining was done with 4% w/v

normal goat serum (NGS; Sigma-Aldrich) in dPBS for 1 hour at RT. Cells were subsequently incubated with the Click-iT reaction mixture for 30 minutes at RT and rinsed with once dPBS, followed by immunohistochemistry.

Immunohistochemistry
Following fixation, permeabilization, and EdU labeling (as described above), primary rabbit IgG anti-Cdt1 (diluted 1:200; #8064, Cell Signaling Technologies) and mouse IgG1 anti-geminin (diluted 1:50; ab104306, Abcam) antibodies were incubated at 4°C overnight. The next day, cells were incubated with secondary goat anti-rabbit IgG Alexa Fluor 488 (diluted 1:2000; Life Technologies) and goat anti-mouse IgG1 Alexa Fluor 546 (diluted 1:3000; Life Technologies) antibodies at room temperature for 2-4 hours. Following incubation of secondary antibodies, cells were rinsed 3 times with dPBS and stored in dPBS at 4°C until imaging experiments were performed. Primary and secondary antibodies were prepared in 4% NGS in dPBS at the indicated dilution.

Flow Cytometry
Samples were prepared as described above (*EdU Labeling and Detection*) and kept on ice until use. Immediately before use, cells were filtered through a 35 μm cell strainer (Falcon). Flow cytometry was performed with an Attune NxT Acoustic Focusing Cytometer. Hoechst 33342 was excited at 405 nm and emission was collected through a 440/50 nm bandpass emission filter. Alexa Fluor 647 was excited at 638 nm and emission was collected through a 670/14 nm bandpass emission filter. Analysis was completed with Attune Cytometric Software.

Epifluorescence Imaging Parameters
Imaging of EdU labeling in HEK293T cells was performed on an AxioExaminer Z-1 (Zeiss) equipped with a Spectra-X Light engine LED light (Lumencor), controlled with Slidebook (v6, Intelligent Imaging Innovations). Images were acquired with a W-Plan-Apo 20x/1.0 water objective (20x; Zeiss). Images were focused onto an OrcaFlash4.0 sCMOS camera (sCMOS; Hamamatsu). Hoechst 33342 was excited by LED light at 390/22 nm (0.7 W/cm^2, 65 ms exposure time). EdU-AlexaFluor647 was illuminated with LED light at 631/28 nm (3.2 W/cm^2, 120 ms exposure time). All emission was collected with a quadruple emission filter (430/32, 508/14, 586/30, 708/98 nm; Semrock) after passing through a quadruple dichroic mirror (432/38, 509/22, 586/40, 654 nm LP; Semrock).

Imaging for cell cycle phase in MCF-7 cells was performed on an AxioObserver Z-1 (Zeiss), equipped with a Spectra-X Light engine LED light (Lumencor), controlled with μManager (V1.4, opensource, Open Imaging). Images were acquired using an EC-Plan-Neoflaur 40x/1.3 oil immersion objective (40x; Zeiss). Images were focused onto an OrcaFlash4.0 sCMOS camera (sCMOS; Hamamatsu). Cdt1-AlexaFluor488 was excited by LED light at 475/34 nm (4.2 W/cm^2, 30 ms exposure time). Excitation light for Geminin-AlexaFluor546 was delivered by LED at 550/15 nm (2.9 W/cm^2, 20 ms exposure time). EdU-AlexaFluor647 was illuminated with LED light at 635/22 nm (1.6 W/cm^2, 5 ms exposure time). All emission was collected with a quadruple emission filter (432/36, 515/30, 595/30, 730/140 nm; Semrock) after passing through a quadruple dichroic mirror (432/38, 515/30, 595/30, 652 nm LP; Semrock).

Cell Cycle Image Analysis

Analysis of epifluorescence images to determine cell cycle phase was performed in the FIJI installation of ImageJ (NIH). Whole-cell ROIs were manually traced around each individual cell, aided by comparison with the corresponding FLIM images. The fluorescence intensity of each ROI was measured across all three fluorescence channels, and the resulting intensities were thresholded to classify cells as positive or negative for Cdt1, EdU, or geminin. Cells positive for Cdt1 were assigned to G_1 phase, cells positive for EdU and geminin were classified as S phase, and cells positive for geminin were categorized as G_2/M phase. After determining the corresponding lifetime and voltage for each cell (*Fluorescence Lifetime Data Analysis*), cell cycle phase and V_m were then correlated across each field of view

VoltageFluor Loading

For FLIM experiments, VF2.1.Cl was loaded at 100 nM (HEK293T) or 150 nM (MCF-7). Loading solutions were prepared in imaging buffer (IB, made in-house; composition in mM: 139.5 NaCl, 10 HEPES, 5.6 D-glucose, 5.33 KCl, 1.26 $CaCl_2$, 0.49 $MgCl_2$, 0.44 KH_2PO_4, 0.41 $MgSO_4$, 0.34 NaH_2PO_4; 285 mOsm/L; pH 7.25) directly from a 100 μM DMSO stock. Osmolarity was determined with a μOsmette (Precision Instruments). Cells were incubated at 37°C for 20-25 minutes in loading solution, washed once with IB, and transferred to fresh IB in an Attofluor cell imaging chamber (Invitrogen).

Fluorescence Lifetime Data Acquisition

Fluorescence lifetime imaging was performed on an LSM 510 scanning confocal microscope (Zeiss), equipped with an SPC-150N single photon counting card (Becker and Hickl GmbH). 80 MHz pulsed excitation light was supplied by a Ti:Sapphire laser (MaiTai HP; Spectraphysics) tuned to 958 nm and frequency-doubled to 479 nm. Images were acquired with a 40x/1.4 NA oil immersion objective (Zeiss) coated with immersion oil (Immersol 518F; Zeiss). Excitation light power was controlled with a neutral density wheel and a polarizer, followed by a polarizing beamsplitter. The light power was titrated so that lifetimes did not drift up over the course of the experiment, no phototoxicity was notable, and there was no photon pileup on the detector. For optical voltage determinations, typical average power at the sample was 5 μW. To obtain larger photon counts, the confocal pinhole was set between 2.5 and 3.5 airy units, which corresponds to optical section thickness of approximately 2.5 μm. Emitted photons were detected with a hybrid detector, HPM-100-40 (Becker and Hickl), based on a Hamamatsu R10467 GaAsP hybrid photomultiplier tube. Detector dark counts were kept below 1000 per second during acquisition. Emission light was collected through a 550/49 bandpass filter (Semrock) after passing through a 488 LP dichroic mirror (Zeiss). Reference photons for determining photon arrival times were detected with a PHD-400-N high speed photodiode (Becker and Hickl). Data were collected with 256 time channels in the analog-to-digital-converter (ADC), 256 x 256 pixels of spatial resolution, and 90 s acquisition time. Performance of the lifetime recording setup was assessed by regular measurements of three standards: 2 uM fluorescein in 0.1 N NaOH, 1 mg/mL erythrosin B in water, and the measured instrument response function (IRF)**.** The IRF was recorded hourly from a solution of 500 μM fluorescein and 12.2 M sodium iodide in 0.1 N NaOH. All imaging experiments were conducted at room temperature under ambient atmosphere. Cells were used immediately after loading the VF dye, and no cells were kept for longer than an hour at room temperature.

Fluorescence Lifetime Data Analysis

All lifetime data were fit using SPCImage (Becker & Hickl), which solves the nonlinear least squares problem using the Levenberg-Marquadt algorithm. Signal from photons detected in a TCSPC apparatus are convolved with the instrument response (IRF). Measured IRFs were incorporated by the iterative reconvolution method using SPCImage analysis software. VF2.1.Cl lifetime data were fit to a sum of two exponential decay components (**Equation 1**). The weighted average of the two lifetimes, τ_m (**Equation 2**), was used in subsequent analysis.

$$F(t) = a_1 e^{-t/\tau_1} + a_2 e^{-t/\tau_2} \quad (1)$$

$$\tau_m = \frac{a_1\tau_1 + a_2\tau_2}{a_1 + a_2} \quad (2)$$

All lifetime images in this chapter are represented as an overlay of photon count (pixel intensity) and weighted average lifetime (pixel color). Pixels with insufficient signal to fit a fluorescence decay are shown in black. Pixels with photon counts below 300 photons at the peak of the decay (time channel with the most signal) were omitted from analysis to ensure reproducible fits. Because the lifetime of VFs does not fully decay to baseline in a single 12.5 ns laser cycle, the incomplete multiexponentials fitting option was used, allowing the model to attribute some signal early in the decay to the previous laser cycle. Out of 256 time channels from the analog-to-digital converter (ADC), only data from time channels 23 to 240 were used in the final fit. The offset parameter (detector dark counts per ADC time channel per pixel) was set to zero. The number of iterations for the fit in SPCImage was increased to 20 to obtain converged fits. Shift between the IRF and the decay trace was fixed to 0.5 (in units of ADC time channels), which consistently gave lifetimes of standards erythrosin B (1 mg/mL in H_2O) and fluorescein (2 μM in 0.1 N NaOH, H_2O) closest to reported values. To obtain sufficient photons but keep excitation light power minimal, binning between neighboring pixels was employed during fitting. This procedure effectively takes the lifetime as a spatial moving average across the image by including adjacent pixels in the decay for a given pixel. Images were acquired with an unbinned pixel width of 0.44 μm, and a bin size of 3 was used for analysis, resulting in binned pixels of 3.08 μm. Lifetime-intensity overlay images are displayed at the native resolution (0.44 μm pixel width).

Conversion of Lifetime to Voltage

For analysis of populations of unsynchronized and thymidine-treated HEK293T and MCF-7 cells (**Figures 2.1-2.2**), images were divided into cell groups, with each cell group as a single region of interest (ROI). ROIs were automatically determined from raw photon intensity images by sharpening and then thresholding the signal intensity with custom MATLAB code. Regions of images that were partially out of the optical section or contained punctate debris were omitted. For analysis of single MCF-7 cells **(Figure 2.3**), ROIs were manually traced in FIJI around each individual cell membrane. The mean τ_m across all pixels in an ROI (either a cell group or a single cell) was used as the lifetime for that ROI. Lifetime values were converted to voltage via the lifetime-V_m standard curve for each cell type previously determined with whole-cell patch-clamp electrophysiology.[32]

The relationship between the weighted average lifetime (τ_m) and membrane potential for each patch-clamped cell was determined by linear regression, yielding a sensitivity (*m,* ps/mV) and a 0

mV lifetime (b, ps), which were subsequently averaged to give an overall linear calibration for each cell type (**Equation 3**). The average sensitivity and 0 mV point across all cells of a given type were used to convert subsequent lifetime measurements (τ) to V_m (**Equation 4**).

$$\tau = m * V_m + b \tag{3}$$

$$V_m = \frac{(\tau - b)}{m} \tag{4}$$

Where standard error of the mean of a voltage determination (δV_m) is given, error was propagated to include the standard errors of the slope (δm) and y-intercept (δb) of the voltage calibration, as well as the standard error of the lifetime measurements ($\delta\tau$) in the condition of interest (**Equation 5**).

$$\delta V_m = |V_m| \sqrt{\left(\frac{\sqrt{\delta\tau^2 + \delta b^2}}{\tau - b}\right)^2 + \left(\frac{\delta m}{m}\right)^2}$$

Statistical Analysis

Hypothesis testing was performed as indicated with either analysis of variance (ANOVA) followed by appropriate post hoc testing or two-sided, unpaired, unequal variances t-tests. All statistical analysis was performed in Prism 10 (GraphPad).

References

(1) Abdul Kadir, L.; Stacey, M.; Barrett-Jolley, R. Emerging Roles of the Membrane Potential: Action Beyond the Action Potential. *Front. Physiol.* **2018**, *9*. https://doi.org/10.3389/fphys.2018.01661.

(2) Tsuchiya, W.; Okada, Y. Membrane Potential Changes Associated with Differentiation of Enterocytes in the Rat Intestinal Villi in Culture. *Dev. Biol.* **1982**, *94* (2), 284–290. https://doi.org/10.1016/0012-1606(82)90348-7.

(3) Cone, C. D.; Cone, C. M. Induction of Mitosis in Mature Neurons in Central Nervous System by Sustained Depolarization. *Science* **1976**, *192* (4235), 155–158. https://doi.org/10.1126/science.56781.

(4) Huang, X.; Jan, L. Y. Targeting Potassium Channels in Cancer. *J. Cell Biol.* **2014**, *206* (2), 151–162. https://doi.org/10.1083/jcb.201404136.

(5) Chen, L.; Becker, T. M.; Koch, U.; Stauber, T. The LRRC8/VRAC Anion Channel Facilitates Myogenic Differentiation of Murine Myoblasts by Promoting Membrane Hyperpolarization. *J. Biol. Chem.* **2019**, *294* (39), 14279–14288. https://doi.org/10.1074/jbc.RA119.008840.

(6) Lim, S.; Kaldis, P. Cdks, Cyclins and CKIs: Roles beyond Cell Cycle Regulation. *Development* **2013**, *140* (15), 3079–3093. https://doi.org/10.1242/dev.091744.

(7) Vermeulen, K.; Van Bockstaele, D. R.; Berneman, Z. N. The Cell Cycle: A Review of Regulation, Deregulation and Therapeutic Targets in Cancer. *Cell Prolif.* **2003**, *36* (3), 131–149. https://doi.org/10.1046/j.1365-2184.2003.00266.x.

(8) Barnum, K. J.; O'Connell, M. J. Cell Cycle Regulation by Checkpoints. In *Cell Cycle Control: Mechanisms and Protocols*; Noguchi, E., Gadaleta, M. C., Eds.; Springer: New York, NY, 2014; pp 29–40. https://doi.org/10.1007/978-1-4939-0888-2_2.

(9) Johnson, D. G.; Walker, C. L. CYCLINS AND CELL CYCLE CHECKPOINTS. *Annu. Rev. Pharmacol. Toxicol.* **1999**, *39* (Volume 39, 1999), 295–312. https://doi.org/10.1146/annurev.pharmtox.39.1.295.

(10) Rao, V. R.; Perez-Neut, M.; Kaja, S.; Gentile, S. Voltage-Gated Ion Channels in Cancer Cell Proliferation. *Cancers* **2015**, *7* (2), 849–875. https://doi.org/10.3390/cancers7020813.

(11) Blackiston, D. J.; McLaughlin, K. A.; Levin, M. Bioelectric Controls of Cell Proliferation: Ion Channels, Membrane Voltage and the Cell Cycle. *Cell Cycle* **2009**, *8* (21), 3527–3536. https://doi.org/10.4161/cc.8.21.9888.

(12) Yang, M.; Brackenbury, W. J. Membrane Potential and Cancer Progression. *Front. Physiol.* **2013**, *4*. https://doi.org/10.3389/fphys.2013.00185.

(13) Sundelacruz, S.; Levin, M.; Kaplan, D. L. Role of Membrane Potential in the Regulation of Cell Proliferation and Differentiation. *Stem Cell Rev. Rep.* **2009**, *5* (3), 231–246. https://doi.org/10.1007/s12015-009-9080-2.

(14) Cone, C. D. Electroosmotic Interactions Accompanying Mitosis Initation in Sarcoma Cells in Vitro. *Trans. N. Y. Acad. Sci.* **1969**, *31* (4), 404–427. https://doi.org/10.1111/j.2164-0947.1969.tb02926.x.

(15) Cone, C. D.; Tongier, M. Mitotic Synchronization of L-Strain Fibroblasts with 5-Aminouracil as Determined by Time-Lapse Cinephotography. NASA TN D-5021. *Tech. Note U. S. Natl. Aeronaut. Space Adm.* **1969**, 1–27.

(16) Cone, C. D.; Tongier, M. Control of Somatic Cell Mitosis by Simulated Changes in the Transmembrane Potential Level. *Oncology* **1971**, *25* (2), 168–182. https://doi.org/10.1159/000224567.
(17) Cone Jr., C. D.; Tongier Jr., M. Contact Inhibition of Division: Involvement of the Electrical Transmembrane Potential. *J. Cell. Physiol.* **1973**, *82* (3), 373–386. https://doi.org/10.1002/jcp.1040820307.
(18) Stillwell, E. F.; Cone, C. M.; Cone, C. D. Stimulation of DNA Synthesis in CNS Neurones by Sustained Depolarisation. *Nature. New Biol.* **1973**, *246* (152), 110–111. https://doi.org/10.1038/newbio246110a0.
(19) Cone, C. D.; Cone, C. M. Induction of Mitosis in Mature Neurons in Central Nervous System by Sustained Depolarization. *Science* **1976**, *192* (4235), 155–158. https://doi.org/10.1126/science.56781.
(20) Cone, C. D. Unified Theory on the Basic Mechanism of Normal Mitotic Control and Oncogenesis. *J. Theor. Biol.* **1971**, *30* (1), 151–181. https://doi.org/10.1016/0022-5193(71)90042-7.
(21) Binggeli, R.; Weinstein, R. C. Membrane Potentials and Sodium Channels: Hypotheses for Growth Regulation and Cancer Formation Based on Changes in Sodium Channels and Gap Junctions. *J. Theor. Biol.* **1986**, *123* (4), 377–401. https://doi.org/10.1016/S0022-5193(86)80209-0.
(22) Cone, Jr., Clarence D. Variation of the Transmembrane Potential Level as a Basic Mechanism of Mitosis Control. *Oncology* **1970**, *24* (6), 438–470. https://doi.org/10.1159/000224545.
(23) Wonderlin, W. F.; Woodfork, K. A.; Strobl, J. S. Changes in membrane potential during the progression of MCF-7 human mammary tumor cells through the cell cycle. *J. Cell. Physiol.* **1995**, *165* (1), 177–185. https://doi.org/10.1002/jcp.1041650121.
(24) Strobl, J. S.; Wonderlin, W. F.; Flynn, D. C. Mitogenic Signal Transduction in Human Breast Cancer Cells. *Gen. Pharmacol. Vasc. Syst.* **1995**, *26* (8), 1643–1649. https://doi.org/10.1016/0306-3623(95)00062-3.
(25) Wang, S.; Melkoumian, Z.; Woodfork, K. A.; Cather, C.; Davidson, A. G.; Wonderlin, W. F.; Strobl, J. S. Evidence for an Early G1 Ionic Event Necessary for Cell Cycle Progression and Survival in the MCF-7 Human Breast Carcinoma Cell Line. *J. Cell. Physiol.* **1998**, *176* (3), 456–464. https://doi.org/10.1002/(SICI)1097-4652(199809)176:3<456::AID-JCP2>3.0.CO;2-N.
(26) Klimatcheva, E.; Wonderlin, W. F. An ATP-Sensitive K+ Current That Regulates Progression Through Early G1 Phase of the Cell Cycle in MCF-7 Human Breast Cancer Cells. *J. Membr. Biol.* **1999**, *171* (1), 35–46. https://doi.org/10.1007/s002329900556.
(27) Ouadid-Ahidouch, H.; Le Bourhis, X.; Roudbaraki, M.; Toillon, R. A.; Delcourt, P.; Prevarskaya, N. Changes in the K+ Current-Density of MCF-7 Cells during Progression through the Cell Cycle: Possible Involvement of a h-Ether.a-Gogo K+ Channel. *Receptors Channels* **2001**, *7* (5), 345–356.
(28) Dubois, J.-M.; Rouzaire-Dubois, B. Role of Potassium Channels in Mitogenesis. *Prog. Biophys. Mol. Biol.* **1993**, *59* (1), 1–21. https://doi.org/10.1016/0079-6107(93)90005-5.
(29) MacFarlane, S. N.; Sontheimer, H. Changes in Ion Channel Expression Accompany Cell Cycle Progression of Spinal Cord Astrocytes. *Glia* **2000**, *30* (1), 39–48. https://doi.org/10.1002/(SICI)1098-1136(200003)30:1<39::AID-GLIA5>3.0.CO;2-S.

(30) Lazzari-Dean, J. R.; Gest, A. M. M.; Miller, E. W. Measuring Absolute Membrane Potential Across Space and Time. *Annu. Rev. Biophys.* **2021**, *50*, 447–468. https://doi.org/10.1146/annurev-biophys-062920-063555.
(31) Berezin, M. Y.; Achilefu, S. Fluorescence Lifetime Measurements and Biological Imaging. *Chem. Rev.* **2010**, *110* (5), 2641–2684. https://doi.org/10.1021/cr900343z.
(32) Lazzari-Dean, J. R.; Gest, A. M.; Miller, E. W. Optical Estimation of Absolute Membrane Potential Using Fluorescence Lifetime Imaging. *eLife* **2019**, *8*, e44522. https://doi.org/10.7554/eLife.44522.
(33) Miller, E. W.; Lin, J. Y.; Frady, E. P.; Steinbach, P. A.; Kristan, W. B.; Tsien, R. Y. Optically Monitoring Voltage in Neurons by Photo-Induced Electron Transfer through Molecular Wires. *Proc. Natl. Acad. Sci.* **2012**, *109* (6), 2114–2119. https://doi.org/10.1073/pnas.1120694109.
(34) Chen, G.; Deng, X. Cell Synchronization by Double Thymidine Block. *Bio-Protoc.* **2018**, *8* (17), e2994. https://doi.org/10.21769/BioProtoc.2994.
(35) Ligasová, A.; Koberna, K. Strengths and Weaknesses of Cell Synchronization Protocols Based on Inhibition of DNA Synthesis. *Int. J. Mol. Sci.* **2021**, *22* (19), 10759. https://doi.org/10.3390/ijms221910759.
(36) Wang, R. C.; Wang, Z. Synchronization of Cultured Cells to G1, S, G2, and M Phases by Double Thymidine Block. In *Cell-Cycle Synchronization: Methods and Protocols*; Wang, Z., Ed.; Springer US: New York, NY, 2022; pp 61–71. https://doi.org/10.1007/978-1-0716-2736-5_5.
(37) Salic, A.; Mitchison, T. J. A Chemical Method for Fast and Sensitive Detection of DNA Synthesis in Vivo. *Proc. Natl. Acad. Sci. U. S. A.* **2008**, *105* (7), 2415–2420. https://doi.org/10.1073/pnas.0712168105.
(38) Flomerfelt, F. A.; Gress, R. E. Analysis of Cell Proliferation and Homeostasis Using EdU Labeling. *Methods Mol. Biol. Clifton NJ* **2016**, *1323*, 211–220. https://doi.org/10.1007/978-1-4939-2809-5_18.
(39) Sakaue-Sawano, A.; Kurokawa, H.; Morimura, T.; Hanyu, A.; Hama, H.; Osawa, H.; Kashiwagi, S.; Fukami, K.; Miyata, T.; Miyoshi, H.; Imamura, T.; Ogawa, M.; Masai, H.; Miyawaki, A. Visualizing Spatiotemporal Dynamics of Multicellular Cell-Cycle Progression. *Cell* **2008**, *132* (3), 487–498. https://doi.org/10.1016/j.cell.2007.12.033.
(40) Caillat, C.; Perrakis, A. Cdt1 and Geminin in DNA Replication Initiation. In *The Eukaryotic Replisome: a Guide to Protein Structure and Function*; MacNeill, S., Ed.; Springer Netherlands: Dordrecht, 2012; pp 71–87. https://doi.org/10.1007/978-94-007-4572-8_5.
(41) Bruno, S.; Di Vinci, A.; Geido, E.; Giaretti, W. Cell Cycle Synchronization Induced by Tamoxifen and 17β-Estradiol on MCF-7 Cells Using Flow Cytometry and a Monoclonal Antibody against Bromodeoxyuridine. *Breast Cancer Res. Treat.* **1988**, *11* (3), 221–229. https://doi.org/10.1007/BF01807280.

Chapter 3
Tracking Changes in Membrane Potential Throughout the Cell Cycle

Abstract

New methods like VF-FLIM offer minimally invasive and high throughput approaches towards characterizing membrane potential dynamics during essential biophysical processes like cell cycle progression. Previous experiments were suggestive of variations in membrane potential across the cell cycle, showing a 10 mV depolarization in G_2/M cells compared to cells in G_1 and S phase. However, these measurements are only representative of a single point during the cell cycle and do not fully illustrate how membrane potential may fluctuate over time. Here, we shift to tracking changes in voltage throughout cell cycle progression by combining VF-FLIM with the cell cycle sensor DHB-mVenus. We generated a line of MCF-7 cells stably expressing DHB-mVenus to enable simultaneous recording of membrane potential and cell cycle progression. Preliminary work does not reveal a clear trend in membrane potential over time, however, the MCF-7-DHB-mVenus cell line will be a useful tool for further analysis of V_m throughout cell cycle progression.

Introduction

All cells maintain a membrane potential (V_m) that is critical for cell function. Electrically excitable cells like neurons and cardiomyocytes undergo large, rapid changes in V_m which trigger signaling pathways. These changes in potential occur over milliseconds to seconds and are around 100 mV in magnitude. However, smaller scale changes in V_m occurring over seconds to hours in non-electrically excitable cells have also been linked to essential cellular processes including differentiation, migration, volume control, cell division, and cell cycle progression.[1–5]

Regulation of the cell cycle has been extensively studied due to its fundamental role in biology. Cell cycle progression is primarily driven by cyclin-dependent kinases (CDKs) that are sequentially activated by an array of regulatory cyclin proteins. CDK activity can be inhibited by binding of cyclin-dependent kinase inhibitor proteins (CKIs).[6,7] Two cell cycle checkpoints at the G_1/S and the G_2/M transitions are highly regulated through activation or inhibition of CDK/cyclin complexes to either drive cell cycle progression or, in the case of DNA damage or incomplete replication, arrest cells until the proper repair pathways can be completed.[8,9] Although preliminary evidence suggests that changes in membrane potential may occur during the cell cycle, particularly at highly regulated junctures like the G_1/S and G_2/M checkpoints,[10–12] these fluctuations in V_m have not been well characterized due to limitations in voltage imaging.

Patch-clamp electrophysiology has long been the gold-standard for quantifying V_m, but the technique is low-throughput, highly invasive, and difficult to maintain over timescales of interest from seconds to hours. Intensity-based voltage imaging is not ideal for quantitatively measuring V_m because intensity is affected by fluorophore concentration, photobleaching, and illumination intensity. To address these pitfalls, the Miller lab has developed a series of VoltageFluors (VFs), which are voltage-sensitive fluorophores that localize to the plasma membrane. They respond to changes in V_m through a photoinduced electron transfer mechanism, resulting in modulation of fluorescence intensity and lifetime. Conversely, fluorescence lifetime is an intrinsic property of the dye and is independent of the factors that affect intensity,[13] allowing us to quantify membrane potential through fluorescence lifetime imaging (FLIM). The VF-FLIM method enables non-invasive and high-throughput optical determination of absolute V_m using linear, cell-type specific calibrations between membrane potential and fluorescence lifetime.[14,15]

Our initial work used VF-FLIM to measure V_m in MCF-7 breast cancer cells, which have previously been shown to hyperpolarize as cells transition through G_1 and into S phase, followed by depolarization corresponding with progression from G_2 to M phase.[16–20] We identified differences in V_m between cell cycle phases, with cells in G_2 or M phase depolarized by approximately 10 mV relative to cells in G_1 or S phase (**Chapter 2**). However, after making fluorescence lifetime measurements to determine V_m, the cells were subsequently fixed to determine cell cycle phase. We were thus unable to make multiple measurements of V_m over time, preventing any way of observing how V_m may be modulated throughout the cell cycle.

Additionally, VF-FLIM is most accurate when measuring changes of membrane potential within a single cell, rather than making comparisons between populations of cells. The resolution of VF-FLIM can be expressed as the root-mean-square deviation (RMSD) between the optically measured voltage (V_{FLIM}) and the voltage set by patch-clamp electrophysiology (V_{ephys}) during lifetime-voltage calibration (**Methods**, *Lifetime-Voltage Calibration*). The inter-cell RMSD reports the average difference between V_{ephys} and corresponding V_{FLIM} calculated from the measured lifetime using the overall best-fit calibration. It conservatively estimates the maximum possible error arising from calculating absolute V_m for a particular cell group from the overall calibration. Conversely, the intra-cell RMSD describes the average difference between V_{ephys} and the corresponding V_{FLIM} calculated from the measured lifetime using an individual cell's best-fit calibration. It thus approximates the error expected from quantifying changes in voltage within an individual cell. In all dyes and cell lines calibrated through VF-FLIM, the intra-cell RMSD is around 5 to 6 mV, compared to inter-cell RMSDs ranging from 10 to 23 mV, highlighting the strength of VF-FLIM in measuring small changes in V_m within individual cells.[15,21] These values approximate the maximum amount of error for an individual cell, either from a single measurement (inter-cell RMSD) or when recorded over time (intra-cell RMSD), assuming the electrophysiology recordings used for the calibration are perfectly accurate. In practice, some of the error in the calibration likely arises from varying voltage clamp quality, so the RMSD values are a conservative estimate of the maximum possible error.

To utilize the VF-FLIM technique to its maximum capabilities, we sought to make measurements of V_m over time to investigate how voltage may change as cells progress through the cell cycle. However, our previous method of determining cell cycle phase relied on fixation and immunostaining, preventing us from recording individual cells at multiple time points. Instead, we looked for a sensor suitable for tracking cell cycle phase over time in live cells. FUCCI has been well-characterized as a reporter of cell cycle progression for live cells.[22] However, it relies on two fluorophores and necessitates separation between the two spectra to avoid overlapping signals, which would be difficult to achieve since a third color is also required for the VoltageFluor. As an alternative, we proposed using the single-color fluorescent probe DHB-mVenus to monitor cell cycle progression.

DHB-mVenus was developed by Spencer et al. and consists of a fragment of DNA Helicase B tagged to the fluorescent protein mVenus[6]. DHB-mVenus localization shifts from the nucleus to the cytoplasm in response to CDK2 activity throughout the cell cycle (**Figure 3.1a**). CDK2 is initially activated by cyclin E to regulate the transition from G_1 to S phase, and CDK2 activity continues to increase as cells progress through the rest of the cell cycle. Spencer et al. demonstrated that DHB-mVenus is primarily localized to the nucleus in G_1 cells. DHB-mVenus is

phosphorylated by CDK2 as it becomes active and is subsequently translocated to the cytoplasm. This translocation continues as CDK2 activity increases until DHB-mVenus localization is largely cytosolic in M phase. After cell division, DHB-mVenus returns to the nucleus. Measuring the ratio between cytosolic and nuclear fluorescence intensity can thus be used to approximate cell cycle phase in live cells (**Figure 3.1b**, **Table 3.1**).

The cytosolic-to-nuclear (Cyt/Nuc) ratio compares the mean fluorescence intensity of the nuclear region of interest (ROI) with the mean fluorescence intensity of a ring-shaped ROI of the cytosol surrounding the nucleus (**Figure 3.1b**). During G_1, cytoplasmic translocation of DHB-mVenus is just beginning, so fluorescence is primarily nuclear and the Cyt/Nuc ratio is less than 1 and increasing over time. Entry into S phase corresponds with a Cyt/Nuc ratio around 1, and fluorescence is nearly equal between the nuclear and cytosolic ROIs. As cells continue through G_2, cytosolic fluorescence continues to increase, and the Cyt/Nuc ratio is seen increasing above 1. This trend continues into M phase, with the Cyt/Nuc ratio reaching approximately 2, before rapidly decreasing during cell division before the process begins again. We aimed to use these Cyt/Nuc values to identify cell cycle phase as shown in **Table 3.1**.

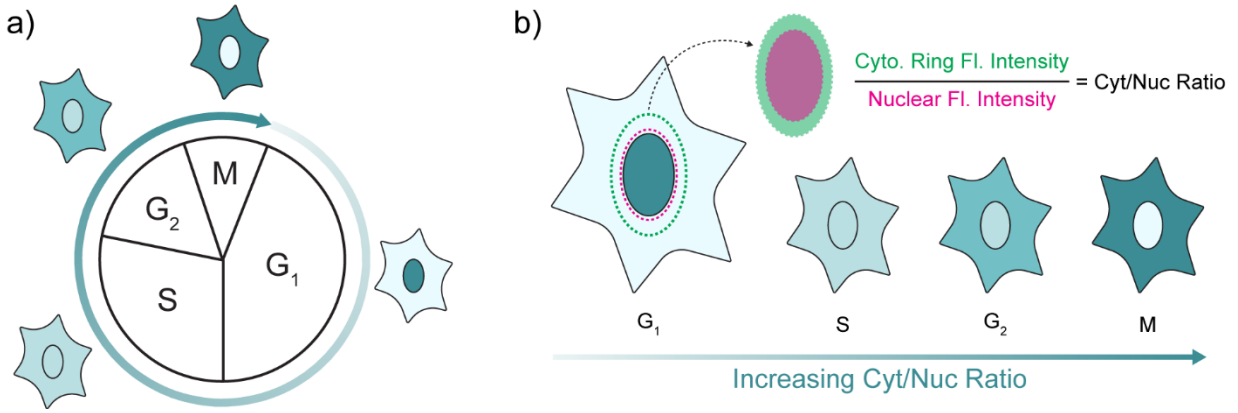


Figure 3.1. DHB-mVenus expression is cell cycle dependent.
a) Expression and localization of DHB-mVenus varies throughout the cell cycle. In G_1, cells have high nuclear DHB-mVenus fluorescence and low cytosolic fluorescence. As cells progress through the cell cycle, DHB-mVenus is translocated to the cytosol, resulting in decreasing nuclear intensity and increasing cytosolic intensity. Following cell division in M phase, DHB-mVenus returns to the nucleus. **b)** The ratio of cytosolic-to-nuclear fluorescence tracks progression through the cell cycle.[23] After identifying the nuclear region of interest (ROI), the ROI is expanded by a specified number of pixels to create a cytosolic ring ROI. By calculating the ratio between the cytosolic and nuclear intensity, it is possible to approximate the location in the cell cycle.

Approximate Cyt/Nuc Ratio	Cell Cycle Phase
< 1, increasing	G_1
≈ 1, increasing	S
> 1, increasing	G_2
> 1, decreasing	M

Table 3.1. Relationship between Cyt/Nuc ratio and cell cycle phase.
Cyt/Nuc ratio can be used to approximate cell cycle phase, as shown in Spencer et al.[23]

We also wanted to be able to easily generate a line of cells with stable DHB-mVenus expression to avoid issues associated with transient transfections such as low transfection efficiency or large differences in expression levels between cells. The Sleeping Beauty (SB) transposon system facilitates quick generation of stable cell lines. Transposons are sequences of DNA that can move around within a genome. The SB100X transposase was reconstructed from an extinct salmonid transposase and optimized to perform gene insertion in mammalian cells. The corresponding SB transposon element was also designed to enable transposition of genes of interest.[24,25]

The transposon consists of the gene of interest flanked by inverted terminal repeat (ITR) sequences that contain binding sites for the transposase (**Figure 3.2a**). When the transposase binds, DNA cleavage occurs on either side of the ITRs and the transposon sequence is excised. The SB transposase can then integrate the gene of interest at one of the thousands of TA dinucleotide sequences in the target genome, resulting in transfer of the gene of interest and duplication of the TA sequence.[26] Kowarz et al. constructed a series of SB plasmids with a bidirectional promoter to drive expression of the gene of interest and an antibiotic resistance gene to aid in selection.[27] We designed a plasmid to insert DHB-mVenus into one of these vector backbones (pSBbi-Neo) to easily enable stable expression (**Figure 3.2b**).

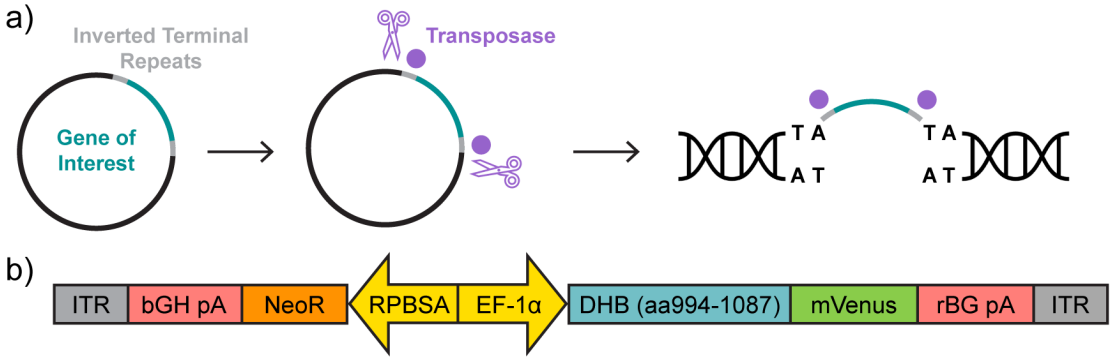


Figure 3.2. Sleeping Beauty transposons enable stable cell line generation with a gene of interest.
a) Overview of Sleeping Beauty transposon system.[26] The transposon plasmid includes the gene of interest (teal) flanked by inverted terminal repeat sequences (gray). The transposase binds to the ITRs, excises the DNA, and inserts it into the target genome at a TA dinucleotide. **b)** Construction of pSBbi-DHB-mVenus-Neo plasmid for stable cell line generation through Sleeping Beauty transposons.[27] DHB-mVenus was cloned into the pSBbi-Neo backbone, in between the EF-1α promoter and beta-globin polyadenylation signal (rBG pA). The backbone also contains the RPBSA promoter in the opposite direction to drive expression of the Neomycin resistance (NeoR) gene, followed by the bovine growth hormone polyadenylation signal (bGH pA). The construct is flanked by inverse terminal repeat (ITR) sequences, which are recognized by the SB100X transposase and facilitate integration into the genome.

The red-shifted VoltageFluor CRhOMe is spectrally compatible with mVenus, making this combination feasible for dual measurements of V_m and cell cycle progression in cells. This chapter presents the development of a stable line of MCF-7-DHB-mVenus cells for tracking cell cycle progression and characterization of their resting lifetime and Cyt/Nuc ratio.

Results and Discussion

We designed and constructed the pSBbi-DHB-mVenus-Neo plasmid to enable stable cell line generation through the Sleeping Beauty transposon system (**Figure 3.2b**). The DHB-mVenus fragment from the original lentiviral plasmid developed by Spencer et al. was inserted into the

empty pSBbi-Neo backbone. After assembling the plasmid and confirming its sequence, we wanted to validate the expression in cells. We started by transiently co-transfecting MCF-7 cells with the DHB-mVenus plasmid and SB100X transposase at ratios of 5:1 and 10:1 (DHB:transposase). Transfection at both 5:1 and 10:1 ratios showed similar DHB-mVenus expression levels (**Figure 3.3**).

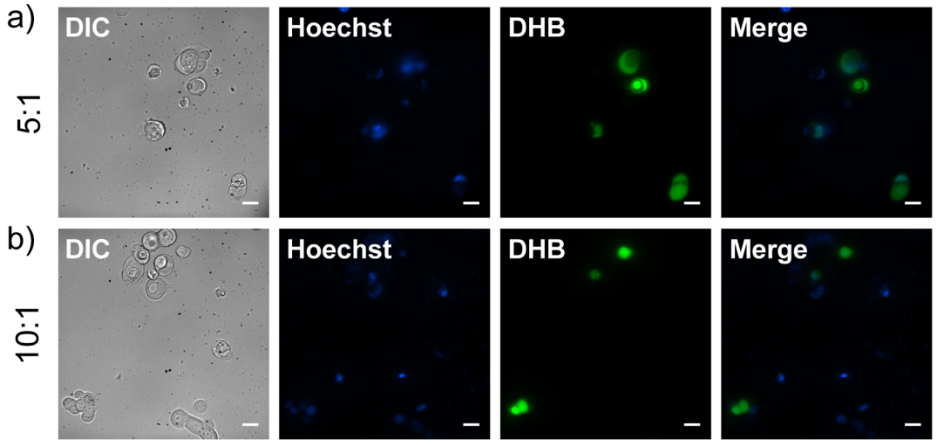


Figure 3.3. Transient expression of DHB-mVenus in MCF-7 cells.
Representative DIC and epifluorescence images of MCF-7 cells transiently co-transfected with pSBbi-DHB-mVenus-Neo and SB100X at a ratio of **a)** 5:1 or **b)** 10:1 of DHB-mVenus : transposase. Cells were also loaded with 10 μM Hoechst 33342. Hoechst and DHB-mVenus images are scaled to one another. Scale bars are 20 μm.

We also evaluated DHB-mVenus expression over time by acquiring one Hoechst and DHB-mVenus image set every 10 minutes for one hour (**Figure 3.4**). The cytosolic-to-nuclear (Cyt/Nuc) ratio was calculated by measuring the nuclear and cytosolic intensity of DHB-mVenus. This analysis was automated by building a custom pipeline in CellProfiler (**Methods**, *Cyt/Nuc Ratio Analysis*). The nuclear regions of interest (ROIs) were identified via thresholding of the Hoechst image (**Figure 3.4a**). These ROIs were subsequently expanded by a specified number of pixels, and the cytosolic ring ROI was defined as the ring-shaped ROI between the inner nuclear ROI and the outer edge of the expanded ROI. The Cyt/Nuc ratio was the calculated by dividing the mean cytosolic ring fluorescence intensity by the mean nuclear fluorescence intensity measured from the DHB-mVenus image.

The Cyt/Nuc ratio steadily increased or decreased over one hour in different cells which indicates that DHB-mVenus expression is changing over time, consistent with the original DHB-mVenus plasmid developed by Spencer et al. (**Figure 3.4b, left**). We acquired two additional images during the first and last five minutes to track the Cyt/Nuc ratio over a smaller timescale (**Figure 3.4b, middle, right**). FLIM images typically require a one to two minute long exposure, so we wanted to be sure that DHB-mVenus images acquired before FLIM would be representative of the Cyt/Nuc ratio throughout the lifetime acquisition. Over the first and last five minutes of the time series, the Cyt/Nuc ratio changed minimally.

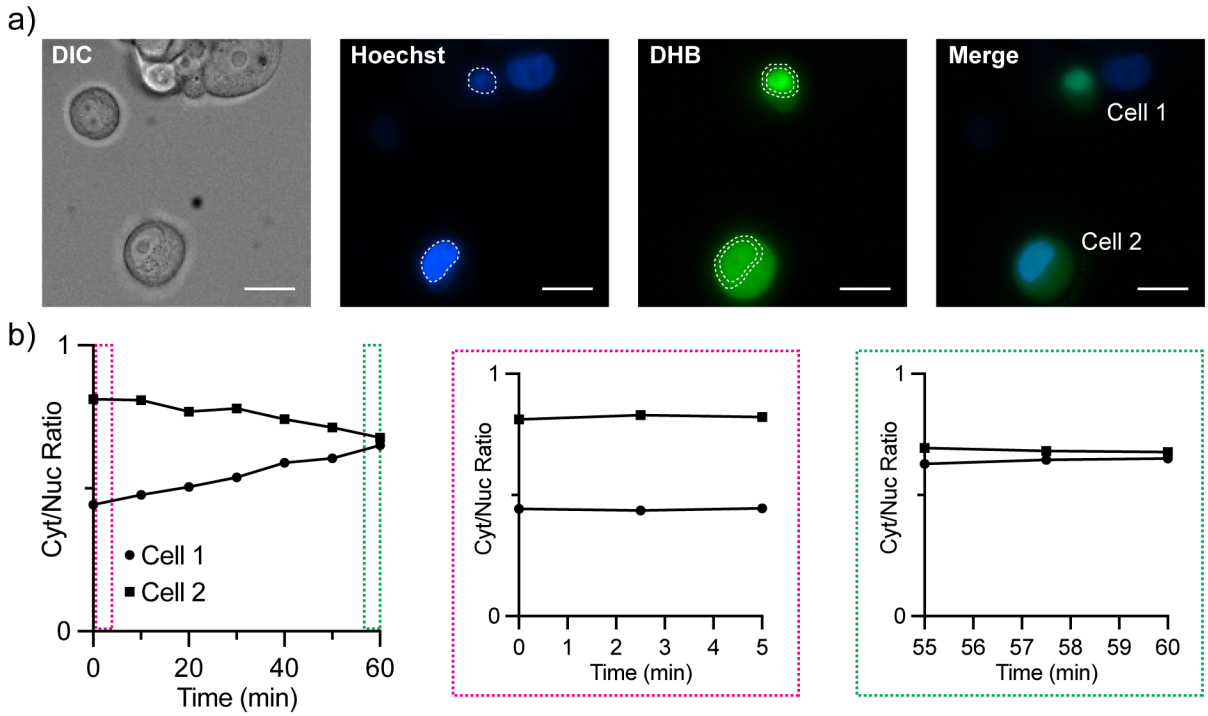


Figure 3.4. DHB-mVenus expression varies over time in MCF-7 cells.
a) Representative DIC and epifluorescence images of MCF-7 cells transiently expressing pSBbi-DHB-mVenus-Neo and loaded with 10 µM Hoechst 33342. White dashed lines on the Hoechst image indicate identified nuclear ROIs. On the DHB-mVenus image, the inner white dashed line demarcates the nuclear ROI, while the cytosolic ring is defined by expanding the nuclear ROI (outer white dashed line) and measuring the fluorescence between the inner and outer dashed lines. **b)** Graphs showing the quantification of the Cyt/Nuc ratio for the two cells identified in **a)** over 60 minutes, with subplots highlighting the first (pink) and last (green) five minutes. The Cyt/Nuc is seen increasing (Cell 1) or decreasing (Cell 2) over the full time scale, as expected, but the ratio is relatively stable over shorter periods.

After validating the transient expression of DHB-mVenus, we wanted to develop a stable cell line, which is easily facilitated by antibiotic selection with G418. We treated MCF-7 cells with varying concentrations of G418 and used Trypan Blue to assess the number of dead vs surviving cells after 7 days in culture (**Figure 3.5a**). We decided to proceed with several concentrations (400, 600, 800, and 1000 µg/mL) for antibiotic selection. MCF-7 cells were plated in 6-well plates and co-transfected with pSBbi-DHB-mVenus-Neo and SB100X in a 5:1 ratio. After three days in culture, the cells were media changed to fresh media containing G418 antibiotic. Cells were routinely maintained with fresh media and antibiotic every 2-3 days for 2 weeks, at which point we imaged cells to confirm stable polyclonal expression of DHB-mVenus. We then isolated single cells from each of the four polyclonal lines (corresponding to the four G418 concentrations used for selection) by limiting dilution to grow monoclonal lines. The best growing monoclonal line was isolated from the polyclonal MCF-7-DHB-mVenus cell line selected with 400 µg/mL G418 (**Figure 3.5b**).

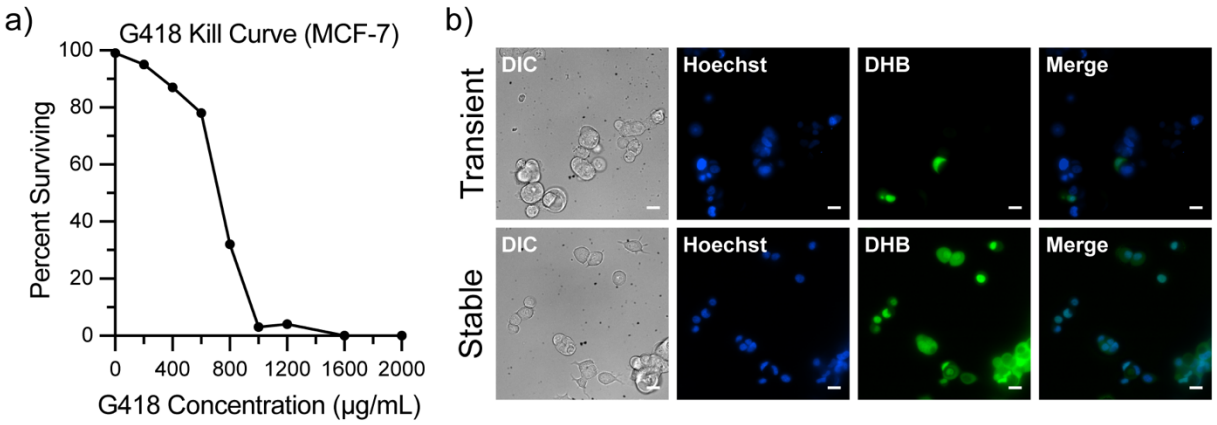


Figure 3.5. Stable expression of DHB-mVenus in MCF-7 cells.
a) MCF-7 cells were grown in the presence of varying concentrations of G418 to determine the optimal concentration for antibiotic selection. **b)** Representative DIC and epifluorescence images of MCF-7 cells transiently and stably expressing pSBbi-DHB-mVenus-Neo. Cells were also loaded with 10 µM Hoechst 33342. Stable MCF-7-DHB-mVenus cells were selected with 400 µg/mL G418 to generate a polyclonal line, and subsequently single cells were isolated to generate a monoclonal line (shown here). Hoechst and DHB-mVenus images are scaled to one another. Scale bars are 20 µm.

After successfully isolating a monoclonal cell line, we proceeded with FLIM using the VoltageFluor CRhOMe to characterize the resting lifetime in monoclonal cells compared to wild-type MCF-7 cells without DHB-mVenus expression (**Figure 3.6a,c,d,f**). Both cell types have a similar resting lifetime slightly above 2.7 ns (**Table 3.2**). We later measured the resting lifetime in polyclonal MCF-7-DHB-mVenus cells and found that they have a longer lifetime by about 200 ps compared to both monoclonal MCF-7-DHB-mVenus and non-expressing MCF-7 cells, indicating a hyperpolarized resting V_m (**Figure 3.6b,e**, **Table 3.2**). Cells were also imaged with and without co-staining of Hoechst 33342 to determine whether Hoechst would interfere with lifetime measurements or affect the resting lifetime of cells. For each subset of cells, there was not a significant difference between the resting lifetime measured with or without Hoechst (two-sided, unpaired, unequal variances t-test for non-expressing and polyclonal cells or ordinary one-way ANOVA for monoclonal cells). Monoclonal cells were also imaged after being cultured with or without G418 antibiotic, and there was not a significant difference between the resting lifetime measured at each condition (ordinary one-way ANOVA).

While there is not a significant difference between the resting lifetimes of monoclonal and non-expressing cells, there is a difference between each of these populations and the resting lifetime of polyclonal MCF-7-DHB-mVenus cells (ordinary one-way ANOVA, **Figure 3.6g**, **Table 3.3**). Since Sleeping Beauty transposons can insert the gene of interest at multiple locations in the genome, there is much more variability within the polyclonal MCF-7-DHB-mVenus cells compared to wild-type MCF-7 cells or monoclonal MCF-7-DHB-mVenus cells.

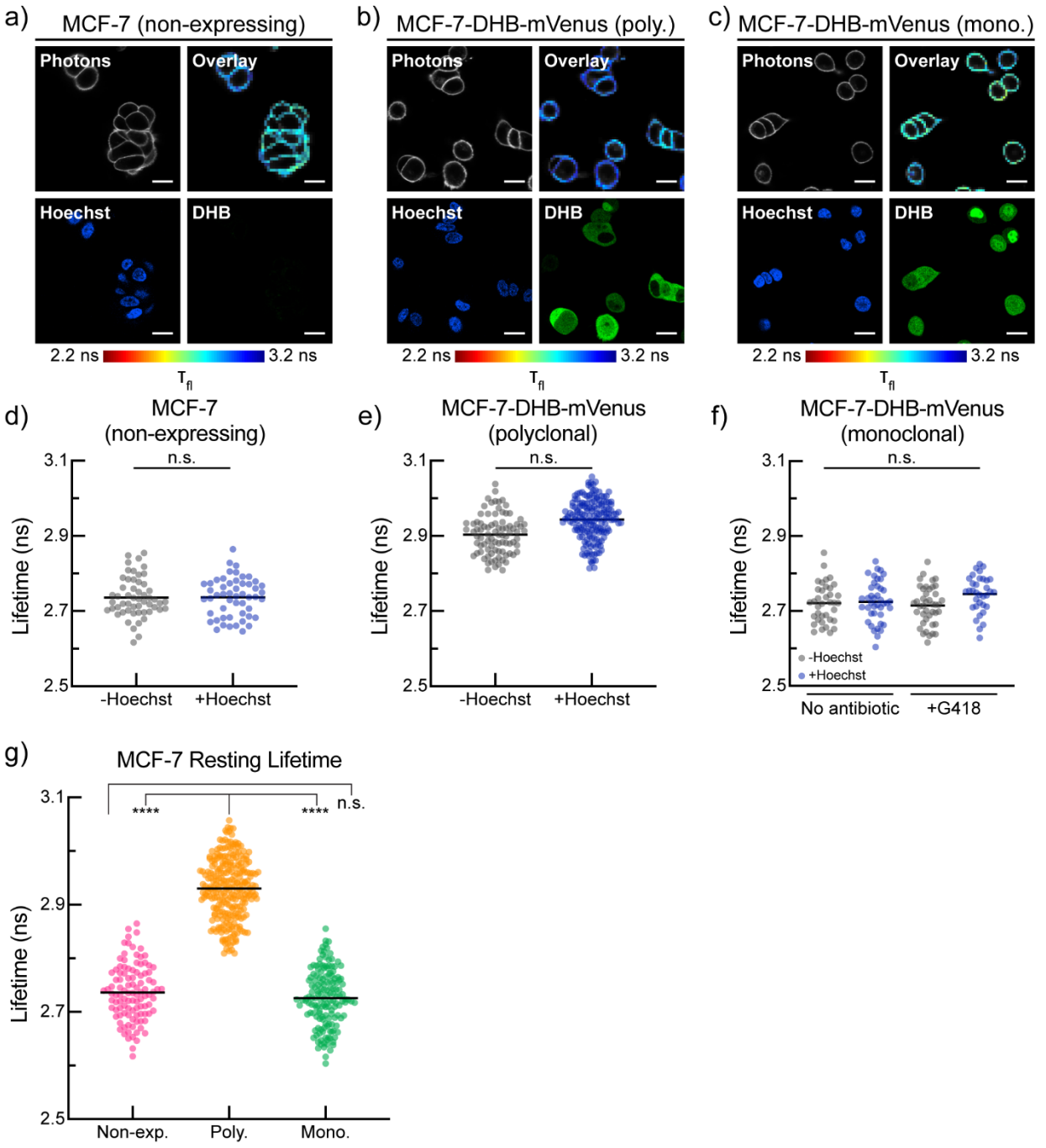


Figure 3.6. Comparison of CRhOMe resting lifetime in MCF-7 cells without DHB-mVenus expression, polyclonal MCF-7-DHB-mVenus cells, and monoclonal MCF-7-DHB-mVenus cells.
Representative raw photon intensity, lifetime-intensity overlay, Hoechst 33342, and DHB-mVenus images of **a)** wild-type MCF-7 cells without DHB-mVenus expression, **b)** polyclonal MCF-7-DHB-mVenus cells, or **c)** monoclonal MCF-7-DHB-mVenus cells. Cells were loaded with 300 nM CRhOMe and 20 μM Hoechst. Scale bars are 20 μm. All Hoechst and all DHB-mVenus images are scaled to one another, but photon intensity and lifetime images are not. Scatter plots of CRhOMe lifetime in **d)** wild-type MCF-7 cells without DHB-mVenus expression, **e)** polyclonal MCF-7-DHB-mVenus cells, or **f)** monoclonal MCF-7-DHB-mVenus cells. Monoclonal cells were grown with or without G418 antibiotic. All cells were either loaded with only 300 nM CRhOMe (gray) or co-loaded with 300 nM CRhOMe and 10 μM Hoechst (blue). Each point represents a cell group ROI, consisting of approximately 1-10 cells on average. There is not a statistically significant difference between the

lifetimes of cells with or without Hoechst, or between the lifetimes of cells grown with or without G418 (n.s. $p > 0.05$, two-sided, unpaired, unequal variances t-test for non-expressing and polyclonal cells or ordinary one-way ANOVA for monoclonal cells). **g)** Scatter plot of CRhOMe lifetime in wild-type MCF-7 cells without DHB-mVenus expression (pink), polyclonal MCF-7-DHB-mVenus cells (orange), or monoclonal MCF-7-DHB-mVenus cells (green). Data is compiled from graphs shown in **d-f**. Asterisks note significant differences between indicated populations of cells (n.s. $p > 0.05$, * $p < 0.05$, ** $p < 0.01$, *** $p < 0.001$, **** $p < 0.0001$, ordinary one-way ANOVA). Lines on graphs indicate the mean. Resting lifetime values (mean ± SEM) are given in **Table 3.2**. Sample sizes (number of cell groups): Non-expressing (-Hoechst) 52, Non-expressing (+Hoechst) 54, Non-expressing (Overall) 106, Polyclonal (-Hoechst) 86, Polyclonal (+Hoechst) 170, Polyclonal (Overall) 256, Monoclonal (-G418, -Hoechst) 37, Monoclonal (-G418, +Hoechst) 41, Monoclonal (+G418, -Hoechst) 42, Monoclonal (+G418, +Hoechst) 34, Monoclonal (Overall) 154.

	CRhOMe Resting Lifetime (ns)		
MCF-7 Cell Type	**-Hoechst**	**+Hoechst**	**Overall**
Non-expressing	2.737 ± 0.007	2.736 ± 0.007	2.736 ± 0.005
Polyclonal	2.904 ± 0.005	2.944 ± 0.004	2.930 ± 0.003
Monoclonal -G418	2.721 ± 0.008	2.725 ± 0.008	2.726 ± 0.004
Monoclonal +G418	2.714 ± 0.008	2.745 ± 0.008	

Table 3.2. CRhOMe resting lifetime in MCF-7 cells without DHB-mVenus expression, polyclonal MCF-7-DHB-mVenus cells, and monoclonal MCF-7-DHB-mVenus cells.
Summary of graphs in **Figure 3.6d-g** showing CRhOMe lifetime in wild-type MCF-7 cells without DHB-mVenus expression, polyclonal MCF-7-DHB-mVenus cells, or monoclonal MCF-7-DHB-mVenus cells. Monoclonal cells were grown with or without G418 antibiotic. Lifetime values are mean ± SEM. Sample sizes (number of cell groups): Non-expressing (-Hoechst) 52, Non-expressing (+Hoechst) 54, Non-expressing (Overall) 106, Polyclonal (-Hoechst) 86, Polyclonal (+Hoechst) 170, Polyclonal (Overall) 256, Monoclonal (-G418, -Hoechst) 37, Monoclonal (-G418, +Hoechst) 41, Monoclonal (+G418, -Hoechst) 42, Monoclonal (+G418, +Hoechst) 34, Monoclonal (Overall) 154.

We also developed a lifetime-voltage calibration through patch-clamp electrophysiology (**Figure 3.7**, **Table 3.3**). Wild-type MCF-7 cells and MCF-7-DHB-mVenus cells were patch-clamped at potentials ranging from -80 mV to +80 mV while FLIM images were simultaneously acquired to correlate lifetime and voltage. The slope of the calibration describes the sensitivity of CRhOMe lifetime to changes in voltage, while the y-intercept is equivalent to the lifetime at 0 mV. In non-expressing MCF-7 cells, we recorded a slope of 2.33 ± 0.08 ps/mV with the y-intercept at 2.80 ± 0.02 ns (mean ± SEM for n = 4 cells). These values are in good agreement with the slope of 2.28 ± 0.01 ps/mV and y-intercept at 2.82 ± 0.05 ns obtained for monoclonal MCF-7-DHB-mVenus cells (mean ± SEM for n = 3 cells).

The inter-cell RMSD represents the expected variability in quantifying V_m from a single measurement, while the intra-cell RMSD describes the accuracy in recording voltage changes in a particular cell (**Methods**, *Lifetime-Voltage Calibration*). There is some variation between the inter-cell RMSD values (16 mV for non-expressing MCF-7 cells versus 35 mV for MCF-7-DHB-mVenus cells). However, these values roughly align with the 23 mV inter-cell RMSD determined for the VoltageFluor VF2.1.Cl in MCF-7 cells. The intra-cell RMSD is much smaller at 3.4 ± 0.3 mV.[15] The intra-cell RMSD values in non-expressing MCF-7 and MCF-7-DHB-mVenus cells remained low at 5.6 ± 0.9 mV and 3 ± 1 mV (mean ± SEM), respectively, highlighting the success of this technique in tracking relatively small changes in voltage within a cell.

Using the lifetime-voltage calibrations to convert the mean resting lifetimes to voltages, we calculated resting V_m to be -28 ± 10 mV for non-expressing MCF-7 cells and -44 ± 22 mV for MCF-7-DHB-mVenus cells (mean ± SEM including propagated error from calibration). The difference in V_m between the two types of cells is not statistically significant ($p > 0.05$, two-sided, unpaired, unequal variances t-test).These potentials are consistent with the resting V_m measured using VF2.1.Cl (-29 ± 5 mV),[15] as well as other values of MCF-7 resting membrane potential reported in the literature.[16,18,20,28,29]

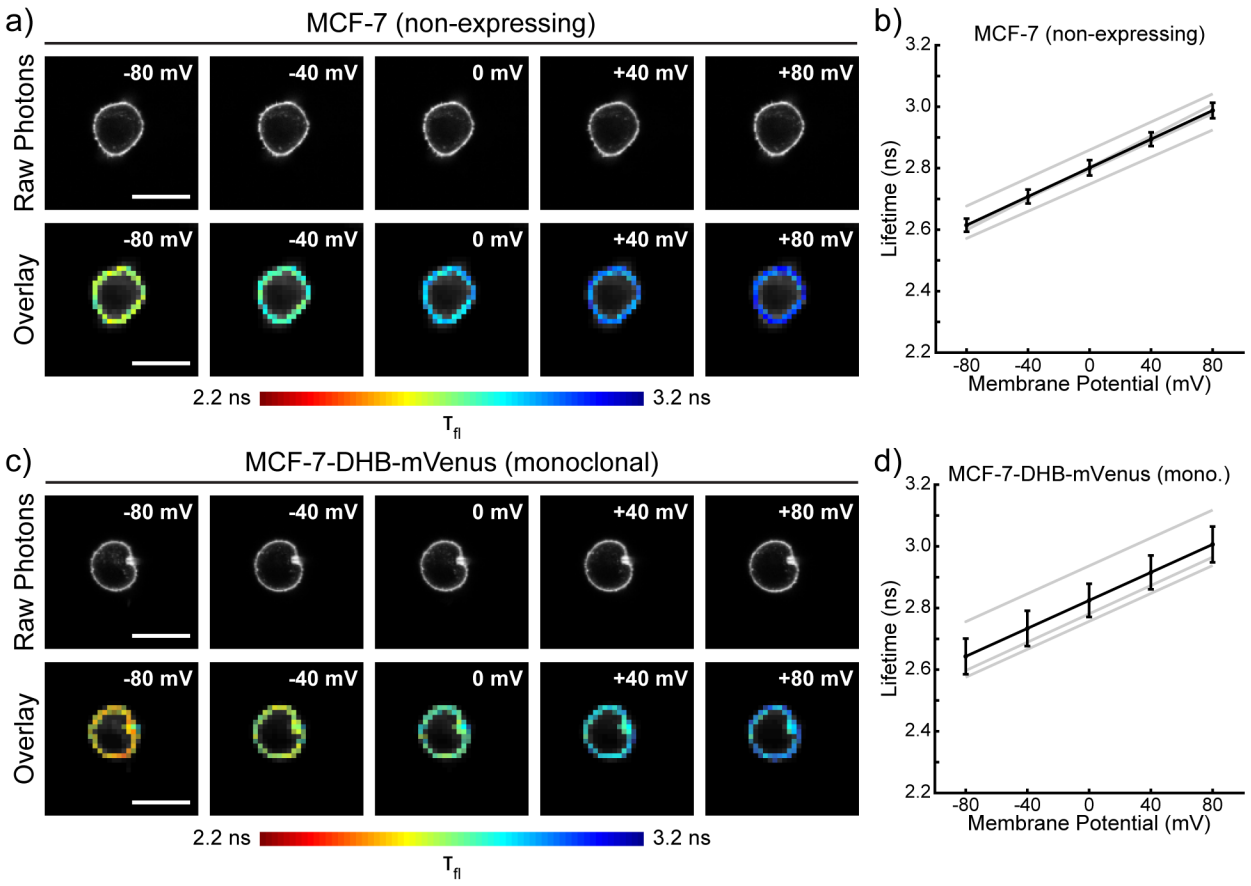


Figure 3.7. CRhOMe lifetime-voltage calibration in MCF-7 cells without DHB-mVenus expression and monoclonal MCF-7-DHB-mVenus cells.
a) Representative raw photon intensity and binned lifetime-intensity overlay images of an MCF-7 cell without DHB-mVenus expression loaded with 300 nM CRhOMe and patch-clamped at the indicated voltages. Scale bars are 20 µm. **b)** Plot of CRhOMe lifetime vs voltage in non-expressing MCF-7 cells. Gray lines are individual cell calibrations (n = 4). The average calibration is in black. Error bars are mean ± SEM. **c)** Representative raw photon intensity and binned lifetime-intensity overlay images of a monoclonal MCF-7-DHB-mVenus cell loaded with 300 nM CRhOMe and patch-clamped at the indicated voltages. Scale bars are 20 µm. **b)** Plot of CRhOMe lifetime vs voltage in MCF-7-DHB-mVenus cells. Gray lines are individual cell calibrations (n = 3). The average calibration is in black. Error bars are mean ± SEM.

	Slope (ps/mV)	Y-Intercept (ns)	Inter-Cell RMSD (mV)	Intra-Cell RMSD (mV)
Non-expressing	2.33 ± 0.08	2.80 ± 0.02	16	5.6 ± 0.9
Monoclonal	2.28 ± 0.01	2.82 ± 0.05	35	3 ± 1

Table 3.3. CRhOMe lifetime-voltage calibration in MCF-7 cells without DHB-mVenus expression and monoclonal MCF-7-DHB-mVenus cells.
Slope, y-intercept, inter-cell RMSD, and intra-cell RMSD for CRhOMe in in wild-type MCF-7 cells without DHB-mVenus expression and monoclonal MCF-7-DHB-mVenus cells. Calculation of intra- and inter-cell accuracies are performed via root-mean-square deviation (RMSD) and discussed further under Experimental Details. Data are mean ± SEM for 4 non-expressing MCF-7 cells or 3 monoclonal MCF-7-DHB-mVenus cells.

After characterizing the resting lifetime and developing a calibration for MCF-7-DHB-mVenus cells, we wanted to correlate the Cyt/Nuc ratio with lifetime and voltage for single cells. The lifetime data presented thus far was analyzed using a pixelwise method of lifetime fitting (**Figure 3.8a**). The pixelwise method begins with standard spatial binning of adjacent pixels to achieve photon counts above a specified threshold at each binned pixel. The photon histograms from each individual pixel are combined to produce one decay for the resulting binned pixel. Each binned pixel is then fit to an exponential decay to obtain the lifetime. Regions of interest (ROIs) are identified as single cells or small groups of approximately 2-10 cells clustered together. The mean lifetime is then calculated by averaging the lifetime of all binned pixels within each specified ROI. Conversely, global fitting employs ROI identification prior to exponential fitting, which enables selection of individual cell ROIs, rather than groups of cells. After manually tracing ROIs around individual cell membranes, all photon histograms within each ROI are combined to generate one decay per ROI. Each decay is then fit to an exponential model to give the average lifetime for each identified cell.

Since the previous pixelwise data included small groups of cells, rather than only single cells, we reanalyzed the lifetime data following the global method (**Figure 3.8b, Table 3.4**). The average lifetimes calculated through global analysis were about 50-60 ps lower than the corresponding pixelwise lifetimes. However, the average global lifetimes of non-expressing MCF-7 and MCF-7-DHB-mVenus cells were still similar to one another, measured at 2.663 ± 0.003 ns and 2.678 ± 0.003 ns, respectively (mean ± SEM).

We also recalculated the lifetime-voltage calibration using globally fit lifetime values (**Figure 3.8**, **Table 3.5**). In non-expressing MCF-7 cells, the global slope was 2.41 ± 0.08 ps/mV, which is comparable to the previously calculated pixelwise slope of 2.33 ± 0.08 ps/mV. Similarly, the newly calculated global slope in MCF-7-DHB-mVenus cells (2.39 ± 0.01) was close to the pixelwise slope (2.28 ± 0.01). The inter-cell and intra-cell RMSD values were also similar to the RMSDs obtained from the pixelwise calibrations. The globally fit y-intercept of each cell type was lower than the corresponding pixelwise y-intercept, however, this is consistent with the slightly lower global resting lifetime values.

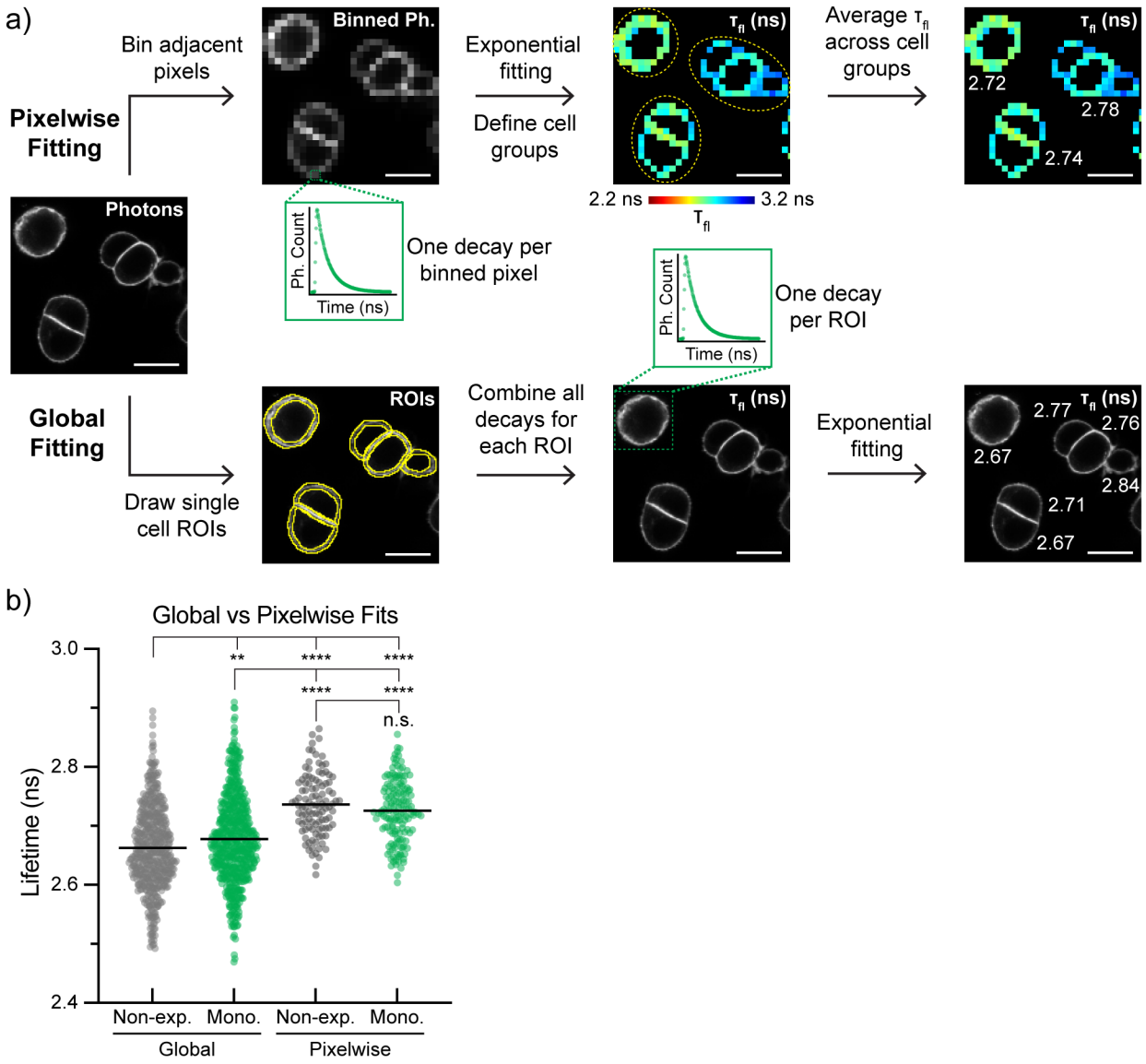


Figure 3.8. Comparison of pixelwise and global fitting of CRhOMe lifetime.
a) Overview of pixelwise **(top)** and global **(bottom)** fluorescence lifetime fitting methods. The pixelwise method involves binning adjacent pixels and summing their photon histograms to produce one decay per binned pixel, which is then fit to an exponential model. ROIs are identified as single cells or small groups of approximately 2-10 cells, and the mean lifetime is determined by averaging the lifetime of all binned pixels within each specified ROI. To fit data globally, individual cell ROIs are manually traced prior to exponential fitting, and the photon histograms within each ROI are combined to obtain one decay. Each ROI decay is then fit to an exponential model to give the average lifetime for each identified cell. Scale bars are 20 μm. **b)** Scatter plot of global and pixelwise fits of CRhOMe lifetime in wild-type MCF-7 cells without DHB-mVenus expression and monoclonal MCF-7-DHB-mVenus cells. Global data points represent single cells, while pixelwise data points represent groups of approximately 1-10 cells. Asterisks note significant differences between indicated populations of cells (n.s. $p > 0.05$, * $p < 0.05$, ** $p < 0.01$, *** $p < 0.001$, **** $p < 0.0001$, Brown-Forsythe and Welch ANOVA with Dunnett's T3 multiple comparisons test). Lines on graphs indicate the mean. Resting lifetime values (mean ± SEM) are given in **Table 3.2** (pixelwise) and **Table 3.4** (global). Sample sizes (number of single cells or cell groups): Non-expressing (global) 488, Non-expressing (pixelwise) 106, Monoclonal (global) 602, Monoclonal (pixelwise) 154.

	CRhOMe Resting Lifetime (ns)	
MCF-7 Cell Type	**Global**	**Pixelwise**
Non-expressing	2.663 ± 0.003	2.736 ± 0.007
Monoclonal	2.678 ± 0.003	2.726 ± 0.004

Table 3.4. Comparison of global and pixelwise fitting of CRhOMe resting lifetime in MCF-7 cells without DHB-mVenus expression and monoclonal MCF-7-DHB-mVenus cells.
Summary of graph in **Figure 6b** showing global and pixelwise fits of CRhOMe lifetime in wild-type MCF-7 cells without DHB-mVenus expression and monoclonal MCF-7-DHB-mVenus cells. Lifetime values are mean ± SEM. Sample sizes (number of single cells or cell groups): Non-expressing (global) 488, Non-expressing (pixelwise) 106, Monoclonal (global) 602, Monoclonal (pixelwise) 154.

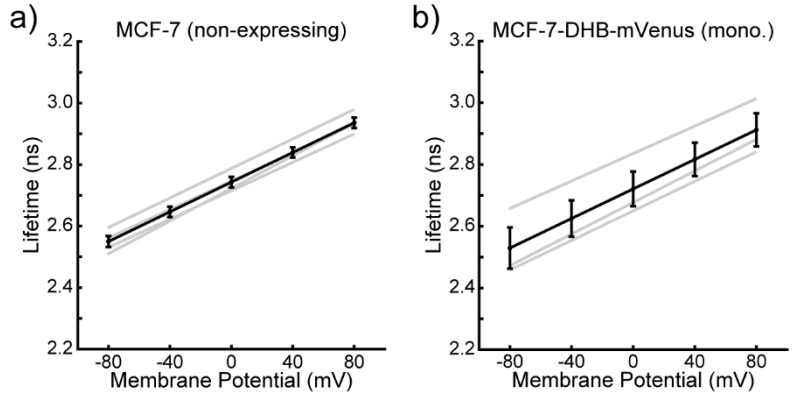


Figure 3.9. Global CRhOMe lifetime-voltage calibration in MCF-7 cells without DHB-mVenus expression and monoclonal MCF-7-DHB-mVenus cells.
Plot of CRhOMe lifetime vs voltage in **a)** non-expressing MCF-7 cells or **b)** monoclonal MCF-7-DHB-mVenus cells. Gray lines are individual cell calibrations (Non-expressing: n = 4; Monoclonal: n = 3). The average calibration is in black. Error bars are mean ± SEM.

	Slope (ps/mV)	Y-Intercept (ns)	Inter-Cell RMSD (mV)	Intra-Cell RMSD (mV)
Non-expressing	2.41 ± 0.08	2.74 ± 0.02	12	6.0 ± 0.6
Monoclonal	2.39 ± 0.01	2.72 ± 0.05	34	5.5 ± 0.8

Table 3.5. Global CRhOMe lifetime-voltage calibration in MCF-7 cells without DHB-mVenus expression and monoclonal MCF-7-DHB-mVenus cells.
Slope, y-intercept, inter-cell RMSD, and intra-cell RMSD for CRhOMe in wild-type MCF-7 cells without DHB-mVenus expression and monoclonal MCF-7-DHB-mVenus cells. Lifetime data was fit globally and is given as mean ± SEM for 4 non-expressing MCF-7 cells or 3 monoclonal MCF-7-DHB-mVenus cells. The corresponding pixelwise calibrations are provided in **Table 3.3**.

To correlate global fluorescence lifetime and Cyt/Nuc ratio, we completed analysis of the Hoechst and DHB-mVenus images in CellProfiler and manually circled the corresponding membrane ROIs in FIJI (**Figure 3.10**) to ultimately create plots of resting lifetime and resting V_m versus the Cyt/Nuc ratio (**Figure 3.11**).



Figure 3.10. Membrane, cytosolic ring, and nuclear ROIs for lifetime and Cyt/Nuc ratio analysis. Representative raw photon intensity, Hoechst, and DHB-mVenus images of monoclonal MCF-7-DHB-mVenus cells loaded with 300 nM CRhOMe and 10 µM Hoechst 33342. The hand-drawn membrane ROIs from FIJI ("Membranes") and identified cytosolic ring (white) and nuclear (pink) ROIs from CellProfiler ("Cyt/Nuc ROIs") are also shown. Scale bar is 20 µm.

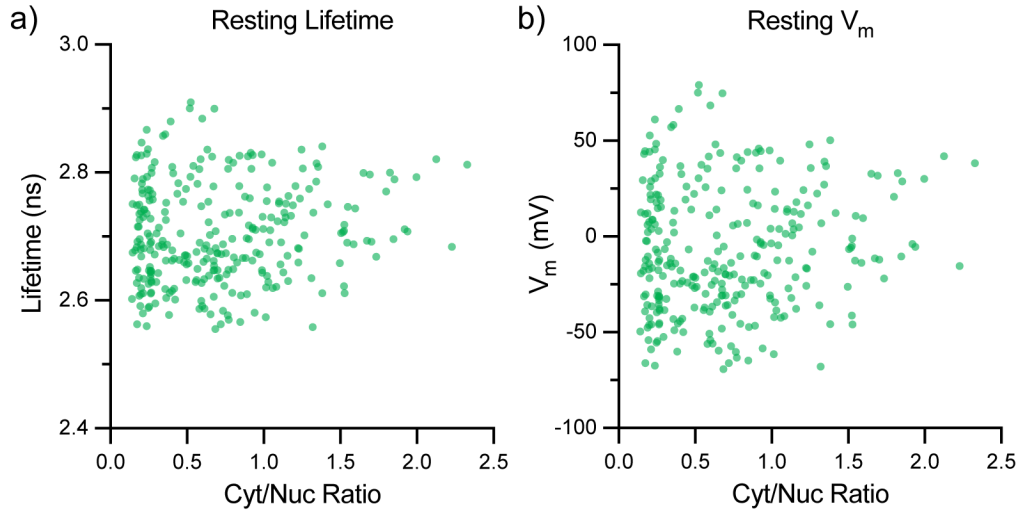


Figure 3.11. Relationship between resting lifetime or V_m and Cyt/Nuc ratio in MCF-7-DHB-mVenus cells. Plots of **a)** globally calculated CRhOMe resting lifetime or **b)** resting V_m vs Cyt/Nuc ratio for monoclonal MCF-7-DHB-mVenus cells. Cells were co-loaded with 300 nM CRhOMe and 10 µM Hoechst 33342. Each point represents a single cell (n = 287). $R^2 = 0.01329$ (simple linear regression).

The measured Cyt/Nuc ratios ranged from 0.14 to 2.3. Based on the Cyt/Nuc ratio data presented in Spencer et al., cells in G_1 are likely to have a Cyt/Nuc ratio less than 1, while cells in G_2 or M have a higher ratio greater than 1, and cells in S phase generally have a Cyt/Nuc ratio close to 1 (**Table 3.1**). The approximate percentages of cells in each phase are given in **Table 3.6** and are consistent with the expected cell cycle distribution for MCF-7 cells.[16,18,29] The resting lifetimes observed ranged from 2.56 to 2.91 ns, corresponding to -69 to +79 mV, which is comparable to the spread of voltages measured in MCF-7 cells with VF2.1.Cl.[15] The average V_m within each cell cycle phase is also reported in **Table 3.6**. There is not a significant difference between the mean resting potentials in G_1 and S or between S and G_2/M, however, there is a difference between G_1 and G_2/M ($p = 0.03$, n.s. $p > 0.05$, Brown-Forsythe and Welch ANOVA with Dunnett's T3 multiple comparisons test). Based on the graph in **Figure 3.11b**, we observed that most of the cells with a high Cyt/Nuc ratio above 1.8 also had a more depolarized membrane potential, which may be indicative of a depolarizing transition between G_2 and M phase. However, there are still many cells at similarly depolarized potentials with lower Cyt/Nuc ratios, and cells in G_1 and S phase span a wide range of membrane potentials. There does not appear to be not a clear correlation between

resting lifetime or V_m and Cyt/Nuc ratio determined at a single timepoint ($R^2 = 0.01329$, simple linear regression).

Cyt/Nuc Ratio	Cell Cycle Phase	Percentage of Cells	V_m (mV)
< 0.8	G_1	64%	-10 ± 3
0.8 to 1.2	S	21%	-7 ± 4
> 1.2	G_2, M	15%	3 ± 4

Table 3.6. Distribution of cell cycle phase in MCF-7-DHB-mVenus cells according to Cyt/Nuc ratio. Approximate cell cycle phase of MCF-7-DHB-mVenus cells based on calculated Cyt/Nuc ratio at a single time point. The Cyt/Nuc ratio data is shown graphically in **Figure 3.10**. V_m is given as mean ± SEM. Sample sizes (number of cells): G_1 182 S 60, G_2/M 44.

Since the DHB-mVenus plasmid was originally designed to track cell cycle progression over time, and CRhOMe is most accurate when measuring lifetime changes within an individual cell, we wanted to try recording lifetime and the Cyt/Nuc ratio over a longer timescale. We acquired a set of confocal Hoechst 33342 and DHB-mVenus images followed by a 75 second long FLIM acquisition every 30 minutes for 90 minutes across four different fields of view on a coverslip. Images and corresponding lifetime and Cyt/Nuc plots for one of these fields of view is shown in **Figure 3.12**, and the others are shown in **Figures S3.1-S3.3**.

Most of the cells analyzed did not show significant changes in the Cyt/Nuc ratio. Of the cells that did exhibit a changing Cyt/Nuc ratio, the ratio tended to fluctuate rather than consistently increase or decrease, making it difficult to conclusively determine cell cycle phase. Over the course of imaging, one cell divided in between the 30 and 60 minute time points (**Figure 3.12a**, Cells 9 and 10). Though the Cyt/Nuc ratio of the mitotic cell (Cell 9) was decreasing over the first three timepoints, as would be expected for a cell in mitosis, the ratio increased slightly by the final timepoint. Although we do observe some changes in the Cyt/Nuc ratio over time, 90 minutes may not be long enough to reliably identify a trend in the Cyt/Nuc ratio that indicates cell cycle phase.

Most cells generally showed a decrease in lifetime of approximately 100 to 200 ps, corresponding to changes on the order of tens of millivolts. Voltage changes on this scale do not make sense physiologically, so the shortening of lifetime observed must be attributed to something other than large changes in V_m. We have previously demonstrated that CRhOMe is highly photostable and minimally phototoxic by making consistent and continuous measurements of lifetime over 15 minutes,[21] so the lifetime changes are not likely to be caused by extended light exposure. However, changes in dye orientation or degradation of the dye within the membrane could contribute to unwanted changes in lifetime over time. Additionally, aggregation of CRhOMe could lead to self-quenching between fluorophores and result in a shortened fluorescence lifetime. Further experiments are necessary to examine the stability of CRhOMe over longer imaging timescales. The calibrations for non-expressing MCF-7 and MCF-7-DHB-mVenus cells were also calculated from small numbers of cells, so additional patching experiments are necessary to robustly characterize the lifetime-voltage response and improve the reliability of voltage calculations.

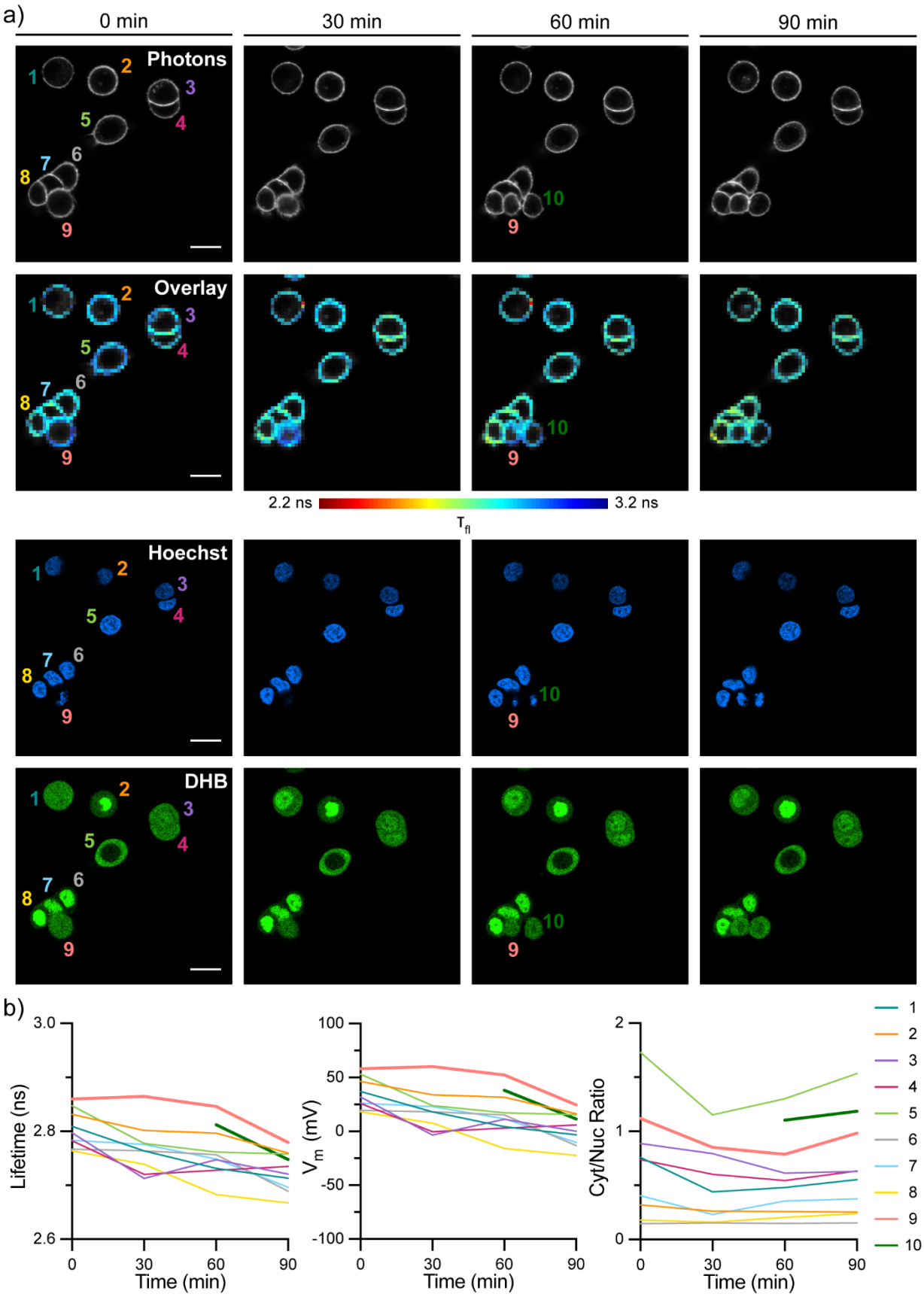

a)
0 min
30 min
60 min
90 min
Photons
Overlay
2.2 ns
3.2 ns
T_{fl}
Hoechst
DHB
b)
Lifetime (ns)
V_m (mV)
Cyt/Nuc Ratio
Time (min)
1
2
3
4
5
6
7
8
9
10

Figure 3.10. Lifetime and Cyt/Nuc ratio in MCF-7-DHB-mVenus cells over 90 minutes.
a) Raw photon intensity, pixelwise fluorescence lifetime-intensity overlay, Hoechst 33342, and DHB-mVenus images of MCF-7-DHB-mVenus cells tracked over 90 minutes. At each time point, confocal Hoechst and DHB-mVenus images were acquired, followed by a 75 second FLIM acquisition. Individual cells are numbered 1 to 10. Scale bars are 20 μm. Images and lifetime and Cyt/Nuc traces for additional fields of view are shown in **Figures S3.1-S3.3**. **b)** Traces of global CRhOMe lifetime and Cyt/Nuc ratio over time for single MCF-7-DHB-mVenus cells shown in **a)**. The bolded lines highlight division of Cell 9 (coral) and formation of the daughter cell (Cell 10, dark green).

Conclusion

This chapter highlights the development and preliminary characterization of the MCF-7-DHB-mVenus stable cell line for simultaneous recording of resting membrane potential and cell cycle progression. MCF-7-DHB-mVenus cells display the expected changes in Cyt/Nuc intensity over time arising from cell cycle dependent localization of DHB-mVenus. However, our initial attempts to relate the Cyt/Nuc ratio and thus cell cycle progression to membrane potential were inconclusive. When evaluated at a single point in time, there was not a clear correlation between resting lifetime and Cyt/Nuc ratio. Furthermore, when Cyt/Nuc ratio and resting lifetime were recorded over time, the measured fluctuations in lifetime would correspond to large and physiologically impossible changes in V_m using our current lifetime-voltage calibration. Additional electrophysiological recordings are needed to improve the accuracy of the calibration, as well as further experiments to evaluate the stability of CRhOMe over time and whether factors like degradation, aggregation, or changes in dye orientation could account for variations in lifetime.

The average resting lifetimes observed in non-expressing and monoclonal MCF-7 cells were similar, but resting lifetime in polyclonal MCF-7-DHB-mVenus cells was notably elevated, suggesting that the polyclonal cells are more depolarized. Single cell RNA sequencing of the monoclonal and polyclonal cells could identify transcriptional differences arising from DHB-mVenus integration that account for the depolarization.

Additionally, the FLIM setup is equipped with an incubation box for temperature control and CO_2 regulation, which could be implemented to allow for longer imaging experiments while retaining cell viability. DHB-mVenus was originally characterized by tracking changes in the Cyt/Nuc ratio over 24 hours to view full cycles of cell growth and division, so recordings over longer time scales could be more informative about changes in the Cyt/Nuc ratio and enable more reliable determination of cell cycle phase. With further characterization, the MCF-7-DHB-mVenus cell line offers a new approach to study the interactions between cell cycle and membrane potential dynamics.

Methods

MCF-7 Cell Culture

MCF-7 cells were obtained from the UC Berkeley Cell Culture Facility. Cells were verified by STR profiling (short tandem repeat) and were tested routinely for mycoplasma. Cell lines were discarded after 25 passages. MCF-7 cells were maintained and plated in Dulbecco's Modified Eagle Medium (DMEM; Gibco) supplemented with 4.5 g/L glucose, 2 mM GlutaMAX (Gibco), 10% seradigm fetal bovine serum (FBS; Gibco), 1 mM sodium pyruvate (Gibco) and 1x non-essential amino acids (NEAA; Gibco) in a 37°C humidified incubator at 5% CO_2. Cells were passaged into fresh complete media every few days following dissociation with 0.25% trypsin-EDTA (Gibco). Residual trypsin was removed by centrifugation for 5 minutes at 300xg before resuspension in fresh complete medium.

For imaging experiments, 25 mm #1.5 glass coverslips were pre-coated with poly-D-lysine (PDL) prior to plating cells. Coverslips were incubated in PDL (0.1 mg/mL in PBS; Sigma-Aldrich) for at least 1 hour in a 37°C humidified incubator and then washed twice with sterile water and twice with 1x Dulbecco's Phosphate Buffered Saline (dPBS; Gibco). For resting lifetime FLIM experiments, MCF-7 cells were plated on 25 mm coverslips in 6-well tissue culture plates at a density of 42,000-63,000 cells/cm^2. For electrophysiology experiments, MCF-7 cells were plated at a density of 21,000-31,000 cells/cm^2. Cells were imaged 16-24 hours after plating.

pSBbi-DHB-mVenus-Neo Plasmid Construction

The original DHB-mVenus plasmid was obtained as an agar stab (a gift from Tobias Meyer and Sabrina Spencer; Addgene plasmid #136461), cultured overnight in LB with 100 μg/mL carbenicillin, and isolated via a spin miniprep kit (Qiagen). The pSBbi-Neo plasmid backbone (a gift from Eric Kowarz; Addgene plasmid #60525) and SB100X transposase (a gift from Zsuzsanna Izsvak; Addgene plasmid #34879) were both obtained as agar plates, courtesy of J. Wren Kim in the Ingolia Lab at UC Berkeley. These plasmids were cultured overnight in LB with 100 μg/mL carbenicillin (pSBbi-Neo) or 25 μg/mL chloramphenicol (SB100X) and isolated via a spin miniprep kit. The DHB-mVenus sequence was cloned into the pSBbi-Neo plasmid backbone via Gibson assembly. The final construct was confirmed by sequencing at the UC Berkeley DNA Sequencing Facility, and the DHB-mVenus sequence used is provided at the end of this Methods section. The pSBbi-DHB-mVenus-Neo plasmid was cultured overnight in LB with 100 μg/mL carbenicillin and isolated via a spin miniprep kit.

G418 Antibiotic Kill Curve

G418 (disulfate salt; Sigma-Aldrich) was made up as a 100 mg/mL stock solution in sterile water and aliquoted for storage at -20°C. Thawed aliquots were stored at 4°C for no longer than 1 week. To determine optimal concentrations of G418 for antibiotic selection, MCF-7 cells were plated in complete medium at a density of 63,000 cells/cm^2 in 6-well tissue culture plates and allowed to recover overnight at 37°C in a humidified incubator. The next morning, the media was exchanged for complete medium containing G418 at eight different concentrations (200, 400, 600, 800, 1000, 1200, 1600, or 2000 μg/mL). Two wells were treated at each concentration, and two additional wells were treated with vehicle (sterile water) instead of antibiotic. Cells were visually inspected for toxicity daily, and media was exchanged every 2 days for fresh complete medium containing the antibiotic or vehicle. After a total of 7 days in culture, cells were dissociated with 0.25% trypsin

and quenched with complete medium. Equal volumes of Trypan Blue (0.4% w/v; Gibco) and each cell suspension were mixed to stain dead cells. The numbers of live and dead cells in each well were assessed via hemocytometer to determine the percentage of surviving cells in each well. The two data points at each concentration were then averaged to produce the kill curve shown in **Figure 3.5a.**

DHB-mVenus Transient Transfection

For transient transfections of DHB-mVenus, MCF-7 cells were plated at 52,000-63,000 cells/cm^2 in complete medium on PDL-coated 25 mm coverslips in a 6-well tissue culture plate. Cells were allowed to recover overnight at 37°C in a humidified incubator before transfection. The next day, pSBbi-DHB-mVenus-Neo and SB100X were co-transfected at ratios of 5:1 or 10:1. Transfections were performed with Lipofectamine 3000 and P3000 reagent according to the manufacturer's protocol (Thermo Fisher) using a total of 2 μg of DNA per well. After 4-6 hours, cells were changed to fresh complete medium after one rinse with dPBS and returned to the incubator. Cells were imaged approximately 18-20 hours later (~24 hours post-transfection).

MCF-7-DHB-mVenus Stable Cell Line Generation

Four wells of MCF-7 cells were plated at 52,000 cells/cm^2 in complete medium in a 6-well tissue culture plate and allowed to recover overnight at 37°C in a humidified incubator. Two wells were co-transfected with pSBbi-DHB-mVenus-Neo and SB100X (5:1 ratio, 2 μg DNA/well) using Lipofectamine 3000 and P3000 reagent according to the manufacturer's protocol (Thermo Fisher). The other two wells were left non-transfected as a control. Cells were returned to the incubator and allowed to grow for 3 days. Media was not changed post-transfection. After 3 days, cells in each well were dissociated with 0.25% trypsin. Residual trypsin was removed by centrifugation for 5 minutes at 300xg before resuspension in fresh complete medium. Each well was passaged at a 1:2 ratio into 6-well tissue culture plates, resulting in 4 transfected and 4 non-transfected wells. G418 was added at a concentration of 400, 600, 800, or 1000 μg/mL to each well. The non-transfected wells were also treated with G418 to ensure efficacy of the antibiotic. Every 2-3 days for 2 weeks, media was exchanged for fresh complete media with G418 after one rinse with 1x dPBS.

After 2 weeks, all of the non-transfected control cells appeared to be dead and were bleached. All wells of transfected cells appeared healthy and were confluent enough to be passaged. Each well was passaged at a 1:2 ratio into two wells split between two different 6-well tissue culture plates. One plate had PDL-coated coverslips for imaging, while cells in the other were plated directly on plastic for maintenance. The cells plated on coverslips were imaged via epifluorescence the next day to confirm stable expression at each concentration. Since cells treated with all concentrations of G418 showed good DHB-mVenus expression, we continued to culture all wells in the other 6-well plate. Each well thus comprised a polyclonal cell line selected with a different concentration of G418. Cells were changed to complete media with G418 after 2 days, and then passaged 2 days later. Cells were dissociated with 0.25% trypsin and centrifuged for 5 minutes at 300xg to remove residual trypsin. Each well was resuspended in 5 mL complete media, and cell density was determined via hemocytometer. Each polyclonal cell line was plated into 48 wells of a 96-well plate at a density of 1 cell/well to isolate monoclonal populations. Cells were not plated with antibiotic. The remaining cell suspensions from each polyclonal line (~5 mL) were added to a 10 cm tissue culture dish with an additional 5 mL complete medium. G418 was also added to the

polyclonal cells at the previously used concentrations for continued maintenance. All cells were returned to the incubator and allowed to grow.

After 3 days, the 10 cm dishes of polyclonal cells were exchanged for fresh complete medium with G418. They continued to be media changed every 2-3 days until reaching suitable confluency for passaging. At this point, cells were passaged into T-75 tissue culture flasks and maintained until it was determined which polyclonal line would be cryopreserved (based on the final isolated monoclonal line). Ultimately, the polyclonal line selected with 400 μg/mL G418 was cryopreserved.

Three days after plating, the 96-well plates were examined under a benchtop microscope to identify wells containing monoclonal colonies. Cells were allowed to grow undisturbed for 1 week after plating, at which point wells containing monoclonal colonies were half-changed for fresh complete media. Monoclonal colonies were monitored daily, and media was half-changed after another week. After 3 more days in culture, 4 monoclonal colonies were growing well and ready to be scaled up. Cells were dissociated with 0.25% trypsin, centrifuged for 5 minutes at 300xg to remove residual trypsin, and resuspended in 500 μL complete media. All 500 μL of each cell suspension was plated into one well of a 24-well tissue culture plate. Cells were grown in the 24-well plate for 1 week, with one media change after 3 days. Each monoclonal line was passaged and resuspended in 2 mL complete media, all which was plated into one well in a 6-well plate. Cells were media changed every 2-3 days for 2 weeks until reaching suitable confluency for passaging. One cell line had largely died out after 2 weeks, but the other 3 lines were growing well and were dissociated with 0.25% trypsin, centrifuged for 5 minutes at 300xg to remove residual trypsin, and resuspended in 10 mL complete media. All 10 mL of each cell suspension was plated in a 10 cm dish. Cells were grown for 1 week, with one media change after 3 days. At this point, one of the monoclonal lines (isolated from a 400 μg/mL polyclonal line) was growing faster and appeared healthier than the other two monoclonal lines. This monoclonal line was passaged into complete medium in a 10 cm dish for continued maintenance, and cells were also plated on 25 mm coverslips in a 6-well plate at 42,000 cells/cm^2 to validate DHB-mVenus expression. Two days after plating, DHB-mVenus expression was confirmed via epifluorescence imaging, and this monoclonal line was selected as the final MCF-7-DHB-mVenus line. After growing for 3 more days in the 10 cm dish, the monoclonal cells were passaged into a T-75 tissue culture flask and maintained until reaching suitable confluency for cryopreservation.

The final monoclonal line, as well as the polyclonal line from which it was isolated (400 μg/mL G418), were tested for mycoplasma and subsequently deposited at the UC Berkeley Cell Culture Facility for cryopreservation.

MCF-7-DHB-mVenus Cell Culture

MCF-7-DHB-mVenus cells were maintained and plated in DMEM supplemented with 4.5 g/L glucose, 2 mM GlutaMAX, 10% seradigm FBS, 1 mM sodium pyruvate, 1x NEAA, and 400 μg/mL G418 in a 37°C humidified incubator at 5% CO_2. Cells were discarded after 15 passages and a new thaw was picked up from the Cell Culture Facility. Cells were passaged into fresh complete media every few days following dissociation with 0.25% trypsin-EDTA. Residual trypsin was removed by centrifugation for 5 minutes at 300xg before resuspension in fresh complete medium.

For imaging experiments, 25 mm #1.5 glass coverslips were pre-coated with PDL (0.1 mg/mL in PBS) prior to plating cells. Coverslips were incubated in PDL for at least 1 hour in a 37°C humidified incubator and then washed twice with sterile water and twice with 1x dPBS. MCF-7-DHB-mVenus cells were plated for imaging in complete media without G418. For resting lifetime or time series FLIM experiments, MCF-7-DHB-mVenus cells were plated on 25 mm coverslips in 6-well tissue culture plates at a density of 42,000-63,000 cells/cm^2. For electrophysiology experiments, MCF-7-DHB-mVenus cells were plated at a density of 21,000-31,000 cells/cm^2. Cells were imaged 16-24 hours after plating.

Epifluorescence Imaging Parameters

Epifluorescence imaging of DHB-mVenus expression in MCF-7 cells was performed on an AxioObserver Z-1 (Zeiss), equipped with a Spectra-X Light engine LED light (Lumencor), controlled with μManager (V1.4, opensource, Open Imaging). Cells were incubated with 10 μM Hoechst 33342 (Invitrogen) in HBSS for 20-25 minutes at 37°C, washed once with HBSS, and transferred to fresh HBSS in an Attofluor cell imaging chamber (Invitrogen). Epifluorescence experiments were conducted at room temperature under ambient atmosphere. Cells were used immediately after loading. Images were acquired using an EC-Plan-Neofluar 40x/1.3 oil immersion objective (40x; Zeiss). Images were focused onto an OrcaFlash4.0 sCMOS camera (sCMOS; Hamamatsu). Hoechst 33342 was excited by LED light at 390/22 nm (0.6 W/cm^2, 5 ms exposure time). Emission was collected with a quadruple emission filter (432/36, 515/30, 595/30, 730/140 nm; Semrock) after passing through a quadruple dichroic mirror (432/38, 515/30, 595/30, 652 nm LP; Semrock). Excitation light for DHB-mVenus was delivered by LED at 475/34 nm (3.1 W/cm^2, 5 ms exposure) and emission was collected with an emission filter (540/50 nm) after passing through a dichroic mirror (510 nm LP).

VoltageFluor Loading

For FLIM experiments, CRhOMe was loaded at 300 nM by itself or co-loaded with 10 μM Hoechst 33342. Loading solutions were prepared in imaging buffer (IB, made in-house; composition in mM: 139.5 NaCl, 10 HEPES, 5.6 D-glucose, 5.33 KCl, 1.26 $CaCl_2$, 0.49 $MgCl_2$, 0.44 KH_2PO_4, 0.41 $MgSO_4$, 0.34 NaH_2PO_4; 285 mOsm/L; pH 7.25) directly from a 1 mM DMSO stock (CRhOMe) or 10 mM stock in water (Hoechst). Osmolarity was determined with a μOsmette (Precision Instruments). Cells were incubated at 37°C for 25 minutes in loading solution, washed once with IB, and transferred to fresh IB in an Attofluor cell imaging chamber (Invitrogen).

Electrophysiology

Pipettes were pulled from borosilicate glass with filament (Sutter Instruments) with resistances ranging from 4 to 8 MΩ with a P97 pipette puller (Sutter Instruments). Internal solution composition, in mM (pH 7.25, 285 mOsmol/L): 125 potassium gluconate, 10 KCl, 5 NaCl, 1 EGTA, 10 HEPES, 2 ATP sodium salt, 0.3 GTP sodium salt. EGTA (tetraacid form) was prepared as a stock solution in 1 M KOH before addition to the internal solution. Pipettes were positioned with an MP-225 micromanipulator (Sutter Instruments). For voltage clamp protocols during fluorescence lifetime experiments, a liquid junction potential of -14 mV was determined by the Liquid Junction Potential Calculator in the pClamp software package (Molecular Devices), and voltage step protocols used in conjunction with fluorescence lifetime measurements were corrected for this offset. Electrophysiology recordings were made with an Axopatch 200B amplifier and digitized with a Digidata 1440A (Molecular Devices). For voltage sensitivity measurements on the

fluorescence lifetime system, cells were held at -60 mV and potentials from +80 to -80 mV were applied. Voltage steps were applied with a variable order of -80, -40, 0, and +40 mV steps, followed by a +80 mV step as the final voltage applied, with each voltage step holding for 15 seconds. Signals were sampled at 50 kHz and filtered with a 5 kHz low-pass Bessel filter. Correction for pipette capacitance was performed in the cell attached configuration. Recordings were only included if they maintained a 30:1 ratio of membrane resistance (R_m) to access resistance (R_a) and an R_a value below 30 MΩ throughout the recording.

Confocal Imaging Parameters

Confocal imaging of DHB-mVenus expression was performed on an inverted LSM 980 confocal microscope (Zeiss) controlled with Zen Blue software (Zeiss). Samples were imaged with a 40x oil/1.3 NA Apochromat objective (Zeiss), immersed in Immersol 518F (Zeiss). The microscope incubation chamber was set to 25°C. Photons were detected with a GaAsP detector using custom emission wavelength cutoffs set in Zen Blue. The confocal pinhole was set to 1 airy unit for all channels. Hoechst 33342 was excited with a 405 nm laser (laser intensity 0.5%, master gain 650 V, pinhole 38 μm) and detected from 420-480 nm. DHB-mVenus was excited with a 488 nm laser (laser intensity 0.8%, master gain 600 V, pinhole 33 μm) and detected from 500-600 nm. CRhOMe was excited with a 639 nm laser (laser intensity 0.3%, master gain 650 V, pinhole 41 μm) and detected from 650-700 nm. Images were acquired with 256x256 pixels of spatial resolution at a pixel width of 0.55 μm. The pixel dwell time was 1.54 μs with a total frame time of 235.93 ms per channel. Channels were scanned sequentially from 405 nm to 639 nm. Confocal images were acquired immediately before corresponding FLIM acquisitions.

Fluorescence Lifetime Data Acquisition

Fluorescence lifetime imaging was performed on an inverted LSM 980 confocal microscope (Zeiss) equipped with a SPC-150NX single photon counting card (Becker and Hickl). The LSM 980 was controlled with Zen Blue software (Zeiss), and the TCSPC unit was controlled with SPCM software (Becker-Hickl). Pulsed excitation at 50 MHz was supplied with a 640 nm diode laser (BDS-SM-640-FBC-101, Becker-Hickl) and controlled through an LHB-104 Laser Hub (Becker-Hickl). Power was adjusted with a neutral density filter wheel to set desired photon count rates. Average power at the sample ranged from 1-3 μW. Excitation light was coupled to the microscope with a polarization-maintaining fiber and passed through a 405/485/560/640 beam splitter (Zeiss). Emitted photons were collected with a 40x oil/1.3 NA Apochromat objective (Zeiss), immersed in Immersol 518F (Zeiss). The confocal pinhole was set to 35 μm (1 airy unit). The emitted photons were passed through a 676/37 bandpass filter (Semrock) and detected with an HPM-100-40 hybrid detector (Becker-Hickl), based on a Hamamatsu R10467 GaAsP hybrid photomultiplier tube. Detector dark counts were kept below 300 per second during acquisition and were generally lower than 200 per second. The detector parameters used were the following: constant fraction discriminator (CFD) -50.98 mV, zero cross 5.29 mV. Sync parameters used were the following: CFD -50.98 mV, zero cross 5.29 mV, offset 5.10 %, sync divider 1, dither range 1/16. Resting lifetime and time series data were acquired with 256 time channels in the analog-to-digital-converter (ADC) and 256x256 pixels of spatial resolution during 75 second exposures. Electrophysiology data were acquired with 256 TCSPC time channels and 128x128 pixels of spatial resolution during five 15 second exposures. The instrument response function (IRF) was measured each day from a solution of 1 mg/mL erythrosin B in water. The TMCRh dye head (1 μM in water) was also routinely recorded as a standard to verify correct instrument function and

fitting parameters. The microscope incubation chamber was set to 25°C to minimize temperature fluctuations during experiments and between days. Cells were used immediately after loading CRhOMe and were generally kept on the microscope for under 30 minutes. No cells were kept for on the microscope for longer than an hour.

Fluorescence Lifetime Data Analysis

CRhOMe lifetime data were modeled as a monoexponential decay (**Equation 1**) in custom MATLAB code via a weighted least-squares approach. In this equation, A represents the amplitude of the photon count signal and τ represents the fluorescence lifetime.

$$F(t) = Ae^{-t/\tau} \tag{1}$$

Minimization of the reduced chi squared (χ^2, **Equation 2**) was used to determine the final parameter values, where n is the number of free parameters (number of fit time channels – number of free parameters in model), st is the first fit time channel, fi is the final fit time channel, z is the value of the fit model, and x is the value of the experimentally measured decay. Poisson weighting of the time channels was used.

$$\chi^2 = \frac{1}{n}\sum_{i=st}^{fi}\frac{(z_i - x_i)^2}{|z|} \tag{2}$$

The built-in minimization function fmincon with the interior-point algorithm was used, with the following settings: StepTolerance 1e-4, OptimalityTolerance 1e-4, ConstraintTolerance 1e-6. All fits converged in fewer than the maximum number of function evaluations (1e5). The fluorescence lifetime τ was constrained between 0 and 10 ns. The experimentally measured instrument response function (IRF, erythrosin B fluorescence decay) was cropped to time channels 36-50 or 36-52 out of 256 ADC channels and reconvolved with the decay model before the reduced chi squared was determined. Time channels 20 through 256 of the measured time resolved decays were used in fitting. The shift between the IRF and the measured time resolved decays was fixed to -0.3 (in units of ADC time channels). The offset (time-independent background) was fixed to 0, as the dark counts were generally negligible (below 200 counts per second during experiments). A threshold of 5000 total photons was used in pixelwise analysis. Pixels with photon counts below this threshold were excluded from analysis and appear black in lifetime images. Standard spatial binning was performed before fitting for pixel-by-pixel analysis. For resting lifetime images, the raw pixel width was 0.55 μm. Pixels were generally binned 4x4 or 5x5, resulting in binned pixel widths of 2.2 μm or 2.8 μm, respectively. Electrophysiology images were acquired with a raw pixel width of 0.41 μm and binned 4x4, giving a binned pixel width of 1.6 μm. Raw photon intensity images are displayed at the native resolution, while binned photon, lifetime, and lifetime-intensity overlay images reflect spatial binning.

Regions of interest (ROIs) for pixelwise fitting were automatically determined from raw photon intensity images by sharpening and then thresholding the signal intensity with custom MATLAB code. Regions of images that were partially out of the optical section or contained punctate debris were omitted. In general, ROIs were single cells or small groups of 2-10 cells. For

pixelwise analysis, each binned pixel was fit to a decay and the resulting lifetimes across all pixels in each ROI were averaged to give one mean lifetime per ROI. For global lifetime analysis, ROI identification was completed manually in the FIJI installation of ImageJ (NIH) using the unbinned photon intensity images. ROIs were traced by hand around each individual cell membrane. Regions of membrane shared between adjacent cells were generally included in both ROIs. For lifetime fitting, all photons within each ROI were combined to fit one decay per ROI.

Lifetime-Voltage Calibration

The relationship between the lifetime (τ_{fl}) and membrane potential for each patch-clamped cell was determined by linear regression, yielding a sensitivity (*m,* ps/mV) and a 0 mV lifetime (*b*, ps), which were subsequently averaged to give an overall linear calibration (**Equation 3**).

$$\tau_{fl} = m * V_m + b \tag{3}$$

Differences in the measured lifetime at a defined reference point (for us, the 0 mV lifetime) across measured cells provides an estimate of the voltage-independent noise for the lifetime-voltage calibration of CRhOMe, and thus the resolution we can expect when using this calibration. We report this resolution as the root-mean-square deviation (RMSD) between the optically determined voltage using the developed calibration (V_{FLIM}) and the voltage of the cell as set by voltage clamp (V_{ephys}). The RMSD of a set of n measurements (**Equation 4**) can be determined from the variance (**Equation 5**) and the bias (**Equation 6**) of the estimator (V_{FLIM}) as compared to the assumed "true" value, in this case determined by electrophysiology (V_{ephys}).

$$RMSD = \sqrt{\sigma^2 + Bias^2} \tag{4}$$

$$\sigma^2 = \frac{1}{n}\sum_{i=1}^{n}\left(V_{FLIM,i} - V_{ephys,i}\right)^2 \tag{5}$$

$$Bias = \frac{1}{n}\sum_{i=1}^{n} V_{FLIM,i} - \frac{1}{n}\sum_{i=1}^{n} V_{ephys,i} \tag{6}$$

The voltage-independent variations in lifetime are larger between cells than within a cell, and thus the voltage resolution in cells can be estimated with two values: the intra-cell resolution and the inter-cell resolution. The intra-cell resolution is a measure of the resolution expected for tracking and quantifying changes within an individual cell, determined by the RMSD between an individual cell's "optical guess" at the lifetime for a particular voltage step, from its individual line of best fit, and the actual measured lifetime at that point. The inter-cell resolution is the single-trial resolution of estimating an individual cell's membrane potential from its lifetime, determined from the RMSD between the 0 mV τ_{fl} value from each individual cell's determined lifetime-voltage relation and the 0 mV τ_{fl} determined by the average calibration. The inter-cell RMSD quantifies how well the lifetime-V_m relationship for a given cell line is likely to represent an individual cell's lifetime-V_m relationship. This method of calculating error assumes that the electrophysiology measurement is perfectly accurate and precise. Realistically, it is likely that some of the variation

seen is due to the quality of the voltage clamp. As a result, these RMSD values provide a conservative upper bound for the voltage errors in VF-FLIM.

Conversion of Lifetime to Voltage

The lifetime-V_m calibration was used to convert resting lifetime values to voltage (**Equation 7**). Where standard error of the mean of a voltage determination (δV_m) is given, error was propagated to include the standard errors of the slope (δm) and y-intercept (δb) of the voltage calibration, as well as the standard error of the lifetime measurements ($\delta\tau_{fl}$) in the condition of interest (**Equation 8**).

$$V_m = \frac{(\tau_{fl} - b)}{m} \tag{7}$$

$$\delta V_m = |V_m| \sqrt{\left(\frac{\sqrt{\delta\tau_{fl}{}^2 + \delta b^2}}{\tau_{fl} - b} \right)^2 + \left(\frac{\delta m}{m} \right)^2} \tag{8}$$

Cyt/Nuc Ratio Analysis

Analysis of the Cyt/Nuc ratio for epifluorescence and confocal images was automated by building a custom pipeline in CellProfiler 4.2.6 (Broad Institute). Hoechst and DHB images were imported into CellProfiler as 8-bit TIF files. The IdentifyPrimaryObjects module was first used to automatically identify nuclear ROIs using the Hoechst image. The typical diameter of objects was set at 10 to 40 pixels, and objects outside of the diameter range were automatically discarded. Nuclei were identified using adaptive two-class Otsu thresholding. Gaussian smoothing ($\sigma = 1$) was applied to the input image before thresholding. Adaptive thresholding calculates a different threshold for each pixel based on adjacent pixels in a surrounding window, rather than setting one threshold for the entire image. The size of this window was set to 20 pixels. A threshold correction factor of 0.75 was applied to make the threshold slightly less stringent. Clumped objects were distinguished and separated by shape using a smoothing filter of 10 pixels. After automatic ROI identification, the EditObjectsManually module was used to manually edit ROIs and separate any nuclei still clumped together.

The cytosolic ROIs were defined via the IdentifySecondaryObjects module, starting by applying the defined nuclear ROIs to each corresponding DHB-mVenus image. The nuclear ROIs were then expanded by 3 pixels (4.5 μm, epifluorescence images) or 6 pixels (3.3 μm, confocal images) using the "Distance – B" method. This method expands ROIs while using thresholding to exclude regions of background. After Gaussian smoothing ($\sigma = 1$) of the DHB-mVenus image, adaptive minimum cross-entropy thresholding with an adaptive window of 10 pixels was used to expand the nuclear ROIs. The IdentifyTertiaryObjects module was then used to subtract the nuclear ROI region from the expanded ROI, producing the final cytosolic ring ROI.

MeasureObjectIntensity was applied to measure mean DHB-mVenus fluorescence intensity across the nuclear and cytosolic ring ROIs, followed by CalculateMath to determine the Cyt/Nuc ratio. The measured intensities and Cyt/Nuc ratios were saved via ExportToSpreadsheet.

OverlayOutlines, DisplayDataOnImage, and SaveImages were used to display the numbered nuclear and cytosolic ring ROIs on the DHB-mVenus image.

Statistical Analysis

Hypothesis testing was performed as indicated with either analysis of variance (ANOVA) followed by appropriate post hoc testing or two-sided, unpaired, unequal variances t-tests. All statistical analysis was performed in Prism 10 (GraphPad).

DHB-mVenus

The following DHB-mVenus sequence (5' to 3') was cloned into the pSBbi-Neo backbone:

TTACTTGTACAGCTCGTCCATGCCGAGAGTGATCCCGGCGGCGGTCACGAACTCCAG
CAGGACCATGTGATCGCGCTTCTCGTTGGGGTCTTTGCTCAGCTTGGACTGGTAGCTC
AGGTAGTGGTTGTCGGGCAGCAGCACGGGGCCGTCGCCGATGGGGGTGTTCTGCTGG
TAGTGGTCGGCGAGCTGCACGCCGCCGTCCTCGATGTTGTGGCGGATCTTGAAGTTG
GCCTTGATGCCGTTCTTCTGCTTGTCGGCGGTGATATAGACGTTGTGGCTGTTGTAGTT
GTACTCCAGCTTGTGCCCCAGGATGTTGCCGTCCTCCTTGAAGTCGATGCCCTTCAGC
TCGATGCGGTTCACCAGGGTGTCGCCCTCGAACTTCACCTCGGCGCGGGTCTTGTAG
TTGCCGTCGTCCTTGAAGAAGATGGTGCGCTCCTGGACGTAGCCTTCGGGCATGGCG
GACTTGAAGAAGTCGTGCTGCTTCATGTGGTCGGGGTAGCGGGCGAAGCACTGCAG
GCCGTAGCCCAGGGTGGTCACGAGGGTGGGCCAGGGCACGGGCAGCTTGCCGGTGG
TGCAGATCAGCTTCAGGGTCAGCTTGCCGTAGGTGGCATCGCCCTCGCCCTCGCCGG
ACACGCTGAACTTGTGGCCGTTTACGTCGCCGTCCAGCTCGACCAGGATGGGCACCA
CCCCGGTGAACAGCTCCTCGCCCTTGCTCACGCCGCTGCCCTGGGCCCCGGATCCAG
TTTCTTGATTATCGGTGGGCTTGAAAAGTTGCCTGGGAATTAAATTATTCAGTCTCAAA
TTCTGAAGTCTGGAAGACACTTGTGGAGATTCTCCCACCATAAAAATTTTGCTTGGAC
TTTCATCATCATTCACACCACAGGTTCTTTTGGATGCTCGCGATTTTGGTAAATCATCA
TCTGTATCTACTCCATCAGGTGAAGATAATTGCCATCTTTCAGCAAAGGTGAGTGTCCT
CTCATCAGGCGAAGAGGCCTCGCTCCAGGTGACATCATTTGTCATGGTGAATTCTCGC
GACCGGT

Benchling link to full pSBbi-DHB-mVenus-Neo plasmid: https://benchling.com/s/seq-CJDi0qC5fFZDinqnp8Ax?m=slm-7ploFMVUWaFfaIz268Na

Supporting Figures and Tables

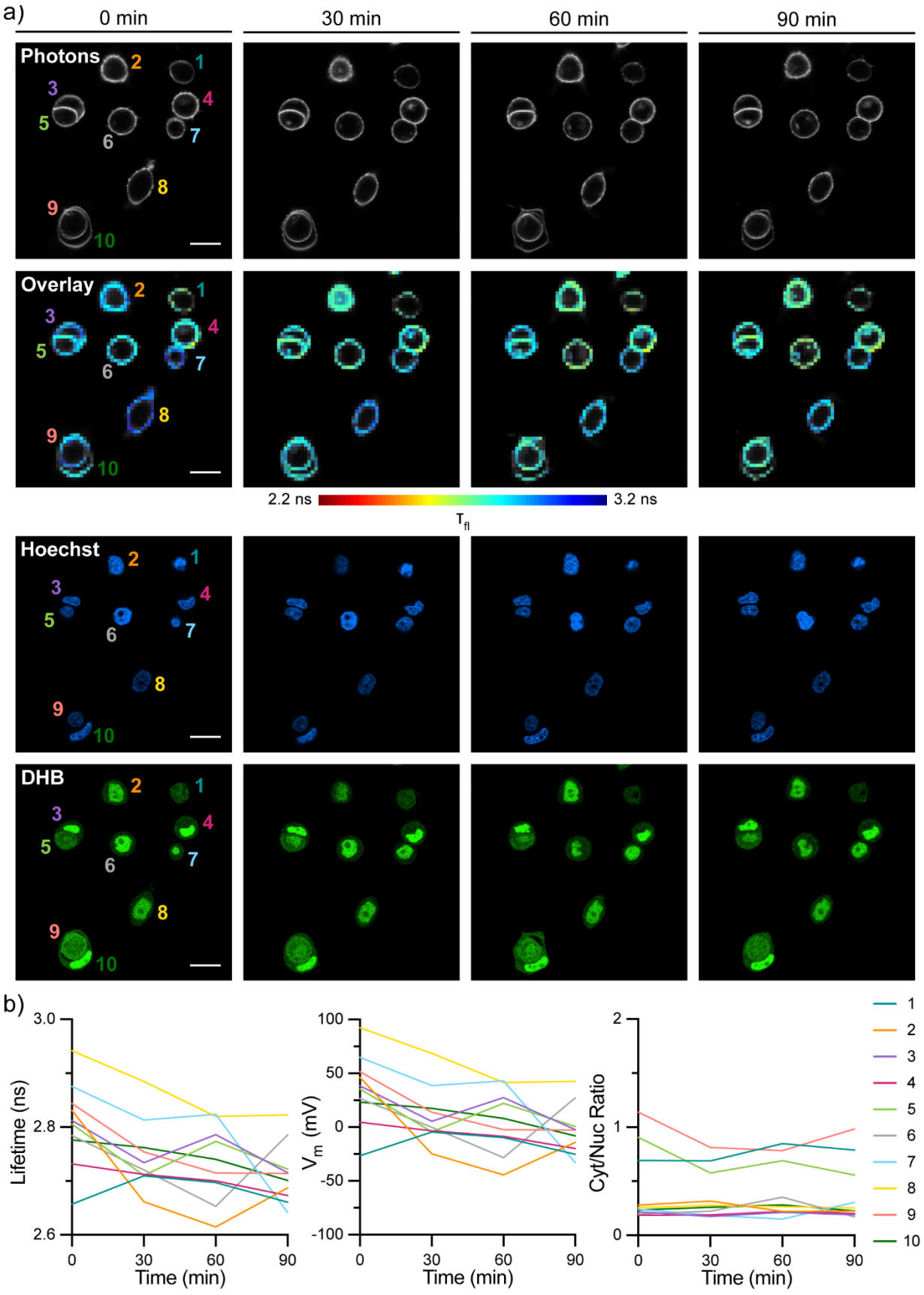

a)
0 min
30 min
60 min
90 min
Photons
Overlay
2.2 ns
3.2 ns
T_{fl}
Hoechst
DHB
b)
Lifetime (ns)
3.0
2.8
2.6
V_m (mV)
100
50
0
-50
-100
Cyt/Nuc Ratio
2
1
0
0
30
60
90
Time (min)
1
2
3
4
5
6
7
8
9
10

Figure S3.1. Lifetime and Cyt/Nuc ratio in MCF-7-DHB-mVenus cells over 90 minutes.
a) Raw photon intensity, pixelwise fluorescence lifetime-intensity overlay, Hoechst 33342, and DHB-mVenus images of MCF-7-DHB-mVenus cells tracked over 90 minutes. At each time point, confocal Hoechst and DHB-mVenus images were acquired, followed by a 75 second FLIM acquisition. Individual cells are numbered 1 to 10. Scale bars are 20 μm. **b)** Traces of global CRhOMe lifetime and Cyt/Nuc ratio over time for single MCF-7-DHB-mVenus cells shown in **a)**.

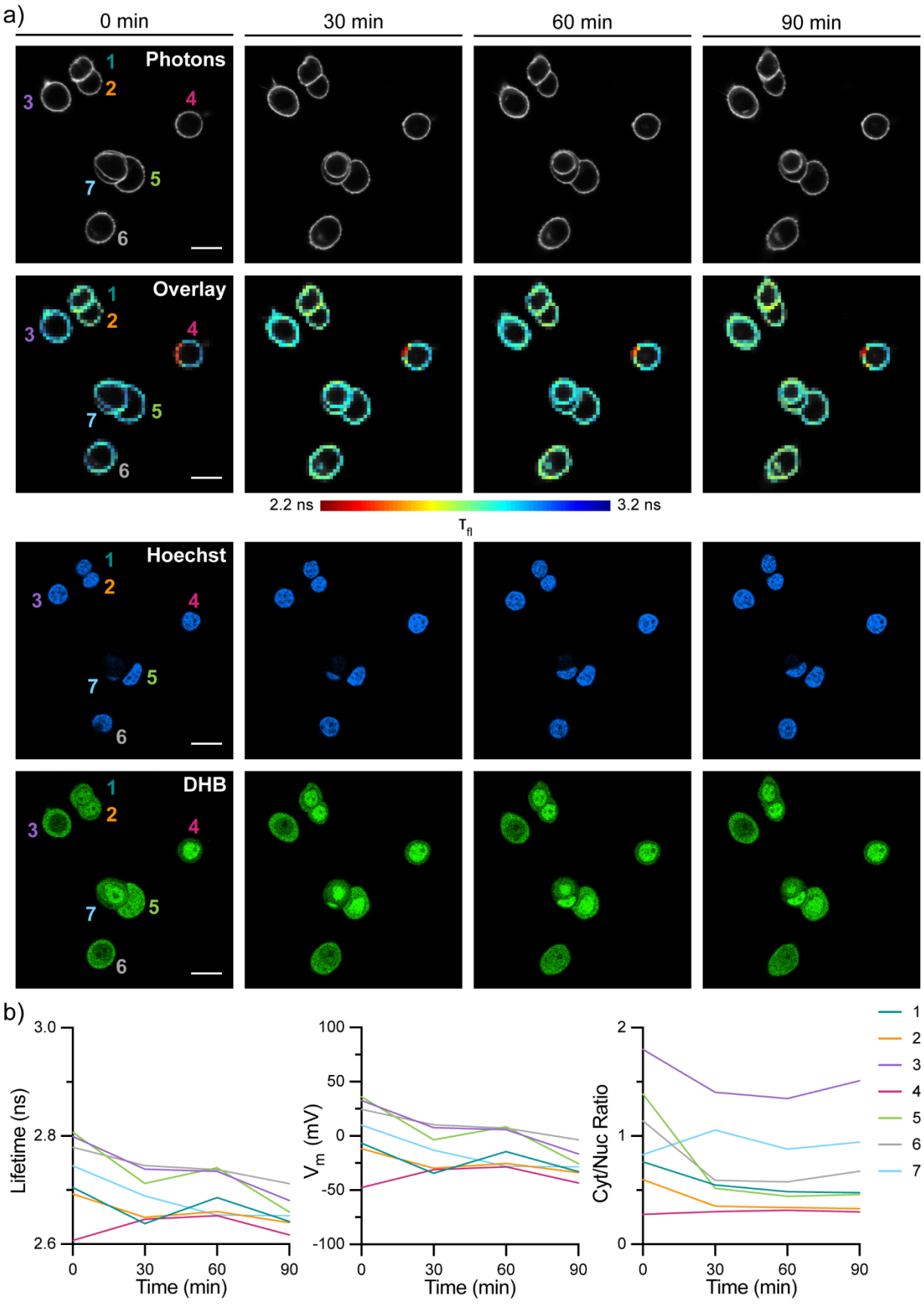

a)
0 min
30 min
60 min
90 min
Photons
Overlay
Hoechst
DHB
1
2
3
4
5
6
7
2.2 ns
3.2 ns
T_{fl}
b)
Lifetime (ns)
3.0
2.8
2.6
V_m (mV)
100
50
0
-50
-100
Cyt/Nuc Ratio
2
1
0
0
30
60
90
Time (min)

Figure S3.2. Lifetime and Cyt/Nuc ratio in MCF-7-DHB-mVenus cells over 90 minutes.
a) Raw photon intensity, pixelwise fluorescence lifetime-intensity overlay, Hoechst 33342, and DHB-mVenus images of MCF-7-DHB-mVenus cells tracked over 90 minutes. At each time point, confocal Hoechst and DHB-mVenus images were acquired, followed by a 75 second FLIM acquisition. Individual cells are numbered 1 to 10. Scale bars are 20 μm. **b)** Traces of global CRhOMe lifetime and Cyt/Nuc ratio over time for single MCF-7-DHB-mVenus cells shown in **a)**.

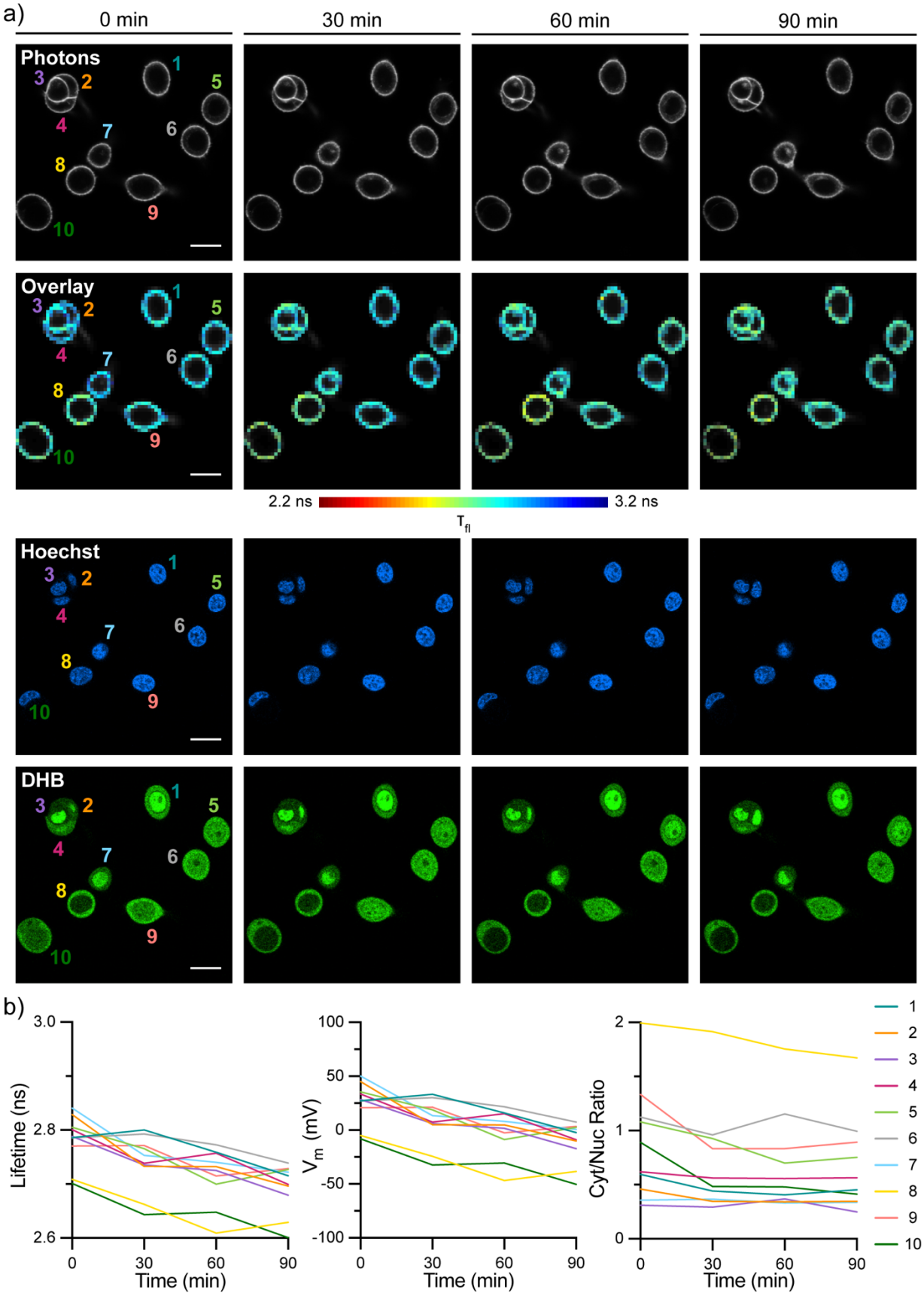

a)
0 min
30 min
60 min
90 min
Photons
Overlay
Hoechst
DHB
2.2 ns
3.2 ns
T_{fl}
b)
Lifetime (ns)
V_m (mV)
Cyt/Nuc Ratio
Time (min)
1
2
3
4
5
6
7
8
9
10

Figure S3.3. Lifetime and Cyt/Nuc ratio in MCF-7-DHB-mVenus cells over 90 minutes.
a) Raw photon intensity, pixelwise fluorescence lifetime-intensity overlay, Hoechst 33342, and DHB-mVenus images of MCF-7-DHB-mVenus cells tracked over 90 minutes. At each time point, confocal Hoechst and DHB-mVenus images were acquired, followed by a 75 second FLIM acquisition. Individual cells are numbered 1 to 10. Scale bars are 20 μm. **b)** Traces of global CRhOMe lifetime and Cyt/Nuc ratio over time for single MCF-7-DHB-mVenus cells shown in **a)**.

References

(1) Abdul Kadir, L.; Stacey, M.; Barrett-Jolley, R. Emerging Roles of the Membrane Potential: Action Beyond the Action Potential. *Front. Physiol.* **2018**, *9*. https://doi.org/10.3389/fphys.2018.01661.

(2) Tsuchiya, W.; Okada, Y. Membrane Potential Changes Associated with Differentiation of Enterocytes in the Rat Intestinal Villi in Culture. *Dev. Biol.* **1982**, *94* (2), 284–290. https://doi.org/10.1016/0012-1606(82)90348-7.

(3) Cone, C. D.; Cone, C. M. Induction of Mitosis in Mature Neurons in Central Nervous System by Sustained Depolarization. *Science* **1976**, *192* (4235), 155–158. https://doi.org/10.1126/science.56781.

(4) Huang, X.; Jan, L. Y. Targeting Potassium Channels in Cancer. *J. Cell Biol.* **2014**, *206* (2), 151–162. https://doi.org/10.1083/jcb.201404136.

(5) Chen, L.; Becker, T. M.; Koch, U.; Stauber, T. The LRRC8/VRAC Anion Channel Facilitates Myogenic Differentiation of Murine Myoblasts by Promoting Membrane Hyperpolarization. *J. Biol. Chem.* **2019**, *294* (39), 14279–14288. https://doi.org/10.1074/jbc.RA119.008840.

(6) Lim, S.; Kaldis, P. Cdks, Cyclins and CKIs: Roles beyond Cell Cycle Regulation. *Development* **2013**, *140* (15), 3079–3093. https://doi.org/10.1242/dev.091744.

(7) Vermeulen, K.; Van Bockstaele, D. R.; Berneman, Z. N. The Cell Cycle: A Review of Regulation, Deregulation and Therapeutic Targets in Cancer. *Cell Prolif.* **2003**, *36* (3), 131–149. https://doi.org/10.1046/j.1365-2184.2003.00266.x.

(8) Barnum, K. J.; O'Connell, M. J. Cell Cycle Regulation by Checkpoints. In *Cell Cycle Control: Mechanisms and Protocols*; Noguchi, E., Gadaleta, M. C., Eds.; Springer: New York, NY, 2014; pp 29–40. https://doi.org/10.1007/978-1-4939-0888-2_2.

(9) Johnson, D. G.; Walker, C. L. CYCLINS AND CELL CYCLE CHECKPOINTS. *Annu. Rev. Pharmacol. Toxicol.* **1999**, *39* (Volume 39, 1999), 295–312. https://doi.org/10.1146/annurev.pharmtox.39.1.295.

(10) Rao, V. R.; Perez-Neut, M.; Kaja, S.; Gentile, S. Voltage-Gated Ion Channels in Cancer Cell Proliferation. *Cancers* **2015**, *7* (2), 849–875. https://doi.org/10.3390/cancers7020813.

(11) Blackiston, D. J.; McLaughlin, K. A.; Levin, M. Bioelectric Controls of Cell Proliferation: Ion Channels, Membrane Voltage and the Cell Cycle. *Cell Cycle* **2009**, *8* (21), 3527–3536. https://doi.org/10.4161/cc.8.21.9888.

(12) Yang, M.; Brackenbury, W. J. Membrane Potential and Cancer Progression. *Front. Physiol.* **2013**, *4*. https://doi.org/10.3389/fphys.2013.00185.

(13) Berezin, M. Y.; Achilefu, S. Fluorescence Lifetime Measurements and Biological Imaging. *Chem. Rev.* **2010**, *110* (5), 2641–2684. https://doi.org/10.1021/cr900343z.

(14) Lazzari-Dean, J. R.; Gest, A. M. M.; Miller, E. W. Measuring Absolute Membrane Potential Across Space and Time. *Annu. Rev. Biophys.* **2021**, *50*, 447–468. https://doi.org/10.1146/annurev-biophys-062920-063555.

(15) Lazzari-Dean, J. R.; Gest, A. M.; Miller, E. W. Optical Estimation of Absolute Membrane Potential Using Fluorescence Lifetime Imaging. *eLife* **2019**, *8*, e44522. https://doi.org/10.7554/eLife.44522.

(16) Wonderlin, W. F.; Woodfork, K. A.; Strobl, J. S. Changes in membrane potential during the progression of MCF-7 human mammary tumor cells through the cell cycle. *J. Cell. Physiol.* **1995**, *165* (1), 177–185. https://doi.org/10.1002/jcp.1041650121.

(17) Strobl, J. S.; Wonderlin, W. F.; Flynn, D. C. Mitogenic Signal Transduction in Human Breast Cancer Cells. *Gen. Pharmacol. Vasc. Syst.* **1995**, *26* (8), 1643–1649. https://doi.org/10.1016/0306-3623(95)00062-3.
(18) Ouadid-Ahidouch, H.; Le Bourhis, X.; Roudbaraki, M.; Toillon, R. A.; Delcourt, P.; Prevarskaya, N. Changes in the K+ Current-Density of MCF-7 Cells during Progression through the Cell Cycle: Possible Involvement of a h-Ether.a-Gogo K+ Channel. *Receptors Channels* **2001**, *7* (5), 345–356.
(19) Klimatcheva, E.; Wonderlin, W. F. An ATP-Sensitive K+ Current That Regulates Progression Through Early G1 Phase of the Cell Cycle in MCF-7 Human Breast Cancer Cells. *J. Membr. Biol.* **1999**, *171* (1), 35–46. https://doi.org/10.1007/s002329900556.
(20) Wang, S.; Melkoumian, Z.; Woodfork, K. A.; Cather, C.; Davidson, A. G.; Wonderlin, W. F.; Strobl, J. S. Evidence for an Early G1 Ionic Event Necessary for Cell Cycle Progression and Survival in the MCF-7 Human Breast Carcinoma Cell Line. *J. Cell. Physiol.* **1998**, *176* (3), 456–464. https://doi.org/10.1002/(SICI)1097-4652(199809)176:3<456::AID-JCP2>3.0.CO;2-N.
(21) Gest, A. M. M.; Lazzari-Dean, J. R.; Ortiz, G.; Yaeger-Weiss, S. K.; Boggess, S. C.; Miller, E. W. A Red-Emitting Carborhodamine for Monitoring and Measuring Membrane Potential. *Proc. Natl. Acad. Sci.* **2024**, *121* (14), e2315264121. https://doi.org/10.1073/pnas.2315264121.
(22) Sakaue-Sawano, A.; Kurokawa, H.; Morimura, T.; Hanyu, A.; Hama, H.; Osawa, H.; Kashiwagi, S.; Fukami, K.; Miyata, T.; Miyoshi, H.; Imamura, T.; Ogawa, M.; Masai, H.; Miyawaki, A. Visualizing Spatiotemporal Dynamics of Multicellular Cell-Cycle Progression. *Cell* **2008**, *132* (3), 487–498. https://doi.org/10.1016/j.cell.2007.12.033.
(23) Spencer, S. L.; Cappell, S. D.; Tsai, F.-C.; Overton, K. W.; Wang, C. L.; Meyer, T. The Proliferation-Quiescence Decision Is Controlled by a Bifurcation in CDK2 Activity at Mitotic Exit. *Cell* **2013**, *155* (2), 369–383. https://doi.org/10.1016/j.cell.2013.08.062.
(24) Ivics, Z.; Hackett, P. B.; Plasterk, R. H.; Izsvák, Z. Molecular Reconstruction of Sleeping Beauty, a Tc1-like Transposon from Fish, and Its Transposition in Human Cells. *Cell* **1997**, *91* (4), 501–510. https://doi.org/10.1016/S0092-8674(00)80436-5.
(25) Mátés, L.; Chuah, M. K. L.; Belay, E.; Jerchow, B.; Manoj, N.; Acosta-Sanchez, A.; Grzela, D. P.; Schmitt, A.; Becker, K.; Matrai, J.; Ma, L.; Samara-Kuko, E.; Gysemans, C.; Pryputniewicz, D.; Miskey, C.; Fletcher, B.; VandenDriessche, T.; Ivics, Z.; Izsvák, Z. Molecular Evolution of a Novel Hyperactive Sleeping Beauty Transposase Enables Robust Stable Gene Transfer in Vertebrates. *Nat. Genet.* **2009**, *41* (6), 753–761. https://doi.org/10.1038/ng.343.
(26) Izsvák, Z.; Ivics, Z. Sleeping Beauty Transposition: Biology and Applications for Molecular Therapy. *Mol. Ther.* **2004**, *9* (2), 147–156. https://doi.org/10.1016/j.ymthe.2003.11.009.
(27) Kowarz, E.; Löscher, D.; Marschalek, R. Optimized Sleeping Beauty Transposons Rapidly Generate Stable Transgenic Cell Lines. *Biotechnol. J.* **2015**, *10* (4), 647–653. https://doi.org/10.1002/biot.201400821.
(28) Berzingi, S.; Newman, M.; Yu, H.-G. Altering Bioelectricity on Inhibition of Human Breast Cancer Cells. *Cancer Cell Int.* **2016**, *16* (1), 72. https://doi.org/10.1186/s12935-016-0348-8.
(29) Marino, A. A.; Iliev, I. G.; Schwalke, M. A.; Gonzalez, E.; Marler, K. C.; Flanagan, C. A. Association between Cell Membrane Potential and Breast Cancer. *Tumor Biol.* **1994**, *15* (2), 82–89. https://doi.org/10.1159/000217878.

Chapter 4
EGFR-Induced Changes in Membrane Potential Across Cell Lines

Abstract

Epidermal growth factor receptor (EGFR) signaling is essential to pathways involved in key processes like cell proliferation. Previous work with VF-FLIM revealed that A431 cells undergo a 15 mV hyperpolarization in response to EGF stimulation, suggesting a possible role for membrane potential in EGFR signal transduction. Here, we report membrane potential dynamics in A431 and MCF-7 cells following stimulation with varying concentrations of four EGFR ligands: EGF, transforming growth factor α (TGFα), epigen (EPG), and epiregulin (EPR). EGF and TGFα show a similar hyperpolarizing response in A431 cells, while the effect is lessened with EPG and EPR. In contrast, stimulation with all four ligands seems to produce a small depolarization in MCF-7 cells. These disparate responses to EGFR stimulation between ligands and cell types highlight the complexity of EGFR signaling and prompt further investigation of possible interactions with membrane potential.

Introduction

Receptor tyrosine kinases (RTKs) are a family of cell surface receptors that are implicated in a variety of cellular processes including proliferation, differentiation, metabolism, cell migration, and cell cycle control. In their monomeric form, RTKs are inactive. Ligand binding induces a conformational change and stabilizes dimerization between RTKs. In this active conformation, one RTK can phosphorylate tyrosine residues on an adjacent RTK, which creates binding sites for downstream signaling proteins.[1] Epidermal growth factor receptor (EGFR) is a specific RTK that is activated by seven different ligands of varying sizes and characteristics (**Table 1**). These ligands are divided into two different classes based on their binding affinity. Epidermal growth factor (EGF), transforming growth factor-α (TGF), betacellulin, and heparin binding EGF-like growth factor are classified as high affinity ligands with dissociation constants (K_d) in the range of 0.1-10 nM. Epigen (EPG), epiregulin (EPR), and amphiregulin are low affinity ligands and have K_d values roughly 10 to 100 times those of high affinity ligands in the micromolar range.[2–5]

Ligand	Molecular Weight (kDa)	K_d[3]	Binding Affinity
EGF	6.2	0.6 nM	High
TGFα	5.5	9.2 nM	High
EPG	7.9	2.8 μM	Low
EPR	5.6	> 500 nM	Low

Table 1. Characteristics of selected EGFR ligands.
Molecular weight, dissociation constant (K_d), and binding affinity classification of EGFR ligands epidermal growth factor (EGF), transforming growth factor α (TGFα), epigen (EPG), and epiregulin (EPR).

Different EGFR ligands promote varying cellular processes between cell lines, though the mechanism by which EGFR generates different signaling responses remains incompletely characterized.[2,6,7] Across cell lines, EGFR signaling is essential in proliferation. EGFR is upregulated across many types of cancer, making it a possible target for therapeutics and motivating further study of EGFR signal transduction.[8] Previous crystallography studies focused on the interaction between the extracellular EGFR domain and its ligands revealed that high and low affinity ligands induce EGFR dimers of varying stability. The high affinity ligands EGF and TGFα stabilize the EGFR dimer, while the low affinity ligands EPG and EPR induce less stable and shorter lived dimers. In MCF-7 breast adenocarcinoma cells, the stable EGF/TGFα-induced

dimers promote proliferation through transient signaling pathways. Conversely, the less stable dimers formed with EPG and EPR result in differentiation through sustained signaling.[2]

A431 epidermoid carcinoma cells have very high EGFR expression levels and are commonly used to study EGFR stimulation. In A431 cells, EGF inhibits proliferation at nanomolar concentrations but has a mitogenic effect at picomolar concentrations.[9] TGFα and EPR also have an inhibitory effect on proliferation at nanomolar concentrations.[10,11] EPG binds to EGFR in A431 cells and stimulates phosphorylation in EGFR similarly to TGFα, but it is unclear whether EPG has an inhibitory or mitogenic effect.[12]

Previous work in the Miller Lab has focused on elucidating the effect of EGF/EGFR activation on membrane potential (V_m) in A431 cells using voltage-sensitive VoltageFluor (VF) dyes in conjunction with fluorescence lifetime imaging (FLIM). VFs respond to changes in membrane potential through a photoinduced-electron transfer mechanism in which hyperpolarizing potentials result in a shorter fluorescence lifetime of the VF, while depolarizing potentials lead to a longer lifetime. VF-FLIM has provided a new method to directly observe EGFR-induced membrane potential dynamics over longer timescales.[13]

One possible mechanism by which EGFR may influence membrane potential is through interactions with intracellular Ca^{2+}. EGFR can mediate Ca^{2+} signaling through activation of phospholipase C, formation of 1,4,5-trisphosphate (IP_3),[14,15] and release of Ca^{2+} from internal stores.[16] When internal Ca^{2+} is depleted, store-operated calcium entry (SOCE) allows for uptake of external Ca^{2+}.[17,18] EGFR activation by both EGF and TGFα has been shown to result in increased intracellular Ca^{2+} concentrations.[14,15,19]

In previous experiments, serum-starved A431 cells stained with VF2.1.Cl were stimulated with 500 ng/mL EGF and the lifetime response was recorded intermittently over 15 minutes, revealing a rapid 15 mV decrease in lifetime followed by a slow return towards baseline.[13] Addition of EGFR inhibitors, canertinib and gefitinib, significantly decreased the voltage response. Blockade of the Ca^{2+}-activated K^+ channel $K_{Ca}3.1$ eliminated the EGF-induced hyperpolarization, supporting the hypothesis that EGFR activity results in release of internal Ca^{2+} stores and subsequent opening of $K_{Ca}3.1$ channels, leading to hyperpolarization. Additional experiments sought to further examine the relationship between Ca^{2+} concentration and V_m following EGFR activation. A431 cells stained with the Ca^{2+} indicator Oregon Green BAPTA (OGB) showed an acute increase in Ca^{2+} levels after EGF addition, followed by a slower decrease in Ca^{2+} concentration. These results suggest that EGFR-V_m interactions may regulate resting Ca^{2+} or modulate a driving force for Ca^{2+} over time, such as SOCE following depletion of internal calcium.

Given the wide variation of biological responses to EGFR stimulation, we were interested in investigating whether different EGFR ligands would generate distinct membrane potential dynamics. In this work, we sought to investigate the effect of EGFR stimulation on membrane potential through treatment with two high affinity (EGF and TGFα) and two low affinity (EPG and EPR) EGFR ligands. We also recorded the response of serum-starved MCF-7 cells to stimulation with EGF, TGF, EPG, and EPR to assess the generalizability of this voltage change across cell lines.

Results and Discussion

Recent development of a red-shifted VF, tetramethyl carborhodamine (CRhOMe), has enabled further study of membrane potential dynamics with reduced phototoxicity compared to VF2.1.Cl. We started by measuring the resting lifetime of CRhOMe in serum-starved A431 cells, which is 2.647 ± 0.004 ns (mean ± SEM, n = 109, **Figure 4.1**).

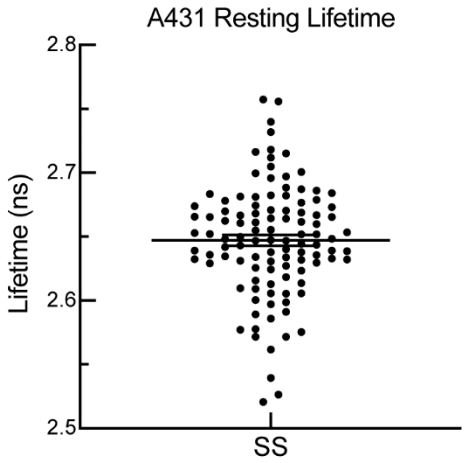


Figure 4.1. Resting lifetime of serum-starved A431 cells.
Scatter plot of lifetimes observed with 300 nM CRhOMe in groups of serum-starved (SS) A431 cells at rest. Each point represents an individual region of interest (ROI; 109 total), consisting of approximately 20-40 cells on average. Error bar is mean ± SEM (2.647 ± 0.004 ns).

After establishing the resting lifetime, we recharacterized the effect of EGFR stimulation with the high-affinity ligand EGF. We measured the lifetime change of CRhOMe in serum-starved A431 cells in response to 500 ng/mL EGF (**Figure** 4.**2a,b**, **Figure 4.3**). After acquiring two sequential FLIM images with 60 second exposures (-3 and -2 minute timepoints), 500 ng/mL (16 nM) EGF was added, and another acquisition was started. Additional images were acquired 3, 6, 9, and 12 minutes after EGF was added. The average change in lifetime 3 minutes after 500 ng/mL EGF stimulation was -65 ± 11 ps (mean ± SEM, n = 6, **Figure 4.4a**, **Table 4.1**). At subsequent time points, the lifetime remained shortened but slowly started to increase. This lifetime response is consistent with previous measurements of CRhOMe in A431 cells, which demonstrated a 75 ps decrease in lifetime in response to 500 ng/mL EGF.[20]

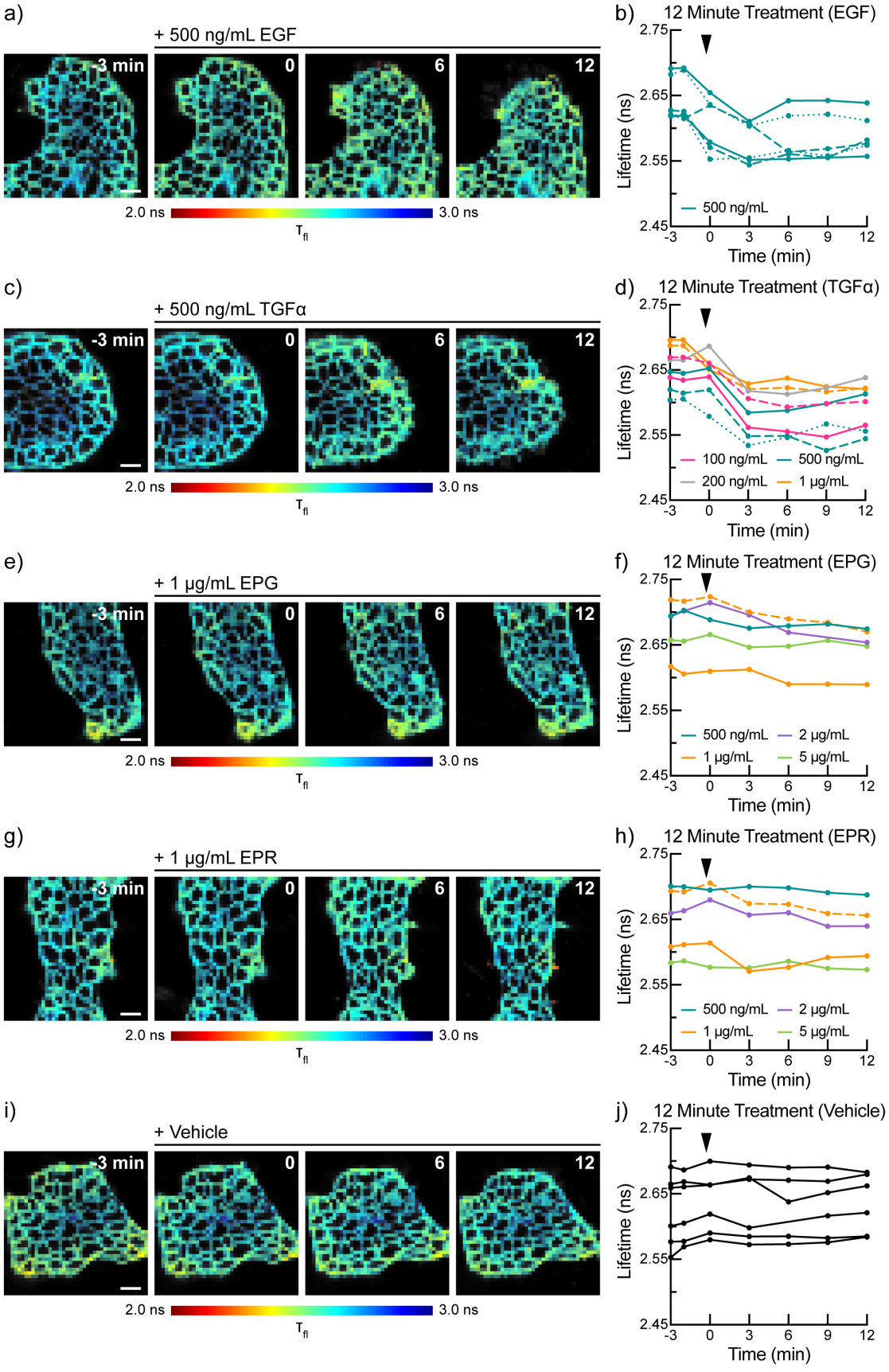

a)
+ 500 ng/mL EGF
-3 min
0
6
12
2.0 ns
3.0 ns
T_{fl}
b)
12 Minute Treatment (EGF)
Lifetime (ns)
2.75
2.65
2.55
2.45
500 ng/mL
-3
0
3
6
9
12
Time (min)
c)
+ 500 ng/mL TGFα
-3 min
0
6
12
2.0 ns
3.0 ns
T_{fl}
d)
12 Minute Treatment (TGFα)
Lifetime (ns)
2.75
2.65
2.55
2.45
100 ng/mL
500 ng/mL
200 ng/mL
1 µg/mL
-3
0
3
6
9
12
Time (min)
e)
+ 1 µg/mL EPG
-3 min
0
6
12
2.0 ns
3.0 ns
T_{fl}
f)
12 Minute Treatment (EPG)
Lifetime (ns)
2.75
2.65
2.55
2.45
500 ng/mL
2 µg/mL
1 µg/mL
5 µg/mL
-3
0
3
6
9
12
Time (min)
g)
+ 1 µg/mL EPR
-3 min
0
6
12
2.0 ns
3.0 ns
T_{fl}
h)
12 Minute Treatment (EPR)
Lifetime (ns)
2.75
2.65
2.55
2.45
500 ng/mL
2 µg/mL
1 µg/mL
5 µg/mL
-3
0
3
6
9
12
Time (min)
i)
+ Vehicle
-3 min
0
6
12
2.0 ns
3.0 ns
T_{fl}
j)
12 Minute Treatment (Vehicle)
Lifetime (ns)
2.75
2.65
2.55
2.45
-3
0
3
6
9
12
Time (min)

Figure 4.2. CRhOMe lifetime of A431 cells following addition of EGFR ligands or vehicle.
Representative lifetime-intensity overlay images of serum-starved A431 cells loaded with 300 nM CRhOMe at four different time points during treatment with **a)** 500 ng/mL EGF, **c)** 500 ng/mL TGFα, **e)** 1 µg/mL EPG, **g)**1 µg/mL EPR, or **i)** imaging buffer vehicle. Scale bars are 20 µm. Two baseline images were acquired 3 and 2 minutes before treatment started, and ligand or vehicle was added just before the 0 minute time point. Traces of CRhOMe lifetime in A431 cells over 12 minutes during treatment with **b)** EGF, **d)** TGFα, **f)** EPG, **h)** EPR, or **j)** vehicle. Solid, dashed, or dotted lines represent different recordings at the indicated concentration. Arrow indicates ligand or vehicle addition.

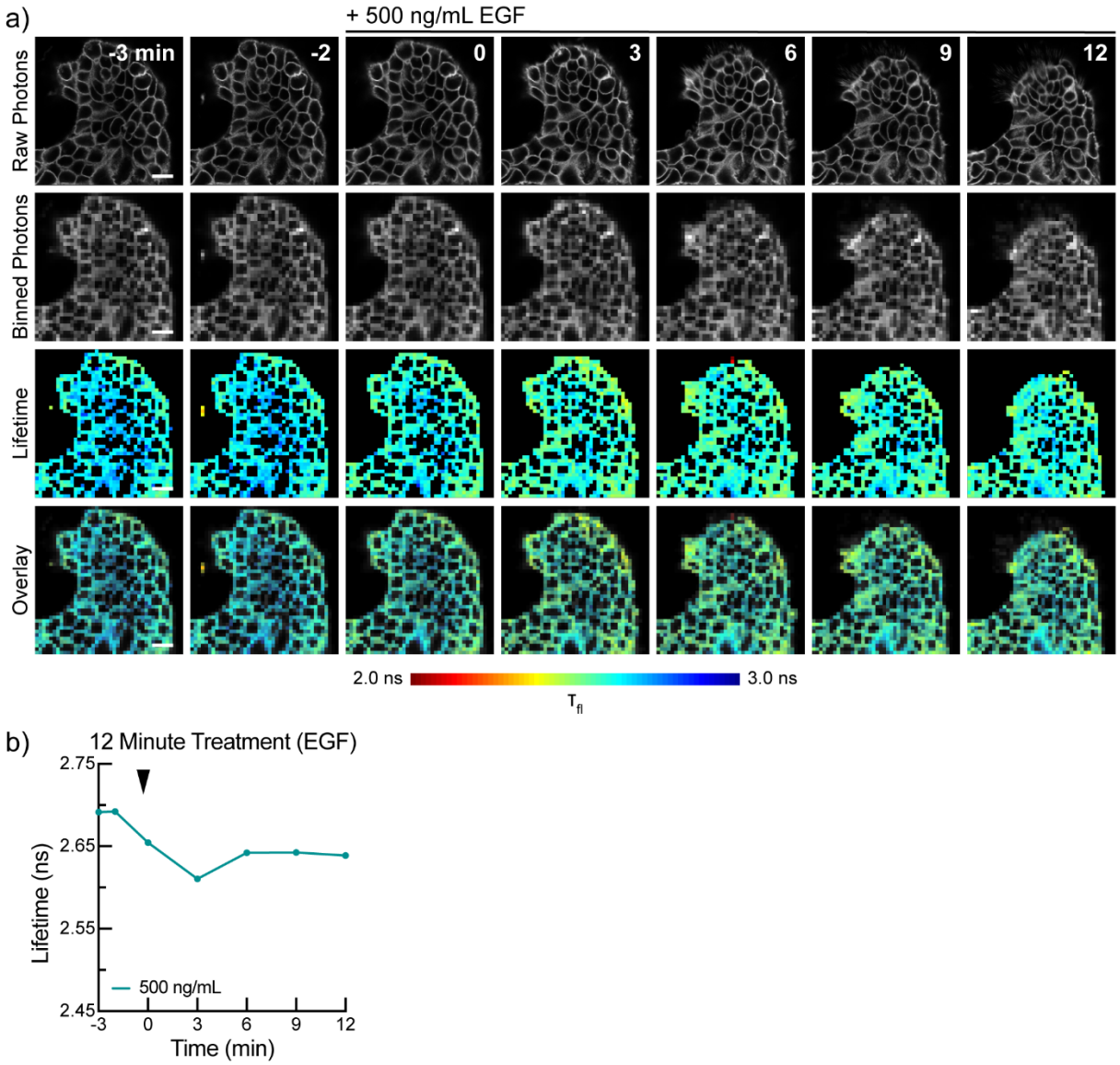


Figure 4.3. CRhOMe lifetime of A431 cells following addition of 500 ng/mL EGF.
a) Representative raw photon intensity, binned photon intensity, lifetime, and intensity-lifetime overlay images of serum-starved A431 cells loaded with 300 nM CRhOMe at all recorded time points during treatment with 500 ng/mL EGF. EGF was added just before the 0 minute time point. Scale bars are 20 µm. **b)** Quantification of CRhOMe lifetime images shown in **a)**. Arrow indicates EGF addition.

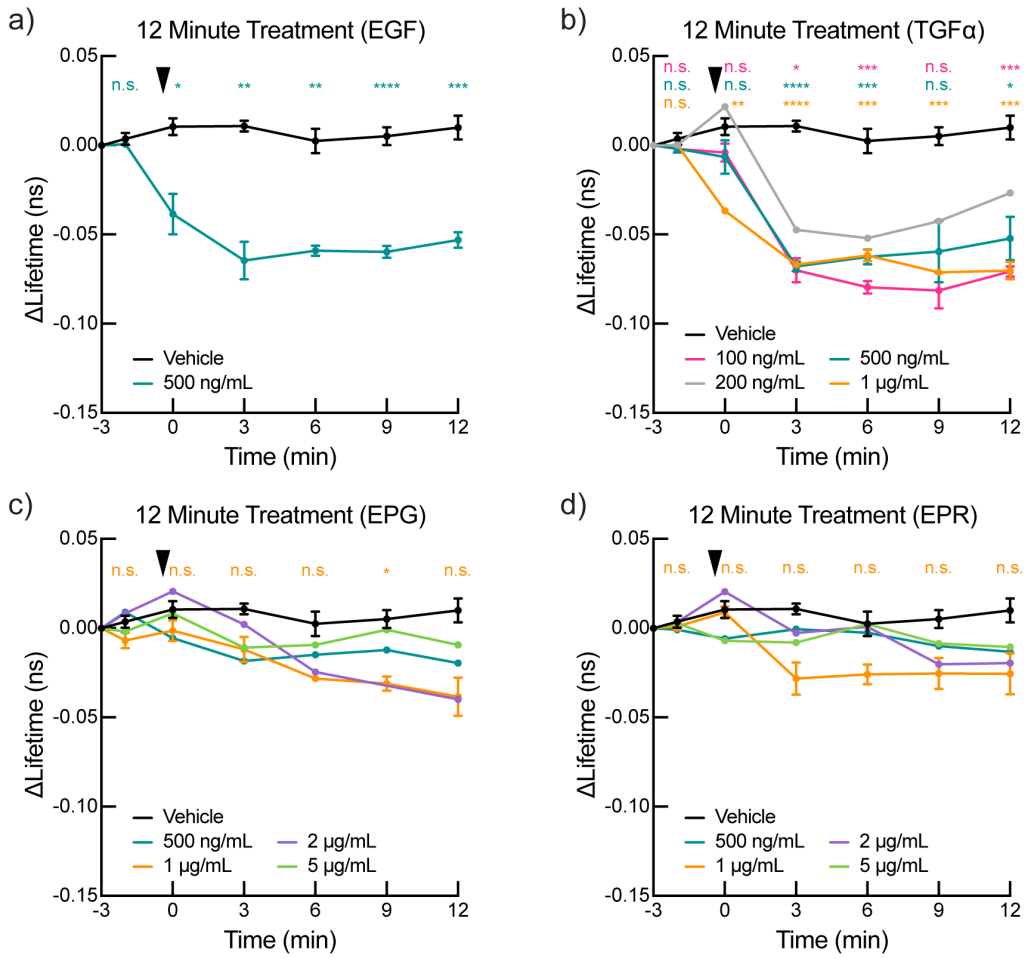


Figure 4.4. Average CRhOMe lifetime change in A431 cells following addition of EGFR ligands or vehicle. Average CRhOMe lifetime change of serum-starved A431 cells during treatment with different EGFR ligands over 12 minutes. Error bars are mean ± SEM. Each recording consisted of a group of 20-40 cells. Arrow indicates ligand or vehicle addition. **a)** Cells treated with imaging buffer vehicle (black) or 500 ng/mL EGF (teal). Sample sizes (number of recordings): Vehicle 5, 500 ng/mL 6. **b)** Cells treated with imaging buffer vehicle (black), 100 ng/mL TGFα (pink), 200 ng/mL TGFα (gray), 500 ng/mL TGFα (teal), or 1 µg/mL TGFα (orange). Sample sizes (number of recordings): Vehicle 5, 100 ng/mL 2, 200 ng/mL 1, 500 ng/mL 3, 1 µg/mL 2. **c)** Cells treated with imaging buffer vehicle (black), 500 ng/mL EPG (teal), 1 µg/mL EPG (orange), 2 µg/mL EPG (purple), or 5 µg/mL EPG (green). Sample sizes (number of recordings): Vehicle 5, 500 ng/mL 1, 1 µg/mL 2, 2 µg/mL 1, 5 µg/mL 1. **d)** Cells treated with imaging buffer vehicle (black), 500 ng/mL EPR (teal), 1 µg/mL EPR (orange), 2 µg/mL EPR, (purple), or 5 µg/mL EPR (green). Sample sizes (number of recordings): Vehicle 5, 500 ng/mL 1, 1 µg/mL 2, 2 µg/mL 1, 5 µg/mL 1. Asterisks indicate significant differences between vehicle and ligand at the specified time point (n.s. $p > 0.05$, * $p < 0.05$, ** $p < 0.01$, *** $p < 0.001$, **** $p < 0.0001$, two-way ANOVA with Geissler-Greenhouse correction, Šídák (EGF, EPG, EPR) or Dunnett (TGFα) post hoc testing).

	Average ΔLifetime, 3 minutes (ps)				
Concentration	**EGF**	**TGFα**	**EPG**	**EPR**	**Vehicle**
100 ng/mL	—	-70 ± 7	—	—	11 ± 3
200 ng/mL	—	-47	—	—	
500 ng/mL	-65 ± 11	-68 ± 3	-18	-1	
1 µg/mL	—	-67.0 ± 0.1	-12 ± 7	-28 ± 9	
2 µg/mL	—	—	2	-3	
5 µg/mL	—	—	-11	-8	
	Average ΔLifetime, 6 minutes (ps)				
Concentration	**EGF**	**TGFα**	**EPG**	**EPR**	**Vehicle**
100 ng/mL	—	-80 ± 3	—	—	2 ± 7
200 ng/mL	—	-52	—	—	
500 ng/mL	-59 ± 3	-63 ± 4	-15	-3	
1 µg/mL	—	-62 ± 3	-28 ± 1	-26 ± 6	
2 µg/mL	—	—	-25	1	
5 µg/mL	—	—	-9	2	

Table 4.1. Average CRhOMe lifetime change in A431 cells following addition of EGFR ligands.
Average CRhOMe lifetime change of serum-starved A431 cells 3 or 6 minutes after EGFR ligand or imaging buffer vehicle addition. Data are taken from corresponding time points in the 12 minute time series shown in **Figure 4.4**. Values are reported as mean ± SEM for concentrations with multiple recordings. Sample sizes (number of recordings): 500 ng/mL EGF 6, 100 ng/mL TGFα 2, 200 ng/mL TGFα 1, 500 ng/mL TGFα 3, 1 µg/mL TGFα 2, 1 µg/mL EPG 2, 1 µg/mL EPR 2, Vehicle 5.

We also characterized the response of another high-affinity EGFR ligand, TGFα (**Figure 4.2c,d**, **Figure 4.5**). Treatment with 500 ng/mL (18 nM) TGFα resulted in an average lifetime change of -68 ± 3 ps after 3 minutes (mean ± SEM, n = 3, **Figure 4.4b, Table 4.1**). After 3 minutes, the lifetime started to slowly increase again, occurring more rapidly following TGFα addition compared to EGF.

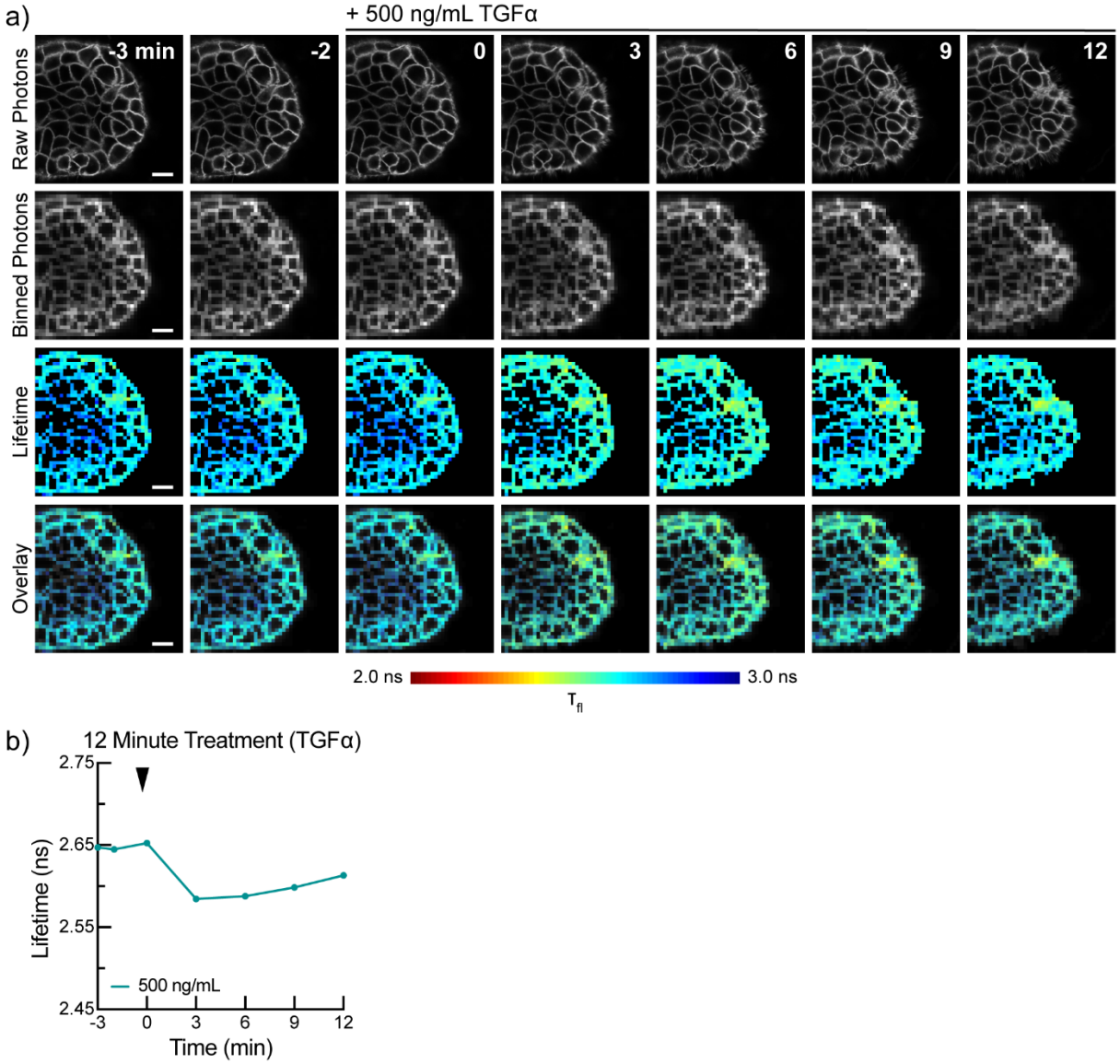


Figure 4.5. CRhOMe lifetime of A431 cells following addition of 500 ng/mL TGFα.
a) Representative raw photon intensity, binned photon intensity, lifetime, and intensity-lifetime overlay images of serum-starved A431 cells loaded with 300 nM CRhOMe at all recorded time points during treatment with 500 ng/mL TGFα. TGFα was added just before the 0 minute time point. Scale bars are 20 μm. **b)** Quantification of CRhOMe lifetime images shown in **a)**. Arrow indicates TGFα addition.

After establishing the effect of 500 ng/mL TGFα, we wanted to determine whether the lifetime response was dose-dependent, as with EGF. We repeated the 12 minute time series with 100 ng/mL, 200 ng/mL, and 1 μg/mL TGFα and observed a similar drop in lifetime, followed by a slow return to baseline (**Figure 4.2d**, **Figure 4.5**, **Table 4.1**). We also recorded the lifetime response at several

concentrations below 100 ng/mL to develop a dose-response curve. For these experiments, we acquired one initial image, added TGFα, and acquired subsequent images after 3 and 6 minutes of treatment (**Figure 4.6a,b**). The average lifetime changes 3 and 6 minutes after TGFα addition were fit to a four-parameter logistic function to develop a dose response curve. The EC_{50} for TGFα-induced hyperpolarization after 3 minutes is 35 ng/mL (6.3 nM), but the 95% CI could not be determined. At 6 minutes, the EC_{50} is 28 ng/mL (5.0 nM) with the 95% CI from 14 ng/mL to 49 ng/mL) (**Figure 4.6c,d**). The largest average lifetime change was observed at 6 minutes with 100 ng/mL TGFα (-82 ± 10 ps, mean ± SEM, n = 3). However, there is not a statistically significant difference compared to the average lifetime changes at higher concentrations (200 ng/mL, 500 ng/mL, or 1 μg/mL; two-way ANOVA with Geissler-Greenhouse correction, Tukey's multiple comparisons test).

Previous measurements of 500 ng/mL EGF with VF2.1.Cl displayed a 40 ps decrease in lifetime corresponding to a 15 mV hyperpolarization. These results suggest that the 65 ps decrease observed with CRhOMe is also indicative of a 15 mV hyperpolarization. The lifetime changes following TGFα addition were of a similar magnitude, suggesting that TGFα may also induce a 15 mV hyperpolarization in V_m.

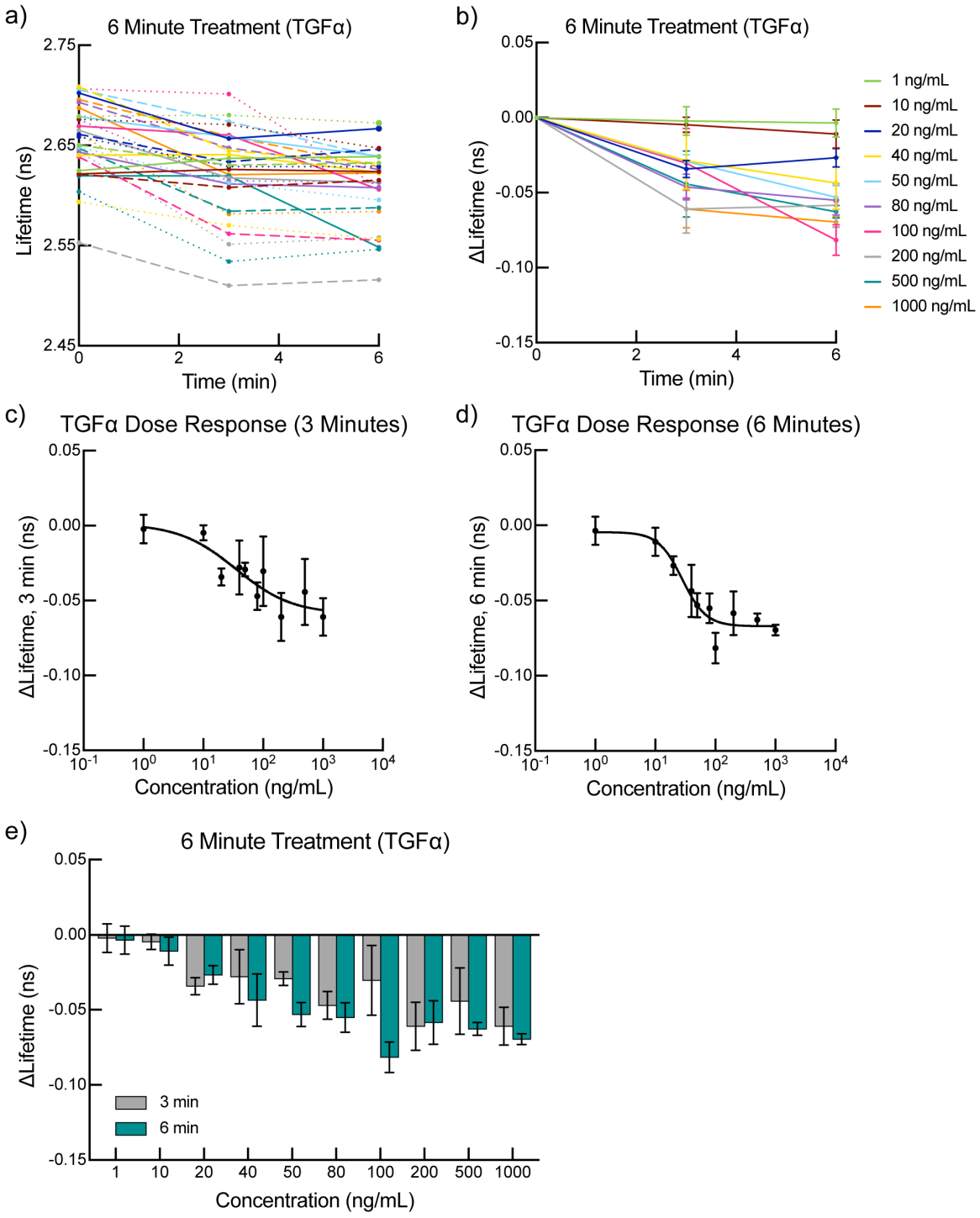


Figure 4.6. Dose-response of CRhOMe lifetime change following TGFα stimulation.
a) Traces of CRhOMe lifetime in serum-starved A431 cells during 6 minute treatment with TGFα at varying concentrations. TGFα was added after acquiring the 0 minute time point. Solid, dashed, and dotted lines represent different recordings at the indicated concentration. **b)** Average CRhOMe lifetime change of serum-starved A431 cells during treatment with TGFα over 6 minutes. TGFα was added after acquiring the 0 minute time point. Dose-response relationship of CRhOMe lifetime change after **c)** 3 minutes or **d)** 6 minutes of TGFα treatment. Data were fit to a four-parameter logistic function to obtain EC_{50} values of 35 ng/mL (95% CI could not be

calculated) or 28 ng/mL (95% CI: 14-49 ng/mL) after 3 or 6 minutes of treatment, respectively. **e)** Average CRhOMe lifetime change of serum-starved A431 cells after 3 minutes (gray) or 6 minutes (teal) of TGFα treatment. All errors bars are mean ± SEM for 3 recordings at each concentration. Each recording consisted of a group of 20-40 cells.

Following characterization of the lifetime response to EGF and TGFα, we turned to two low-affinity ligands, EPG and EPR. In contrast to EGF and TGFα, addition of 1 μg/mL (127 nM) EPG led to a minimal change in lifetime (**Figure 4.2e,f**, **Figure 4.7**). The average lifetime change at 6 minutes was -28 ± 1 ps, after which the lifetime continued to decrease slowly (mean ± SEM, n = 2, **Figure 4.4c**, **Table 4.1**). However, the average change at all time points (except 9 minutes) was not significant compared to the vehicle trace at the corresponding points. Addition of 2 μg/mL EPG showed a comparable lifetime trend to 1 μg/mL, however, 500 ng/mL and 5 μg/mL displayed negligible changes in lifetime. However, these recordings are single trials, so additional replicates will be necessary to further investigate the possible differences between concentrations.

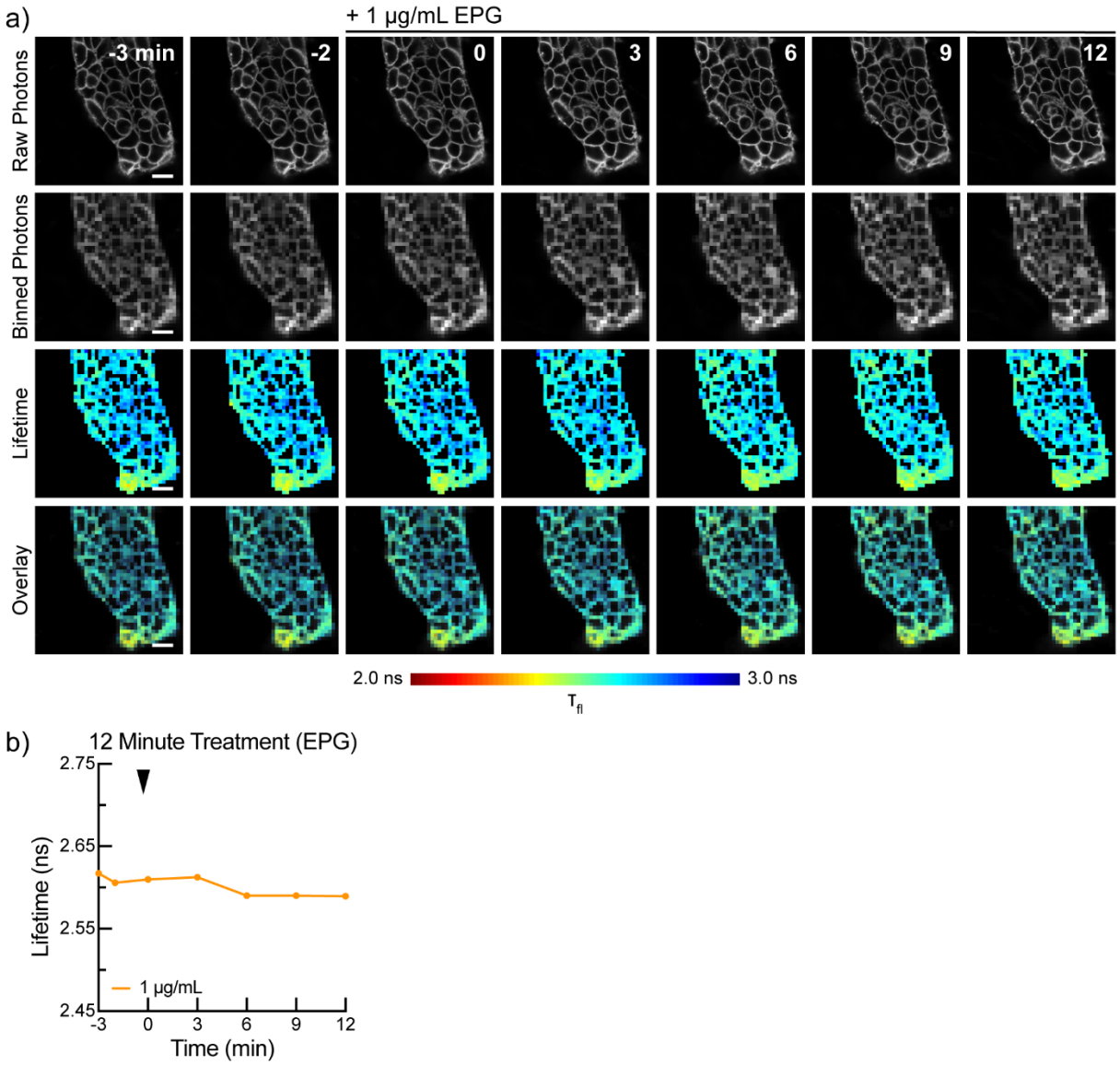


Figure 4.7. CRhOMe lifetime of A431 cells following addition of 1 µg/mL EPG.
a) Representative raw photon intensity, binned photon intensity, lifetime, and intensity-lifetime overlay images of serum-starved A431 cells loaded with 300 nM CRhOMe at all recorded time points during treatment with 1 µg/mL EPG. EPG was added just before the 0 minute time point. Scale bars are 20 µm. **b)** Quantification of CRhOMe lifetime images shown in **a)**. Arrow indicates EPG addition.

Stimulation with 1 µg/mL (179 nM) EPR similarly showed a slight decrease in lifetime (**Figure 4.2g,h**, **Figure 4.8**). The average lifetime change was comparable to that of EPG, at -26 ± 6 ps after 6 minutes (mean ± SEM, n = 2, **Figure 4.4d**, **Table 4.1**). In contrast to EPG, the lifetime did not continue to decrease, but instead started to plateau 3 minutes after EPR addition. Single trials at 500 ng/mL and 5 µg/mL did not reveal a noticeable trend in lifetime, while a recording of 2 µg/mL showed a gradual decrease in lifetime over the full 12 minutes. As with EPG, additional replicates at 500 ng/mL, 2 µg/mL, and 5 µg/mL are necessary to fully evaluate any differences between concentrations.

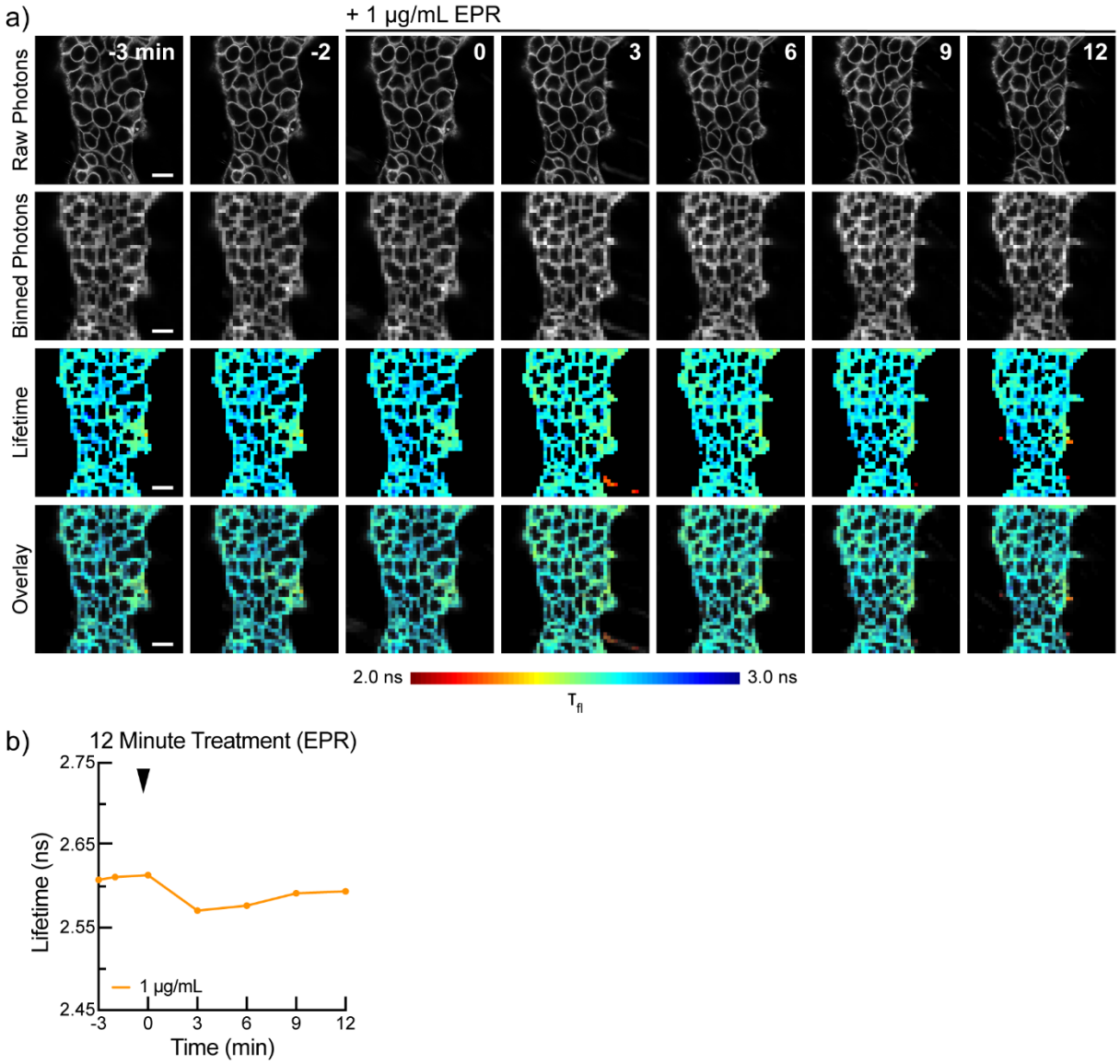


Figure 4.8. CRhOMe lifetime of A431 cells following addition of 1 µg/mL EPR.

a) Representative raw photon intensity, binned photon intensity, lifetime, and intensity-lifetime overlay images of serum-starved A431 cells loaded with 300 nM CRhOMe at all recorded time points during treatment with 1 μg/mL EPR. EPR was added just before the 0 minute time point. Scale bars are 20 μm. **b)** Quantification of CRhOMe lifetime images shown in **a)**. Arrow indicates EPR addition.

The maximal changes in lifetime after 6 minutes for EPG and EPR (-28 ps and -26 ps, respectively) are approximately half of the changes observed for EGF and TGFα. Comparatively, samples treated with the imaging buffer vehicle displayed a comparatively smaller change in lifetime (**Figure 4.2i,j**, **Figure 4.9**). These traces appeared mostly flat, with a slight increase in lifetime over the full 15 minutes. The average change 6 minutes after adding the vehicle was 2 ± 7 ps (mean ± SEM, n = 5, **Table 1**). Similar experiments performed with the voltage-insensitive control compound CRhOMeZero showed a slight decrease in lifetime over the time series (**Figures 4.10-4.11, Figures S4.1-4.5, Table 4.2**).

If the ~60 ps decrease from EGF does indeed correspond to a 15 mV hyperpolarization, the shortened lifetimes from EPG and EPR treatment may reflect hyperpolarizations of half the magnitude, around 7-8 mV. However, the lifetime changes observed with CRhOMeZero following ligand addition were on a similar scale to those observed with EPG and EPR using CRhOMe (**Tables 4.1-4.2**). This suggests that the smaller lifetime changes resulting from EPG and EPR treatment may not be indicative of a change in voltage.

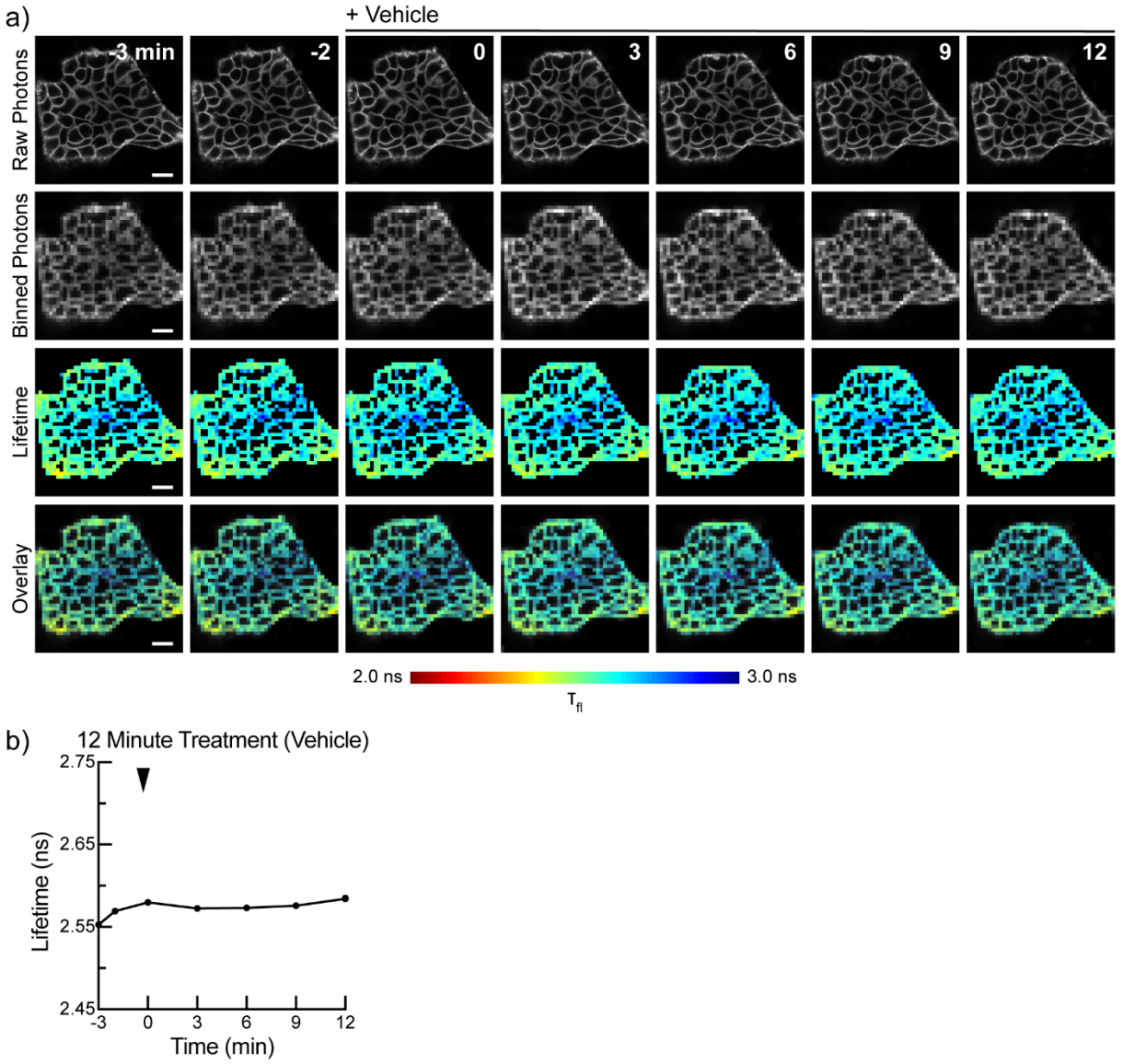


Figure 4.9. CRhOMe lifetime of A431 cells following addition of imaging buffer vehicle.
a) Representative raw photon intensity, binned photon intensity, lifetime, and intensity-lifetime overlay images of serum-starved A431 cells loaded with 300 nM CRhOMe at all recorded time points during treatment with imaging buffer vehicle. Vehicle was added just before the 0 minute time point. Scale bars are 20 μm. **b)** Quantification of CRhOMe lifetime images shown in **a)**. Arrow indicates vehicle addition.

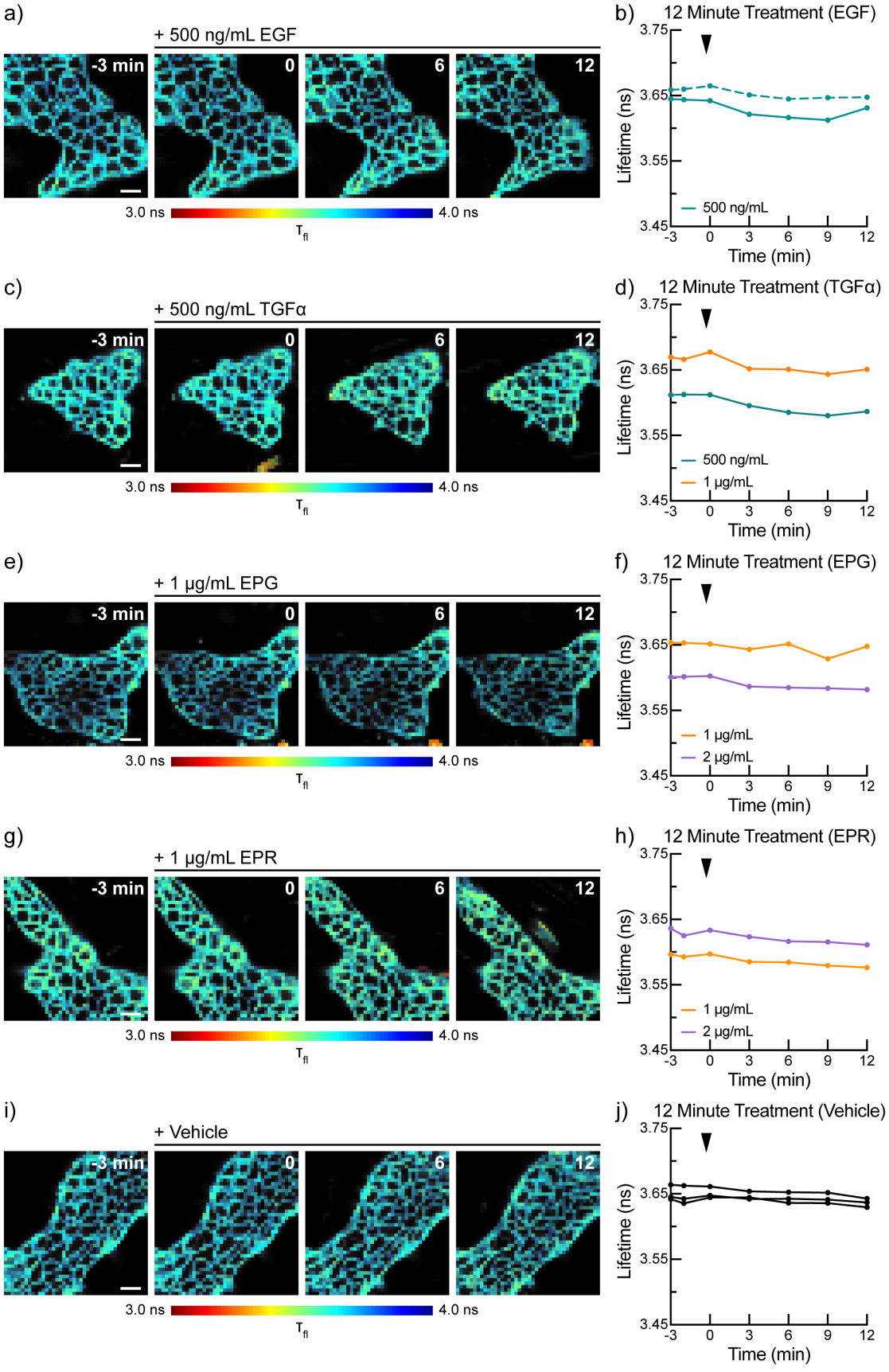

a)
+ 500 ng/mL EGF
-3 min
0
6
12
3.0 ns
4.0 ns
T_{fl}
b)
12 Minute Treatment (EGF)
Lifetime (ns)
3.75
3.65
3.55
3.45
500 ng/mL
-3
0
3
6
9
12
Time (min)
c)
+ 500 ng/mL TGFα
-3 min
0
6
12
3.0 ns
4.0 ns
T_{fl}
d)
12 Minute Treatment (TGFα)
Lifetime (ns)
3.75
3.65
3.55
3.45
500 ng/mL
1 µg/mL
-3
0
3
6
9
12
Time (min)
e)
+ 1 µg/mL EPG
-3 min
0
6
12
3.0 ns
4.0 ns
T_{fl}
f)
12 Minute Treatment (EPG)
Lifetime (ns)
3.75
3.65
3.55
3.45
1 µg/mL
2 µg/mL
-3
0
3
6
9
12
Time (min)
g)
+ 1 µg/mL EPR
-3 min
0
6
12
3.0 ns
4.0 ns
T_{fl}
h)
12 Minute Treatment (EPR)
Lifetime (ns)
3.75
3.65
3.55
3.45
1 µg/mL
2 µg/mL
-3
0
3
6
9
12
Time (min)
i)
+ Vehicle
-3 min
0
6
12
3.0 ns
4.0 ns
T_{fl}
j)
12 Minute Treatment (Vehicle)
Lifetime (ns)
3.75
3.65
3.55
3.45
-3
0
3
6
9
12
Time (min)

Figure 4.10. CRhOMeZero lifetime of A431 cells following addition of EGFR ligands or vehicle.
Representative lifetime-intensity overlay images of serum-starved A431 cells loaded with 300 nM CRhOMeZero at four different time points during treatment with **a)** 500 ng/mL EGF, **c)** 500 ng/mL TGFα, **e)** 1 µg/mL EPG, **g)**1 µg/mL EPR, or **i)** imaging buffer vehicle. Scale bars are 20 µm. Two baseline images were acquired 3 and 2 minutes before treatment started, and ligand or vehicle was added just before the 0 minute time point. Traces of CRhOMeZero lifetime in A431 cells over 12 minutes during treatment with **b)** EGF, **d)** TGFα, **f)** EPG, **h)** EPR, or **j)** vehicle. Arrow indicates ligand or vehicle addition.

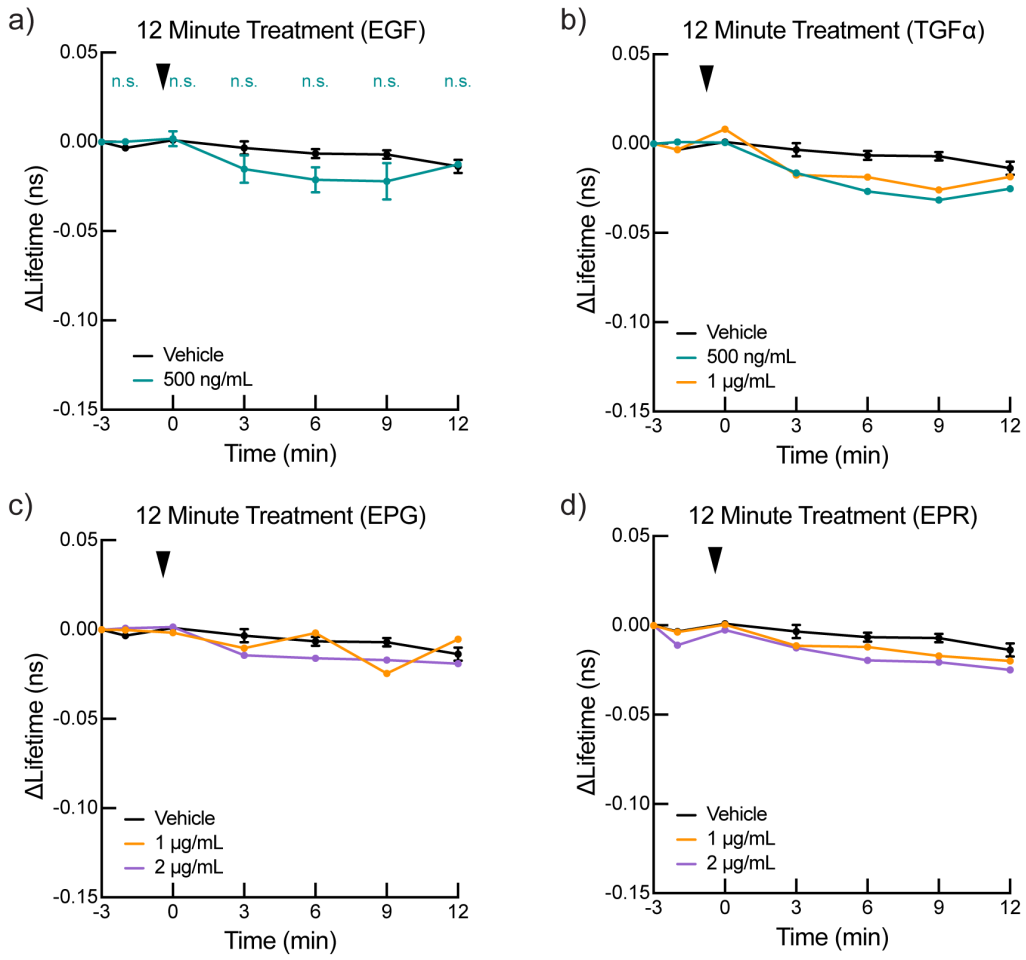


Figure 4.11. Average CRhOMeZero lifetime change in A431 cells following addition of EGFR ligands or vehicle.
Average CRhOMeZero lifetime change of serum-starved A431 cells during treatment with different EGFR ligands over 12 minutes. Error bars are mean ± SEM. Each recording consisted of a group of 20-40 cells. Arrow indicates ligand or vehicle addition. **a)** Cells treated with imaging buffer vehicle (black) or 500 ng/mL EGF (teal). Sample sizes (number of recordings): Vehicle 3, 500 ng/mL 2. **b)** Cells treated with imaging buffer vehicle (black), 500 ng/mL TGFα (teal), or 1 µg/mL TGFα (orange). Sample sizes (number of recordings): Vehicle 3, 500 ng/mL 1, 1 µg/mL 1. **c)** Cells treated with imaging buffer vehicle (black), 1 µg/mL EPG (orange), or 2 µg/mL EPG (purple). Sample sizes (number of recordings): Vehicle 3, 1 µg/mL 1, 2 µg/mL 1. **d)** Cells treated with imaging buffer vehicle (black), 1 µg/mL EPR (orange), or 2 µg/mL EPR, (purple). Sample sizes (number of recordings): Vehicle 3, 1 µg/mL 1, 2 µg/mL 1. Asterisks indicate significant differences between vehicle and EGF at the specified time point (n.s. $p > 0.05$, * $p < 0.05$, ** $p < 0.01$, *** $p < 0.001$, **** $p < 0.0001$, two-way ANOVA with Geissler-Greenhouse correction, Šídák post hoc testing)

	Average ΔLifetime, 3 minutes (ps)				
Concentration	**EGF**	**TGFα**	**EPG**	**EPR**	**Vehicle**
500 ng/mL	-15 ± 8	-16	—	—	-3 ± 4
1 µg/mL	—	-18	-10	-11	
2 µg/mL	—	—	-14	-13	
	Average ΔLifetime, 6 minutes (ps)				
Concentration	**EGF**	**TGFα**	**EPG**	**EPR**	**Vehicle**
500 ng/mL	-21 ± 7	-27	—	—	-7 ± 3
1 µg/mL	—	-19	-2	-12	
2 µg/mL	—	—	-16	-20	

Table 4.2. Average CRhOMeZero lifetime change in A431 cells following addition of EGFR ligands. Average CRhOMeZero lifetime change of serum-starved A431 cells 3 or 6 minutes after EGFR ligand or imaging buffer vehicle addition. Data are taken from corresponding time points in the 12 minute time series shown in **Figure 4.11**. Values are reported as mean ± SEM for concentrations with multiple recordings. Sample sizes (number of recordings): 500 ng/mL EGF 2, 500 ng/mL TGFα 1, 1 µg/mL TGFα 1, 1 µg/mL EPG 1, 2 µg/mL EPG 1, 1 µg/mL EPR 1, 2 µg/mL EPR 1, Vehicle 3.

After evaluating the lifetime response of EGF, TGFα, EPG, and EPR in A431 cells, we wanted to assess the generalizability of these lifetime changes in another cell line. We turned to MCF-7 breast cancer cells, which have lower EGFR expression than A431 cells.[2] We initially measured the lifetime of CRhOMe in MCF-7 cells grown under serum-starvation or full-serum conditions (**Figure 4.12**). The lifetime of CRhOMe in serum-starved MCF-7 cells is 2.838 ± 0.007 ns (mean ± SEM, n = 44), while the lifetime in MCF-7 cells grown under full-serum conditions is 2.839 ± 0.008 ns (mean ± SEM, n = 40). There is not a significant difference in resting lifetime between the two conditions (n.s. $p > 0.05$, two-sided, unpaired, unequal variances t-test).

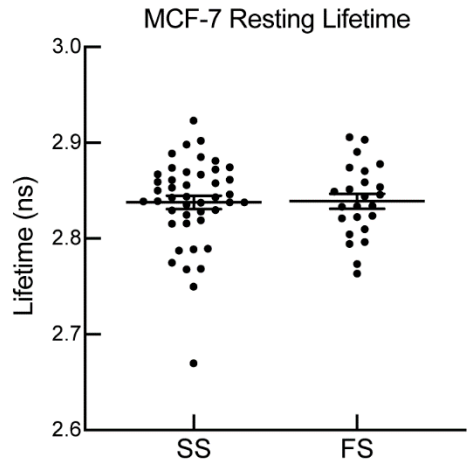


Figure 4.12. Resting lifetime of MCF-7 cells grown under serum-starvation or full-serum conditions. Scatter plot of resting lifetimes observed with 300 nM CRhOMe in groups of MCF-7 cells grown under serum-starvation (SS, 2% FBS) or full-serum (FS, 10% FBS) conditions. Each point represents an individual ROI (SS: n = 44; FS: n = 24), consisting of approximately 10-30 cells on average. Error bar is mean ± SEM (SS: 2.838 ± 0.007 ns; FS: 2.839 ± 0.008 ns). There is not a significant difference in resting lifetime between the two conditions (n.s. $p > 0.05$, two-sided, unpaired, unequal variances t-test).

We then recorded MCF-7 cells in response to treatment with 500 ng/mL, 1 μg/mL, and 2 μg/mL EGF (**Figure 4.13a,b**, **Figure 4.14, Figure 4.15a**). Traces of 500 ng/mL treatments were mostly flat, while cells treated with 1 μg/mL and 2 μg/mL showed a slight increase in lifetime. After 6 minutes of treatment, the lifetime increased by 21 ± 8 ps (n = 3) for 1 μg/mL and 13 ± 4 ps (n = 2) for 2 μg/mL (mean ± SEM, **Table 4.3**). Cells treated with TGFα ranging from 100 ng/mL to 2 μg/mL did not display a marked change in lifetime (**Figure 4.13c,d**, **Figure 4.16**). All traces were relatively flat, and the maximal change in lifetime of the TGFα concentrations tested occurred with 2 μg/mL (9 ps, n = 1, **Figure 4.15b**, **Table 4.3**). For all tested concentrations of EGF and TGFα, there was not a significant difference compared to the vehicle trace at the corresponding time points (two-way ANOVA with Geissler-Greenhouse correction, Dunnett's (EGF) or Šídák's (TGFα) multiple comparisons test).

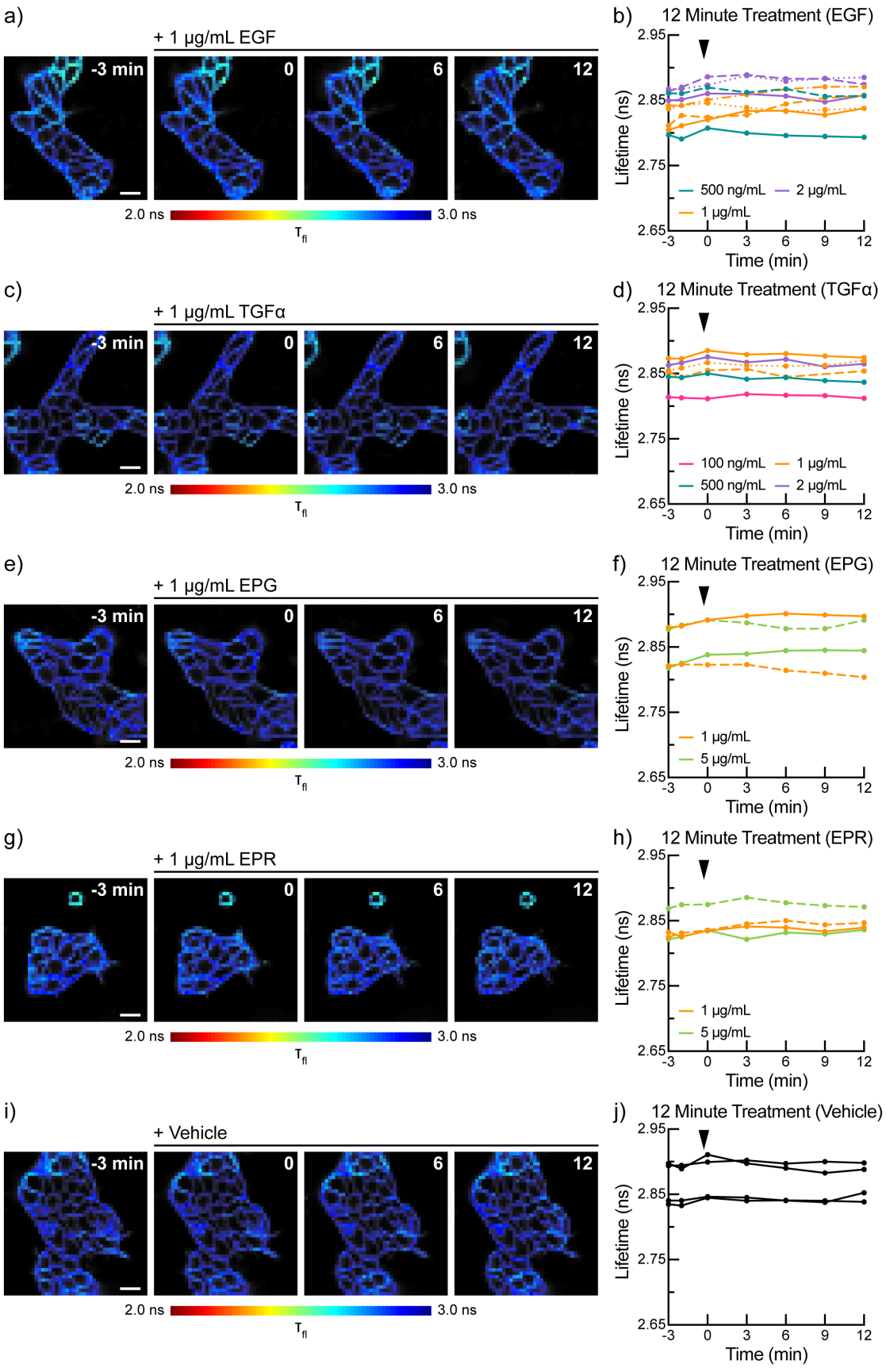

a)
+ 1 µg/mL EGF
-3 min
0
6
12
2.0 ns
3.0 ns
T_{fl}
b)
12 Minute Treatment (EGF)
Lifetime (ns)
Time (min)
500 ng/mL
1 µg/mL
2 µg/mL
c)
+ 1 µg/mL TGFα
d)
12 Minute Treatment (TGFα)
100 ng/mL
500 ng/mL
1 µg/mL
2 µg/mL
e)
+ 1 µg/mL EPG
f)
12 Minute Treatment (EPG)
1 µg/mL
5 µg/mL
g)
+ 1 µg/mL EPR
h)
12 Minute Treatment (EPR)
i)
+ Vehicle
j)
12 Minute Treatment (Vehicle)

Figure 4.13. CRhOMe lifetime of MCF-7 cells following addition of EGFR ligands or vehicle.
Representative lifetime-intensity overlay images of serum-starved MCF-7 cells loaded with 300 nM CRhOMe at four different time points during treatment with **a)** 1 µg/mL EGF, **c)** 1 µg/mL TGFα, **e)** 1 µg/mL EPG, **g)**1 µg/mL EPR, or **i)** imaging buffer vehicle. Scale bars are 20 µm. Two baseline images were acquired 3 and 2 minutes before treatment started, and ligand or vehicle was added just before the 0 minute time point. Traces of CRhOMe lifetime in A431 cells over 12 minutes during treatment with **b)** EGF, **d)** TGFα, **f)** EPG, **h)** EPR, or **j)** vehicle. Solid, dashed, or dotted lines represent different recordings at the indicated concentration. Arrow indicates ligand or vehicle addition.

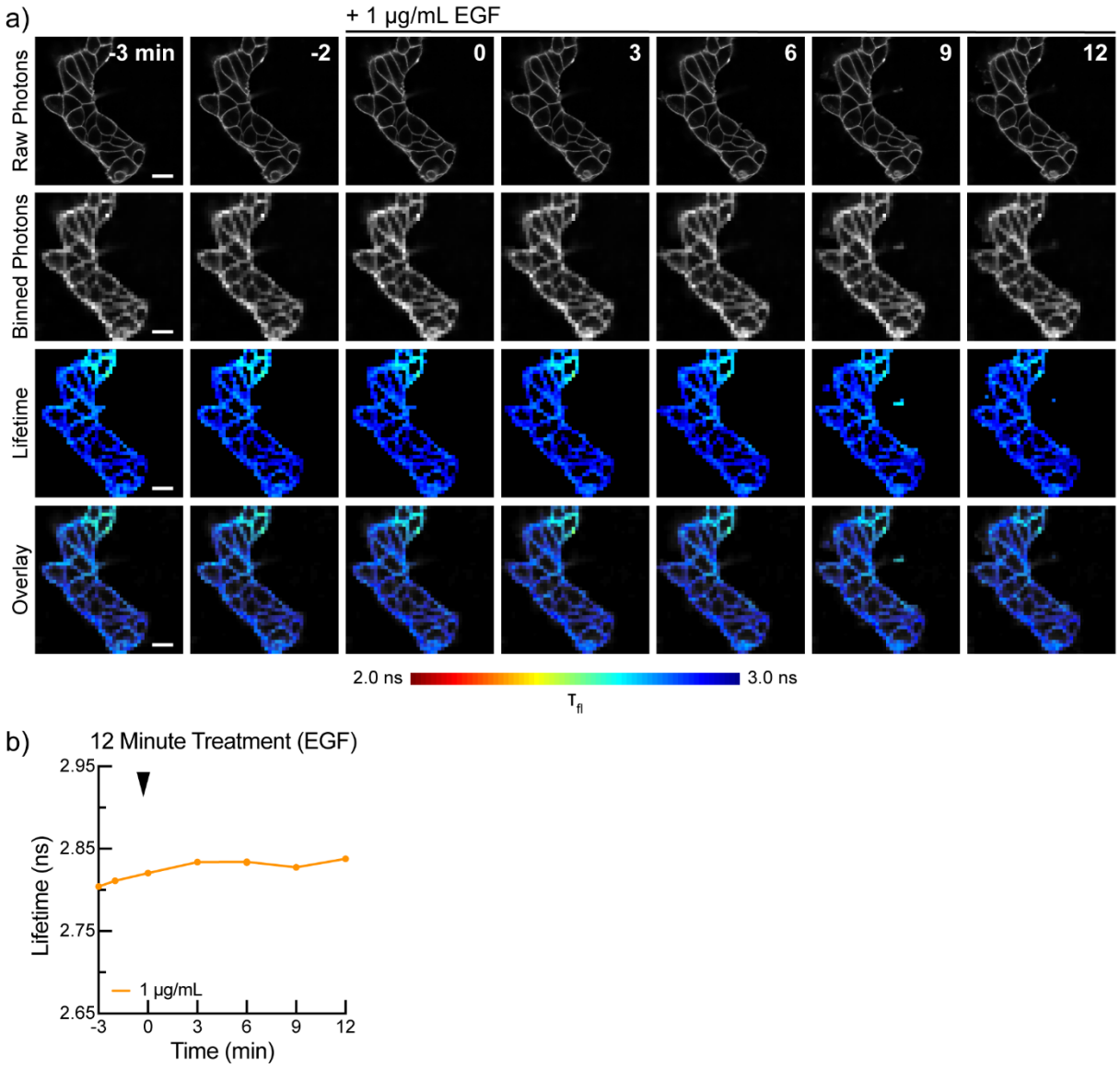


Figure 4.14. CRhOMe lifetime of MCF-7 cells following addition of 1 µg/mL EGF.
a) Representative raw photon intensity, binned photon intensity, lifetime, and intensity-lifetime overlay images of serum-starved MCF-7 cells loaded with 300 nM CRhOMe at all recorded time points during treatment with 1 µg/mL EGF. EGF was added just before the 0 minute time point. Scale bars are 20 µm. **b)** Quantification of CRhOMe lifetime images shown in **a)**. Arrow indicates EGF addition.

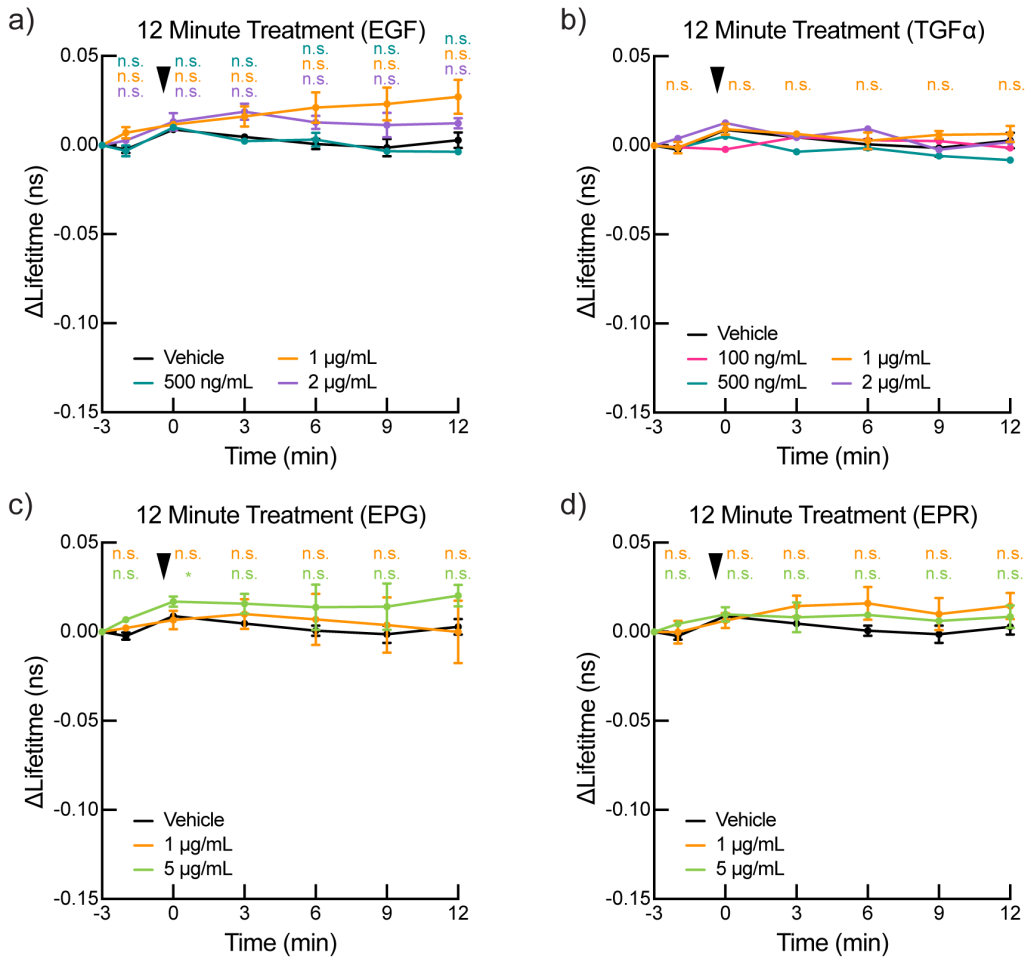


Figure 4.15. Average CRhOMe lifetime change in MCF-7 cells following addition of EGFR ligands or vehicle.

Average CRhOMe lifetime change of serum-starved MCF-7 cells during treatment with different EGFR ligands over 12 minutes. Error bars are mean ± SEM. Each recording consisted of a group of 10-20 cells. Arrow indicates ligand or vehicle addition. **a)** Cells treated with imaging buffer vehicle (black), 500 ng/mL EGF (teal) 1 µg/mL EGF (orange), or 2 µg/mL EGF (purple). Sample sizes (number of recordings): Vehicle 4, 500 ng/mL 2, 1 µg/mL 4, 2 µg/mL 1. **b)** Cells treated with imaging buffer vehicle (black), 100 ng/mL TGFα (pink), 500 ng/mL TGFα (teal), 1 µg/mL TGFα (orange), or 2 µg/mL TGFα (purple). Sample sizes (number of recordings): Vehicle 4, 100 ng/mL 1, 500 ng/mL 1, 1 µg/mL 3, 2 µg/mL 1. **c)** Cells treated with imaging buffer vehicle (black), 1 µg/mL EPG (orange), or 5 µg/mL EPG (green). Sample sizes (number of recordings): Vehicle 4, 1 µg/mL 2, 5 µg/mL 2. **d)** Cells treated with imaging buffer vehicle (black), 1 µg/mL EPR (orange), or 5 µg/mL EPR (green). Sample sizes (number of recordings): Vehicle 4, 1 µg/mL 2, 5 µg/mL 2. Asterisks indicate significant differences between vehicle and ligand at the specified time point (n.s. $p > 0.05$, * $p < 0.05$, ** $p < 0.01$, *** $p < 0.001$, **** $p < 0.0001$, two-way ANOVA with Geissler-Greenhouse correction, Dunnett (EGF, EPG, EPR) or Šídák (TGFα) post hoc testing).

	Average ΔLifetime, 3 minutes (ps)				
Concentration	**EGF**	**TGFα**	**EPG**	**EPR**	**Vehicle**
100 ng/mL	—	5	—	—	5 ± 2
500 ng/mL	-2 ± 1	-4	—	—	
1 µg/mL	16 ± 6	6 ± 1	10 ± 8	14 ± 6	
2 µg/mL	19 ± 5	4	—	—	
5 µg/mL	—	—	16 ± 6	8 ± 8	
	Average ΔLifetime, 6 minutes (ps)				
Concentration	**EGF**	**TGFα**	**EPG**	**EPR**	**Vehicle**
100 ng/mL	—	3	—	—	1 ± 3
500 ng/mL	-3 ± 4	-1	—	—	
1 µg/mL	21 ± 8	3 ± 5	7 ± 14	16 ± 9	
2 µg/mL	13 ± 4	9	—	—	
5 µg/mL	—	—	14 ± 13	9 ± 1	

Table 4.3. Average CRhOMe lifetime change in MCF-7 cells following addition of EGFR ligands.
Average CRhOMe lifetime change of serum-starved MCF-7 cells 3 or 6 minutes after EGFR ligand or imaging buffer vehicle addition. Data are taken from the corresponding time points in the 12 minute time series shown in **Figure 4.15**. Values are reported as mean ± SEM for concentrations with multiple recordings. Sample sizes (number of recordings): 500 ng/mL EGF 2, 1 µg/mL EGF 4, 2 µg/mL EGF 3, 100 ng/mL TGFα 1, 500 ng/mL TGFα 1, 1 µg/mL TGFα 3, 2 µg/mL TGFα 1, 1 µg/mL EPG 2, 5 µg/mL EPG 2, 1 µg/mL EPR 2, 5 µg/mL EPR 2, Vehicle 4.

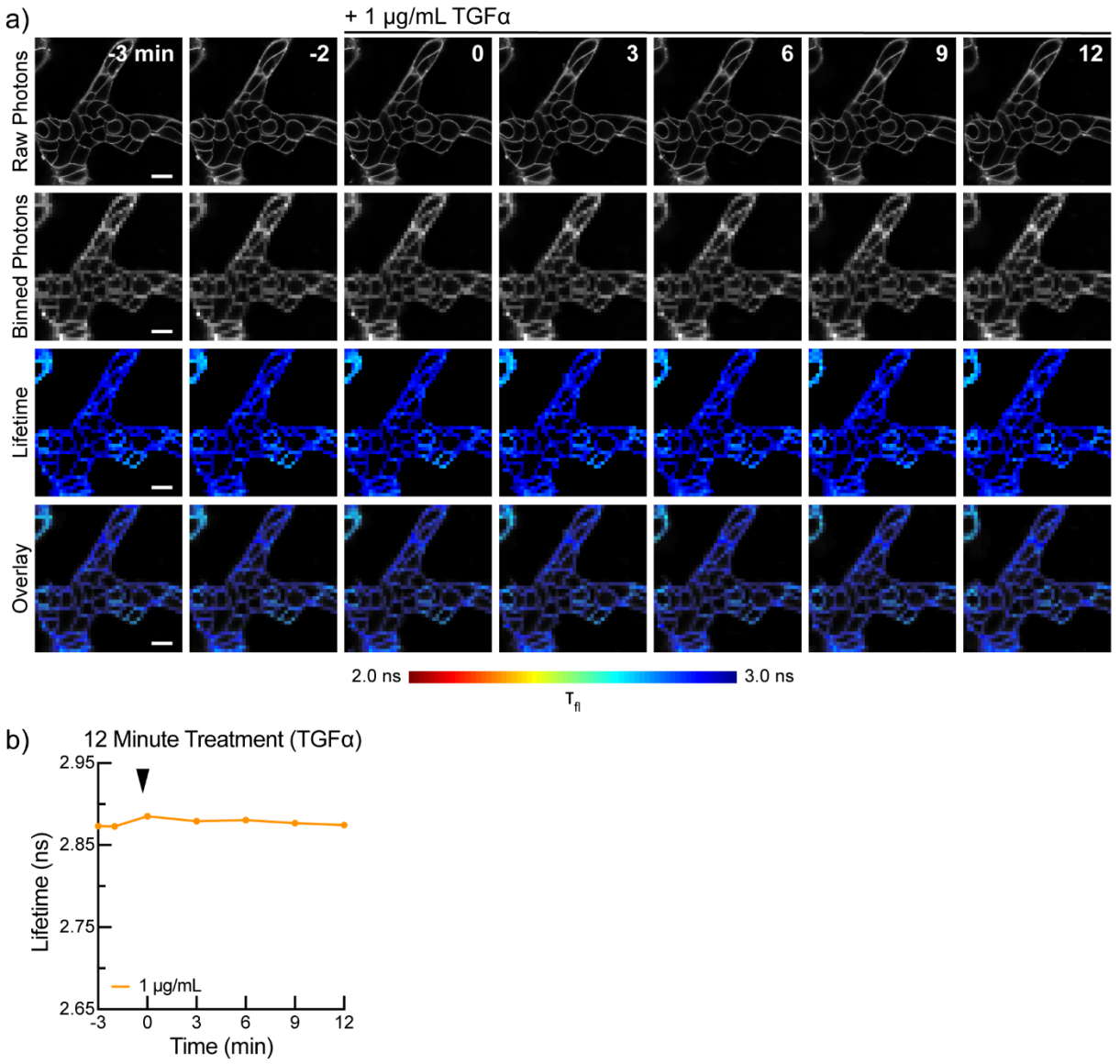


Figure 4.16. CRhOMe **lifetime of MCF-7 cells following addition of 1 µg/mL TGFα.**
a) Representative raw photon intensity, binned photon intensity, lifetime, and intensity-lifetime overlay images of serum-starved MCF-7 cells loaded with 300 nM CRhOMe at all recorded time points during treatment with 1 µg/mL TGFα. TGFα was added just before the 3 minute time point. Scale bars are 20 µm. **b)** Quantification of CRhOMe lifetime images shown in **a)**. Arrow indicates TGFα addition.

In response to 1 µg/mL (127 nM) or 5 µg/mL (633 nM) EPG, the lifetime increased slightly, though not as noticeably as the increase resulting from 1 µg/mL EGF (**Figure 4.13e,f**, **Figure 4.17**). Treatment with 1 µg/mL (179 nM) or 5 µg/mL (893 nM) EPR similarly showed a minimal increase in lifetime (**Figure 4.13g,h**, **Figure 4.18**). The largest changes in lifetime were observed with 5 µg/mL EPG (14 ± 13 ps, n =2) and 1 µg/mL EPR (16 ± 9 ps, n = 2) after 6 minutes of ligand treatment (**Table 3**). Traces of vehicle-treated cells were relatively flat and displayed a negligible change in lifetime of only 1 ± 3 ps after 6 minutes of treatment (mean ± SEM, n = 4, **Figure 4.13i,j**, **Figure 4.19**, **Table 4.3**). Recordings of MCF-7 cells loaded with CRhOMeZero and treated with EGF, TGFα, EPG, or EPR show a minimal decrease in lifetime (**Figures 4.20-4.21**, **Table 4.4**).

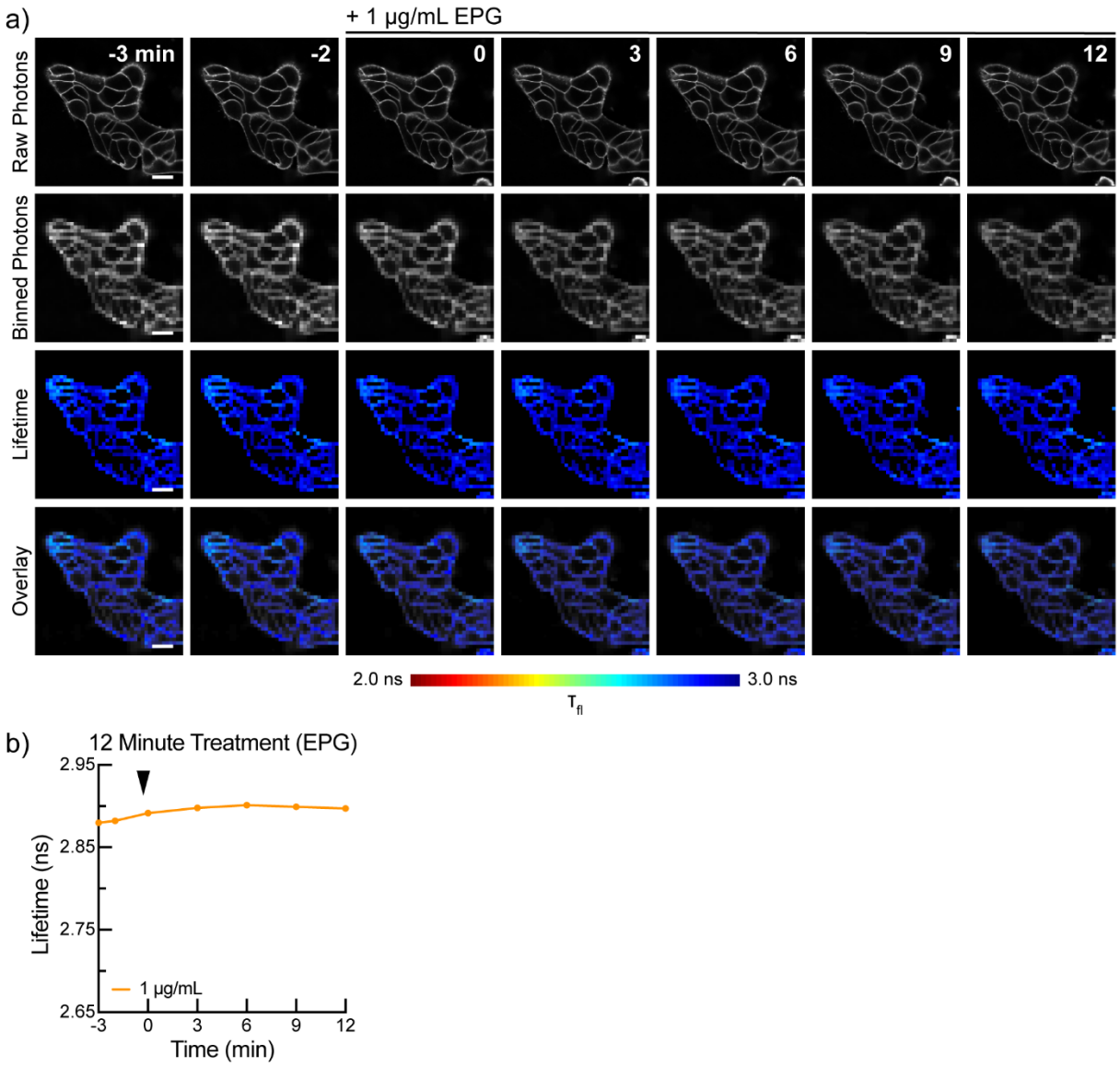


Figure 4.17. CRhOMe lifetime of MCF-7 cells following addition of 1 µg/mL EPG.
a) Representative raw photon intensity, binned photon intensity, lifetime, and intensity-lifetime overlay images of serum-starved MCF-7 cells loaded with 300 nM CRhOMe at all recorded time points during treatment with 1 µg/mL EPG. EPG was added just before the 0 minute time point. Scale bars are 20 µm. **b)** Quantification of CRhOMe lifetime images shown in **a)**. Arrow indicates EPG addition.

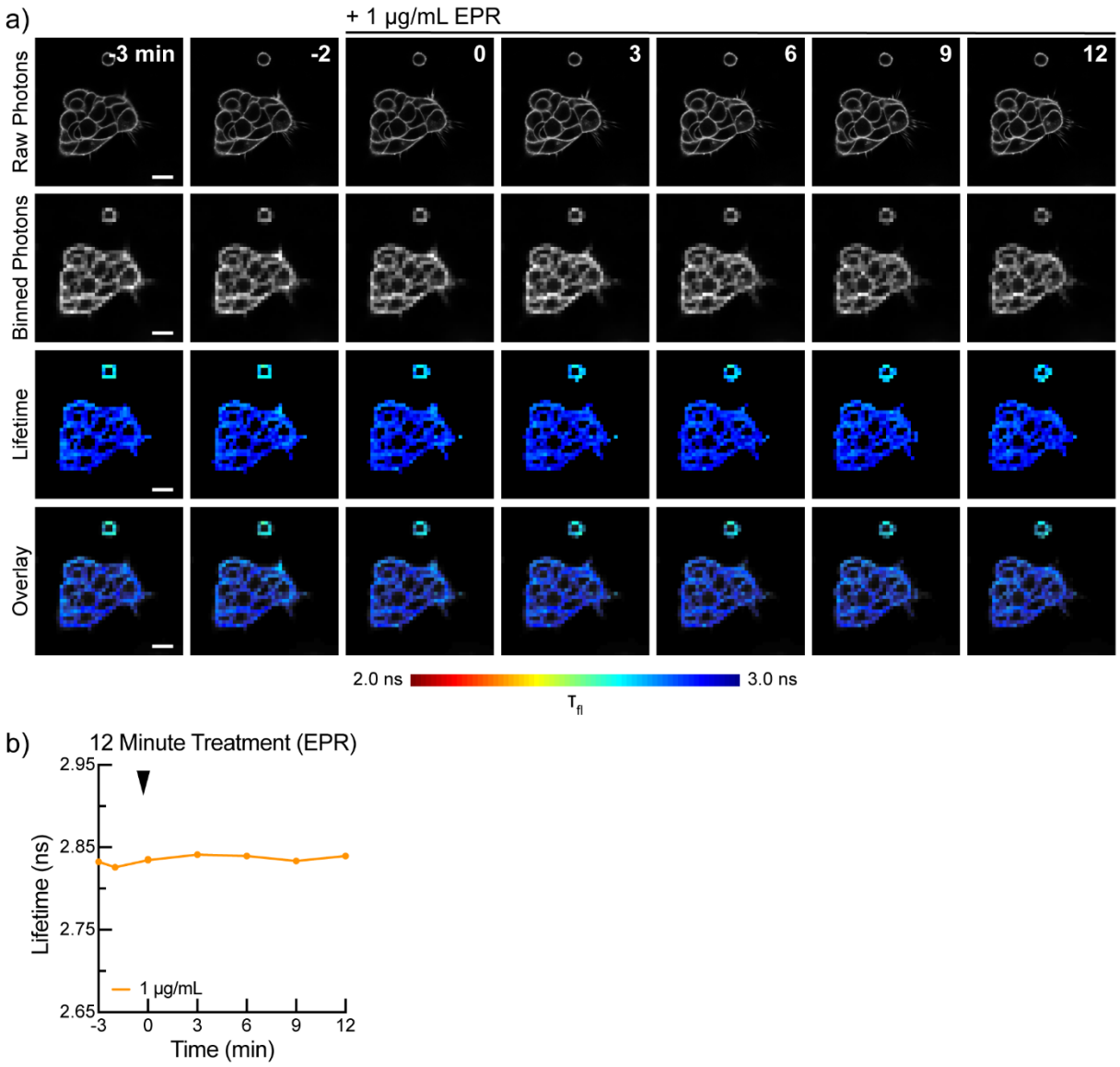


Figure 4.18. CRhOMe lifetime of MCF-7 cells following addition of 1 µg/mL EPR.
a) Representative raw photon intensity, binned photon intensity, lifetime, and intensity-lifetime overlay images of serum-starved MCF-7 cells loaded with 300 nM CRhOMe at all recorded time points during treatment with 1 µg/mL EPR. EPR was added just before the 0 minute time point. Scale bars are 20 µm. **b)** Quantification of CRhOMe lifetime images shown in **a)**. Arrow indicates EPR addition.

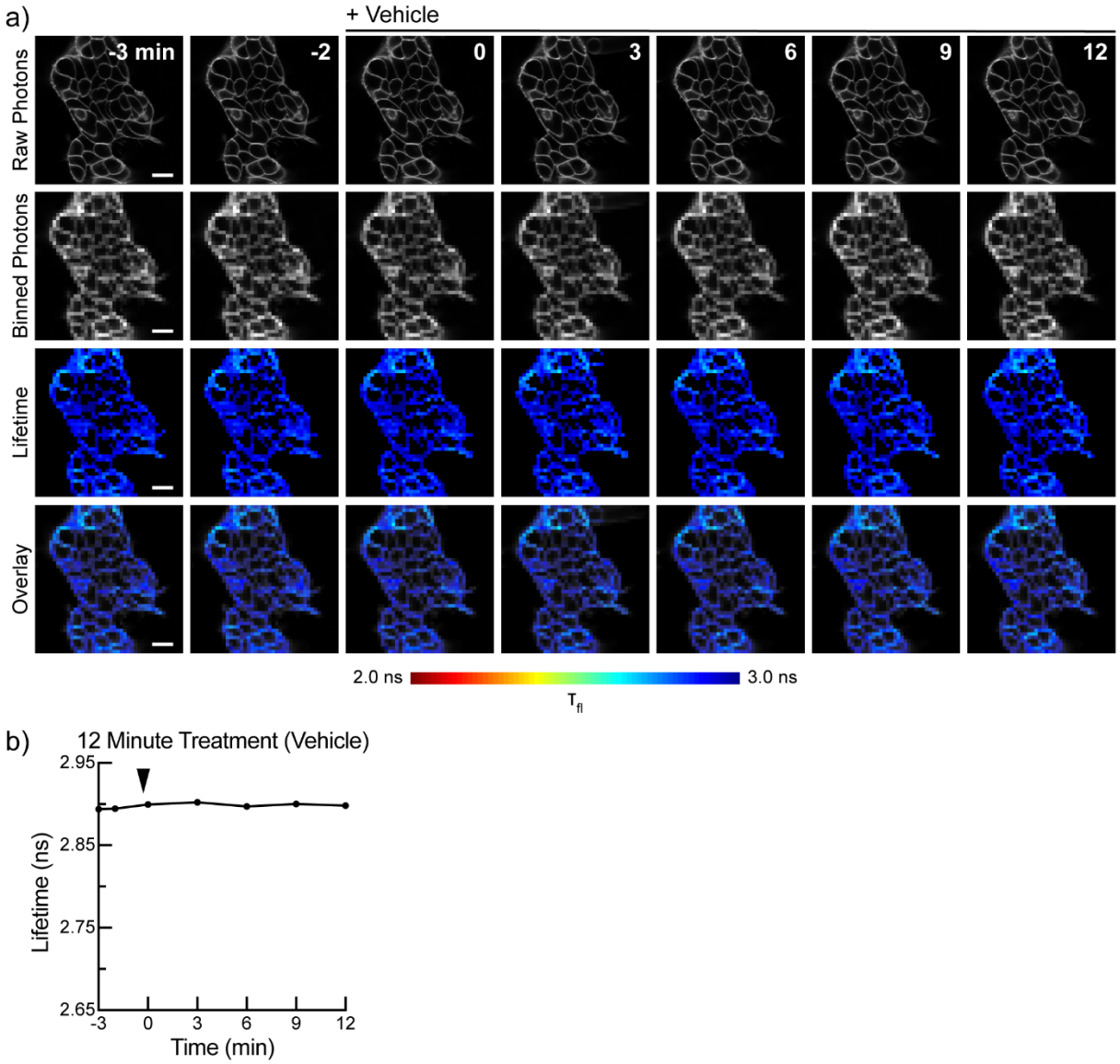


Figure 4.19. CRhOMe lifetime of MCF-7 cells following addition of imaging buffer vehicle.
a) Representative raw photon intensity, binned photon intensity, lifetime, and intensity-lifetime overlay images of serum-starved MCF-7 cells loaded with 300 nM CRhOMe at all recorded time points during treatment with imaging buffer vehicle. Vehicle was added just before the 0 minute time point. Scale bars are 20 μm. **b)** Quantification of CRhOMe lifetime images shown in **a)**. Arrow indicates vehicle addition.

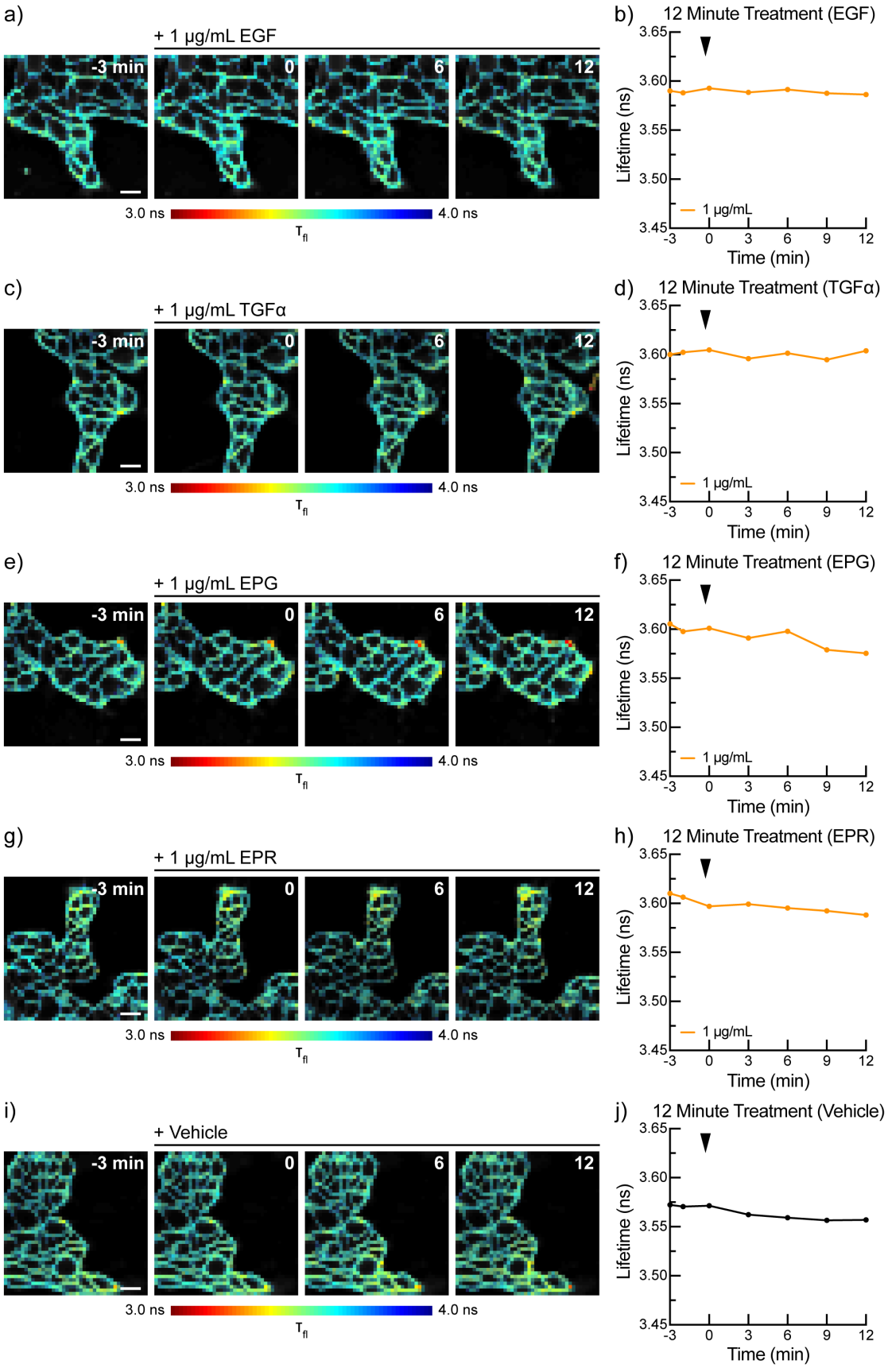

a)
+ 1 µg/mL EGF
-3 min
0
6
12
3.0 ns
4.0 ns
T_{fl}
b)
12 Minute Treatment (EGF)
Lifetime (ns)
Time (min)
1 µg/mL
c)
+ 1 µg/mL TGFα
d)
12 Minute Treatment (TGFα)
e)
+ 1 µg/mL EPG
f)
12 Minute Treatment (EPG)
g)
+ 1 µg/mL EPR
h)
12 Minute Treatment (EPR)
i)
+ Vehicle
j)
12 Minute Treatment (Vehicle)

Figure 4.20. CRhOMeZero lifetime of MCF-7 cells following addition of EGFR ligands or vehicle. Representative lifetime-intensity overlay images of serum-starved MCF-7 cells loaded with 300 nM CRhOMeZero at four different time points during treatment with **a)** 1 µg/mL EGF, **c)** 1 µg/mL TGFα, **e)** 1 µg/mL EPG, **g)**1 µg/mL EPR, or **i)** imaging buffer vehicle. Scale bars are 20 µm. Two baseline images were acquired 3 and 2 minutes before treatment started, and ligand or vehicle was added just before the 0 minute time point. Traces of CRhOMe lifetime in A431 cells over 12 minutes during treatment with **b)** EGF, **d)** TGFα, **f)** EPG, **h)** EPR, or **j)** vehicle. Arrow indicates ligand or vehicle addition.

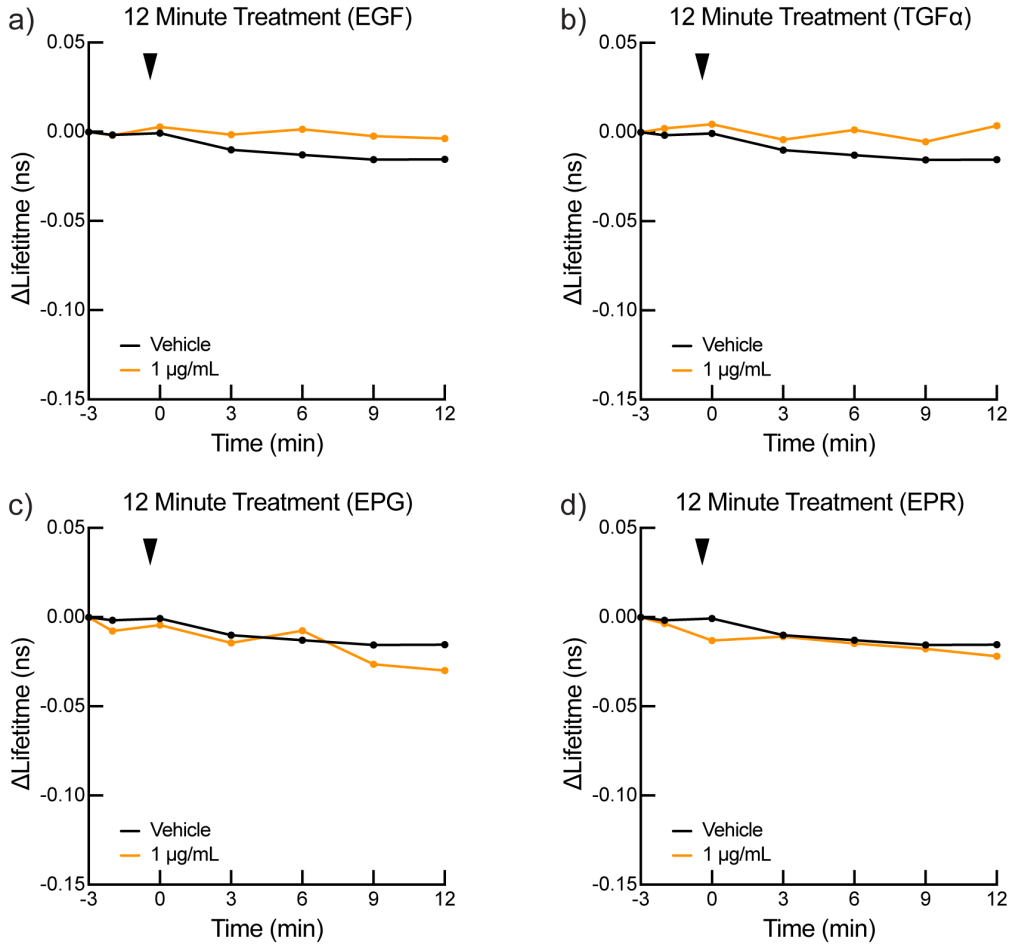


Figure 4.21. CRhOMeZero lifetime change in MCF-7 cells following addition of EGFR ligands or vehicle. CRhOMeZero lifetime change of serum-starved MCF-7 cells during treatment with different EGFR ligands over 12 minutes. Each recording consisted of a group of 10-20 cells. All traces are single recordings. Arrow indicates ligand or vehicle addition. **a)** Cells treated with imaging buffer vehicle (black) or 1 µg/mL EGF. **b)** Cells treated with imaging buffer vehicle (black) or 1 µg/mL TGFα (orange). **c)** Cells treated with imaging buffer vehicle (black) or 1 µg/mL EPG (orange). **d)** Cells treated with imaging buffer vehicle (black) or 1 µg/mL EPR (orange).

	ΔLifetime, 3 minutes (ps)				
Concentration	**EGF**	**TGFα**	**EPG**	**EPR**	**Vehicle**
1 µg/mL	-2	4	-14	-11	-10
	ΔLifetime, 6 minutes (ps)				
Concentration	**EGF**	**TGFα**	**EPG**	**EPR**	**Vehicle**
1 µg/mL	1	-4	-8	-15-	-13

Table 4.4. Average CRhOMeZero lifetime change in MCF-7 cells following addition of EGFR ligands. Average CRhOMeZero lifetime change of serum-starved MCF-7 cells 3 or 6 minutes after EGFR ligand or imaging buffer vehicle addition. Data are taken from corresponding time points in the 12 minute time series shown in **Figure 4.15**. All values reported are from single recordings.

Notably, the lifetime in MCF-7 cells generally increase in response to EGFR ligand addition, while the lifetime in A431 cells tends to decrease. In both cell lines, samples loaded with CRhOMeZero display a decrease in lifetime around 15 to 20 ps for most ligand concentrations (**Table 4.2, Table 4.4**). The opposite trends in lifetime may suggest that while EGFR stimulation causes a hyperpolarization in A431 cells, MCF-7 cells become slightly depolarized instead. This could be consistent with observations that EGFR ligands generally inhibit proliferation A431 cells,[9–11] while stimulating proliferation or differentiation in MCF-7 cells.[2] Previous work also indicated that the hyperpolarization observed with EGF in A431 cells is driven by K^+ efflux through $K_{Ca}3.1$ channels following the depletion of internal Ca^{2+} and triggering of SOCE.[13,21] Transcript levels of $K_{Ca}3.1$ are roughly four times lower in MCF-7 cells compared to A431 cells.[22] Therefore, if Ca^{2+} release is initiated in MCF-7 cells, the increase of intracellular Ca^{2+} without corresponding K^+ efflux could lead to mild depolarization.

Conclusion

This work presents characterization of distinct EGFR-mediated membrane potential dynamics between different ligands in A431 and MCF-7 cells. EGF and TGFα produce a similar marked decrease in resting lifetime in A431 cells, consistent with membrane hyperpolarization. Treatment with EPG and EPR shortens the lifetime to a much lesser extent, which may or may not be indicative of a significant change in membrane potential. In MCF-7 cells, stimulation with all four ligands generally resulted in a small but inconsistent increase in resting lifetime. This change is suggestive of a slight depolarization, however, additional experiments are necessary to more robustly characterize this response.

In future work, we intend to use patch-clamp electrophysiology to develop lifetime-voltage calibrations for both cell types to enable calculation of V_m. Additionally, ion channel blockers or siRNA knockdown could illustrate whether $K_{Ca}3.1$ or other ion channels are responsible for the observed changes in membrane potential across the different ligands evaluated. Further experiments could also be expanded to the other three EGFR ligands or different types of cells, particularly those with high EGFR expression levels.

Methods

A431 and MCF-7 Cell Culture

A431 and MCF-7 cells were obtained from the UC Berkeley Cell Culture Facility. Both cell lines were verified by STR profiling (short tandem repeat) and were tested routinely for mycoplasma. Cell lines were discarded after 25 passages. Cells were maintained and plated in Dulbecco's Modified Eagle Medium (DMEM; Gibco) supplemented with 4.5 g/L glucose, 2 mM GlutaMAX (Gibco), and 10% seradigm fetal bovine serum (FBS; Gibco) in a 37°C humidified incubator at 5% CO_2. Media for MCF-7 cells was supplemented with 1 mM sodium pyruvate (Gibco) and 1x non-essential amino acids (NEAA; Gibco). Cells were passaged into fresh complete media every few days following dissociation with 0.25% trypsin-EDTA (Gibco). Residual trypsin was removed by centrifugation for 5 minutes at 300xg before resuspension in fresh complete medium.

For imaging experiments, 25 mm #1.5 glass coverslips were pre-coated with poly-D-lysine (PDL) prior to plating cells. Coverslips were incubated in PDL (0.1 mg/mL in PBS; Sigma-Aldrich) for at least 1 hour in a 37°C humidified incubator and then washed twice with sterile water and twice with 1x Dulbecco's Phosphate Buffered Saline (dPBS; Gibco).

A431 and MCF-7 cells were serum deprived prior to use. Two days before imaging experiments, cells were trypsinized and quenched with complete medium with 10% FBS. The cells were then spun down for 5 minutes at 300xg and resuspended in low serum DMEM (4.5 g/L glucose, 2 mM GlutaMAX, 2% FBS). Cells were then plated onto PDL-coated glass coverslips at a density of 83,000 cells/cm^2 (A431) or 63,000 cells/cm^2 (MCF-7) in the low serum DMEM. 4-6 hours prior to imaging, media was exchanged for serum-free DMEM (4.5 g/L glucose, 2 mM GlutaMAX). Cells were loaded with dye after 4-6 hours in the serum-free media.

For some experiments, MCF-7 cells were also plated in full serum DMEM (4.5 g/L glucose, 2 mM GlutaMAX, 10% FBS, 1 mM sodium pyruvate, 1x NEAA). These cells were plated at the same time (2 days prior to imaging) at a density of 63,000 cells/cm^2, and they were not media changed prior to imaging.

VoltageFluor Loading

CRhOMe or CRhOMeZero was loaded at 300 nM in A431 and MCF-7 cells, after 4-6 hours in serum-free media. Loading solutions were prepared in imaging buffer (IB, made in-house; composition in mM: 139.5 NaCl, 10 HEPES, 5.6 D-glucose, 5.33 KCl, 1.26 $CaCl_2$, 0.49 $MgCl_2$, 0.44 KH_2PO_4, 0.41 $MgSO_4$, 0.34 NaH_2PO_4; 285 mOsm/L; pH 7.25) directly from a 1 mM DMSO stock. Osmolarity was determined with a μOsmette (Precision Instruments). Cells were incubated at 37°C for 25 minutes in loading solution, washed once with IB, and transferred to fresh IB in an Attofluor cell imaging chamber (Invitrogen).

EGFR Ligand Treatment and Time Series

Recombinantly expressed epidermal growth factor (EGF; PeproTech), epigen (EPG; Thermo Fisher), and epiregulin (EPR; Thermo Fisher) were made up as 1 mg/mL solutions in water and stored at -80°C. Recombinantly expressed transforming growth factor α (TGFα; Thermo Fisher) was made up as a 0.2 mg/mL solution in water and stored at -80°C.

On the day of imaging, 2x solutions of each ligand concentration were prepared in IB. Each solution was prepared at the same time the corresponding coverslip was loaded with dye. Ligand solutions (or IB vehicle) were then placed in the microscope incubation chamber and warmed to 25°C for 25-30 minutes before use. After dye loading was complete, cells were transferred to the microscope. In general, 2-3 control images were first acquired at different fields of view on each coverslip. A new field of view was then selected for imaging during EGFR treatment.

For the 12 minute time series, two initial 60 second recordings were acquired (represented as -3 and -2 minute time points on graphs). Approximately 45 seconds after the second recording, 500 µL of the pre-warmed 2x ligand solution or IB vehicle was gently pipetted into the imaging chamber. The imaging chamber already contained 500 µL of IB to bring the solution to the intended final concentration of ligand. Immediately after adding the solution, a 60 second acquisition was started, marking the 0 minute time point. Five more sequential 60 second recordings were made every 3 minutes, with a 2 minute gap without laser illumination between each acquisition. Time points given throughout the text correspond to the start of an exposure.

For the 6 minute time series, one initial 60 second recording was acquired as the 0 minute time point. Immediately after acquisition, the ligand solution or IB was added to the imaging chamber as described above, and a timer was started. Additional FLIM recordings were made 3 minutes and 6 minutes after ligand addition, with a 2 minute gap without laser illumination in between.

Fluorescence Lifetime Data Acquisition

Fluorescence lifetime imaging was performed on an inverted LSM 980 confocal microscope (Zeiss) equipped with a SPC-150NX single photon counting card (Becker and Hickl). The LSM 980 was controlled with Zen Blue software (Zeiss), and the TCSPC unit was controlled with SPCM software (Becker-Hickl). Pulsed excitation at 50 MHz was supplied with a 640 nm diode laser (BDS-SM-640-FBC-101, Becker-Hickl) and controlled through a LHB-104 Laser Hub (Becker-Hickl). Power was adjusted with a neutral density filter wheel to maximize count rate without exceeding pile-up limit. Average power at the sample ranged from 1-3 µW. Excitation light was coupled to the microscope with a polarization-maintaining fiber and passed through a 405/485/560/640 beam splitter (Zeiss). Emitted photons were collected with a 40x oil/1.3 NA Apochromat objective (Zeiss), immersed in Immersol 518F (Zeiss). The confocal pinhole was set to 35 µm (1 airy unit). The emitted photons were passed through a 676/37 bandpass filter (Semrock) and detected with an HPM-100-40 hybrid detector (Becker-Hickl), based on a Hamamatsu R10467 GaAsP hybrid photomultiplier tube. Detector dark counts were kept below 300 per second during acquisition and were generally lower than 200 per second. The detector parameters used were the following: constant fraction discriminator (CFD) -50.98 mV, zero cross 5.29 mV. Sync parameters used were the following: CFD -50.98 mV, zero cross 5.29 mV, offset 5.10 %, sync divider 1, dither range 1/16. Data acquired with 256 time channels in the analog-to-digital-converter (ADC) and 256x256 pixels of spatial resolution during 60 second exposures. The instrument response function (IRF) was measured each day from a solution of 1 mg/mL erythrosin B in water. The TMCRh dye head (1 µM in water) was also routinely recorded as a standard to verify correct instrument function and fitting parameters. The microscope incubation chamber was set to 25°C to minimize temperature fluctuations during experiments and between days. Cells were used immediately after loading CRhOMe and were generally kept on the microscope for under 30 minutes. No cells were kept for on the microscope for longer than an hour.

Fluorescence Lifetime Data Analysis

CRhOMe and CRhOMeZero lifetime data were modeled as monoexponential decays (**Equation 1**) in custom MATLAB code via a weighted least-squares approach. In this equation, A represents the amplitude of the photon count signal and τ represents the fluorescence lifetime.

$$F(t) = Ae^{-t/\tau} \quad (1)$$

Minimization of the reduced chi squared (χ^2, **Equation 2**) was used to determine the final parameter values, where n is the number of free parameters (number of fit time channels – number of free parameters in model), st is the first fit time channel, fi is the final fit time channel, z is the value of the fit model, and x is the value of the experimentally measured decay. Poisson weighting of the time channels was used.

$$\chi^2 = \frac{1}{n}\sum_{i=st}^{fi}\frac{(z_i - x_i)^2}{|z|} \quad (2)$$

The built-in minimization function fmincon with the interior-point algorithm was used, with the following settings: StepTolerance 1e-4, OptimalityTolerance 1e-4, ConstraintTolerance 1e-6. All fits converged in fewer than the maximum number of function evaluations (1e5). The fluorescence lifetime τ was constrained between 0 and 10 ns. The experimentally measured instrument response function (IRF, erythrosin B fluorescence decay) was cropped to time channels 36 to 50 out of 256 ADC channels and reconvolved with the decay model before the reduced chi squared was determined. Time channels 20 through 256 of the measured time resolved decays were used in fitting. The shift between the IRF and the measured time resolved decays was fixed to -0.3 (in units of ADC time channels). The offset (time-independent background) was fixed to 0, as the dark counts were generally negligible (below 200 counts per second during experiments). A threshold of 5000 total photons was used in pixelwise analysis. Pixels with photon counts below this threshold were excluded from analysis and appear black in lifetime images. Standard spatial binning was performed before fitting for pixel-by-pixel analysis. The raw pixel width was 0.55 μm, and pixels were binned 6x6, resulting in a binned pixel width of 3.3 μm. Raw photon intensity images are displayed at the native resolution, while binned photon, lifetime, and lifetime-intensity overlay images reflect spatial binning.

Regions of interest (ROIs) were automatically determined from raw photon intensity images by sharpening and then thresholding the signal intensity with custom MATLAB code. Regions of images that were partially out of the optical section or contained punctate debris were omitted. In general, there was one large ROI per image consisting of a group of 20-40 cells (A431) or 10-30 cells (MCF-7). The τ across all pixels in each ROI was averaged to give one mean lifetime per ROI/image. For ΔLifetime graphs and EC_{50} determination, the lifetime change at each time point was calculated from the difference between the initial image (-3 minute time point for 12 minute time series, 0 minute time point for 6 minute time series) and the image acquired at the indicated time point.

TGFα EC_{50} Determination

The average lifetime changes 3 and 6 minutes after TGFα addition were calculated for each concentration tested in A431 cells (3 replicates per concentration). These means were fit to a four parameter logistic function in Prism 10 (GraphPad) to calculate the EC_{50} values for 3 and 6 minutes of TGFα treatment.

Statistical Analysis

Hypothesis testing was performed as indicated with either analysis of variance (ANOVA) followed by appropriate post hoc testing or two-sided, unpaired, unequal variances t-tests. All statistical analysis was performed in Prism 10 (GraphPad).

Supporting Figures and Tables

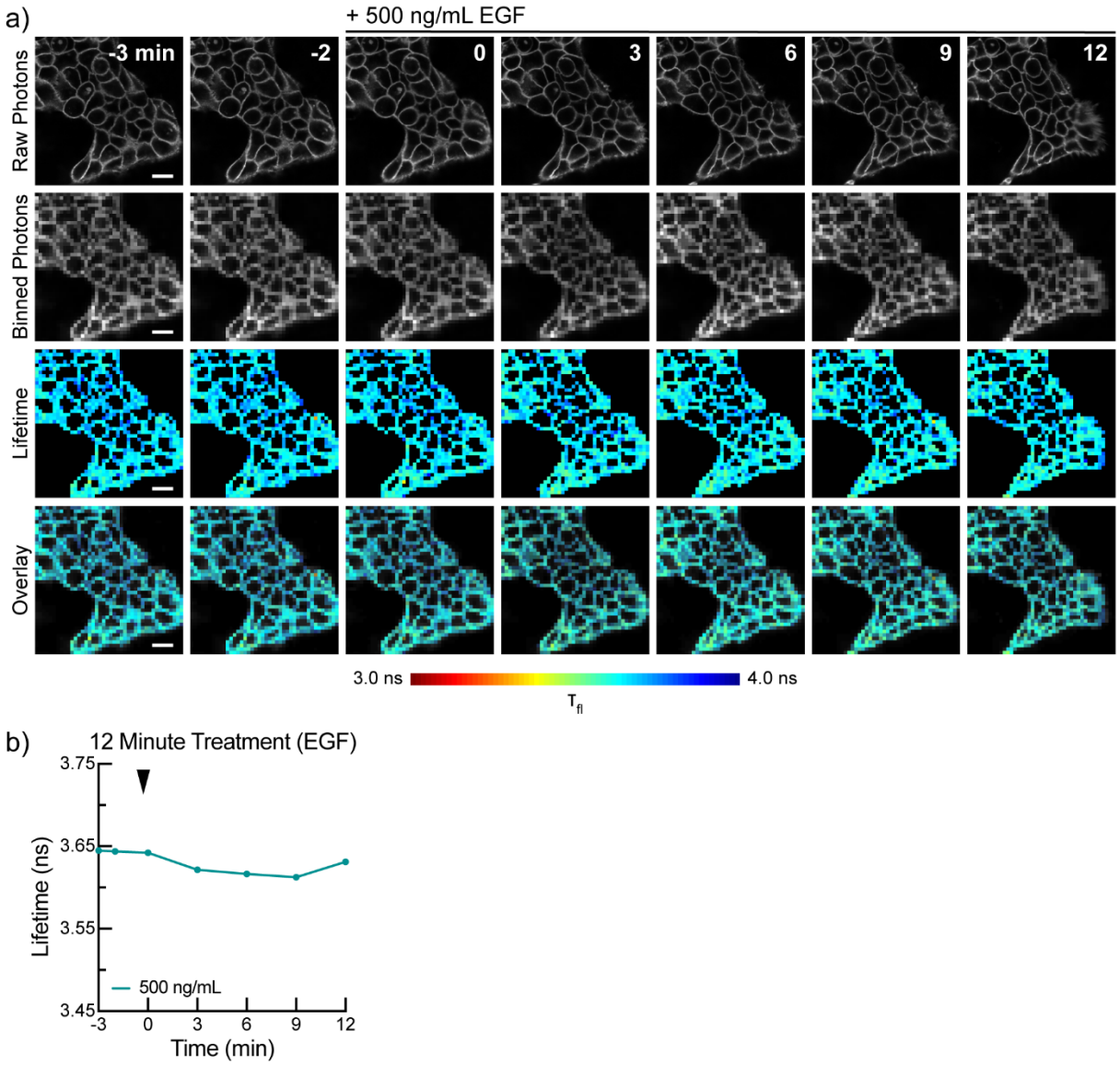


Figure S4.1. CRhOMeZero lifetime of A431 cells following addition of 1 µg/mL EGF.
a) Representative raw photon intensity, binned photon intensity, lifetime, and intensity-lifetime overlay images of serum-starved A431 cells loaded with 300 nM CRhOMe at all recorded time points during treatment with 1 µg/mL EGF. Vehicle was added just before the 0 minute time point. Scale bars are 20 µm. **b)** Quantification of CRhOMe lifetime images shown in **a)**. Arrow indicates EGF addition.

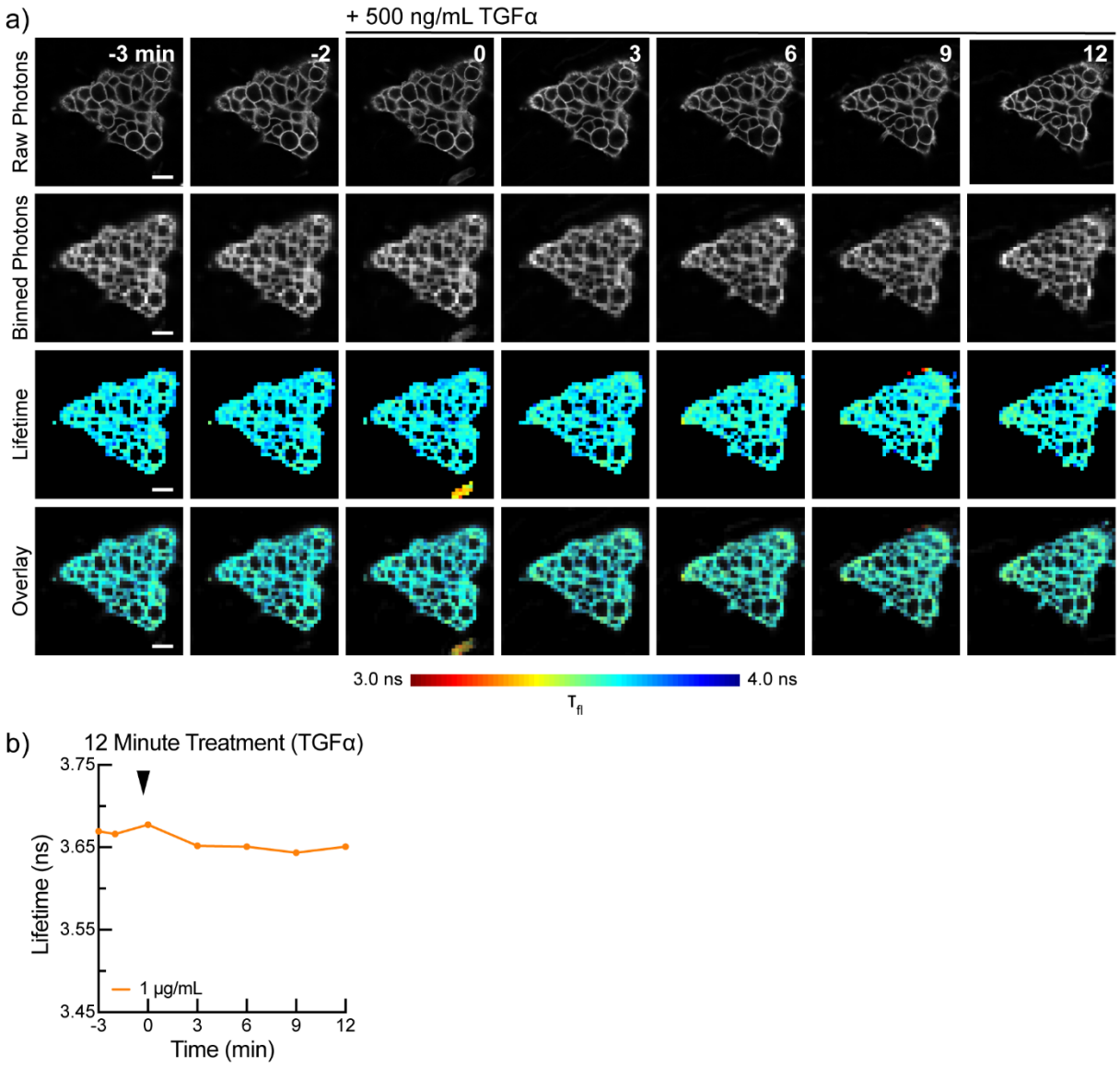


Figure S4.2. CRhOMeZero lifetime of A431 cells following addition of 1 µg/mL TGFα.
a) Representative raw photon intensity, binned photon intensity, lifetime, and intensity-lifetime overlay images of serum-starved A431 cells loaded with 300 nM CRhOMe at all recorded time points during treatment with 500 ng/mL TGFα. Vehicle was added just before the 0 minute time point. Scale bars are 20 µm. **b)** Quantification of CRhOMe lifetime images shown in **a)**. Arrow indicates TGFα addition.

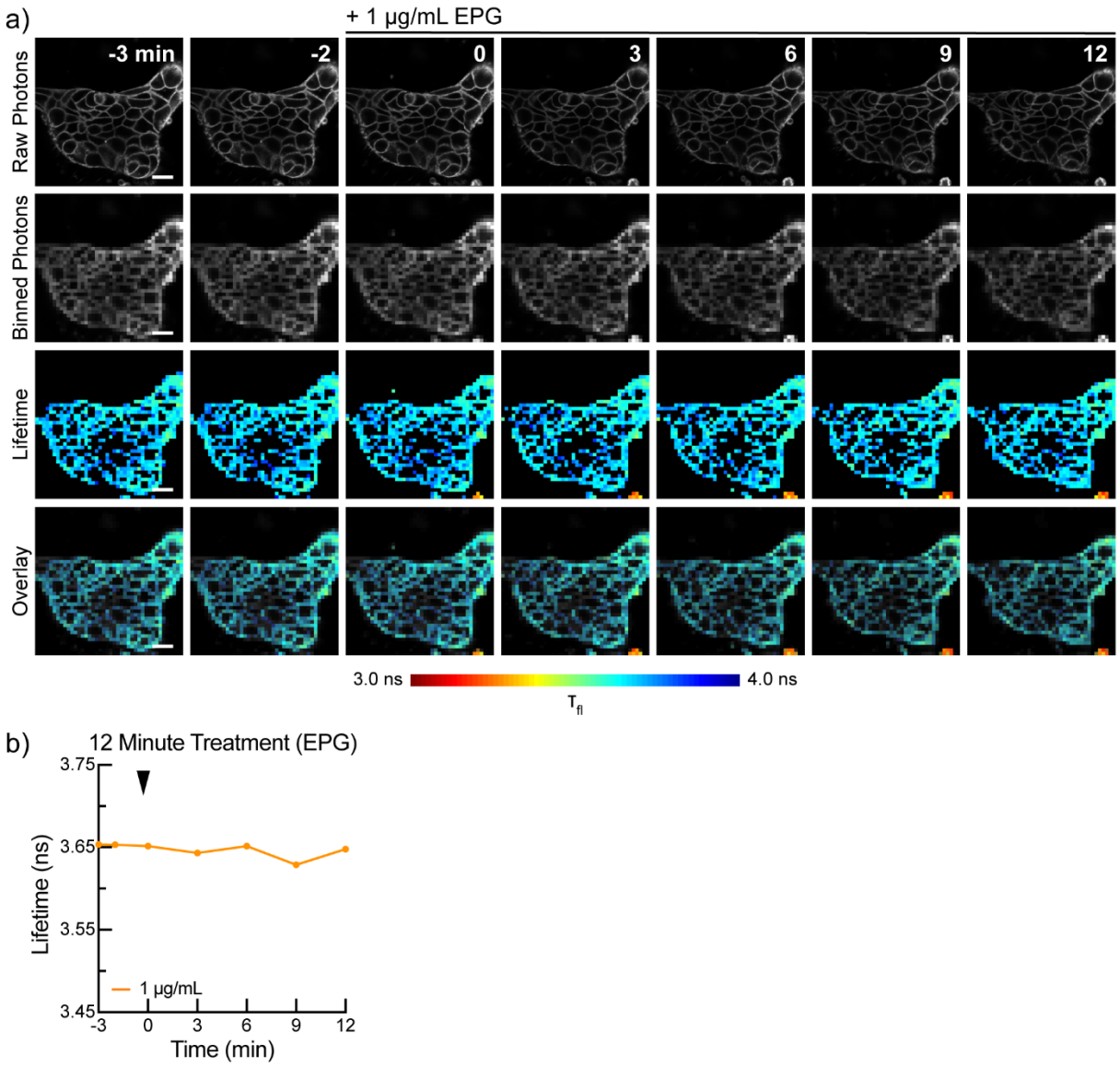


Figure S4.3. CRhOMeZero lifetime of A431 cells following addition of 1 µg/mL EPG.
a) Representative raw photon intensity, binned photon intensity, lifetime, and intensity-lifetime overlay images of serum-starved A431 cells loaded with 300 nM CRhOMe at all recorded time points during treatment with 1 µg/mL EPG. Vehicle was added just before the 0 minute time point. Scale bars are 20 µm. **b)** Quantification of CRhOMe lifetime images shown in **a)**. Arrow indicates EPG addition.

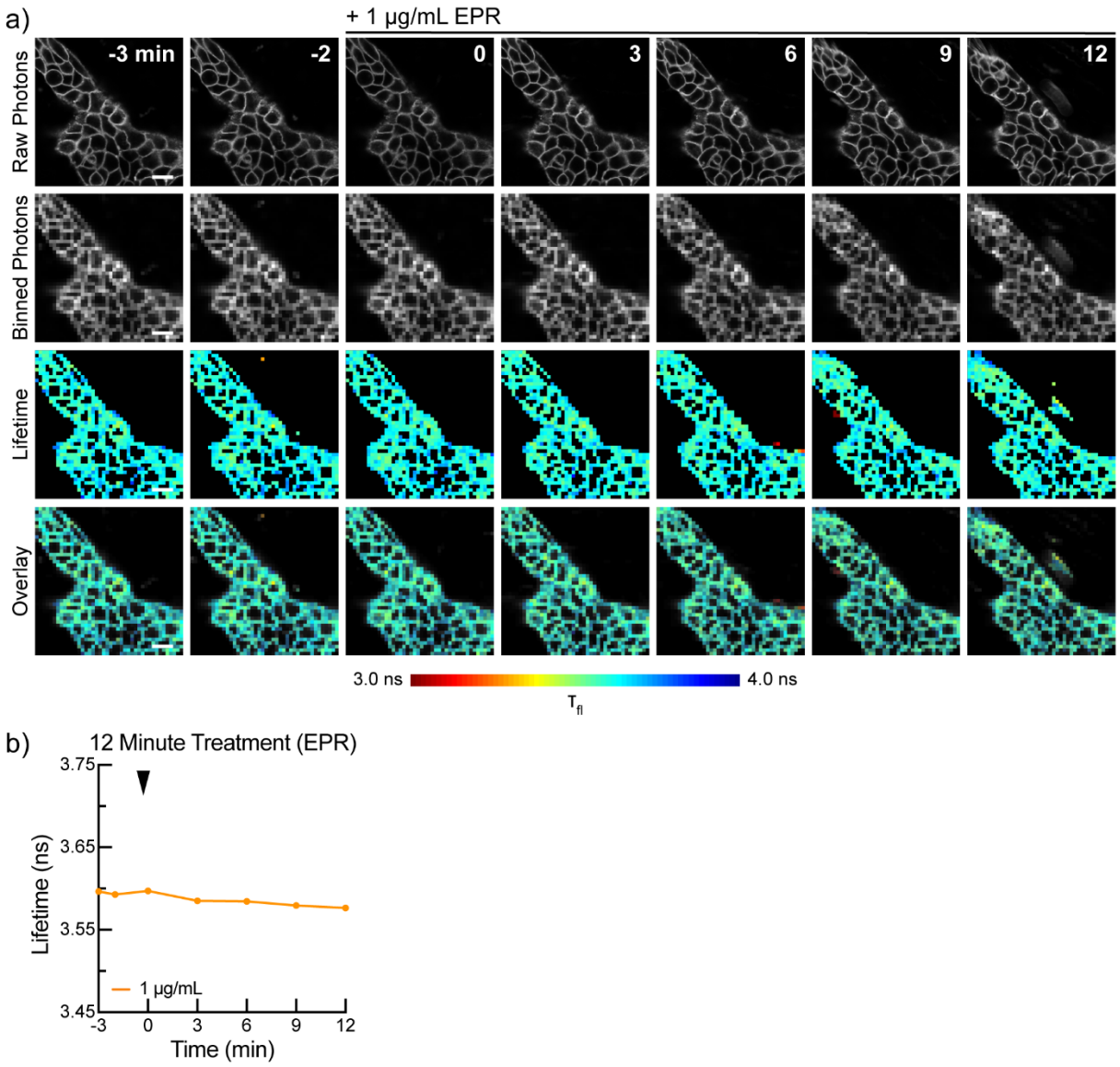


Figure S4.4. CRhOMeZero lifetime of A431 cells following addition of 1 µg/mL EPR.
a) Representative raw photon intensity, binned photon intensity, lifetime, and intensity-lifetime overlay images of serum-starved A431 cells loaded with 300 nM CRhOMe at all recorded time points during treatment with 1 µg/mL EPR. Vehicle was added just before the 0 minute time point. Scale bars are 20 µm. **b)** Quantification of CRhOMe lifetime images shown in **a)**. Arrow indicates EPR addition.

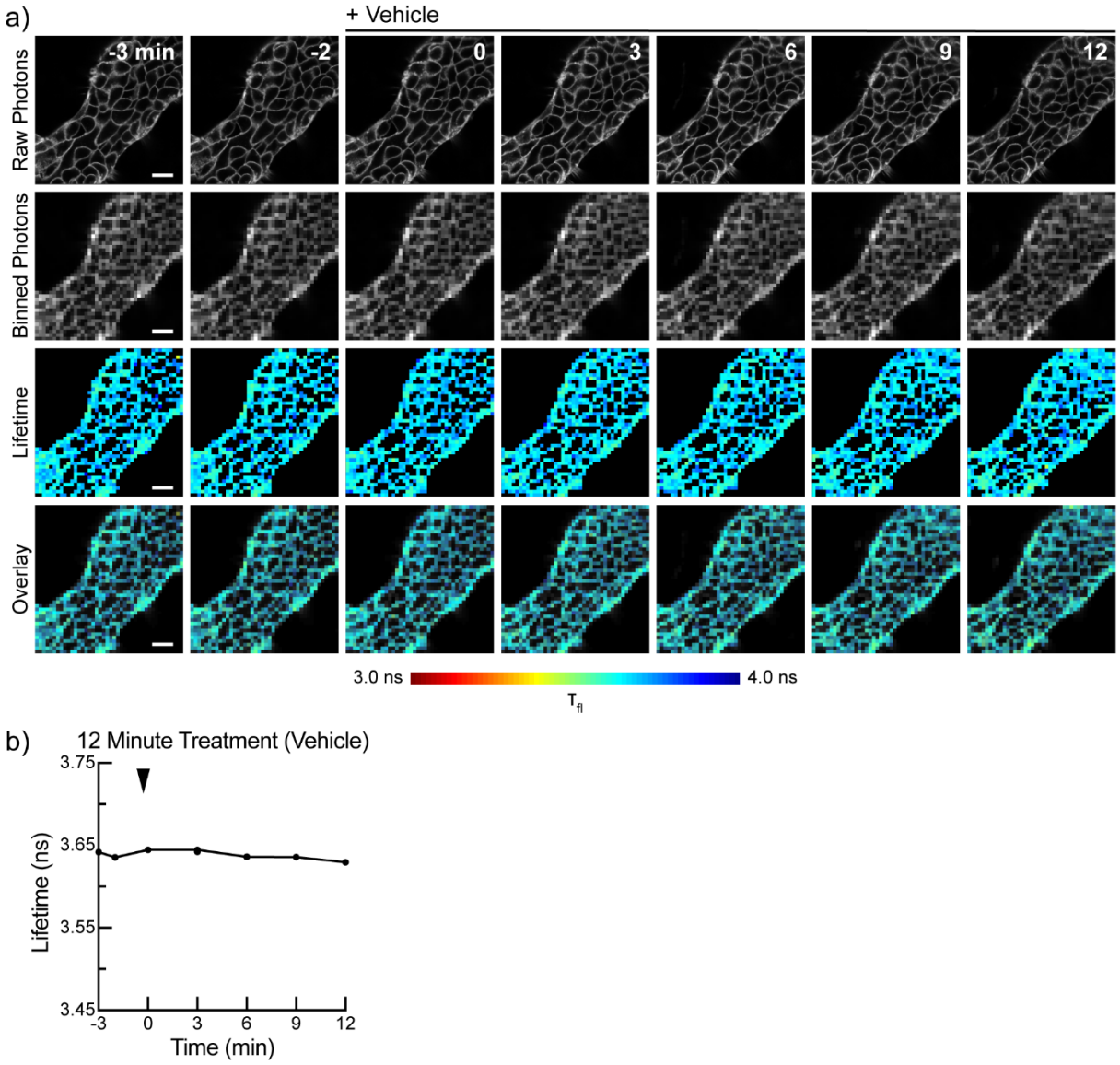


Figure S4.5. CRhOMeZero lifetime of A431 cells following addition of imaging buffer vehicle.
a) Representative raw photon intensity, binned photon intensity, lifetime, and intensity-lifetime overlay images of serum-starved A431 cells loaded with 300 nM CRhOMe at all recorded time points during treatment with imaging buffer vehicle. Vehicle was added just before the 0 minute time point. Scale bars are 20 μm. **b)** Quantification of CRhOMe lifetime images shown in **a)**. Arrow indicates vehicle addition.

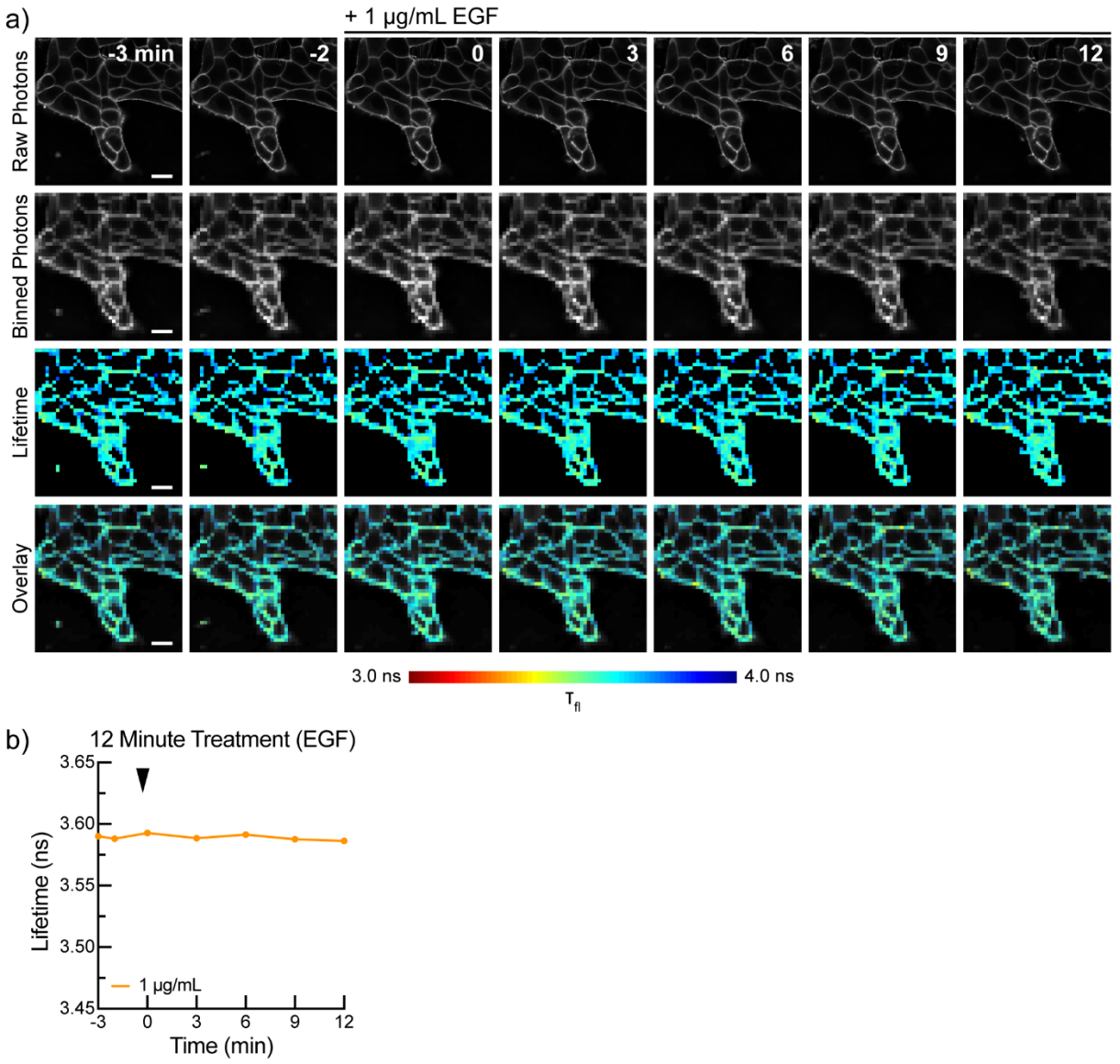


Figure S4.6. CRhOMeZero lifetime of MCF-7 cells following addition of 1 µg/mL EGF.
a) Representative raw photon intensity, binned photon intensity, lifetime, and intensity-lifetime overlay images of serum-starved MCF-7 cells loaded with 300 nM CRhOMe at all recorded time points during treatment with 1 µg/mL EGF. EGF was added just before the 0 minute time point. Scale bars are 20 µm. **b)** Quantification of CRhOMeZero lifetime images shown in **a)**. Arrow indicates EGF addition.

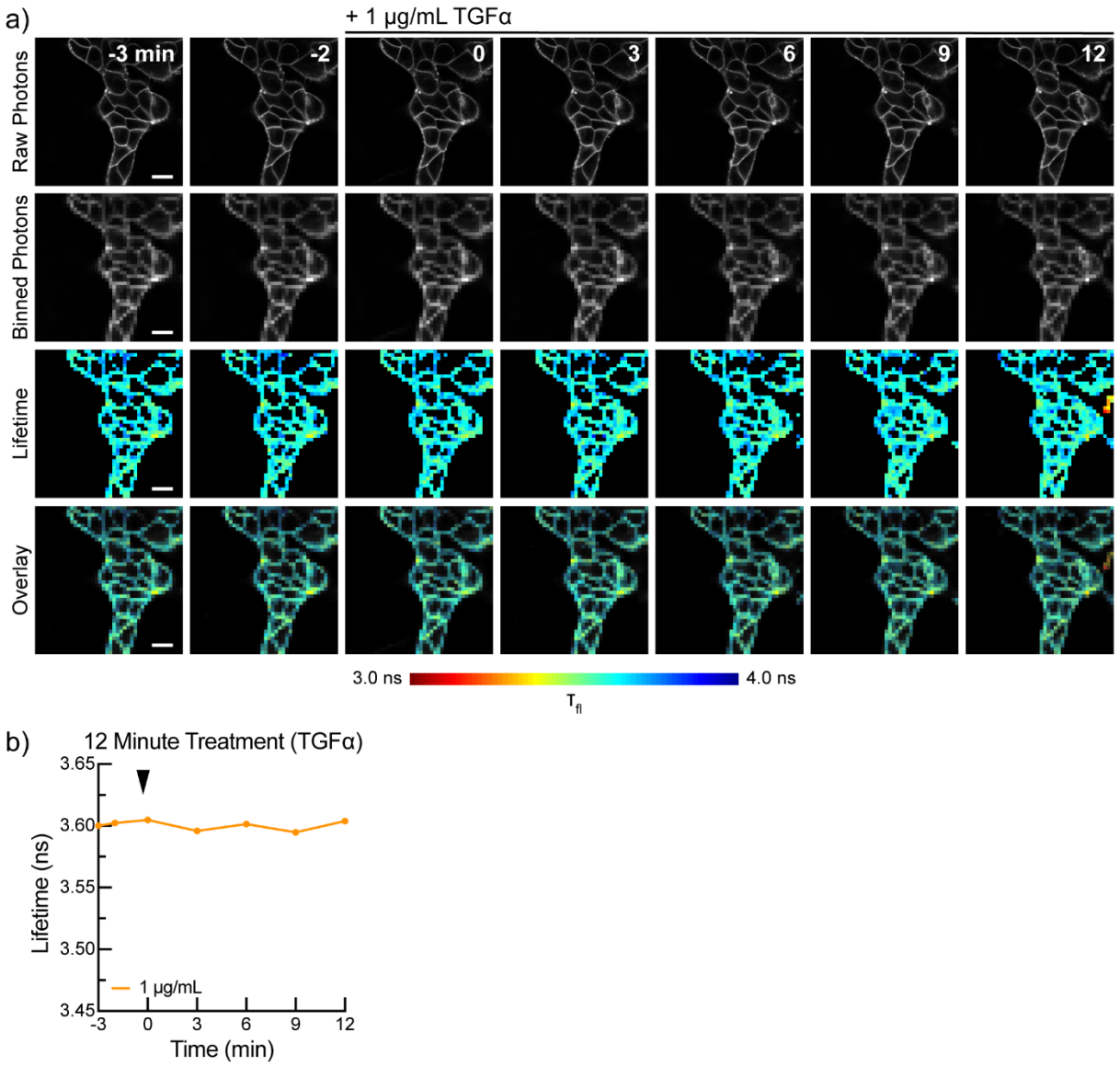


Figure S4.7. CRhOMeZero lifetime of MCF-7 cells following addition of 1 µg/mL TGFα.
a) Representative raw photon intensity, binned photon intensity, lifetime, and intensity-lifetime overlay images of serum-starved MCF-7 cells loaded with 300 nM CRhOMe at all recorded time points during treatment with 1 µg/mL TGFα. TGFα was added just before the 0 minute time point. Scale bars are 20 µm. **b)** Quantification of CRhOMeZero lifetime images shown in **a)**. Arrow indicates TGFα addition.

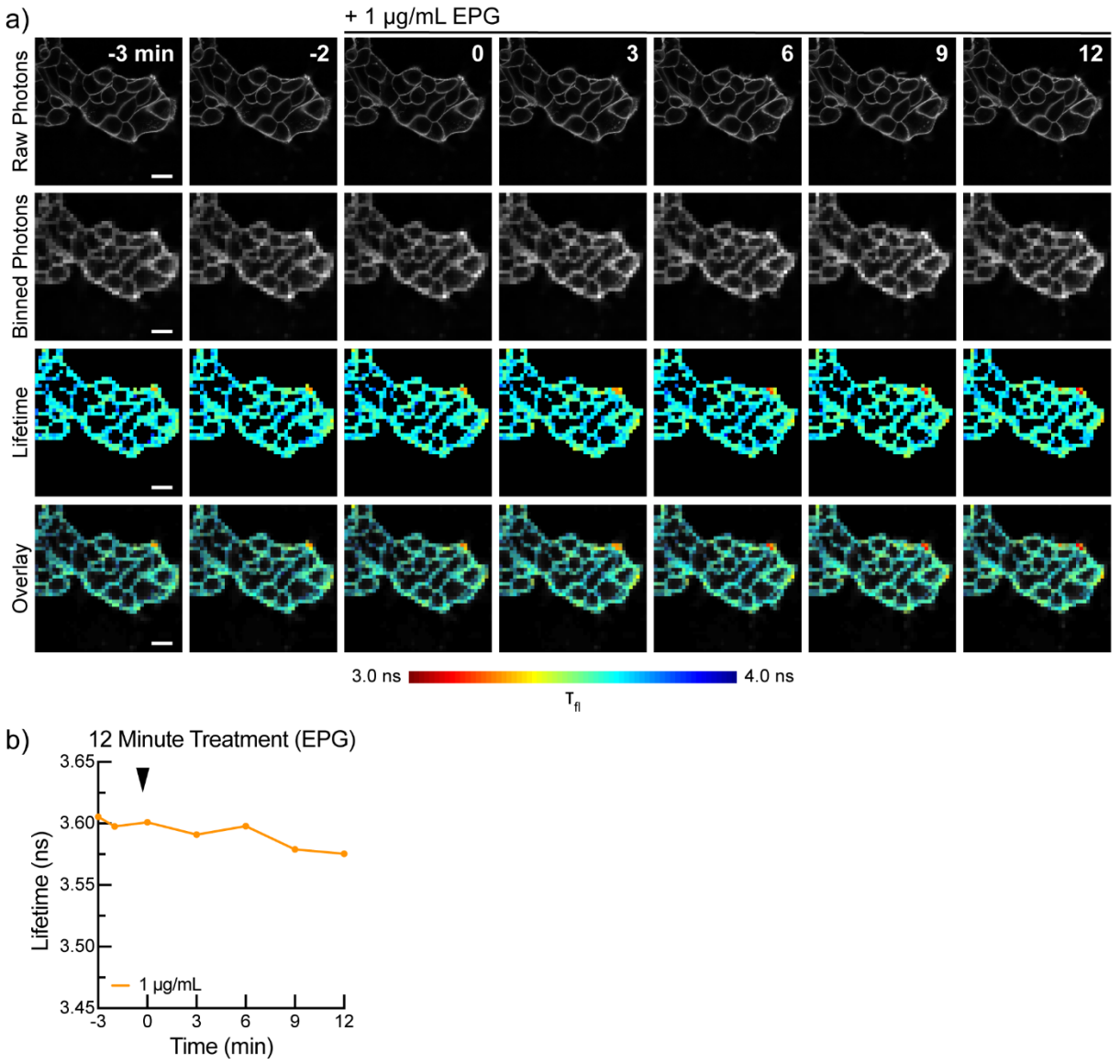


Figure S4.8. CRhOMeZero lifetime of MCF-7 cells following addition of 1 µg/mL EPG.
a) Representative raw photon intensity, binned photon intensity, lifetime, and intensity-lifetime overlay images of serum-starved MCF-7 cells loaded with 300 nM CRhOMe at all recorded time points during treatment with 1 µg/mL EPG. EPG was added just before the 0 minute time point. Scale bars are 20 µm. **b)** Quantification of CRhOMeZero lifetime images shown in **a)**. Arrow indicates EPG addition.

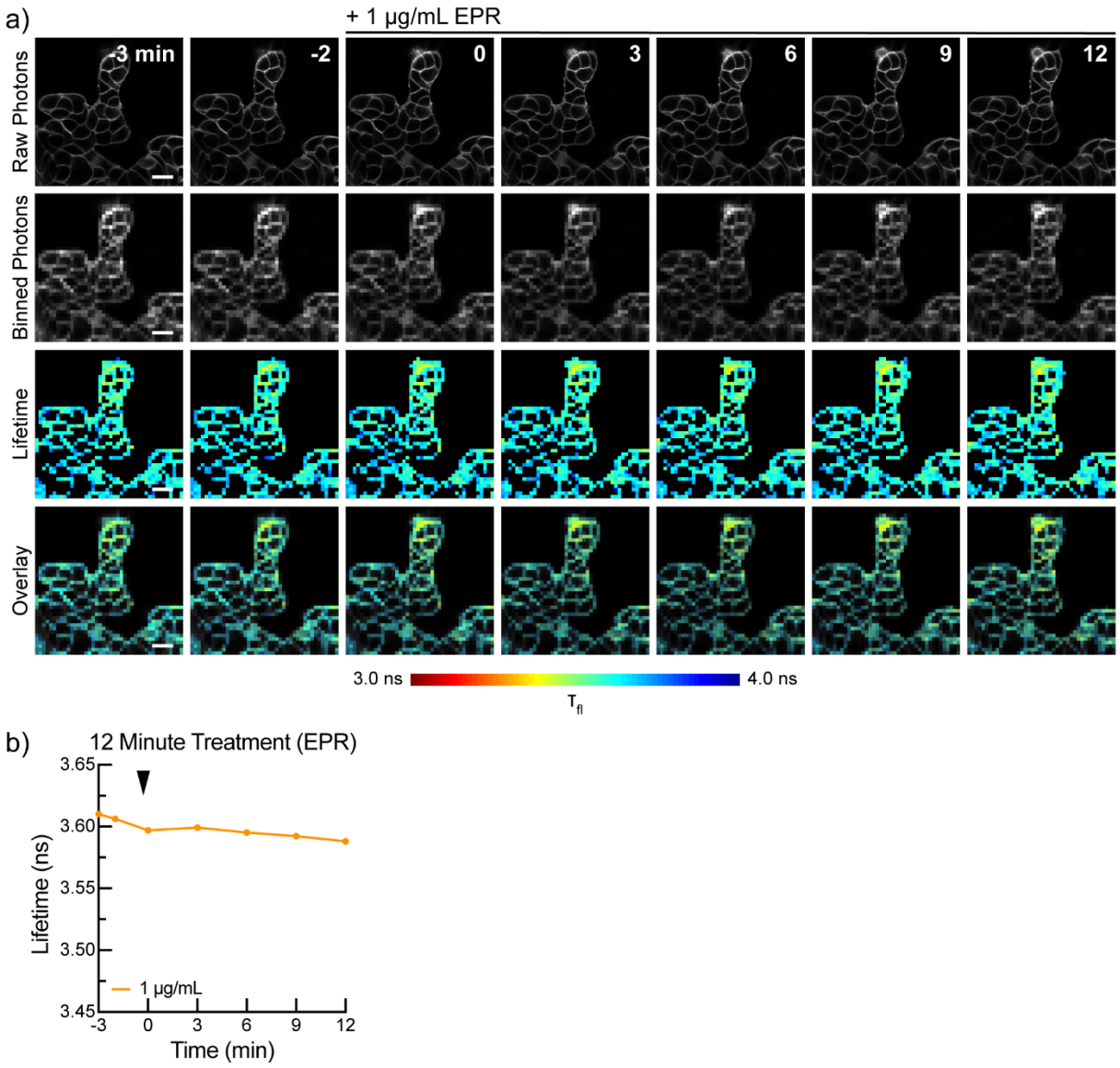


Figure S4.9. CRhOMeZero lifetime of MCF-7 cells following addition of 1 µg/mL EPR.
a) Representative raw photon intensity, binned photon intensity, lifetime, and intensity-lifetime overlay images of serum-starved MCF-7 cells loaded with 300 nM CRhOMe at all recorded time points during treatment with 1 µg/mL EPR. EPR was added just before the 0 minute time point. Scale bars are 20 µm. **b)** Quantification of CRhOMeZero lifetime images shown in **a)**. Arrow indicates EPR addition.

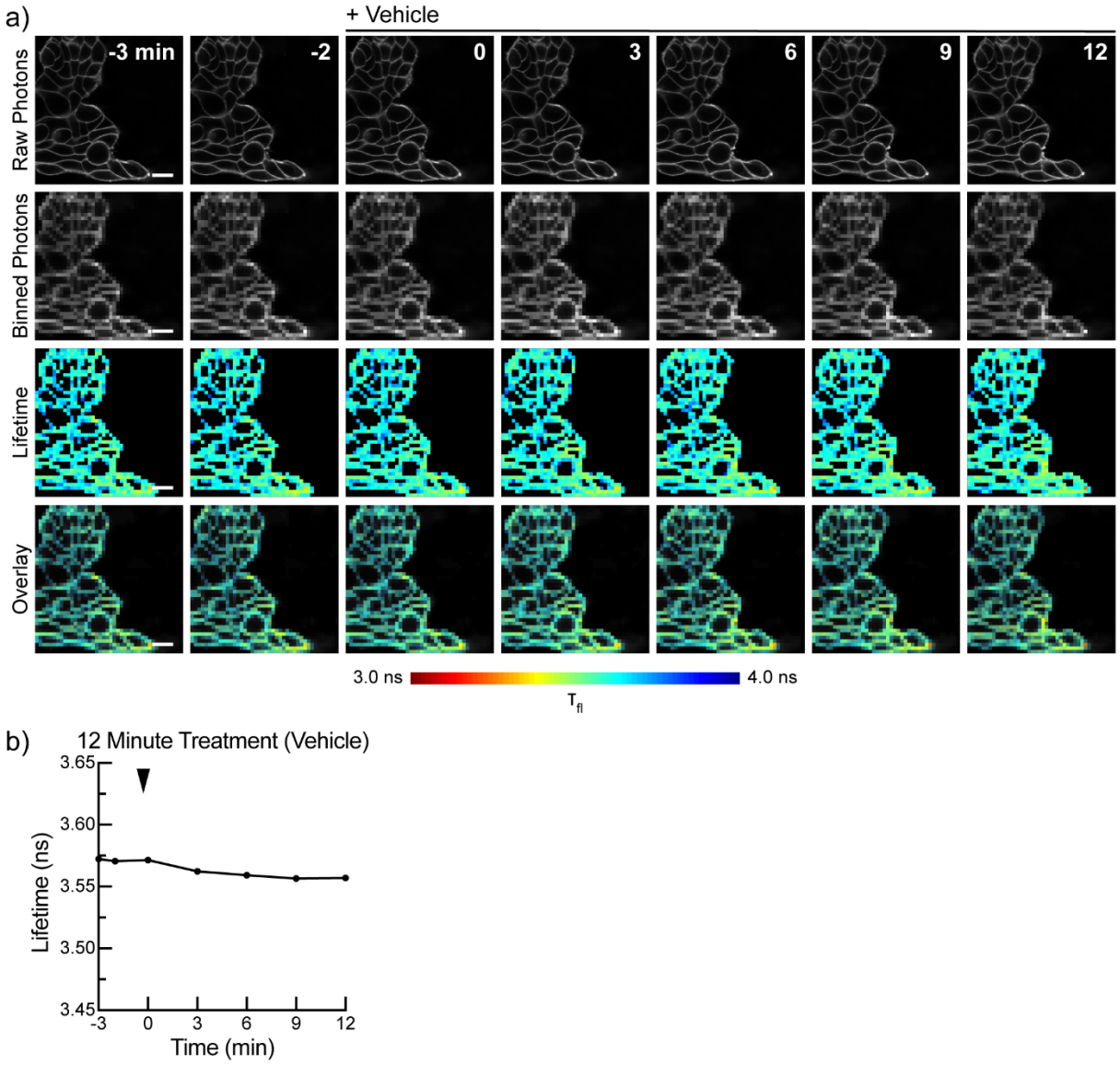


Figure S4.10. CRhOMeZero lifetime of MCF-7 cells following addition of imaging buffer vehicle.
a) Representative raw photon intensity, binned photon intensity, lifetime, and intensity-lifetime overlay images of serum-starved MCF-7 cells loaded with 300 nM CRhOMe at all recorded time points during treatment with imaging buffer vehicle. Vehicle was added just before the 0 minute time point. Scale bars are 20 μm. **b)** Quantification of CRhOMeZero lifetime images shown in **a)**. Arrow indicates vehicle addition.

	Concentration (nM)			
Concentration	**EGF**	**TGFα**	**EPG**	**EPR**
100 ng/mL	16.1	18.0	—	—
200 ng/mL	—	36.1	—	—
500 ng/mL	80.6	90.2	63.3	89.3
1 µg/mL	161.3	180.3	126.6	178.6
2 µg/mL	322.6	360.6	253.2	357.1
5 µg/mL	—	—	632.9	892.9

Table S4.1. Concentrations of EGFR ligands.
Concentrations in molar units and ng/mL of EGFR ligands epidermal growth factor (EGF), transforming growth factor α (TGFα), epigen (EPG), and epiregulin (EPR).

References

(1) Lemmon, M. A.; Schlessinger, J. Cell Signaling by Receptor Tyrosine Kinases. *Cell* **2010**, *141* (7), 1117–1134. https://doi.org/10.1016/j.cell.2010.06.011.

(2) Freed, D. M.; Bessman, N. J.; Kiyatkin, A.; Salazar-Cavazos, E.; Byrne, P. O.; Moore, J. O.; Valley, C. C.; Ferguson, K. M.; Leahy, D. J.; Lidke, D. S.; Lemmon, M. A. EGFR Ligands Differentially Stabilize Receptor Dimers to Specify Signaling Kinetics. *Cell* **2017**, *171* (3), 683-695.e18. https://doi.org/10.1016/j.cell.2017.09.017.

(3) Sanders, J. M.; Wampole, M. E.; Thakur, M. L.; Wickstrom, E. Molecular Determinants of Epidermal Growth Factor Binding: A Molecular Dynamics Study. *PLOS ONE* **2013**, *8* (1), e54136. https://doi.org/10.1371/journal.pone.0054136.

(4) Jones, J. T.; Akita, R. W.; Sliwkowski, M. X. Binding Specificities and Affinities of Egf Domains for ErbB Receptors. *FEBS Lett.* **1999**, *447* (2–3), 227–231. https://doi.org/10.1016/S0014-5793(99)00283-5.

(5) Rayego-Mateos, S.; Rodrigues-Diez, R.; Morgado-Pascual, J. L.; Valentijn, F.; Valdivielso, J. M.; Goldschmeding, R.; Ruiz-Ortega, M. Role of Epidermal Growth Factor Receptor (EGFR) and Its Ligands in Kidney Inflammation and Damage. *Mediators Inflamm.* **2018**, *2018*, 8739473. https://doi.org/10.1155/2018/8739473.

(6) Huang, Y.; Ognjenovic, J.; Karandur, D.; Miller, K.; Merk, A.; Subramaniam, S.; Kuriyan, J. A Molecular Mechanism for the Generation of Ligand-Dependent Differential Outputs by the Epidermal Growth Factor Receptor. *eLife* **2021**, *10*, e73218. https://doi.org/10.7554/eLife.73218.

(7) Wilson, K. J.; Gilmore, J. L.; Foley, J.; Lemmon, M. A.; Riese, D. J. Functional Selectivity of EGF Family Peptide Growth Factors: Implications for Cancer. *Pharmacol. Ther.* **2009**, *122* (1), 1–8. https://doi.org/10.1016/j.pharmthera.2008.11.008.

(8) Wee, P.; Wang, Z. Epidermal Growth Factor Receptor Cell Proliferation Signaling Pathways. *Cancers* **2017**, *9* (5), 52. https://doi.org/10.3390/cancers9050052.

(9) Kawamoto, T.; Sato, J. D.; Le, A.; Polikoff, J.; Sato, G. H.; Mendelsohn, J. Growth Stimulation of A431 Cells by Epidermal Growth Factor: Identification of High-Affinity Receptors for Epidermal Growth Factor by an Anti-Receptor Monoclonal Antibody. *Proc. Natl. Acad. Sci.* **1983**, *80* (5), 1337–1341. https://doi.org/10.1073/pnas.80.5.1337.

(10) Kumar, R.; Mendelsohn, J. Growth Regulation of A431 Cells. Modulation of Expression of Transforming Growth Factor-Alpha mRNA and 2',5'-Oligoadenylate Synthetase Activity. *J. Biol. Chem.* **1990**, *265* (8), 4578–4582.

(11) Toyoda, H.; Komurasaki, T.; Uchida, D.; Takayama, Y.; Isobe, T.; Okuyama, T.; Hanada, K. Epiregulin. A Novel Epidermal Growth Factor with Mitogenic Activity for Rat Primary Hepatocytes. *J. Biol. Chem.* **1995**, *270* (13), 7495–7500. https://doi.org/10.1074/jbc.270.13.7495.

(12) Strachan, L.; Murison, J. G.; Prestidge, R. L.; Sleeman, M. A.; Watson, J. D.; Kumble, K. D. Cloning and Biological Activity of Epigen, a Novel Member of the Epidermal Growth Factor Superfamily. *J. Biol. Chem.* **2001**, *276* (21), 18265–18271. https://doi.org/10.1074/jbc.M006935200.

(13) Lazzari-Dean, J. R.; Gest, A. M.; Miller, E. W. Optical Estimation of Absolute Membrane Potential Using Fluorescence Lifetime Imaging. *eLife* **2019**, *8*, e44522. https://doi.org/10.7554/eLife.44522.

(14) Moolenaar, W. H.; Aerts, R. J.; Tertoolen, L. G.; de Laat, S. W. The Epidermal Growth Factor-Induced Calcium Signal in A431 Cells. *J. Biol. Chem.* **1986**, *261* (1), 279–284.
(15) Pandiella, A.; Malgaroli, A.; Meldolesi, J.; Vicentini, L. M. EGF Raises Cytosolic Ca2+ in A431 and Swiss 3T3 Cells by a Dual Mechanism. *Exp. Cell Res.* **1987**, *170* (1), 175–185. https://doi.org/10.1016/0014-4827(87)90127-3.
(16) Tinhofer, I.; Maly, K.; Dietl, P.; Hochholdinger, F.; Mayr, S.; Obermeier, A.; Grunicke, H. H. Differential Ca2+ Signaling Induced by Activation of the Epidermal Growth Factor and Nerve Growth Factor Receptors*. *J. Biol. Chem.* **1996**, *271* (48), 30505–30509. https://doi.org/10.1074/jbc.271.48.30505.
(17) Crottès, D.; Lin, Y.-H. T.; Peters, C. J.; Gilchrist, J. M.; Wiita, A. P.; Jan, Y. N.; Jan, L. Y. TMEM16A Controls EGF-Induced Calcium Signaling Implicated in Pancreatic Cancer Prognosis. *Proc. Natl. Acad. Sci.* **2019**, *116* (26), 13026–13035. https://doi.org/10.1073/pnas.1900703116.
(18) Emeriau, N.; Clippele, M. de; Gailly, P.; Tajeddine, N. Store Operated Calcium Entry Is Altered by the Inhibition of Receptors Tyrosine Kinase. *Oncotarget* **2018**, *9* (22), 16059–16073. https://doi.org/10.18632/oncotarget.24685.
(19) Wong, S. T.; Winchell, L. F.; McCune, B. K.; Earp, H. S.; Teixido, J.; Massague, J.; Herman, B.; Lee, D. C. The TGF-α Precursor Expressed on the Cell Surface Binds to the EGF Receptor on Adjacent Cells, Leading to Signal Transduction. *Cell* **1989**, *56* (3), 495–506. https://doi.org/10.1016/0092-8674(89)90252-3.
(20) Gest, A. M. M.; Lazzari-Dean, J. R.; Ortiz, G.; Yaeger-Weiss, S. K.; Boggess, S. C.; Miller, E. W. A Red-Emitting Carborhodamine for Monitoring and Measuring Membrane Potential. *Proc. Natl. Acad. Sci.* **2024**, *121* (14), e2315264121. https://doi.org/10.1073/pnas.2315264121.
(21) Magni, M.; Meldolesi, J.; Pandiella, A. Ionic Events Induced by Epidermal Growth Factor. Evidence That Hyperpolarization and Stimulated Cation Influx Play a Role in the Stimulation of Cell Growth. *J. Biol. Chem.* **1991**, *266* (10), 6329–6335.
(22) *Cell line - KCNN4 - The Human Protein Atlas*. https://www.proteinatlas.org/ENSG00000104783-KCNN4/cell+line#skin_cancer (accessed 2024-08-02).

Chapter 5

VoltageFluor Dyes and Fluorescence Lifetime Imaging for Optical Measurement of Membrane Potential

Portions of this chapter were written in collaboration with the following people:
Dr. Anneliese Gest and Dr. Julia Lazzari-Dean

Portions of this chapter were published as a chapter in the following:
Gest, A. M. M.; Yaeger-Weiss, S. K.; Lazzari-Dean, J. R.; Miller, E. W. VoltageFluor Dyes and Fluorescence Lifetime Imaging for Optical Measurement of Membrane Potential. *Methods in Enzymology*; Academic Press Inc., 2021; Vol. 653, pp 267–293.
https://doi.org/10.1016/bs.mie.2021.02.009.

Abstract

Membrane potential is a fundamental biophysical parameter common to all of cellular life. Traditional methods to measure membrane potential rely on electrodes, which are invasive and low-throughput. Optical methods to measure membrane potential are attractive because they have the potential to be less invasive and higher throughput than classic electrode based techniques. However, most optical measurements rely on changes in fluorescence intensity detect changes in membrane potential. In this chapter, we discuss these use of fluorescence lifetime imaging microscopy (FLIM) and Voltage-sensitive Fluorophores (VF dyes) to make estimate of the millivolt value of membrane potentials in living cells. We discuss theory, application, detail a protocol for making these measurements, and discuss shortcomings of the application.

Introduction

Membrane potential, Vm, is an important biophysical parameter in cellular physiology. Fast changes in Vm, such as action potentials on the millisecond timescale, drive the specialized physiology of neurons and cardiomyocytes. Changes over longer timescales, from seconds to minutes to hours, may also be important in cells traditionally considered not to be electrically excitable, and have been implicated in processes such as mitosis,[1] cell cycle progression,[2] differentiation, [3,4] and development.[5]

The "gold standard" method for measuring membrane potential is patch-clamp electrophysiology. Electrophysiology involves direct electrical contact with the cell of interest, thereby providing an accurate and precise measure of the membrane potential of a cell. Additionally, because of this electrical contact, electrophysiology can make fast measurements of voltage changes, and for this reason, it has been useful in recording rapid signals such as action potentials. However, electrophysiology suffers in two main areas: its invasiveness and its lack of throughput. Because patch-clamp electrophysiology requires direct contact with the cell, and the whole-cell configuration ruptures the cell membrane, measurements taken with patch-clamp electrophysiology are inherently invasive and often terminal for the cell under investigation. Also because of the need for direct contact with the cell of interest, patch-clamp techniques are limited in the number of cells that can be measured at once. While there have been improvements in this area with specialized techniques designed for higher-throughput screens, such as planar patch clamp,[6] electrophysiology is still limited in scale, making measurements of Vm across large numbers of cells difficult.

Optical methods that use potentiometric fluorescent dyes address some of the shortcomings of invasiveness and throughput. Because these dyes can often be bath applied to many cells in a dish, or to a whole tissue, they have improved throughput compared to electrophysiology. Additionally, because they read out voltage optically, techniques involving these dyes are less invasive. However, intensity-based measurements of Vm are difficult to perform accurately. While they are useful for reporting changes in membrane potential, absolute measurements of actual millivolt values of Vm are difficult to obtain [7], due to confounding factors such as dye concentration, and photobleaching, which complicate the creation of an accurate calibration.[8]

Fluorescence lifetime imaging microscopy (FLIM) offers an alternative to intensity-based methods and avoids many of these confounding factors. The fluorescence lifetime (τ) is a measure of the time a molecule spends in its excited state, and is intrinsic to the molecule itself, being proportional to the fluorescence quantum yield (φ) (**Equation 5.1**).[9] Because fluorescence lifetime depends only on the rates of radiative (k_r) and nonradiative decay (k_{nr}) pathways out of the excited state (**Equation 5.2**),[9] the fluorescence lifetime of a fluorescent indicator can provide a useful readout based only on the factors that affect these decay pathways, as opposed to confounding experimental artifacts like photobleaching or indicator concentration.[10] Additionally, because lifetime is an optical technique, it can be minimally invasive and can be applied to many cells at once, and thus it is useful for making large-scale measurements.

$$\tau = \frac{\varphi}{k_r} \tag{5.1}$$

$$\tau = \frac{1}{k_r + k_{nr}} \tag{5.2}$$

The utility of fluorescence lifetime as a way to read out membrane potential in particular has been demonstrated first with fluorescent proteins,[11] and then through the use of a photoinduced electron transfer (PeT)-based dye, VF2.1.Cl,[12] one of several dyes in a class known as VoltageFluors (VFs). In these dyes, the rate of PeT is modulated by the voltage across the cell's membrane, making the dye dimmer at more negative potentials and brighter at more positive potentials (**Figure 5.1**).[12,13] PeT is a non-radiative decay pathway out of the fluorophore's excited state; therefore, modulation of PeT also leads to modulation of the fluorescence lifetime. For VF2.1.Cl, negative membrane potentials lead to shorter lifetimes, and positive potentials to longer fluorescence lifetimes.[12] These lifetimes of the probe in the cell membrane can be measured using FLIM and the intensity decay modeled mathematically using a multiexponential decay (**Equation 5.3**). If multiple exponential terms are present, the lifetime of the probe is then expressed as the amplitude-weighted average of the components (τ_m) where the lifetimes of each individual component (τ_n) are weighted by the amplitude of that component (a_n) (**Equation 5.4**).

$$F(t) = a_1 e^{-\frac{t}{\tau_1}} + a_2 e^{-\frac{t}{\tau_2}} + \cdots + a_n e^{-\frac{t}{\tau_n}} \tag{5.3}$$

$$\tau_m = \frac{a_1\tau_1 + a_2\tau_2 + \cdots + a_n\tau_n}{a_1 + a_2 + \cdots + a_n} \tag{5.4}$$

The relationship between membrane potential and lifetime of the voltage-sensitive fluorophore enables a lifetime-voltage calibration to be performed in cultured cells using patch-clamp electrophysiology. This calibration relates the weighted average lifetime (τ_m) to a particular membrane potential value. This is in contrast to $\Delta F/F$ relationships, which cannot easily report on actual membrane potential values, since the baseline F depends not only on membrane potential, but also on other confounding variables like dye concentration, variations in excitation intensity, and photobleaching. Once it has been determined, this lifetime-voltage calibration can then be applied relatively easily to lifetime measurements made on additional cells without re-calibration. Absolute values of V_m can therefore be measured across hundreds of cells or tracked longitudinally in particular cells in only a few hours of experiment time.

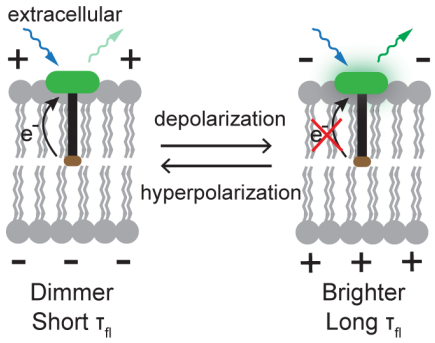


Figure 5.1. VoltageFluor dyes report membrane potential via photoinduced electron transfer.
At rest, electron transfer from the aniline (brown) to the fluorophore (green) quenches fluorescence, resulting in dimmer fluorescence intensity and shorter fluorescence lifetime (τ_{fl}). When the plasma membrane depolarizes, electron transfer is inhibited and fluorescence intensity is brighter. This also corresponds to longer fluorescence lifetime.

1. Materials

Fluorescence lifetime, unlike fluorescence intensity, is a value that is intrinsic to the dye, modulated only by its environment and independent of factors such as photobleaching or the amount of dye present in the location of interest (outside of concentrations at which self-quenching occurs). For this reason, potentiometric dyes with mechanisms of voltage sensitivity which affect the dye's excited state can be used to optically read out absolute membrane potential, once they are calibrated in a given system. VoltageFluors, a class of dye which reports voltage through photoinduced electron transfer (PeT), are one variety of dye which may be calibrated and used to report bulk membrane potential measurements of many cells at once through the use of FLIM, in a technique referred to as VF-FLIM. VF2.1.Cl, a dichlorofluorescein-based VoltageFluor, is sufficiently bright and sensitive for use in FLIM experiments, and has been demonstrated a reliable reporter of membrane potential via VF-FLIM in multiple cultured cell lines, including HEK293T cells. However, this technique should be generalizable to many cultured cell types, other VoltageFluor dyes, and possibly other potentiometric indicators in which changes in membrane potential alter the excited-state lifetime, of suitable brightness and voltage sensitivity [11].

1.1 Equipment

Image Acquisition and Analysis

- Glass coverslips (#1.5, 25 mm diameter) (Electron Microscopy Sciences)
- Attofluor imaging chamber (or similar dish that will allow use of a glass coverslip)
- SPC-150NX photon counting card (Becker-Hickl)
- HPM-100-40 GaAsP hybrid detector (Becker-Hickl)
- DCU-800 laser control unit (Becker-Hickl)
- Laser hub with 488 nm picosecond diode laser (Becker-Hickl)
- Zeiss 980 LSM Microscope (Zeiss)
- ZenBlue LSM software (Zeiss)
- SPCM FLIM acquisition software, version 9.84 (Becker-Hickl)
- SPCImage analysis software, version 8.3 (Becker-Hickl)
- ImageJ or other image processing software

Electrophysiology

- P97 Pipette Puller (Sutter Instruments)
- Pipettes pulled from borosilicate glass with filament, resistances 4 to 7 MOhms (Sutter Instruments)
- Patch-clamp electrophysiology rig
    - MP-225 Micromanipulator (Sutter Instruments)
    - Digitizer (e.g. Digidata 1550B) (Molecular Devices)
    - Amplifier (e.g. Axopatch 200B) (Molecular Devices)
    - Clampex software (Molecular Devices)

1.2 Reagents

Cell Culture

- Complete cell culture medium (e.g. DMEM with 4.5 g/L glucose, 2 mM GlutaMAX, 10% fetal bovine serum)
- Low glucose cell culture medium (e.g. DMEM with 1 g/L glucose, 2 mM GlutaMAX, 10% fetal bovine serum, 1 mM sodium pyruvate)
- Cultured cells (e.g. HEK293T)
- Dulbecco's Phosphate Buffered Saline (dPBS)
- Poly-D-lysine (Sigma-Aldrich, made as a 0.1 mg/mL solution in dPBS with 10 mM Na_3BO_4)
- Cell dissociation reagent

Standards Measurement

- 2 μM fluorescein in 0.1 N NaOH
- Quenched fluorescein for IRF measurements [12.2 M NaI, 500 μM Fluorescein from 4 mM stock in 0.1 N NaOH, in H_2O]

Electrophysiology

- Internal solution for whole-cell patch-clamp electrophysiology [pH 7.25, 285 mOsmol/L, 125 mM potassium gluconate, 10 mM KCl, 5 mM NaCl, 1 mM EGTA, 10 mM HEPES, 2 mM ATP sodium salt, 0.3 mM GTP sodium salt]

VF-FLIM in Cells

- VoltageFluor VF2.1.Cl (solid or stock in DMSO)
- DMSO
- HEPES Buffer [1.26 mM $CaCl_2$*$2H_2O$, 0.49 mM $MgCl_2$*$6H_2O$, 0.41 mM $MgSO_4$*$7H_2O$, 5.33 mM KCl, 0.44 mM KH_2PO_4, 10 mM HEPES (pH 7), 139.5 mM NaCl, 0.34 mM Na_2HPO_4, 5.56 mM D-Glucose]
- High-K+ HEPES Buffer [1.26 mM $CaCl_2$*$2H_2O$, 0.49 mM $MgCl_2$*$6H_2O$, 0.41 mM $MgSO_4$*$7H_2O$, 119.6 mM KCl, 0.44 mM KH_2PO_4, 10 mM HEPES (pH 7), 23.6 mM NaCl, 0.34 mM Na_2HPO_4, 5.56 mM D-Glucose]

2. Protocol

Note: While we specify a particular microscope and FLIM system and software, the protocol outlined below can be generalized to any point-scanning confocal microscope and any FLIM system. Software-related instructions in the protocol that follows are specific to the setup outlined above, but the theory and use of the VF2.1.Cl probe in FLIM applications should be generalizable to any system.

Critical: The protocol outlined below gives specific timings and photon counts per second for each data acquisition type. These are intended as examples of what worked on the specific system used in the design of VF-FLIM. Individual FLIM systems will vary, and the protocol is flexible to be used with any of them. Count rates up to 1% of the laser rep rate (80 MHz for the system this protocol is based on, though it has also been performed at 50 MHz) can be used, to avoid photon pileup, and consequent incorrect lifetime values.[14]

2.1 Measurement of Standards and Determination of Fit Parameters

2.1.1 Measuring Instrument Response Function

Note: SPCM, along with other TCSPC software programs, allow for the use of an electronically-generated instrument response function (IRF) based on the laser pulse and system electronics. However, our protocol gives directions for a measured IRF, which we find gives more accurate lifetime determinations where short lifetime components are present.

1. Insert a 25 mm coverslip into the attofluor chamber. Place a small drop of 500 μM fluorescein quenched with iodide, the quenched fluorescein solution from the reagents above, in the center of the coverslip (around 20 μL is sufficient, only a droplet is needed), or other fluorophore with a very short lifetime to use as a measure of the instrument response function, depending on the wavelength at which you are working.
2. Locate the droplet of solution and adjust the focal plane. Doing this using the LSM software and 488 laser is recommended for fluorescein. Adjust as appropriate for other fluorophores and laser lines.
    a) Using the Zen Smart Setup tool, select fluorescein from the drop-down, and select "Smartest" setting.
    b) Enter the "live" imaging mode, and adjust the focus until fluorescence comes into view and reaches a maximum intensity value.
3. Switch the dichroic so that light is directed towards the photon counting detector for FLIM.
    a) Be careful at this point not to saturate the detector. The quenched fluorescein solution outlined for use here is quite bright, and high laser power could cause saturation of the FLIM detector. Low laser power, around 5-10% and a small pinhole will help to avoid this.
4. In SPCM, first make sure that the relevant detector and laser line (488) are turned on.
5. In "Oscilloscope" imaging mode, set acquisition time and repetition time to 1 second. This is for optimizing the laser power and pinhole size for the standards.
6. In Zen, select the "Time Series" experiment option, and then set the time series to go for an arbitrarily long number of frames (around 10,000 is sufficient for most experiments; the

purpose is just so that the scanning in Zen will not end prior to the completion of the FLIM acquisition). Set the zoom setting to 1 and the scan speed to 8.

7. Select start on the oscilloscope in SPCM, and the start the experiment in Zen.
8. Adjust the pinhole in Zen (invisible light pinhole) and the optical laser power by selecting the "Laser Power Down" button, until the counts displayed for the analog to digital converter (ADC) in SPCM are around $3*10^3$ counts per second (cps).
    a) You can use a small pinhole to reduce the signal if necessary.
9. Stop the acquisition in both SPCM and Zen. Switch to "Single" mode in SPCM, and set up autosave, if desired. Set the acquisition time to 10 s and the repetition time to 10 s.
10. Start the experiment in Zen, and then in SPCM. Acquire two single decays in SPCM, so that an average can be taken, and to establish that the IRF remains consistent.
11. Stop the experiment in both programs.
12. Open the first decay trace in SPCImage via the "Import" function.
13. The data should appear as a very short decay early in the time window. Adjust the time gates to clip closely on either side of the decay, where the peak meets baseline on either side.
14. Select the IRF menu from the top tool bar, then select "Copy From Decay Data." Then select "Copy to Clipboard."
15. Paste the data from the first decay into a program like Microsoft Excel, or other analysis program.
16. Repeat steps 12-15 for the second trace, making sure to use the same time gates as for the first trace.
17. Take the average for every time bin between the two traces, producing a third trace that represents the average of the two at each time bin.
18. Copy the average trace from the spreadsheet, and import it for use in analysis in SPCImage by selecting the IRF menu from the tool bar, then selecting "paste from clipboard."

Note: On a stable system, a single IRF measurement should suffice, but if using a measured IRF, taking a new one every hour of imaging time can aid in getting more reliable and consistent fits, especially if the temperature in the imaging room changes over time.

2.1.2 Measuring Fluorescein Standard and Setting Value of Shift for Analysis

Note: Use measurements of a standard (fluorescein in solution in this case) to determine that the FLIM system is working properly and to optimize fit parameters. Other fluorophores can be used as additional lifetime standards to confirm the system is working well. Erythrosin B, for example, with a lifetime of 85 ps, is an example of a possible short-lifetime standard to use under these conditions in conjunction with fluorescein[15] Erythrosin B also works well as an IRF on this system for redder wavelengths than 488.

1. Insert a 25 mm coverslip into the attofluor chamber. Place a small drop of 2 μM fluorescein solution in the center of the coverslip (around 20 μL is sufficient, only a droplet is needed).
2. Follow steps 2-11 from 2.1.1, with the following changes:
    a. Adjust the pinhole and laser power until the counts displayed for the ADC in SPCM are around $5*10^4$ cps.
    b. You can use a small pinhole to reduce the signal if necessary.

3. Open the first decay trace in SPCImage via the "Import" function.
4. Import the instrument response function (IRF), either from a measured IRF taken previously or an electronically generated one.
5. Using the options tab, select the model window. Change the model to be an incomplete decay, and change the fit model to WLS (weighted least squares) if not already the default.

Note: SPCImage also has other fit models, including maximum-likelihood estimation (MLE) in the newer versions of the software, that may provide more reliable fits, as do other FLIM analysis software packages. The protocol outlined here uses WLS, however, the points are generalizable to use with other fitting algorithms.

6. In the window to the right of the decay, the fit parameters window, change the parameters as follows:
    a. Single component decay.
    b. Fix the offset to zero.
    c. Fix the scatter to zero.
    d. Fix the shift, adjusting the value in the box until the average lifetime (τ_m) displayed is near the literature value for fluorescein (4000 ps)[16] and the Chi^2 value is near one.
        i. This empirically derived value for the shift should be used in subsequent analyses of decays derived from cellular data. Fixing the shift makes analysis more accurate and faster, but an incorrect value for the shift can drastically change the calculated lifetime values.[14] Measure a known standard to determine the ideal shift, and then fix it for analysis of unknowns to ensure accurate fits.
        ii. The shift should be close to 0 if the instrument response solution and the standard solution are spectrally similar.
7. Repeat steps 12-15 for the second decay trace. The shift determined in step 15 for the first trace should replicate a good fit for the second trace.

Critical: Make sure that the ADC resolution of the measured IRF and the standards taken match that in the FIFO Image mode (the first-in-first-out time-tagged imaging mode that produces the FLIM image). For instance, if using an ADC resolution of 256 for your images, make sure that the ADC resolution is also 256 for any measured IRF or standards.[14]

2.2 Determination of Non-Quenching Concentrations

2.2.1 Fluorescence Lifetime Imaging at Multiple Dye Concentrations

Note**:** Higher concentrations of fluorophore in the membrane can lead to shorter measured lifetimes due to concentration-dependent quenching.[17] This step is important to select a concentration for use in future experiments that avoids this quenching regime, but is still at high enough concentration to provide enough photons for analysis.

1. In a 6-well cell culture plate, place one 25 mm #1.5 coverslip in each well. Coat each coverslip with 500 µL of poly-d-lysine (PDL). Place plate with coverslips in incubator at 37 °C for at least one hour, and up to 8 hours (overnight).

2. Pipette or aspirate off the PDL.
3. Wash each coverslip twice with 1 mL of water, and twice with 1 mL of dPBS.
4. Plate cells on each glass coverslip at the density appropriate for the chosen cell line, and using the cell culture protocol appropriate for the cell line. The cells should be around 40 to 50% confluent at the time of imaging, such that they have grown to form discrete groups of cells, but not a monolayer.
5. Determine a range of dye concentrations to test for concentration dependent quenching. For many cultured cell lines, a range from 50 nM to 1 µM VF2.1.Cl showed a clear quenching curve, with a "flat" portion of the curve in which there was no concentration-dependent quenching and an inflection point at which the lifetimes became shorter, suggesting concentration-dependent quenching. This range allowed for determination of a concentration that was bright enough to utilize but avoided this concentration-dependent quenching (**Figure 5.2a**).

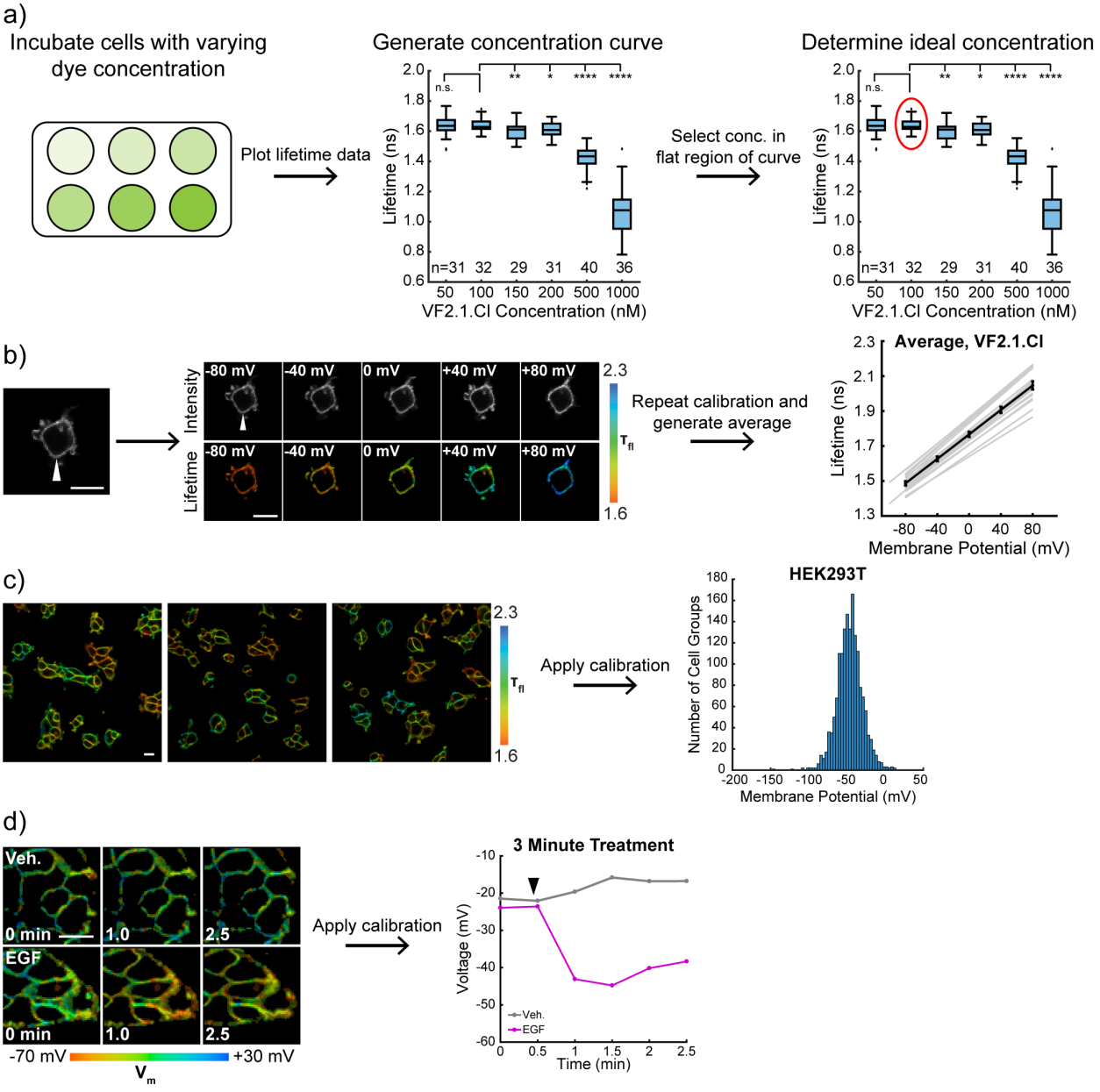


Figure 5.2. Overview of VF-FLIM data acquisition.
a) Determination of optimal dye concentration. Incubate cells with a range of dye concentrations and plot the weighted average lifetimes. From the concentration curve, select a concentration in the flat region (red oval) to avoid concentration-dependent quenching at higher concentrations. Example data from HEK293T cells loaded with VF2.1.Cl. Scale bar is 20 μm. **b)** Development of calibration between fluorescence lifetime and membrane potential. Voltage clamp single cells over a range of membrane potentials and acquire fluorescence lifetime data at each potential. Repeat this process for multiple single cells to generate an average calibration between fluorescence lifetime and membrane potential. Example intensity and lifetime images show HEK293T cells loaded with 100 nM VF2.1.Cl. Scale bar is 20 μm. **c)** Bulk measurement of membrane potential. Take FLIM images of many cells. Use the calibration to convert fluorescence lifetime to voltage for each ROI and plot the data. The resulting histogram shows the distribution of membrane potential across the population of cells. Example FLIM images and data are for HEK293T cells loaded with 100 nM VF2.1.Cl. Scale bar is 20 μm. **d)** Time series for tracking changes in membrane potential over time. Take FLIM images over the desired time scale. Apply the lifetime-voltage calibration and plot the voltage over time. Example FLIM images and data are for A431 cells loaded with 100 nM VF2.1.Cl and treated with imaging buffer vehicle or 500 ng/mL EGF. Scale bar is 20 μm.

6. To a 1.5 mL Eppendorf tube, add 999 μL of HEPES buffer, and the appropriate amount of concentrated VF2.1.Cl stock solution in DMSO, and additional DMSO such that the concentration is 0.1% DMSO by volume.
7. From one well of the 6-well culture plate, aspirate or pipette off culture media. Add in the dye solution in buffer, then return to the incubator at 37 C for 20 minutes. This allows time for the dye to selectively stain the plasma membrane.
8. After 20 minutes, remove the plate from the incubator, and pipette or aspirate off the dye solution. Replace the dye solution with 1 mL of buffer.
9. Using tweezers, gently lift the coverslip out of the well, and carefully place it in an Attofluor chamber, closing the chamber to form a tight seal, without cracking the glass. Add 1 mL of buffer to the chamber.
10. Using the same objective as was used in 2.1.1 and the eyepieces, locate the cells using transmitted light, and select a field of view.
11. Adjust the focal plane using the LSM software and 488 laser in Zen, as the fluorescence focal plane of the cells will be somewhat different from the transmitted light.
    a. Using the Zen Smart Setup tool, select fluorescein or YFP from the drop-down, and select “Smartest” setting.
    b. Enter the “Live” imaging mode and adjust the focus until fluorescence comes into view and the image displayed on the screen is bright and clear.
12. At this point, adjust the “Zoom” setting in Zen, and make sure that the image size in Zen matches the image size desired in SPCImage (256x256 or 512x512). “Zoom” setting 2 works well for investigating concentration-dependent quenching, as generally several cell groups can be located in one field of view.
13. Switch the dichroic so that light is directed towards the photon counting detector for FLIM.
14. In SPCM, first make sure that the relevant detector and laser line (488) are turned on.
15. In “Oscilloscope” imaging mode, set acquisition time and repetition time to 1 second. This is for optimizing the laser power and pinhole size.
16. In Zen, select the “Time Series” experiment option, and then set the time series to go for an arbitrarily long number of frames (around 10,000 is appropriate for most

experiments; the purpose is just so that the scanning in Zen will not quit before the FLIM acquisition is done).

17. Select start on the oscilloscope in SPCM, and the start the experiment in Zen.
18. Adjust the pinhole in Zen (invisible light pinhole) and the laser power until the counts displayed for the ADC in SPCM are at least $1*10^5$ counts per second (cps), and ideally closer to $3*10^5$ cps, though this value will fluctuate as the laser scans across dark areas not stained with dye.
    a. To achieve this count rate, it may be advantageous to increase the size of the pinhole above 1 AU. Values between 2 and 3 AU (e.g. 100 μm in Zen) often still give acceptable optical sectioning of membranes but allow for more photons to be collecting, enabling faster FLIM recordings. Longer recording times could also be used, at a lower count rate, for more light-sensitive samples, for instance.
    b. The electronic laser power should be the same as used to measure any standards taken, and determined empirically for the samples used such that the pulse shape is good, meaning that the IRF is narrow and the decay traces are monotonic, with no bumps or aberrations, and enough counts are able to be generated by the sample of interest, without causing damage to the sample or photobleaching the dye.

Note: It is better to do coarse adjustments of laser power in the software by directly editing the laser power box, and typing the desired laser power. This adjusts the electronic power, and should be adjusted for what fits the sample and gives the best pulse shape, and then held constant across all experiments in a system (though this is generally best at medium power levels, and high laser power should be avoided). Fine adjustments should be done by clicking the L2 (or whichever is the appropriate laser line) UP or DOWN buttons, which adjusts a neutral density wheel to affect the optical laser power reaching the sample. Changing the electronic laser power changes the pulse shape and so will affect the IRF, while adjusting the optical power using the power UP and DOWN buttons will not.[14]

19. Stop the acquisition in both SPCM and Zen. Switch to "FIFO Image" mode in SPCM, and set up autosave, if desired. Set the acquisition time to between 60 and 90 s, and the repetition time to match the acquisition time.
    a. The exact time for a particular combination of dye and cell type may take some optimization.
20. Start the experiment in Zen, and then in SPCM.
21. Repeat steps 6-19 for all chosen concentrations of dye.

2.2.2 Analysis of FLIM Images in SPCImage

1. Import the first image file into SPCImage, using the "File" menu, and the "Import" feature.
2. Import the measured IRF into the analysis pane by first copying the measured IRF from the spreadsheet it was generated from to the clipboard, then selecting "IRF" and "Paste From Clipboard."

3. Select the “Options” menu on the toolbar, then the “model” menu. Check the box marked “Incomplete Multiexponential” and make sure the default fit method is weighted least squares (WLS). Increase the number of iterations to twenty.
4. Adjust the T1 time gate to rest shortly before the peak of the decay, such that it catches some of the “tail” of the previous, incomplete decay. This should be a few time bins before the decay peak. T2 should end near the end of the measured decay, but not all the way at the end. Time bin 240 is appropriate for ADC resolution of 256.
5. Set the shift to the value determined in protocol 2.1.2 and check the box to fix it at that value. Fix the offset and scatter values to zero.
6. Change the number of components in the multiexponential decay. For VF2.1.Cl in cultured cell lines, 2 components generally gives the best, most consistent fits.[12]
7. Adjust the “Threshold” setting. This value should be adjusted empirically to a value that allows for consistent fits, and includes all of the bright membrane pixels, while excluding interior pixels. For the settings given in this protocol, a threshold of 300 at the peak of the decay has produced consistent fits.
8. Adjust the “Bin” setting. For images that are 256x256 and taken at zoom setting 2 in Zen on a 40x objective, setting that bin value to 3 allows for consistent fits across multiple images, and ensures there are sufficient photons in each binned pixel stained with dye.
    a. The important point here is to bin such that there are sufficient photons for a consistent fit. There are enough photons with the bin settings used if the following are true:
        i. Adding more photons (e.g. by binning further) doesn’t change the result significantly.
        ii. Results are not notably different, beyond mild fluctuations, between successive measurements of the same sample.

Note: Binning in SPCImage is not “standard” binning, rather, it bins by essentially creating a moving average of binned pixels across the image, resulting in some pixels being double counted. Additionally, if using an analysis software other than SPCImage that uses a different definition of binning, 3 may not be sufficient to have enough photons at the pixels of interest.[12,14]

9. Select the “Calculate” menu from the toolbar, and then select “Decay Matrix”. This will apply the binning and the threshold to the image and produce a color-coded lifetime-intensity overlay image. The program will also plot a histogram of the weighted average lifetime values versus the number of pixels at each lifetime, and present an average value.
10. Check the quality of the fit by looking at the residuals displayed below the decay trace. These values are for the fit at a specific pixel, as is the decay trace, and will change slightly as the cursor is moved around the image.
11. Set the color to display the weighted average lifetime (Tm) as the color-coded value.
12. Once satisfied with the fits, the rest of the images that share a given measured IRF can be batch processed together. First, store the desired fit conditions as the default, and then select “Calculate” and then “Batch Processing,” and then selecting all the .sdt files that use a given IRF.

13. Copy over the next measured IRF for the next set of images, and repeat steps 1-13 for the remaining images from the experiment.
14. When all initial fits have been completed, export the lifetime and intensity images as .asc files by selecting the "File" menu, and selecting "Export." In the export menu, check the boxes to export "Color Coded Value" (making sure that the color coded value selected from the "color" menu is Tm), and "Pixel Intensities." Then, select "Batch Export" and allow the program to process the images.
    a. Optionally, a bitmap image file can also be produced of the lifetime-intensity overlay image and the intensity image, with or without a color bar legend to display the color range used and the corresponding lifetime range.

2.2.3 Refinement of ROIs and Identification of Non-Quenching Concentrations

1. Use a published routine using custom Matlab code that automatically identifies regions of interest by first sharpening and then thresholding the intensity images. This code is available as source code 2 in previous work.[12]
    a. This code will output a .csv file containing the weighted average lifetimes for each designated ROI, along with metadata including the concentrations and coverslip, as defined by the metadata file required by the script.
    b. Instead of using this script, you may follow steps 2-7 below, which will allow you to run through the same steps accomplished in the code.
2. Convert the .asc files exported from SPCImage into TIFF files.
3. Open the intensity image in ImageJ or other visualization software.
4. Select regions of interest (ROIs). These should include the bright membranes of the cells, and exclude the background coverslip, as well as any debris, and the unstained interiors of cells (**Figure 5.3**). The ROIs should be whole cell groups, and should not be separated by individual cell. (Cells within a group are likely electrically coupled to one another,[18] depending on the chosen cell line; furthermore, the spatial resolution of a standard point-scanning confocal microscope makes separating abutting membranes impossible).
    a. This can be done easily by using the threshold tool in ImageJ, and making a selection from that threshold, then saving that selection as an ROI. The ROI can then be further cleaned up from there.
5. Once all the ROIs for an image are defined from the intensity image, open the corresponding lifetime image. If binning was used during lifetime analysis, the lifetime image will have reduced spatial resolution compared to the intensity image.
6. Apply the ROIs to the lifetime image, and for each ROI on the lifetime image, take a measurement. The important value for in this case is the mean, which represents the mean weighted average lifetime across the ROI.
7. Copy these average values into a spreadsheet or other analysis program, such as Microsoft Excel, organizing them by dye concentration and sample.
8. Plot the weighted average lifetimes of each ROI broken down by category in plotting software of choice. Box and whisker plots or violin plots are convenient for this. There should appear to be a curve as in (**Figure 5.2a**), with a "flat" section where the mean lifetimes at different concentrations is fairly consistent, and a point at which the

lifetime starts to decrease as concentration increases, revealing concentration-dependent quenching.

9. Select a concentration from the "flat" portion of the curve to use for future experiments (**Figure 5.2a**).

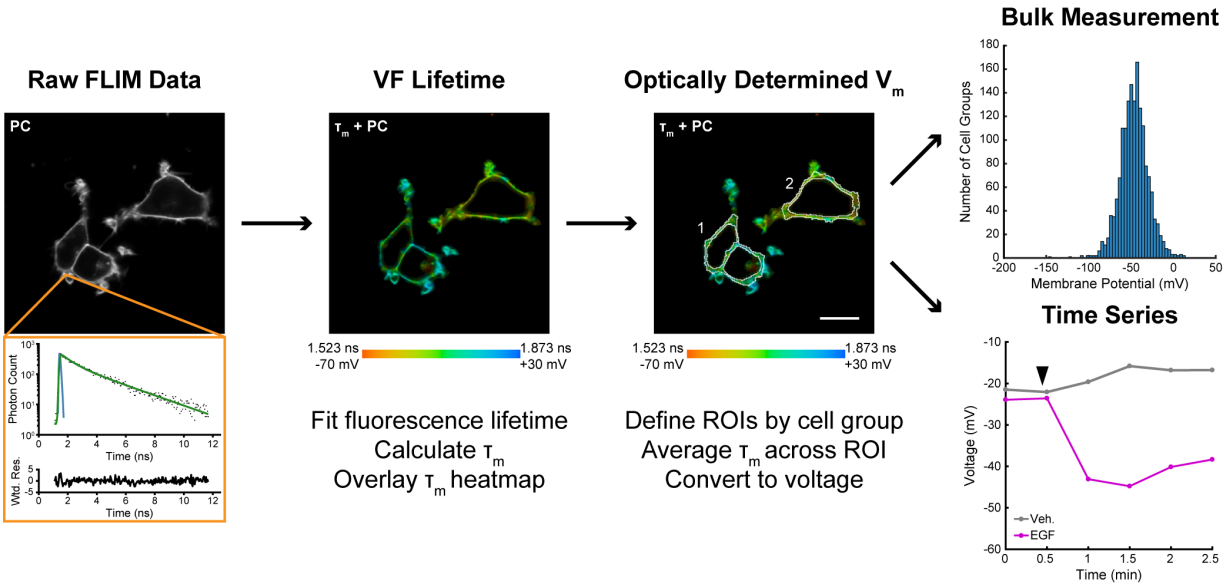


Figure 5.3. Overview of data analysis.
Fit time-correlated photon data to an exponential decay model (first panel). Calculate the weighted average fluorescence lifetime (τ_m) and overlay heatmap onto the photon count (PC) image (second panel). Define regions of interest (ROIs, white outlines) by cell group and average τ_m across each ROI (third panel). Use the lifetime-voltage calibration to convert the averaged τ_m to membrane potential (V_m). Data can be plotted as a histogram showing the bulk membrane potential distribution or, if images were acquired in a time series, as a line graph showing the change in membrane potential over time. Example images and bulk measurement data are for HEK293T cells loaded with 100 nM VF2.1.Cl. Example time series data are for A431 cells loaded with 100 nM VF2.1.Cl and treated with imaging buffer vehicle or 500 ng/mL EGF. Scale bar is 20 µm.

2.3 Generation of Electrophysiological Calibration

2.3.1 Simultaneous FLIM and Electrophysiology

1. In a 6-well cell culture plate, place one 25 mm #1.5 coverslip in each well. Coat each coverslip with 500 µL of poly-D-lysine (PDL). Place plate with coverslips in incubator at 37 C for at least one hour, and up to 8 hours (overnight).
2. Pipette or aspirate off the PDL.
3. Wash each coverslip twice with 1 mL of water, and twice with 1 mL of dPBS.
4. Plate cells on each glass coverslip at an appropriate density, in low glucose media, such that at the time of imaging they will still be single cells.
5. Prepare five voltage-clamp protocols that hold the cell at a given potential for 15 seconds.
    a. -80, -40, 0, +40 and +80 mV are potentials that worked well for HEK293T cells in the development of this protocol, but these values could be adjusted, and more values added.

6. Using the same objective as in 2.1.1 and in previous steps, and the eyepieces, identify a single cell to perform the calibration on. The cell should not be connected to any others, and should have a morphology typical of a healthy cell from the cell line.
7. Follow the imaging protocol in section 2.2.1, with a few key changes:
    a. Set the image size to 64x64 rather than 256 x 256 or 512 x 512, in both Zen and SPCM.
    b. Zoom in on the cell of interest. A setting in Zen of 3 to 4 works well for this.
    c. FIFO Image acquisition times should be 15 s each.
    d. Laser power and pinhole size should be adjusted such that each image is about $1*10^5$ cps at a resting potential. Test that this is the case for a single image before running the full experiment.
8. Fill the glass pipette with internal solution and lower into the bath. Zero the voltage, and follow the steps for whole-cell patch-clamp electrophysiology, heavily abbreviated in steps 9-11. More detailed protocols and considerations can be found in the following references: [19,20,21,22].
9. Locate the borosilicate glass pipette through the eyepieces, and position over the cell of interest.
10. Lower the pipette into contact with the cell's surface, entering cell-attached mode. Correct for pipette capacitance.
11. Enter whole-cell configuration, checking the quality of the patch using the "membrane test" feature. The ratio of membrane resistance to access resistance should be greater than 30.
12. Coordinate voltage clamp protocols and FLIM measurements such that the entire time the FLIM image is being acquired, the cell is being held at the desired voltage.
    a. One way this can optionally be accomplished is by setting up a cable connecting the electrophysiology rig to the laser hub, and setting the voltage clamp protocol to trigger the laser, and setting the "Trigger" setting in SPCM to an external trigger.
13. Assess the quality and stability of the patch after running the voltage clamp protocol. If the patch has degraded or the cell has died, do not continue running the protocol, and start over with a new cell.
14. Repeat steps 11 and 12 with the subsequent potentials, assessing patch quality after each protocol. Apply the protocols in random order, to avoid artifacts such as changes to lifetime brought on by bleaching or cell death.
    a. While random order is best, the +80 mV protocol is sometimes not tolerated as well by cells as the others when held for such a long time. For this reason, it may be useful to perform this one last, and if the patch has degraded or the cell dies during this step, it may be omitted from the calibration.
15. Repeat the above steps for subsequent cells, in order to have multiple cells from which to generate a general calibration (**Figure 5.2b**).[12]

2.3.2 Analysis and Generation of Lifetime-Voltage Calibration

1. Follow the steps outlined in protocol 2.2.2 for analysis in SPCImage, with the modification to step 8 that the "Bin" setting for these smaller, more zoomed-in calibration images should be set at 1 rather than 3.

2. Follow steps 1-6 in protocol 2.2.3, recording mean Tm at each potential, rather than at each concentration. For these images, identifying ROIs by hand, rather than using the MATLAB package mentioned in step 7 is recommended.
3. For each cell, plot the weighted average lifetime (Tm) versus the voltage, and generate a regression line for those points. Determine the equation of that regression line.
4. From all of the linear regressions, determine an average slope and an average y-intercept.
    a. The average slope represents the sensitivity of the calibration, that is, the change in lifetime, in picoseconds, for each mV change in membrane potential.
    b. The y-intercept represents the expected lifetime if the cell is at 0 mV, and is important for calculating membrane potential from a measured lifetime.
5. Calculate an "intra-cell" error for the calibration.
    a. The "intra-cell" error is determined by the root-mean-square deviation (RMSD) between the voltage as defined by electrophysiology (assumed to be 100% accurate) and the voltage as determined using the calibration to convert the lifetime to the voltage for a specific cell, using that individual cell's line of best fit. Perform this calculation for each cell, and report the mean ± SEM as the overall error. This value gives a sense of the resolution for measurements of voltage change in an individual cell, and is discussed in more detail in section 4.1.
    b. Calculate the Bias, variance (σ^2), and RMSD, using the optical guess at Vm for each measured lifetime, using that individual cell's line of best fit, as the values of V_{FLIM}
    c. Equations for RMSD are as follows:[12]
        i. $Bias = \frac{1}{n}\sum_{i=1}^{n} V_{FLIM,i} - \frac{1}{n}\sum_{i=1}^{n} V_{ephys,i}$
        ii. $\sigma^2 = \frac{1}{n}\sum_{i=1}^{n}(V_{FLIM,i} - V_{ephys,i})^2$
        iii. $RMSD = \sqrt{\sigma^2 + Bias^2}$
6. Calculate an "inter-cell" error for the calibration.
    a. Calculate the optical determination of V_m for the 0 mV point on each individual calibration using the overall calibration. Ideally, this value should be 0 mV, however, there will likely be some spread in the individual 0 mV points, such that they give a calculated membrane potential that varies from 0 mV.
    b. Calculate the RMSD using the equations in step 5c, this time using the optical determination of the V_m based on the lifetime, using the overall calibration for the cell line as V_{FLIM}, and the 0 mV value from the individual calibrations as V_{ephys}. This value gives a sense of the resolution for measurements of absolute voltage across many cells, or how well the average calibration predicts an individual cell's membrane potential.

2.4 Membrane Potential Measurements in Large Populations of Cells

1. Plate cells and take FLIM images as in 2.2.1, with three changes.
    a. In step 9, add either the regular HEPES buffer, for bulk measurements of resting membrane potential, or add 1 mL of high-K+ (120 mM) HEPES buffer to the imaging dish for a bulk perturbation that will shift the membrane potential of all cells close to zero.
    b. In step 12, the zoom setting in Zen should be set to zoom 1, in order to image a larger number of cell groups at one time.
    c. In step 19, the acquisition time should be 90 s.
2. Perform initial analysis in SPCImage as outlined in 2.2.2.
3. Follow steps 1-8 in 3.2.3 for ROI refinement and analysis, with the following changes.
    a. Instead of recording the dye concentration used for that sample, list the condition for that sample, i.e. whether low or high-K+ buffer was used.
4. Use the lifetime-voltage calibration generated in 2.3.2 to convert the average lifetimes of each ROI for each condition into the corresponding membrane potential.
5. Plot the membrane potentials for each condition. Histograms are useful here to visualize the distribution of membrane potentials in the population of cells being investigated (**Figure 5.2c**).

2.5 Measuring Membrane Potential Changes Over Time

1. Plate cells onto 25 mm #1.5 glass coverslips, culturing as appropriate for the cell line of interest.
2. Prepare a 2x stock solution of the drug intended for pharmacological perturbation of the membrane potential in buffer.
    a. In serum-starved A431 cells, for instance, treatment with epidermal growth factor (EGF) results in a hyperpolarization that can be measured with VF-FLIM (**Figure 5.2d**).[12] This 2x EGF solution was prepared at 1 μg/mL, for a final concentration of 500 ng/mL in the imaging dish.
    b. Keep this stock solution at the same temperature as your imaging buffer and sample to avoid temperature-dependent artifacts when you add it to the sample.

    Note: This protocol is written for performing this experiment without a perfusion system. However, perfusion could be utilized instead for treating the system with drug/vehicle in these time series experiments.

3. Incubate sample with VoltageFluor dye as outlined in steps 6-9 of protocol 2.2.1, with the following change:
    a. In step 9, when adding buffer back to the imaging chamber, add only 500 μL of imaging solution, rather than 1 mL.
4. Acquire FLIM images as in 3.2.1, with the following changes.
    a. Set collection and repeat time to 30 seconds, to acquire a 30 second exposure.
    b. Adjust laser power such that the ADC reads 4-5*10^5 cps, to accommodate the shorter exposure times.
    c. Set number of cycles to 6, for a 3 minute time series. More cycles can be selected for imaging over a longer time. However, longer timescales can lead to phototoxicity, so

it is recommended that there are pauses between image acquisition periods for longer timescales, rather than the sequential frames used for the 3 minute time series.

i. Make sure that autosave has been selected as on, and that images are saved after each cycle. This will save each image from each cycle as a separate file, appending to the end of each file name "c1" through "c6" or onward, depending on the number of cycles, to differentiate them by their place in the time series.

Critical: Whenever running a new sample or condition, especially those at higher light power or over longer timescales, it is important to first run a control solution in which vehicle, rather than drug, is added, to ensure that the lifetime doesn't drift over the course of the recording period, and to make sure phototoxicity is minimized.

5. After the first frame has been acquired (30 to 35 seconds into the experiment) and just before the second begins, take 500 µL of the 2x drug solution, or the same amount of a 2x vehicle solution, and add it to the imaging dish, being careful not to bump the imaging dish. Continue acquiring data.
6. Perform initial analysis in SPCImage for each frame as outlined in 2.2.2.
7. For this type of data, the code mentioned in 2.2.3 is not ideally set up for analyzing multiple frames of the same condition over time. Thus, it is better to perform the analysis by hand, using the steps outlined in steps 2-7 of 2.2.3 to refine the ROIs and collect the weighted average lifetime data.
8. Apply the lifetime-voltage calibration generated in 2.3.2 to each time point.
9. Plot V_m against time, for both drug-treated and vehicle-treated cells.
    a. A line graph is useful here, for tracking V_m changes over time in each condition (**Figure 5.2d**).

2.6 Generation of Electrophysiological calibration on Zeiss LSM 980 microscope, "K"

Note: This section of the protocol was not included in the original publication. It is included here to clarify specifics of the protocol above for use on the particular system at the UC Berkeley MIC, installed in 2020.

1. Follow steps 1-5 as in 2.3.1.
2. Set up a Faraday cage around the system, or make one from foil.
    i. To assemble a foil Faraday cage, attach foil to the front of the LSM 980 microscope with tape, making sure the foil is long enough to stretch from the top of the microscope body above the incubation chamber to the bottom of the incubation chamber and make contact with the body again (**Figure 5.4**).
    ii. Attach the foil to ground, e.g. by clamping the foil with an alligator clip and connecting to a brass grounding bar.
    iii. Adjust the positioning and grounding of the foil such that noise from surrounding electronics, including controls and computers, is minimized.

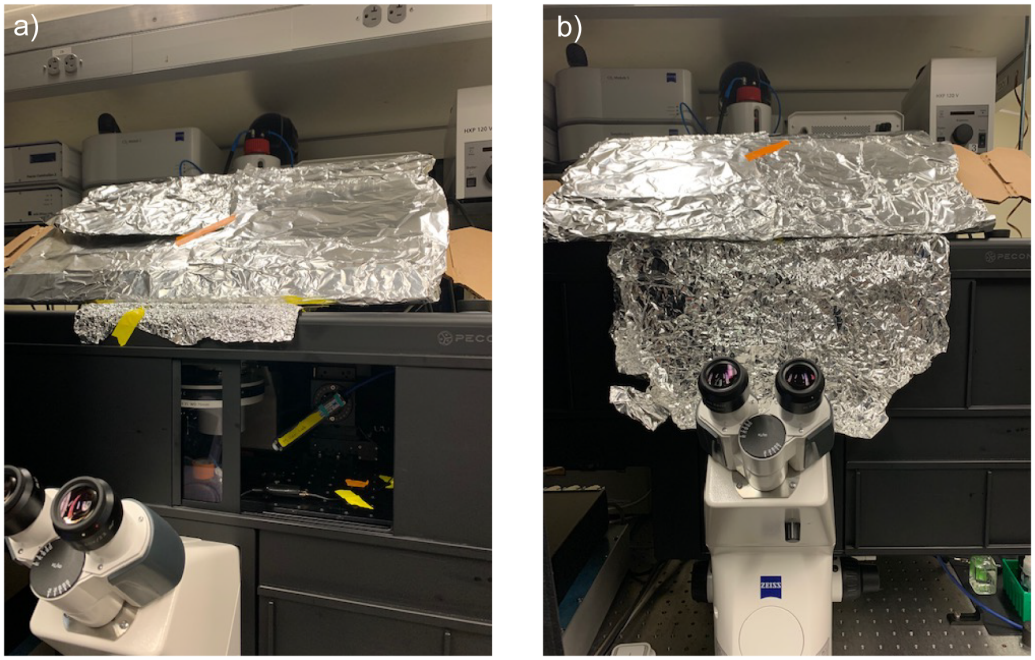


Figure 5.4 Foil setup on microscope "K" to reduce noise.
a) Foil setup to reduce noise when placing sample and locating pipette. There will still be noise with this setup. Make sure the foil is attached to ground (not pictured). b) Foil setup when the foil has been lowered to cover the front of the microscope and stage, as when going into whole-cell mode and applying voltage clamp protocols.

3. Follow step 6 and 7 as in 2.3.1, but change the image size in SPCM to 128x128 pixels, rather than 64x64 as in 2.3.1.
    i. 64x64 pixels leads to artifacts and stretching of the image in a way that has so far not been able to be corrected by changing the "left border" or "pixel clock divider" settings. Note: Ensure that there is enough signal in the desired acquisition time to get reliable fits in a 128x128 pixel image – more photons will be needed than for a 64x64 image.
4. Fill the glass pipette with internal solution and lower into the bath. Zero the voltage, and follow the steps for whole-cell patch-clamp electrophysiology. [19,20,21,22]
5. Locate the borosilicate glass pipette through the eyepieces, and position over the cell of interest, with foil set up as in **Fig. 5.4a**.
    i. The readout in Clampex membrane test will be noisy at this point. Minimize noise as much as possible, but it is unlikely it can be eliminated.
6. Lower the pipette into contact with the cell's surface, entering cell-attached mode. Correct for pipette capacitance.
7. Lower or unroll the foil on the front of the microscope to cover the front of the microscope, since the pipette will not be moved anymore, and looking at the microscope stage is no longer necessary (**Fig. 5.4b**).
    i. This should reduce the noise significantly. If not, make sure the foil is touching the front body of the microscope, contacting the metal.
8. Enter whole-cell configuration, checking the quality of the patch using the "membrane test" feature. The ratio of membrane resistance to access resistance should be greater than 30.

9. Coordinate voltage clamp protocols and FLIM measurements such that the entire time the FLIM image is being acquired, the cell is being held at the desired voltage.
    i. One way this can optionally be accomplished is by setting up a cable connecting the electrophysiology rig to the laser hub, and setting the voltage clamp protocol to trigger the laser, and setting the "Trigger" setting in SPCM to an external trigger.
    ii. Ensure the Zen light path is set to send photons to the FLIM detector and start scanning. Ensure photons are being detected in SPCM. Keep the laser scanning throughout all the protocols of the patch.
        1. This could in the future be optimized further by adding an additional triggering cable to trigger laser scanning with the protocols in Clampex.
10. Assess the quality and stability of the patch after running the voltage clamp protocol. If the patch has degraded or the cell has died, do not continue running the protocol, and start over with a new cell.
11. Repeat steps 9 and 10 with the subsequent potentials, assessing patch quality after each protocol. Apply the protocols in random order, to avoid artifacts such as changes to lifetime brought on by bleaching or cell death.
    i. While random order is best, the +80 mV protocol is sometimes not tolerated as well by cells as the others when held for such a long time. For this reason, it may be useful to perform this one last, and if the patch has degraded or the cell dies during this step, it may be omitted from the calibration.
12. Repeat the above steps for subsequent cells, in order to have multiple cells from which to generate a general calibration (**Figure 5.2b**) [12].

3. Analysis

3.1 Representation of Error in the Lifetime-Voltage Calibration

In order to reliably and accurately utilize the lifetime-voltage calibration obtained in protocol 2.3.2, an understanding of the resolution of the calibration is necessary. The calibration tends to be much more accurate at tracking changes in a particular cell's voltage than identifying the absolute membrane potential for a given cell, based on the calibration. Thus, two different measurements of resolution or error are necessary in order to have a complete understanding of the calibration and the ways it can be used. We have termed these the "intra-cell" error and the "inter-cell" error.[12]

The "intra-cell" error is the error in measuring voltage changes in a given cell over time. In other words, this value is the error expected in estimating a cell's Vm from it's measured lifetime, given that we have the calibrated lifetime-voltage relationship for that particular cell. This value is determined by calculating the root-mean-square deviation (RMSD), based on $V_{FLIM,\ intra}$ and V_{ephys} for a given cell. In this context, $V_{FLIM,\ intra}$ is the Vm estimated from a given lifetime, using that particular cell's line of best fit, and V_{ephys} is the voltage set using electrophysiology at that same measured lifetime (**Figure 5.5a**).

The "inter-cell" error is the error in measuring the absolute voltage of a given cell, based on the overall calibration for that cell line. For the "inter-cell" error, the RMSD is calculated using $V_{FLIM,\ inter}$, defined as the optical guess at Vm for each 0 mV point on each individual calibration using the average overall calibration for that cell line (which would ideally give a value of zero) and

V_{ephys}, which in this case is the y-intercept of each individual cell's calibration, or the 0 mV point on the linear regression for each cell (**Figure 5.5b**). Both of these metrics of error assume that the value set by voltage-clamp is completely accurate, but in practice there is probably some amount of error introduced via the electrophysiology as well.

The "intra-cell" error is much smaller than the "inter-cell" error, supporting that the VF-FLIM method is more accurate at reporting changes in lifetime in a particular cell, or group of cells, as outlined in 2.5.1, than for determining the absolute membrane potential of a given cell, as outlined in 2.4.1. This fact should be kept in mind for experiments using the calibration, and the limitations of the "inter-cell" resolution should especially be discussed when trying to identify absolute voltages and compare those voltages between different groups. If two experimental groups present a different measured voltage based on the lifetime-voltage calibration, but the difference is smaller than the "inter-cell" error, more validation to determine if the difference in measured voltage is meaningful will be necessary, using different techniques, for instance. The protocol outlined in 2.5.1 gives an example of the type of experiment that could be performed to track the membrane potential of a group of cells or a single cell over time, in response to a pharmacological treatment, using the smaller "intra-cell" error as the limit of resolution.

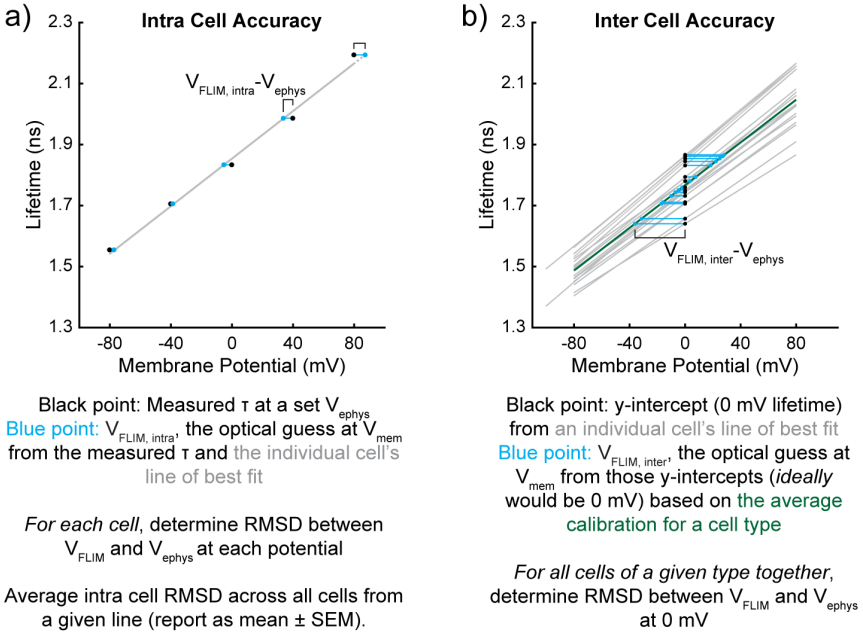


Figure 5.5. Intra and inter-cell V_{mem} resolution calculations.
a) Intra cell values are the RMSD between the voltage equivalent of the measured lifetime (V_{FLIM}) and voltage set by electrophysiology (V_{ephys}). V_{FLIM} values are calculated using that particular cell's line of best fit, so one value is obtained per cell. Here, we present intra cell error as the mean ± SEM of all cells from a given cell line. **b)** Inter cell errors are the RMSD between the voltage-equivalent of the 0 mV lifetime for all cells tested from a cell line (V_{FLIM}, determined with the average slope and y-intercept for that cell line) and the ground truth value of 0 mV. Inter-cell accuracy is calculated from all of the calibration data for a cell line, so there is one value per cell line. Black points are experimental y-intercepts and blue points are the V_{FLIM} optical voltage determinations from those lifetimes. Gray lines are lines of best fit for individual cells. Green line in (B) represents the average τ_{fl}-V_{mem} relationship for a cell line.

Conclusion

In this chapter, we outlined the use of the VoltageFluor-Fluorescence Lifetime Imaging Microscopy (VF-FLIM) method, using the potentiometric VoltageFluor dye VF2.1.Cl to perform bulk determination of membrane potential in large numbers of cells. This protocol takes readers through the steps of determining the proper concentration for use in their model system, generating a lifetime-voltage calibration using patch-clamp electrophysiology, and measuring bulk membrane potentials of hundreds of cells within a few hours. It is our hope that this method allows for the further investigation of membrane potential as a signal in populations of cells, not just in individual cells, and leads to further study of the role of membrane potential in non-electrically excitable systems.

References

(1) Cone, C. D.; Cone, C. M. Induction of Mitosis in Mature Neurons in Central Nervous System by Sustained Depolarization. *Science* **1976**, *192* (4235), 155–158. https://doi.org/10.1126/science.56781.

(2) Huang, X.; Jan, L. Y. Targeting Potassium Channels in Cancer. *J. Cell Biol.* **2014**, *206* (2), 151–162. https://doi.org/10.1083/jcb.201404136.

(3) Chen, L.; Becker, T. M.; Koch, U.; Stauber, T. The LRRC8/VRAC Anion Channel Facilitates Myogenic Differentiation of Murine Myoblasts by Promoting Membrane Hyperpolarization. *J. Biol. Chem.* **2019**, *294* (39), 14279–14288. https://doi.org/10.1074/jbc.RA119.008840.

(4) Tsuchiya, W.; Okada, Y. Membrane Potential Changes Associated with Differentiation of Enterocytes in the Rat Intestinal Villi in Culture. *Dev. Biol.* **1982**, *94* (2), 284–290. https://doi.org/10.1016/0012-1606(82)90348-7.

(5) Levin, M. Molecular Bioelectricity: How Endogenous Voltage Potentials Control Cell Behavior and Instruct Pattern Regulation in Vivo. *Mol. Biol. Cell* **2014**, *25* (24), 3835–3850. https://doi.org/10.1091/mbc.E13-12-0708.

(6) Fertig, N.; Blick, R. H.; Behrends, J. C. Whole Cell Patch Clamp Recording Performed on a Planar Glass Chip. *Biophys. J.* **2002**, *82* (6), 3056–3062. https://doi.org/10.1016/S0006-3495(02)75646-4.

(7) Peterka, D. S.; Takahashi, H.; Yuste, R. Imaging Voltage in Neurons. *Neuron* **2011**, *69* (1), 9–21. https://doi.org/10.1016/j.neuron.2010.12.010.

(8) Lazzari-Dean, J. R.; Gest, A. M. M.; Miller, E. W. Measuring Absolute Membrane Potential Across Space and Time. *Annu. Rev. Biophys.* **2021**, *50*. https://doi.org/10.1146/annurev-biophys-062920-063555.

(9) Berezin, M. Y.; Achilefu, S. Fluorescence Lifetime Measurements and Biological Imaging. *Chem. Rev.* **2010**, *110* (5), 2641–2684. https://doi.org/10.1021/cr900343z.

(10) Yellen, G.; Mongeon, R. Quantitative Two-Photon Imaging of Fluorescent Biosensors. *Current Opinion in Chemical Biology*. Elsevier Ltd August 1, 2015, pp 24–30. https://doi.org/10.1016/j.cbpa.2015.05.024.

(11) Brinks, D.; Klein, A. J.; Cohen, A. E. Two-Photon Lifetime Imaging of Voltage Indicating Proteins as a Probe of Absolute Membrane Voltage. *Biophys. J.* **2015**, *109* (5), 914–921. https://doi.org/10.1016/j.bpj.2015.07.038.

(12) Lazzari-Dean, J. R.; Gest, A. M. M.; Miller, E. W. Optical Estimation of Absolute Membrane Potential Using Fluorescence Lifetime Imaging. *eLife* **2019**, *8*. https://doi.org/10.7554/eLife.44522.

(13) Miller, E. W.; Lin, J. Y.; Frady, E. P.; Steinbach, P. A.; Kristan, W. B.; Tsien, R. Y. Optically Monitoring Voltage in Neurons by Photo-Induced Electron Transfer through Molecular Wires. *Proc. Natl. Acad. Sci.* **2012**, *109* (6), 2114–2119. https://doi.org/10.1073/pnas.1120694109.

(14) Becker, W. *The Bh TCSPC Handbook*; 2019.

(15) Boens, N.; Qin, W.; Basarić, N.; Hofkens, J.; Ameloot, M.; Pouget, J.; Lefèvre, J. P.; Valeur, B.; Gratton, E.; VandeVen, M.; Silva, N. D.; Engelborghs, Y.; Willaert, K.; Sillen, A.; Rumbles, G.; Phillips, D.; Visser, A. J. W. G.; Van Hoek, A.; Lakowicz, J. R.; Malak, H.; Gryczynski, I.; Szabo, A. G.; Krajcarski, D. T.; Tamai, N.; Miura, A. Fluorescence Lifetime Standards for Time and Frequency Domain Fluorescence Spectroscopy. *Anal. Chem.* **2007**, *79* (5), 2137–2149. https://doi.org/10.1021/ac062160k.

(16) Magde, D.; Rojas, G. E.; Seybold, P. G. Solvent Dependence of the Fluorescence Lifetimes of Xanthene Dyes. *Photochem. Photobiol.* **1999**, *70* (5), 737–744. https://doi.org/10.1111/j.1751-1097.1999.tb08277.x.
(17) Chen, R. F.; Knutson, J. R. Mechanism of Fluorescence Concentration Quenching of Carboxyfluorescein in Liposomes: Energy Transfer to Nonfluorescent Dimers. *Anal. Biochem.* **1988**, *172* (1), 61–77. https://doi.org/10.1016/0003-2697(88)90412-5.
(18) Meşe, G.; Richard, G.; White, T. W. Gap Junctions: Basic Structure and Function. *Journal of Investigative Dermatology*. Nature Publishing Group November 1, 2007, pp 2516–2524. https://doi.org/10.1038/sj.jid.5700770.
(19) Hamill, O. P.; Marty, A.; Neher, E.; Sakmann, B.; Sigworth, F. J. Improved Patch-Clamp Techniques for High-Resolution Current Recording from Cells and Cell-Free Membrane Patches. *Pflüg. Arch. Eur. J. Physiol.* **1981**, *391* (2), 85–100. https://doi.org/10.1007/BF00656997.
(20) Cummins, T. R.; Rush, A. M.; Estacion, M.; Dib-Hajj, S. D.; Waxman, S. G. Voltage-Clamp and Current-Clamp Recordings from Mammalian DRG Neurons. *Nat. Protoc.* **2009**, *4* (8), 1103–1112. https://doi.org/10.1038/nprot.2009.91.
(21) Molleman, A. The Practice of Patch Clamping. In *Patch Clamping: an Introductory Guide to Patch Clamp Electrophysiology*; John Wiley & Sons, Ltd: Chichester, UK, 2003; pp 95–114. https://doi.org/10.1002/0470856521.ch4.
(22) Penner, R. A Practical Guide to Patch Clamping. In *Single-Channel Recording*; Springer US, 1995; pp 3–30. https://doi.org/10.1007/978-1-4419-1229-9_1.

Chapter 6

Optimizing Fluorescence Lifetime Acquisition and Fit Parameters for a New Microscope Setup

Abstract

Fluorescence lifetime imaging is a promising tool for quantifying absolute membrane potential with VoltageFluor dyes, since lifetime is independent of the extrinsic factors that complicate intensity-based calibrations. However, improper fitting can lead to inconsistent and incorrect determination of lifetime values, and fit parameters can vary significantly between FLIM systems. Furthermore, acquisition settings must be carefully tuned to provide sufficient photon count rates for accurate analysis while avoiding photon pile-up. Acquisition and analysis parameters must be optimized for each microscope and laser line used to provide reproducible and reliable lifetime measurements. This chapter highlights key considerations for acquisition and exponential fitting of FLIM data, guided by our work towards accurately quantifying CRhOMe lifetime using a new laser line.

Introduction

Membrane potential (V_m) is an essential component of cellular physiology. All cells maintain an ionic gradient across the plasma membrane, giving rise to a transmembrane potential. Rapid, millisecond timescale changes in V_m trigger signaling pathways in electrically excitable cells like neurons and cardiomyocytes, which lead to neurotransmitter release and muscle contraction, respectively. However, smaller changes in V_m occurring over longer timescales in non-electrically excitable cells have also been implicated in biological processes such as cell cycle progression[1–3], differentiation[4,5], and proliferation[6]. Historically, patch-clamp electrophysiology has been the gold-standard for making quantitative measurements of membrane potential. Patch-clamp involves directly probing the cell of interest with a micropipette attached to an electrode. Although this technique enables precise measurements of V_m with high spatiotemporal resolution, it is inherently invasive and low-throughput. Optical techniques employing voltage-sensitive dyes provide a less invasive and higher throughput method to observe changes V_m. However, intensity-based measurements are limited by confounding variables such as dye concentration, dye environment, laser intensity, and photobleaching. Although optical methods can reliably report relative changes in V_m, these external factors make quantification of V_m difficult.[7,8]

Fluorescence lifetime imaging (FLIM) has been established as an alternative optical technique to quantify V_m. As with other optical methods, FLIM is minimally invasive and readily enables high throughput recordings of many cells at once. Fluorescence lifetime (τ) is measured as the amount of time a population of fluorophores remains in the excited state and is intrinsic to the molecule itself, making it independent of the variables that hinder quantification with intensity-based methods.[8,9] VoltageFluor dyes developed in the Miller lab report changes in V_m through a photoinduced electron transfer (PeT) mechanism.[10] In these dyes, the rate of PeT is controlled by the voltage across the plasma membrane. Lifetime is only dependent on the radiative (k_r) and non-radiative (k_{nr}) decay pathways from the excited state (**Equation 6.1**). PeT is a non-radiative decay pathway, meaning modulations in the rate of PeT due to fluctuations in membrane potential also produce changes in lifetime.

$$\tau = \frac{1}{k_r + k_{nr}} \tag{6.1}$$

For VoltageFluors such as VF2.1.Cl or CRhOMe, negative potentials result in a shorter lifetime, while positive potentials correspond to a longer lifetime.[10,11] The relationship between lifetime and voltage can be established through development of a calibration using patch-clamp electrophysiology.

Although FLIM circumvents many of the confounding factors that limit patch-clamp and intensity-based methods, it requires careful setting of acquisition and fit parameters to produce reliable results. During data acquisition, it is essential to carefully monitor photon count rates to avoid photon pile-up, which occurs when photons are emitted too rapidly and abundantly to be accurately detected by the photon counting card. Photon pile-up is anticipated to occur if photon counts exceed 10% of the laser repetition rate.[12]

The acquired decays are subsequently analyzed by fitting to the data to a single or multiexponetial decay function (**Equation 6.2**). If the decay contains multiple exponential components, the lifetime is reported as the amplitude weighted lifetime (**Equation 6.3**). FLIM analysis also frequently employs spatial binning between adjacent pixels to achieve sufficient photons for fitting.

$$F(t) = a_1 e^{-\frac{t}{\tau_1}} + a_2 e^{-\frac{t}{\tau_2}} + \cdots + a_n e^{-\frac{t}{\tau_n}} \tag{6.2}$$

$$\tau_m = \frac{a_1\tau_1 + a_2\tau_2 + \cdots + a_n\tau_n}{a_1 + a_2 + \cdots + a_n} \tag{6.3}$$

When fitting lifetime data, it is important to determine the shift (in units of time bins) between the instrument response function (IRF) and the measured time resolved decays. This parameter can vary between FLIM systems and should be determined for each set up by optimizing fit parameters for data acquired with a fluorophore of a known lifetime value.

Average weighted residuals and average chi^2 are two metrics to evaluate fit quality.[12] Residuals are a measure of the difference between the recorded decay, *n(t)*, and the exponential fit, *f(t)* (**Equation 6.4**). For a well-fit decay, the residuals will vary randomly due to photon statistics but should be between -5 and +5, with most values ranging from -1 to +1.

$$R(t) = \frac{f(t) - n(t)}{\sqrt{f(t)}} \tag{6.4}$$

Chi^2 is another indicator of fit quality that depends on the exponential fit, *f(t)*, the recorded decay, *n(t)*, and the number of time channels, *k*, (**Equation 6.5**). Chi^2 should be close to 1 for an ideal exponential fit.

$$\chi^2 = \sum \frac{\big(f(t) - n(t)\big)^2}{k(n(t) + 1)} \tag{6.5}$$

This chapter presents a method for validating lifetime measurements and adapting fitting parameters for a new FLIM setup using a red-shifted VoltageFluor, CRhOMe.

Results and Discussion

The lifetime of CRhOMe has been previously characterized by fitting to a monoexponential decay. Data were previously collected on two different microscopes, an LSM 880 at 640 nm and LSM 980 at 562 nm. At 640 nm, the resting lifetime of CRhOMe in HEK293T cells was determined to be 2.61 ± 0.1 (mean ± SD, n = 42). The lifetime at 562 nm in HEK293T cells was measured at 2.55 ± 0.06 (mean ± SD, n = 29). Data collected at 640 nm on the LSM 880 microscope were fit with the IRF-decay shift fixed to 0, while data collected at 562 nm on the LSM 980 microscope were fit with the shift fixed to -1.

To determine the optimal shift value for the LSM 980 at 640 nm, CRhOMe was fit varying shift values (-1, -0.3, 0) or allowed to float (**Figure 6.1, Table 6.1)**. When allowed to float, the shift is optimized to minimize chi^2 at each pixel. To evaluate fit quality between differences in fit parameters, histograms of chi^2 (calculated for each binned pixel in an ROI) and plots of weighted residuals vs time were generated.

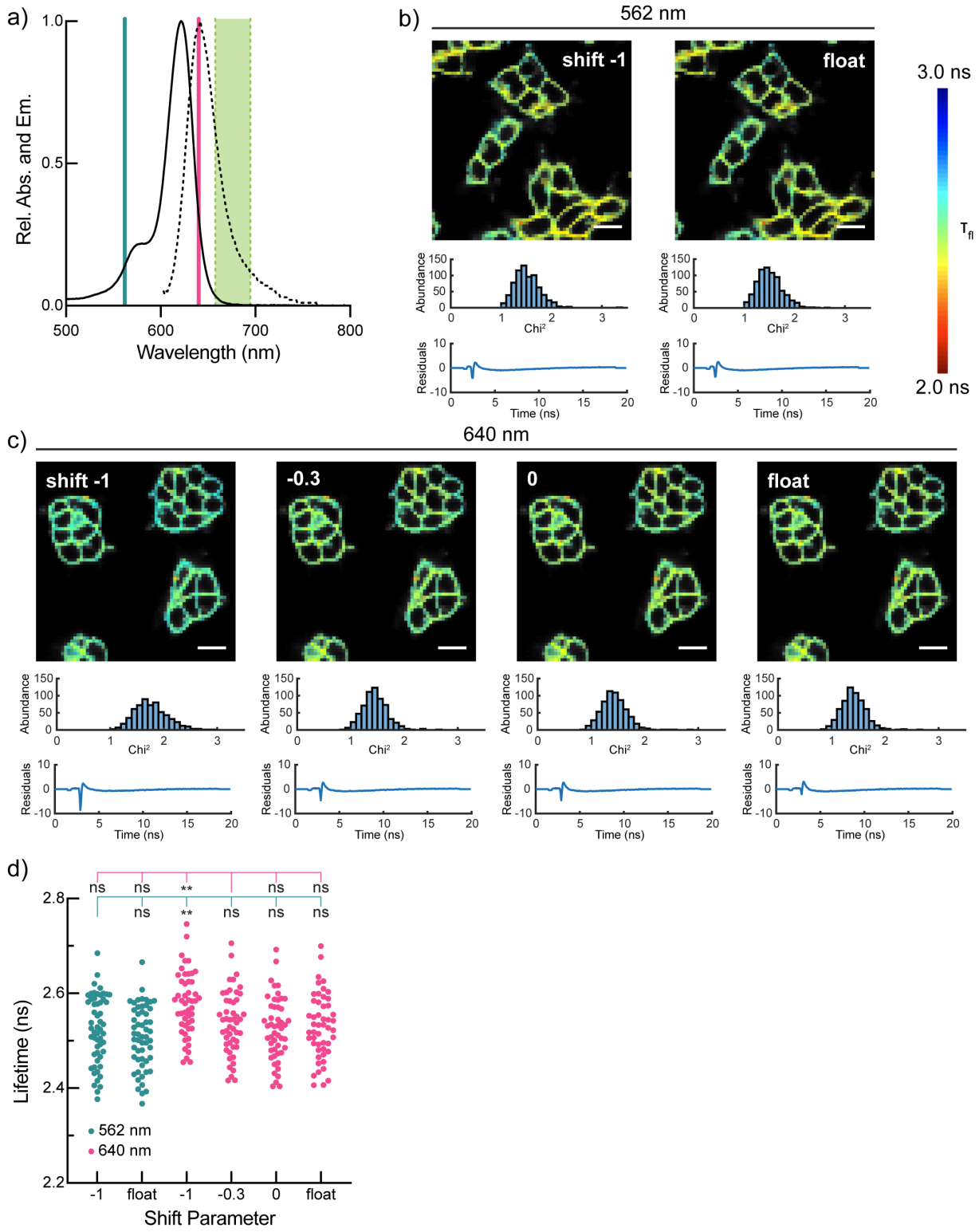


Figure 6.1. Lifetime of CRhOMe in HEK293T cells at 562 nm and 640 nm.
a) Absorbance (solid black line) and emission (dashed black line) of CRhOMe in PBS, pH 7.4, 0.1% SDS. FLIM acquisition settings are overlaid on top of the absorption and emission spectra. Excitation at 562 or 640 nm is indicated by teal or pink vertical lines. Emission was collected at 676/37 nm (shaded green). Representative lifetime-intensity overlay images of HEK293T cells loaded with 300 nM CRhOMe at 562 nm **(b)** or 640 nm **(c)**.

Scale bars are 20 μm. The shift between the instrument response function (IRF) and the measured time resolved decays was fixed to -1, -0.3, or 0, or allowed to float. Shown below each image are histograms of chi^2 (calculated for each binned pixel in an ROI) and plots of weighted residuals vs time. **d)** Scatter plot of lifetimes observed with 300 nM CRhOMe in HEK293T cells measured at 562 nm (teal) or 640 nm (pink). Each point represents an individual ROI (562 nm, n = 55; 650 nm, n = 50) consisting of approximately 1-10 cells. The shift between the IRF and the decays was fixed to -1, -0.3, or 0, or allowed to float. Asterisks indicate significant differences between the selected shift for each laser (-1 for 562 nm, [1–3]-0.3 for 640 nm) and all other fits (n.s. $p > 0.05$, * $p < 0.05$, ** $p < 0.01$, *** $p < 0.001$, **** $p < 0.0001$, ordinary one-way ANOVA, Dunnett post hoc testing).

Laser Wavelength (nm)	Shift Parameter	Lifetime (ns)
562	-1	2.53 ± 0.07
	float	2.51 ± 0.07
640	-1	2.58 ± 0.07
	-0.3	2.54 ± 0.07
	0	2.53 ± 0.07
	float	2.53 ± 0.07

Table 6.1. Lifetime of CRhOMe in HEK293T cells.
Lifetime of 300 nM CRhOMe in HEK293T cells. The data is fit well by a monoexponential decay. To determine the best fit parameters on a different microscope and TSCPC system, the shift between the instrument response function (IRF) and the measured time resolved decays was fixed to -1, -0.3, or 0, or allowed to float. Data are mean ± SD for 55 measurements at 562 nm or 50 measurements at 640 nm. The lifetime has been previously reported at 562 nm (2.55 ± 0.06; shift fixed to -1) and 640 nm (2.61 ± 0.1; shift fixed to 0).

The TMCRh dye head (1 μM in water) has also been previously well-described by fitting to a monoexponential decay. TMCRh data were also fit with the shift fixed to -1, -0.3, or 0, or allowed to float (**Figure 6.2**, **Table 6.2**). At 640 nm with a shift of -0.3, the lifetime of the dye head was 3.07 ± 0.1 ns (mean ± SEM, n = 33), which is consistent with the previously reported value of 3.06 ± 0.2 ns.

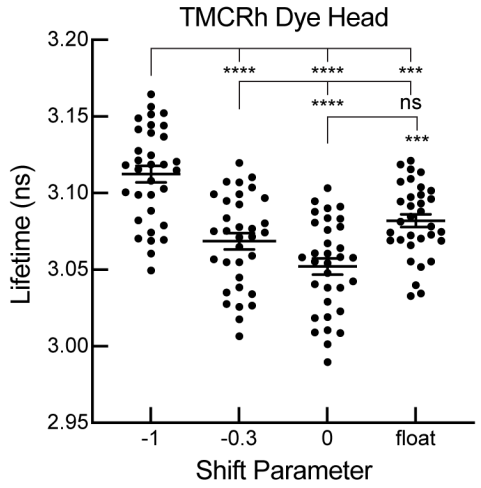


Figure 6.2. Lifetime of TMCRh fluorophore.
Scatter plot of fluorescence lifetime of the TMCRh fluorophore dye head (1 μM in water) fit with varying shift parameters. The shift between the IRF and the decays was fixed to -1, -0.3, or 0, or allowed to float. Data are mean ± SEM for 33 measurements. Asterisks indicate significant differences between fits (-1 for 562 nm, -0.3 for 640 nm) and all other fits (n.s. $p > 0.05$, * $p < 0.05$, ** $p < 0.01$, *** $p < 0.001$, **** $p < 0.0001$, ordinary one-way ANOVA, Dunnett post hoc testing).

Shift Parameter	Lifetime (ns)
-1	3.112 ± 0.005
-0.3	3.069 ± 0.005
0	3.052 ± 0.005
float	3.082 ± 0.004

Table 6.2. Lifetime of TMCRh fluorophore.
The lifetime of the TMCRh fluorophore dye head (1 μM in water) is well described by a monoexponential decay and has been previously reported as 3.06 ± 0.02 ns (mean ± SEM for 16 measurements). To determine the best fit parameters on a different microscope and TSCPC system, the shift between the instrument response function (IRF) and the measured time resolved decays was fixed to -1, -0.3, or 0, or allowed to float. Data are mean ± SEM for 33 measurements.

After evaluating the fit quality with different shift parameters, shifts of -0.3 for 640 nm and –1 for 562 nm were selected for future analyses (**Figure 6.3**). For these shift values, the residuals fell in the optimal range of -5 to +5, with most between -1 to +1. Additionally, the chi^2 values were largely distributed between 1 and 2. The lifetime of CRhOMe was 2.54 ± 0.07 ns (mean ± SD, n = 50) at 640 nm and 2.53 ± 0.07 ns (mean ± SD, n = 55) at 562 nm. These values are both consistent with the previously reported lifetimes of 2.61 ± 0.1 ns at 640 nm and 2.55 ± 0.06 ns at 562 nm. Subsequent experiments were performed at 640 nm, and data were fit with the shift fixed to -0.3.

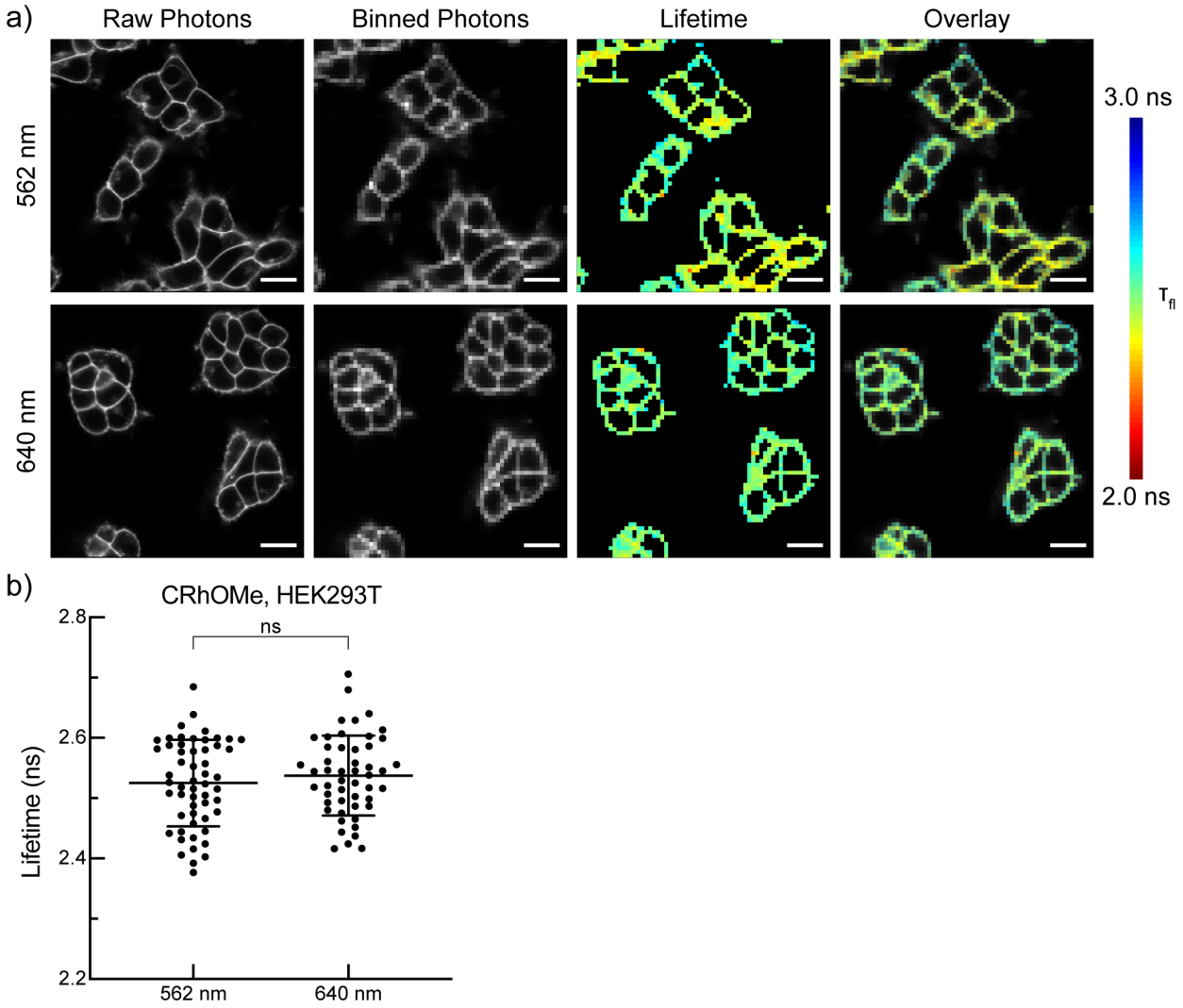


Figure 6.3. Lifetime of CRhOMe in HEK293T cells.
a) Representative raw photon intensity, binned photon intensity, lifetime, and intensity-lifetime overlay images of HEK293T cells loaded with 300 nM CRhOMe at 562 nm or 640 nm. The shift was fixed to -1 at 562 nm or -0.3 at 640 nm. Scale bars are 20 μm. **b)** Scatter plot of lifetimes observed with 300 nM CRhOMe in HEK293T cells measured at 562 nm (shift: -1) or 640 nm (shift: -0.3). Each point represents an individual ROI consisting of approximately 1-10 cells. Data are mean ± SD for 55 measurements at 562 nm or 50 measurements at 640 nm. There is not a significant difference in lifetime between the two conditions (n.s. $p > 0.05$, two-sided, unpaired, unequal variances t-test).

We also considered the possibility of photon pile-up. To reliably avoid pile-up, we aimed to keep photon counts below 1% of the laser repetition rate of 50 MHz, or 5×10^5 counts/second (cps). In SPCM software, the photon count readout averages the photon counts/second across the entire field of view. Although the average readout of photon counts may remain below 5×10^5 cps during image acquisition, the collected photons at some pixels may exceed the photon pile-up limit.

To evaluate the effect of photon pile-up, we collected resting lifetime data in HEK293T cells at varying photon counts (**Figure 6.4**, **Table 6.3**). To acquire this data, the ND wheel was adjusted such that the ADC read 1×10^5 cps, 3×10^5 cps, or 6×10^5 photons/s. At 5×10^5 photons/s, we expected

to exceed the pile-up limit and indeed observed a shortening of the lifetime from 2.54 ± 0.01 ns (3×10^5 cps, mean ± SEM, n = 78) to 2.40 ± 0.01 ns (n = 24). At lower photon counts (1×10^5 cps) the lifetime was measured at 2.51 ± 0.01 ns (n = 18). The difference in lifetime between 1×10^5 and 3×10^5 cps was not statistically significant; however, there was a significant difference between lifetimes at these count rates compared to the lifetimes at 5×10^5 cps (ordinary one-way ANOVA, $p < 0.0001$). It may seem advantageous to keep photon counts as low as possible to completely prevent the possibility of pile-up. However, at lower photon counts, it is necessary to increase pixel binning to obtain sufficient photons for fitting, which decreases spatial resolution. Instead, it is preferable to keep photon counts low enough to avoid pile-up, but as high as possible to minimize the amount of spatial binning required to fit the data. Images acquired at photon counts around 3×10^5 cps reliably yield lifetimes consistently with previous results with spatial binning of 3×3 or 4×4 pixels.

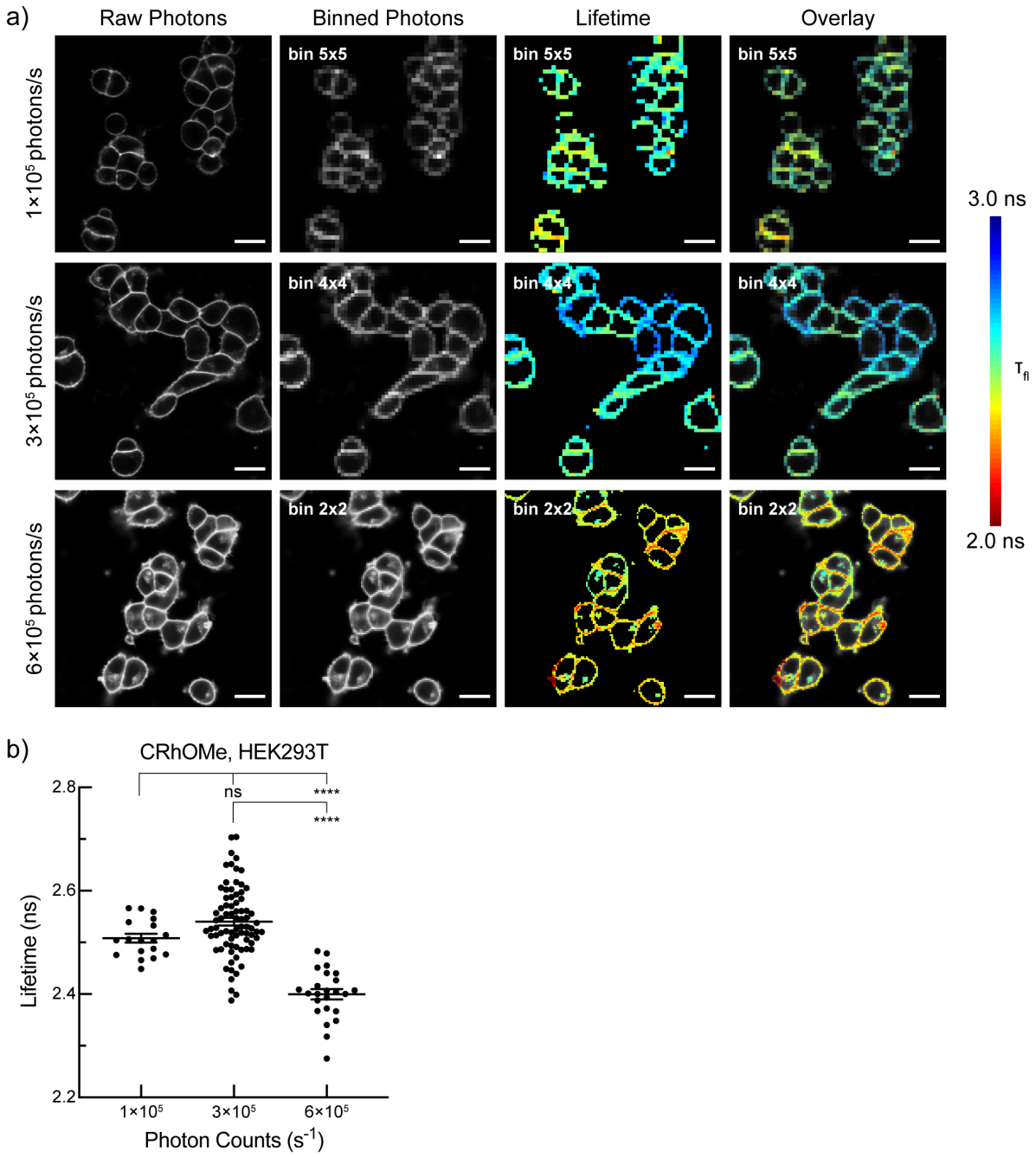


Figure 6.4. CRhOMe lifetime at varying photon count rates.
a) Representative raw photon intensity, binned photon intensity, lifetime, and intensity-lifetime overlay images of HEK293T cells loaded with 300 nM CRhOMe at 640 nm (shift: -0.3). Images were recorded at varying photon count rates (1×10^5, 3×10^5, or 6×10^5 counts per second). Spatial binning of pixels is indicated on each binned image. Scale bars are 20 μm. **b)** Scatter plot of lifetimes observed with 300 nM CRhOMe in HEK293T cells measured at 640 nm (shift: -0.3) with varying photon count rates. Each point represents an individual ROI consisting of approximately 1-10 cells. Data are mean ± SEM for 18 measurements at 1×10^5 counts/second, 78 measurements at 3×10^5 counts/second, and 24 measurements at 6×10^5 counts/second. Asterisks indicate significant differences between the photon count rates (n.s. $p > 0.05$, * $p < 0.05$, ** $p < 0.01$, *** $p < 0.001$, **** $p < 0.0001$, ordinary one-way ANOVA, Dunnett post hoc testing).

Photon Count Rate (s^{-1})	Lifetime (ns)
1×10^5	2.51 ± 0.01
3×10^5	2.54 ± 0.01
6×10^5	2.40 ± 0.01

Table 6.3. Lifetime of CRhOMe at varying photon count rates.
Lifetime of 300 nM CRhOMe in HEK293T cells at 640 nm measured at varying photon count rates. The shift between the instrument response function (IRF) and the measured time resolved decays was fixed to -0.3. Data are mean ± SEM for 18 measurements at 1×10^5 counts/second, 78 measurements at 3×10^5 counts/second, and 24 measurements at 6×10^5 counts/second.

After determining a working range for photon counts (approximately 2.5×10^5 to 3.5×10^5 cps), we wanted to make sure we could identify differences in average lifetime between populations of cells. We measured CRhOMe lifetime in HEK293T cells in response to the ionophore gramicidin, which increases membrane permeability to Na^+ and K^+ ions. We expected to produce a depolarization to approximately 0 mV, corresponding to an increase in CRhOMe lifetime. Accordingly, the lifetime in HEK293T cells treated with 500 ng/mL gramicidin rose to 2.66 ± 0.01 (mean ± SEM, n = 19, **Figure 6.5**). Comparatively, the lifetime was measured at 2.55 ± 0.01 ns in cells treated with the vehicle (0.1% DMSO).

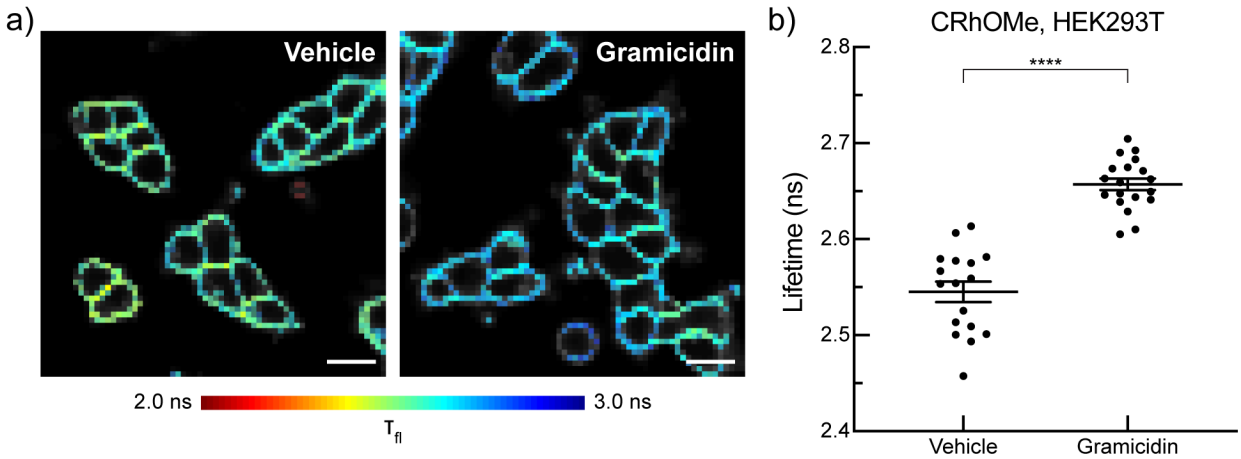


Figure 6.5. Lifetime of CRhOMe in HEK293T cells at rest or depolarized with gramicidin.
a) Representative lifetime-overlay images of HEK293T cells loaded with 300 nM CRhOMe and treated with 500 ng/mL gramicidin or vehicle (0.1% DMSO). Scale bars are 20 µm. **b)** Scatter plot of lifetimes observed with 300 nM CRhOMe in HEK293T cells treated with 500 ng/mL gramicidin or vehicle (0.1% DMSO). Each point represents an individual ROI consisting of approximately 1-10 cells. Data are mean ± SEM for 17 measurements with vehicle (2.55 ± 0.01 ns) or 19 measurements with 500 ng/mL gramicidin (2.66 ± 0.01 ns). The shift between the instrument response function (IRF) and the measured time resolved decays was fixed to -0.3. Asterisks indicate significant differences between the photon count rates (n.s. $p > 0.05$, * $p < 0.05$, ** $p < 0.01$, *** $p < 0.001$, **** $p < 0.0001$, two-sided, unpaired, unequal variances t-test).

After validating the resting lifetime of CRhOMe, we sought to confirm the lifetime-voltage calibration through patch clamp electrophysiology. In prior studies, CRhOMe was voltage-clamped in HEK293T cells, and the sensitivity was calculated at 3.09 ± 0.07 ns with a y-intercept (0 mV lifetime) of 2.71 ± 0.03 ns. Initial attempts to calibrate CRhOMe at 640 nm resulted in a calibration with a slope of 2.74 ± 0.1 ns and y-intercept at 2.39 ± 0.03 ns (mean ± SEM, **Figure 6.6a,b**, **Table 6.4**). These data were collected with the ADC photon counts adjusted to

approximately 2×10^5 counts/second or higher. Since both the slope and y-intercept were lower than expected based on the previous calibration, we again considered the possibility of photon pile-up.

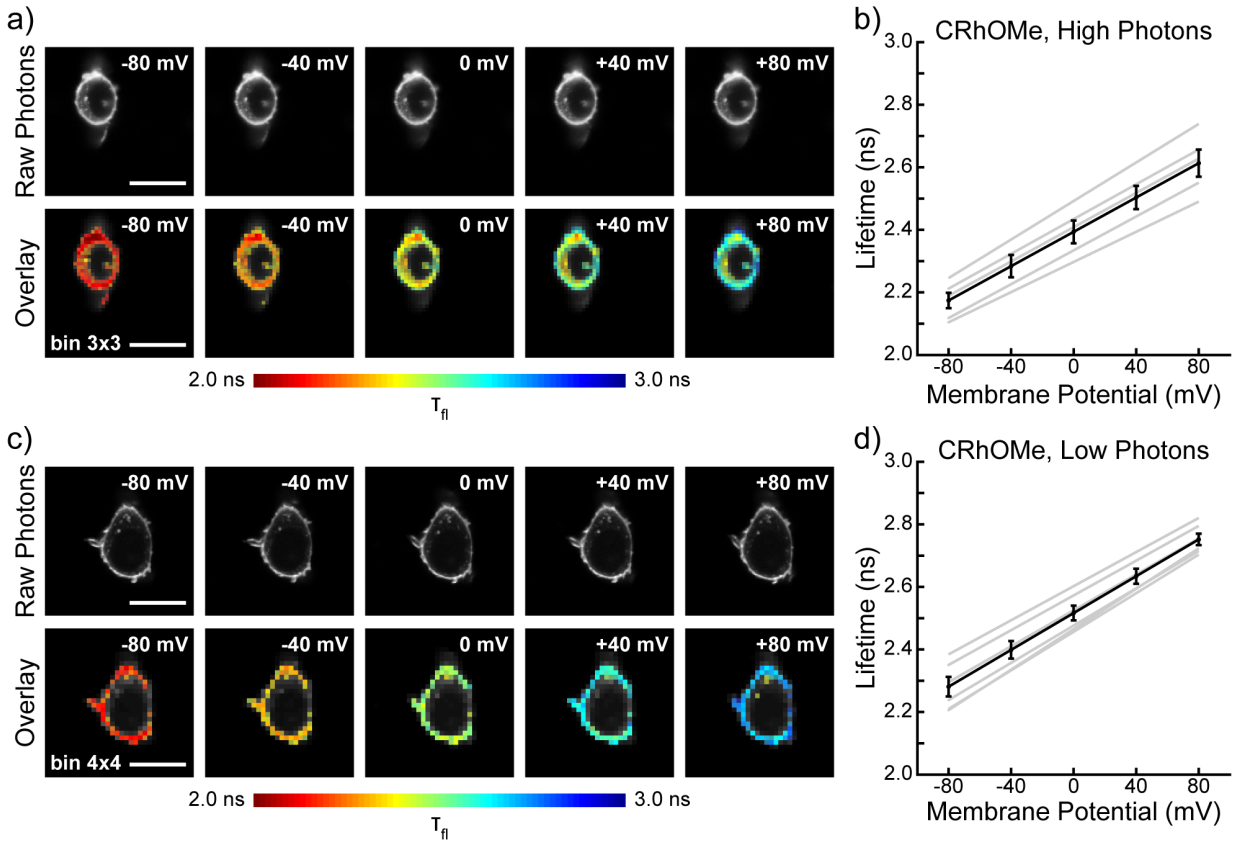


Figure 6.6. CRhOMe lifetime-voltage calibration at high and low photon counts.
a) Representative raw photon intensity and binned lifetime-intensity overlay images of a HEK293T cell loaded with 300 nM CRhOMe and patch-clamped at the indicated voltages. Images were acquired at photon count rates of 2×10^5 counts/second or higher. Scale bars are 20 µm. **b)** Plot of CRhOMe lifetime vs voltage in HEK293T cells measured at photon count rates of 2×10^5 counts/second or higher. Gray lines are individual cell calibrations (n = 5). The average calibration is in black. Error bars are mean ± SEM. **c)** Representative raw photon intensity and binned lifetime-intensity overlay images of a HEK293T cell loaded with 300 nM CRhOMe and patch-clamped at the indicated voltages. Images were acquired at photon count rates of 1×10^5 counts/second. Scale bars are 20 µm. **b)** Plot of CRhOMe lifetime vs voltage in HEK293T cells measured at photon count rates of 1×10^5 counts/second. Gray lines are individual cell calibrations (n = 6). The average calibration is in black. Error bars are mean ± SEM.

	Slope (ps/mV)	Y-Intercept (ns)	Inter-Cell RMSD (mV)	Intra-Cell RMSD (mV)
High Photons	2.74 ± 0.1	2.39 ± 0.03	25	6.62 ± 0.73
Low Photons	2.94 ±0.07	2.51 ± 0.02	19	4.90 ± 0.66

Table 6.4. CRhOMe lifetime-voltage calibration at high and low photon counts.
Slope, y-intercept, inter-cell RMSD, and intra-cell RMSD for CRhOMe in HEK293T cells. Data are mean ± SEM for 6 cells at high photon counts (>2×10^5 counts/second) or 5 cells at low photon counts (1×10^5 counts/second).

The readout of photon counts is averaged across the entire field of view, and previous RMP data was acquired with a field of view of 256×256 pixels (141.42×141.41 μm). Patch-clamp electrophysiology data for the lifetime-voltage calibrations is acquired with a smaller field of view, 128×128 pixels (53×53 μm), so we also needed to determine the optimal photon counts for recordings of single cells. We made five sequential measurements on single HEK293T cells at 1×10^5, 1.5×10^5, or 2×10^5 photons/s to determine how much lifetime is affected by repetitive measurements on the same cell (**Figure 6.7**). At all count rates, the range of measured lifetimes was 40 ps or less.

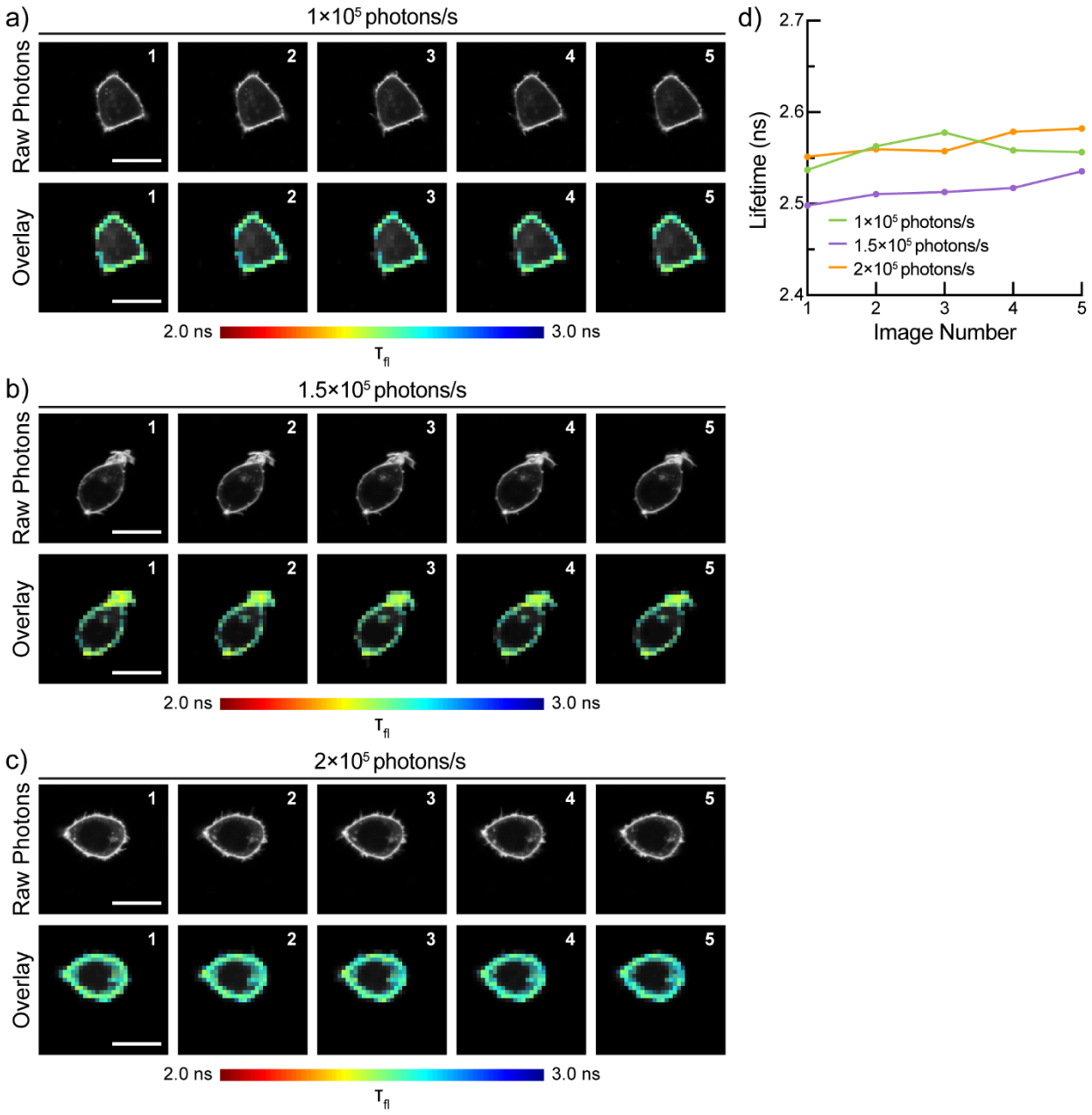


Figure 6.7. Repeated lifetime measurements on single HEK293T cells.
Representative raw photon intensity and binned lifetime-intensity overlay images of HEK293T cells loaded with 300 nM CRhOMe and measured at photon count rates of **a)** 1×10^5 counts/second, **b)** 1.5×10^5 counts/second, and

c) 2×10^5 counts/second. Five sequential images were acquired (each lasting 15 seconds) to replicate the amount and duration of measurements made during patching. **d)** Plot of fluorescence lifetime vs. image acquisition cycle from **a)** (green), **b)** (purple), and **c)** (orange).

In further patching experiments, we aimed to keep photon count rates around 1×10^5 photons/s. This new data produced a calibration with a slope of 2.94 ± 0.07 ns and y-intercept at 2.51 ± 0.02 ns (mean ± SEM, **Figure 6.6c,d**, **Table 6.4**). The difference between these two calibrations highlights the importance of carefully monitoring photon counts to keep them well below reported pile-up limits. Although the y-intercept of the new calibration at lower photon counts remains lower than previously reported, we believe this was primarily due to an unreliable patch-clamp equipment. We have recently repaired the headstage and replaced the amplifier used for patching, and further experiments to validate the CRhOMe lifetime-voltage calibration are ongoing.

Conclusion

We present a method to validate fluorescence lifetime measurements on a new microscope, while avoiding photon pileup and retaining sufficient spatial resolution. In particular, we recommend keeping photon counts near 1×10^5 photons/s for a single cell or 3×10^5 photons/s for larger fields of view to reliably avoid lifetime artifacts from photon pile-up. Acquisition of lifetime data at several count rates and subsequent exponential fitting can inform a reliable working range of photon counts for a particular image size.

Lifetime fit parameters must also be carefully fine-tuned, especially the time shift between the IRF and the recorded fluorescence decay, which is variable between different laser lines and microscopes. To determine the optimal shift, we recommend fitting data with different shift parameters, starting by allowing the shift to float to optimize fit quality. The shift can then be fixed to several values across the range of floating shifts to determine a single, fixed shift value for consistent fitting across experiments. Fit quality can be assessed by evaluating chi^2 and residuals.

Methods

Cell Culture

HEK293T cells were obtained from the UC Berkeley Cell Culture Facility. Cells were verified by STR profiling (short tandem repeat) and were tested routinely for mycoplasma. Cell lines were discarded after 25 passages. Cells were maintained and plated in Dulbecco's Modified Eagle Medium (DMEM; Gibco) supplemented with 4.5 g/L glucose, 2 mM GlutaMAX (Gibco), and 10% seradigm fetal bovine serum (FBS; Gibco) in a 37°C humidified incubator at 5% CO_2. Cells were passaged into fresh complete media every few days following dissociation with 0.05% trypsin-EDTA (Gibco).

For imaging experiments, 25 mm #1.5 glass coverslips were pre-coated with poly-D-lysine (PDL) prior to plating cells. Coverslips were incubated in PDL (0.1 mg/mL in PBS; Sigma-Aldrich) for at least 1 hour in a 37°C humidified incubator and then washed twice with sterile water and twice with 1x Dulbecco's Phosphate Buffered Saline (dPBS; Gibco). For resting lifetime experiments, cells were plated on 25 mm coverslips in 6-well tissue culture plates at a density of 42,000 cells/cm^2. For electrophysiology and single cell recordings, cells were plated at a density of 16,000 cells/cm^2 in low glucose DMEM (Gibco; 1 g/L glucose, 1 mM sodium pyruvate, 2 mM GlutaMAX, 10% FBS). Cells were imaged 16-24 hours after plating.

Gramicidin (Thermo Fisher) was made up as a 1 mg/mL stock in DMSO and stored at -20°C. Working solutions were prepared at 500 ng/mL in IB immediately before use. Immediately after dye loading, HEK293T cells were incubated for 5 minutes at room temperature in IB containing either gramicidin or DMSO vehicle. Coverslips were then transferred to fresh IB with gramicidin or vehicle and imaged.

VoltageFluor Loading

CRhOMe was loaded at 300 nM in HEK293T cells. Loading solutions were prepared in imaging buffer (IB, made in-house; composition in mM: 139.5 NaCl, 10 HEPES, 5.6 D-glucose, 5.33 KCl, 1.26 $CaCl_2$, 0.49 $MgCl_2$, 0.44 KH_2PO_4, 0.41 $MgSO_4$, 0.34 NaH_2PO_4; 285 mOsm/L; pH 7.25) directly from a 1 mM DMSO stock. Osmolarity was determined with a μOsmette (Precision Instruments). Cells were incubated at 37°C for 25 minutes in loading solution, washed once with IB, and transferred to fresh IB in an Attofluor cell imaging chamber (Invitrogen).

Electrophysiology

Pipettes were pulled from borosilicate glass with filament (Sutter Instruments, Novato, CA) with resistances ranging from 4 to 8 MΩ with a P97 pipette puller (Sutter Instruments). Internal solution composition, in mM (pH 7.25, 285 mOsmol/L): 125 potassium gluconate, 10 KCl, 5 NaCl, 1 EGTA, 10 HEPES, 2 ATP sodium salt, 0.3 GTP sodium salt. EGTA (tetraacid form) was prepared as a stock solution in 1 M KOH before addition to the internal solution. Pipettes were positioned with an MP-225 micromanipulator (Sutter Instruments). For voltage clamp protocols during fluorescence lifetime experiments, a liquid junction potential of -14 mV was determined by the Liquid Junction Potential Calculator in the pClamp software package (Molecular Devices), and voltage step protocols used in conjunction with fluorescence lifetime measurements were corrected for this offset. Electrophysiology recordings were made with an Axopatch 200B amplifier and digitized with a Digidata 1440A (Molecular Devices). For voltage sensitivity measurements on the

fluorescence lifetime system, cells were held at -60 mV and potentials from +80 to -80 mV were applied. Voltage steps were applied with a variable order of -80, -40, 0, and +40 mV steps, followed by a +80 mV step as the final voltage applied, with each voltage step holding for 15 seconds. Signals were sampled at 50 kHz and filtered with a 5 kHz low-pass Bessel filter. Correction for pipette capacitance was performed in the cell attached configuration. Recordings were only included if they maintained a 30:1 ratio of membrane resistance (R_m) to access resistance (R_a) and an R_a value below 30 MΩ throughout the recording.

Fluorescence Lifetime Data Acquisition

Fluorescence lifetime imaging was performed on an inverted LSM 980 confocal microscope (Zeiss) equipped with a SPC-150NX single photon counting card (Becker and Hickl). The LSM 980 was controlled with Zen Blue software (Zeiss), and the TCSPC unit was controlled with SPCM software (Becker-Hickl). Pulsed excitation at 50 MHz was supplied with a 562 nm diode laser (BDS-SMY-562, Becker-Hickl) or 640 nm diode laser (BDS-SM-640-FBC-101, Becker-Hickl) and controlled through an LHB-104 Laser Hub (Becker-Hickl). Power was adjusted with a neutral density filter wheel to set desired photon count rates. Average power at the sample ranged from 1-3 μW. Excitation light was coupled to the microscope with a polarization-maintaining fiber and passed through a 405/485/560/640 beam splitter (Zeiss). Emitted photons were collected with a 40x oil/1.3 NA Apochromat objective (Zeiss), immersed in Immersol 518F (Zeiss). The confocal pinhole was set to 35 μm (1 airy unit). The emitted photons were passed through a 676/37 bandpass filter (Semrock) and detected with an HPM-100-40 hybrid detector (Becker-Hickl), based on a Hamamatsu R10467 GaAsP hybrid photomultiplier tube. Detector dark counts were kept below 300 per second during acquisition and were generally lower than 200 per second. The detector parameters used were the following: constant fraction discriminator (CFD) -50.98 mV, zero cross 5.29 mV. Sync parameters used were the following: CFD -50.98 mV, zero cross 5.29 mV, offset 5.10 %, sync divider 1, dither range 1/16. Resting lifetime and gramicidin data were acquired with 256 time channels in the analog-to-digital-converter (ADC) and 256x256 pixels of spatial resolution during 75 second exposures. Electrophysiology and single cell data were acquired with 256 TCSPC time channels and 128x128 pixels of spatial resolution during five 15 second exposures. All five images were acquired sequentially without a break in laser illumination. The instrument response function (IRF) was measured each day from a solution of 1 mg/mL erythrosin B in water. The TMCRh dye head (1 μM in water) was also routinely recorded as a standard to verify correct instrument function and fitting parameters. The microscope incubation chamber was set to 25°C to minimize temperature fluctuations during experiments and between days. Cells were used immediately after loading CRhOMe and were generally kept on the microscope for under 30 minutes. No cells were kept for on the microscope for longer than an hour.

Fluorescence Lifetime Data Analysis

CRhOMe lifetime data were modeled as a monoexponential decay (**Equation 1**) in custom MATLAB code via a weighted least-squares approach. In this equation, A represents the amplitude of the photon count signal and τ represents the fluorescence lifetime.

$$F(t) = Ae^{-t/\tau} \quad (1)$$

Minimization of the reduced chi squared (χ^2, **Equation 2**) was used to determine the final parameter values, where n is the number of free parameters (number of fit time channels – number

of free parameters in model), st is the first fit time channel, fi is the final fit time channel, z is the value of the fit model, and x is the value of the experimentally measured decay. Poisson weighting of the time channels was used.

$$\chi^2 = \frac{1}{n}\sum_{i=st}^{fi}\frac{(z_i - x_i)^2}{|z|} \quad (2)$$

The built-in minimization function fmincon with the interior-point algorithm was used, with the following settings: StepTolerance 1e-4, OptimalityTolerance 1e-4, ConstraintTolerance 1e-6. All fits converged in fewer than the maximum number of function evaluations (1e5). The fluorescence lifetime τ was constrained between 0 and 10 ns. The experimentally measured instrument response function (IRF, erythrosin B fluorescence decay) was cropped to time channels 29 to 48 (562 nm data) or 36 to 52 (640 nm data) out of 256 ADC channels and reconvolved with the decay model before the reduced chi squared was determined. Time channels 20 through 256 of the measured time resolved decays were used in fitting. The shift between the IRF and the measured time resolved decays was allowed to float or fixed to -1, -0.3, or 0 (in units of ADC time channels) as indicated. Ultimately, data were best fit with the shift fixed to -1 (562 nm data) or -0.3 (640 nm data). The offset (time-independent background) was fixed to 0, as the dark counts were generally negligible (below 200 counts per second during experiments). A threshold of 5000 total photons was used in pixelwise analysis. Pixels with photon counts below this threshold were excluded from analysis and appear black in lifetime images. Standard spatial binning was performed before fitting for pixel-by-pixel analysis. For resting lifetime and gramicidin images, the raw pixel width was 0.55 μm. Pixels were generally binned 3x3 or 4x4, resulting in binned pixel widths of 1.7 μm or 2.2 μm, respectively. Resting life data acquired at low photon counts (1×10^5 photons/s) were binned 5x5, producing binned pixels of 2.8 μm, while data acquired at high photon counts (6×10^5 photons/s) were binned 2x2 and resulting binned pixels were 1.1 μm wide. Electrophysiology and single cell images were acquired with a raw pixel width of 0.41 μM. Pixels were binned 3x3 or 4x4, so binned pixels were 1.2 μm or 1.7 μm wide, respectively. Raw photon intensity images are displayed at the native resolution, while binned photon, lifetime, and lifetime-intensity overlay images reflect spatial binning.

Regions of interest (ROIs) were automatically determined from raw photon intensity images by sharpening and then thresholding the signal intensity with custom MATLAB code. Regions of images that were partially out of the optical section or contained punctate debris were omitted. In general, ROIs were single cells or small groups of 2-10 cells. The τ across all pixels in each ROI was averaged to give one overall lifetime per ROI.

Lifetime-Voltage Calibration

The relationship between the lifetime (τ_{fl}) and membrane potential for each patch-clamped cell was determined by linear regression, yielding a sensitivity (*m,* ps/mV) and a 0 mV lifetime (*b*, ps), which were subsequently averaged to give an overall linear calibration (**Equation 3**).

$$\tau_{fl} = m * V_m + b \quad (3)$$

Differences in the measured lifetime at a defined reference point (for us, the 0 mV lifetime) across measured cells provides an estimate of the voltage-independent noise for the lifetime-voltage calibration of CRhOMe, and thus the resolution we can expect when using this calibration. We report this resolution as the root-mean-square deviation (RMSD) between the optically determined voltage using the developed calibration (V_{FLIM}) and the voltage of the cell as set by voltage clamp (V_{ephys}). The RMSD of a set of n measurements (**Equation 4**) can be determined from the variance (**Equation 5**) and the bias (**Equation 6**) of the estimator (V_{FLIM}) as compared to the assumed "true" value, in this case determined by electrophysiology (V_{ephys}).

$$RMSD = \sqrt{\sigma^2 + Bias^2} \tag{4}$$

$$\sigma^2 = \frac{1}{n}\sum_{i=1}^{n}\left(V_{FLIM,i} - V_{ephys,i}\right)^2 \tag{5}$$

$$Bias = \frac{1}{n}\sum_{i=1}^{n} V_{FLIM,i} - \frac{1}{n}\sum_{i=1}^{n} V_{ephys,i} \tag{6}$$

The voltage-independent variations in lifetime are larger between cells than within a cell, and thus the voltage resolution in cells can be estimated with two values: the intra-cell resolution and the inter-cell resolution. The intra-cell resolution is a measure of the resolution expected for tracking and quantifying changes within an individual cell, determined by the RMSD between an individual cell's "optical guess" at the lifetime for a particular voltage step, from its individual line of best fit, and the actual measured lifetime at that point. The inter-cell resolution is the single-trial resolution of estimating an individual cell's membrane potential from its lifetime, determined from the RMSD between the 0 mV τ_{fl} value from each individual cell's determined lifetime-voltage relation and the 0 mV τ_{fl} determined by the average calibration. The inter-cell RMSD quantifies how well the lifetime-V_m relationship for a given cell line is likely to represent an individual cell's lifetime-V_m relationship. This method of calculating error assumes that the electrophysiology measurement is perfectly accurate and precise. Realistically, it is likely that some of the variation seen is due to the quality of the voltage clamp. As a result, these RMSD values provide a conservative upper bound for the voltage errors in VF-FLIM.

Statistical Analysis

Hypothesis testing was performed as indicated with either analysis of variance (ANOVA) followed by appropriate post hoc testing or two-sided, unpaired, unequal variances t-tests. All statistical analysis was performed in Prism 10 (GraphPad).

References

(1) Sutherland, R. L.; Hall, R. E.; Taylor, I. W. Cell Proliferation Kinetics of MCF-7 Human Mammary Carcinoma Cells in Culture and Effects of Tamoxifen on Exponentially Growing and Plateau-Phase Cells. *Cancer Res.* **1983**, *43* (9), 3998–4006.

(2) Wonderlin, W. F.; Woodfork, K. A.; Strobl, J. S. Changes in membrane potential during the progression of MCF-7 human mammary tumor cells through the cell cycle. *J. Cell. Physiol.* **1995**, *165* (1), 177–185. https://doi.org/10.1002/jcp.1041650121.

(3) Huang, X.; Jan, L. Y. Targeting Potassium Channels in Cancer. *J. Cell Biol.* **2014**, *206* (2), 151–162. https://doi.org/10.1083/jcb.201404136.

(4) Chen, L.-C.; Chen, B.-K.; Liu, Y.-W.; Chang, W.-C. Induction of 12-Lipoxygenase Expression by Transforming Growth Factor-α in Human Epidermoid Carcinoma A431 Cells. *FEBS Lett.* **1999**, *455* (1–2), 105–110. https://doi.org/10.1016/S0014-5793(99)00865-0.

(5) Tsuchiya, W.; Okada, Y. Membrane Potential Changes Associated with Differentiation of Enterocytes in the Rat Intestinal Villi in Culture. *Dev. Biol.* **1982**, *94* (2), 284–290. https://doi.org/10.1016/0012-1606(82)90348-7.

(6) Levin, M. Molecular Bioelectricity: How Endogenous Voltage Potentials Control Cell Behavior and Instruct Pattern Regulation in Vivo. *Mol. Biol. Cell* **2014**, *25* (24), 3835–3850. https://doi.org/10.1091/mbc.E13-12-0708.

(7) Peterka, D. S.; Takahashi, H.; Yuste, R. Imaging Voltage in Neurons. *Neuron* **2011**, *69* (1), 9–21. https://doi.org/10.1016/j.neuron.2010.12.010.

(8) Lazzari-Dean, J. R.; Gest, A. M. M.; Miller, E. W. Measuring Absolute Membrane Potential Across Space and Time. *Annu. Rev. Biophys.* **2021**, *50*, 447–468. https://doi.org/10.1146/annurev-biophys-062920-063555.

(9) Berezin, M. Y.; Achilefu, S. Fluorescence Lifetime Measurements and Biological Imaging. *Chem. Rev.* **2010**, *110* (5), 2641–2684. https://doi.org/10.1021/cr900343z.

(10) Miller, E. W.; Lin, J. Y.; Frady, E. P.; Steinbach, P. A.; Kristan, W. B.; Tsien, R. Y. Optically Monitoring Voltage in Neurons by Photo-Induced Electron Transfer through Molecular Wires. *Proc. Natl. Acad. Sci.* **2012**, *109* (6), 2114–2119. https://doi.org/10.1073/pnas.1120694109.

(11) Gest, A. M. M.; Lazzari-Dean, J. R.; Ortiz, G.; Yaeger-Weiss, S. K.; Boggess, S. C.; Miller, E. W. A Red-Emitting Carborhodamine for Monitoring and Measuring Membrane Potential. *Proc. Natl. Acad. Sci.* **2024**, *121* (14), e2315264121. https://doi.org/10.1073/pnas.2315264121.

(12) Becker, W. *The Bh TCSPC Handbook, 10th Edn*; 2023.